A geochemical study of speleothems and cave waters in basaltic caves at Lava Beds National Monument, Northern California, USA

by

Joshua A. Ford

B.A., Hanover College, 2018

A THESIS

submitted in partial fulfillment of the requirements for the degree

MASTER OF SCIENCE

Department of Geology
College of Arts and Sciences

KANSAS STATE UNIVERSITY
Manhattan, Kansas

2020

Approved by:

Co-Major Professor
Matthew Brueseke

Approved by:

Co-Major Professor
Saugata Datta

Abstract

Lava caves within Lava Beds National Monument (LBNM), CA, were selected as terrestrial analog sites for caves observed on other planetary bodies. The lava caves at LBNM were found to contain active microbial communities, including colorful biofilms. Additionally, the caves were discovered to host a variety of morphologically distinct secondary mineral deposits known as speleothems. Speleothems and co-located cave waters were collected to determine their compositions and assess geochemical biosignatures. Speleothems were analyzed for mineralogical, elemental, and internal stratigraphic contents. Cave waters were analyzed for major elements, major ions, DOC, and stable isotopes. Speleothems were found to be comprised primarily of opal-A and calcite, with elemental chemistries dominated by SiO_2 and CaO, alongside lesser concentrations of MgO. Speleothem formation was ultimately interpreted to be driven by both inorganic and biological factors, including availability of water, extent of evaporation, and nucleation influenced by microbial bioaccumulation. Mineral precipitation likely occurs due to evaporation of water films supplied by condensation and capillary action, with opal favored in wet conditions and calcite in dry conditions, where increased evaporative concentration favors the precipitation of calcite and Mg carbonate. Microbes likely mediate precipitation through nucleation of porous opal by bound silanol in microbial extracellular products. This creates a microsystem wherein autotrophic bacteria may encourage carbonate mineral precipitation via CO_2 consumption increasing pH, and may be reflected in the presence of both microstromatolite-like opal and calcite lamina and a predominance of DOC in cave waters. These findings contribute to the further understanding and characterization of lava cave speleothems as potential biosignature targets.

Table of Contents

List of Figures

List of Tables

Acknowledgements

This work is dedicated to all those that made this endeavor possible. I sincerely thank all of you and I cannot properly express my gratitude enough.

I would like to specifically thank all members of the BRAILLE project and the associated PSTAR grant (NNH16ZDA001N) that made this work possible, including Jennifer Blank, Duane Moser, Matt Selensky, Diana Northup, Maggie Osburn, Molly Devlin, Jennifer Hathaway and more. Collaborating on this work has simply been the greatest, and I feel lucky to be a part of such a great team. A big thanks to Jennifer Blank for her wonderful guidance and insights into my work.

A very special thanks to my major advisor Saugata Datta, who made sure to challenge me and help me find new opportunities. Thank you for pushing me to improve my writing and analytical abilities, as well as for your continued kindness, support, and guidance.

Another big thank you to Harshad Kulkarni, whose collaboration and support has been very integral to this work – I loved working with you and I wish you the very best.

To Richard Léveillé – thank you very much for bringing me into Lava Beds National Monument alongside the ATILT team two years ago – you got me off to a great start. The opal samples you provided also proved to be very useful for this work as well!

To everyone at the University of Texas at San Antonio, thank you very much for making me feel at home for the time I was away from K-STATE. Additionally, a massive thank you to Alexis Godet, whose expertise with XRF greatly improved the accuracy of our geochemical analyses – your involvement and help was instrumental, and I am most grateful.

There are many people at K-STATE who made this work possible, and I cannot thank each of you enough for your many contributions: Matthew Brueseke for help with petrography, Brice Lacroix for help with clay fraction and for helping me through the trials and the tribulations of the malfunctioning XRD, Matthew Kirk for your guidance, and the department head, Pamela

Kempton, for your valued support. I would also like to thank all of the students who have helped me through this process: Javil Hansen for running the IC, Creenen McGuire and Emily Fenner for operating the XRD, Kayleigh Rogers for her help with the RAMAN microscope attachment, and everyone for supporting me.

Lastly, and certainly not least, I would like to again thank the committee members: Saugata Datta, Matthew Brueseke, Brice Lacroix, Jennifer Blank, and Richard Léveillé. I whole-heartedly appreciate everything each of you has done to help me on my journey.

1. Introduction and Background

1.1. Introduction to Lava Caves, Extraterrestrial Lava Caves, and BRAILLE

There is currently a burgeoning interest in investigative forays into unique geological and biological environments as terrestrial analogs for extraterrestrial environments, with one objective being to fully characterize potential analog biosignature targets, including secondary mineral deposits (*Léveillé and Datta, 2010; Léveillé 2010; Pontefract et al., 2017; Prieto-Ballesteros et al., 2003)*. Lava caves, and deposits therein, may act as records that harbor evidence of biological life, especially regarding microbial life. Future astrobiology-focused missions to extraterrestrial bodies such as Mars may investigate mineralogical phenomena, as it is possible that life is currently not extant in such environments (*Boston et al., 2001*).

The term lava cave can refer to any cave in any volcanic medium, but the basaltic lava caves in this study are associated with lava tubes. Lava tubes are formed when the exterior of a lava flow cools more quickly than the interior, allowing the less viscous interior to continue flow while the exterior solidifies during the eruption. As the eruption ceases, the remainder of the lava drains away, leaving behind a hollow tube-like structure (**Fig.1.A**). Subsequent cooling and fracturing often creates openings into the lava tube, which may now be regarded as lava caves.

Lava caves are poorly understood environments, containing a plethora of water, rock, and biological interactions. Water enters the caves primarily via fractured basalt, and microbial activity is seen by the form of widespread biofilms that cover significant surface area within the caves (*Lavoie et al., 2017*). Three sub-environments exist in these caves with each one tending to harbor different microbial communities: 1) near the cave entrance, the part of the cave most exposed to sunlight; 2) the twilight zone, the region of the cave where sunlight weakly penetrates; and 3) the aphotic zone, where sunlight is completely absent (*Léveillé and Datta, 2010*). Microbes are not

only abundant where light still permeates but are instead able to persist and thrive in even the most resource-restricted areas of caves (*Boston et al., 2001; Engel et al., 2001*).

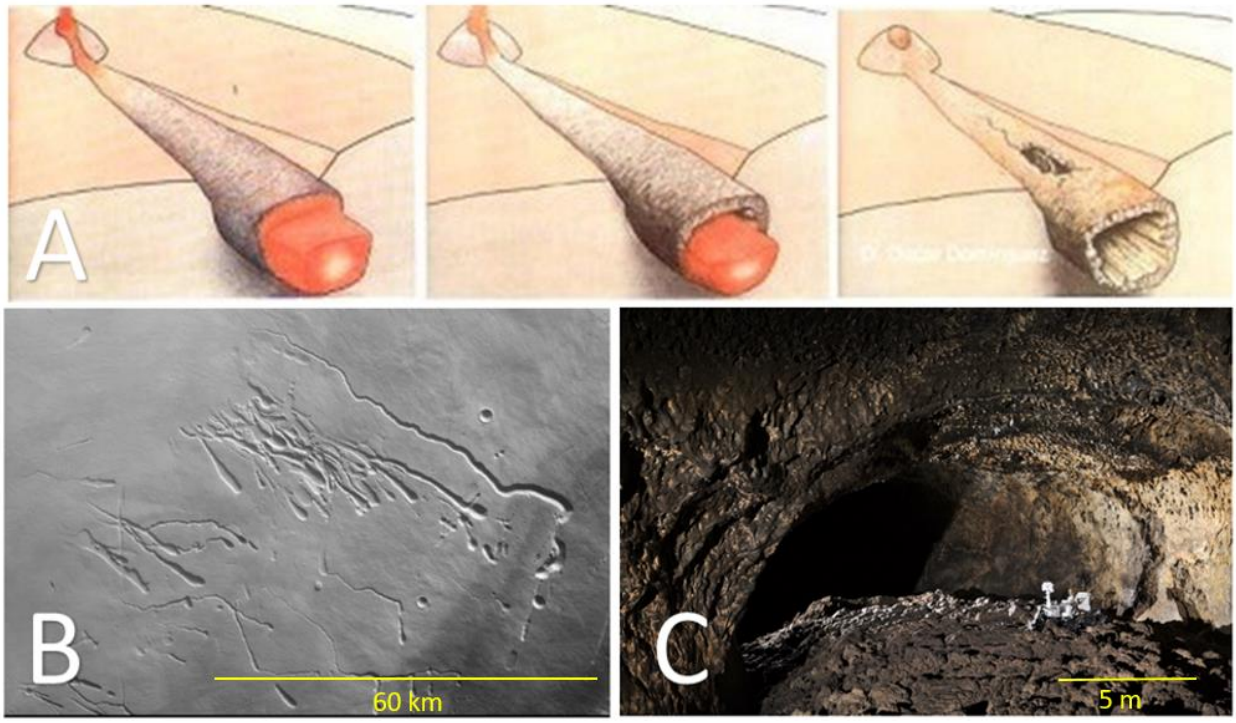

Figure 1. Formation of lava caves and identification of lava tubes on other planetary bodies. A) Formation of lava tubes including initial volcanism and fracturing / collapse (Source: NPS); B) Channel features and pits indicative of lava tubes on Mars (Source: ESA/DLR/FU Berlin (G. Neukum)); C) Interior of lava tube cave at LBNM with CAVR rover visible on the bottom right.

Lava caves can be found around the globe, including South Korea, Hawaii, the Pacific Northwest region of North America, Portugal, Iceland, Japan, and more (*Greely and Hyde, 1972; Howarth et al., 2007; Kempe 2019*). However, lava caves are also present on other planetary bodies, not only on Earth. Lava tubes (and subsequently caves) have been identified on the Moon and Mars (*Keszthelyi et al., 2008*) (**Fig.1.B**). Basalt is pervasive on rocky planetary bodies (*Gounelle et al., 2009; Walker et al., 1979*). As such, lava caves in the form of lava tube systems are expected features on basaltic bodies. Satellite orbiter imaging has revealed chains of pits, interpreted to be collapsed lava tubes due to similar patterns observed on Earth (*Cushing, 2012*).

Uncollapsed lava tubes have also been identified on Mars, recognized by linear ridges radiating from Olympus Mons, a Martian shield volcano (*Léveillé and Datta, 2010*). Lava tubes can be remotely detected using multiple methods, including high-resolution imaging, albedo profiles, thermal measurements, ground-penetrating radar, and other techniques (*Blank et al., 2020*).

Extraterrestrial lava caves may be considered as candidate astrobiology targets due to a number of compounding factors. Firstly, since lava caves can be detected remotely and act as direct conduits underground without the need for drilling, they represent relatively easily accessible subsurface environments. Secondly, terrestrial lava caves are noted to contain diverse microbial communities and have relatively stable humidity conditions (Léveillé *and Datta, 2010; Northup and Lavoie, 2001; Northup et al., 2019; Spilde et al., 2019*). Extraterrestrial lava caves are shielded from cosmic radiation, may represent stable thermal environments, and are protected from impact events relative to the planetary surface (*Blank et al., 2020*). As a consequence of these conditions, extraterrestrial biosignatures, should they exist, are more likely to be preserved over the span of geologic time (*Boston et al., 2001; Léveillé & Datta, 2010*).

Mars (and thus Martian lava caves) in particular holds promise for retention of both past and present biosignatures. Mounting evidence suggests that the Martian atmosphere was once similar to earth's - although the composition of the Martian atmosphere throughout time is still contentious (*Kite, 2019;* Fairén*, 2010; McKay and Stoker, 1989*). Due to Mar's past, possibly hospitable atmosphere, it becomes more likely that life has existed on the planet during the periods of favorable atmospheric conditions. However, it is still possible that life on Mars is extant; extremophilic microorganisms on earth are capable of surviving in low temperature and saline aqueous systems, two properties likely shared by stable liquid water on Mars (*Martin-Torres et al., 2015*). Additionally, liquid water on Mars is increasingly stable in the subsurface, due to strong

evaporative conditions on the surface that would sublimate ice (*Haberle et al., 2001*). Additionally, assuming Earth-like requirements for life on Mars may be incorrect, as there are a variety of theoretical chemical processes that may beget life (*Carrier et al., 2020*). Therefore, seeking conditions on Mars potentially habitable for earth-like organisms is not guaranteed to be successful. Lava caves may also harbor ice and salts, other priority astrobiology targets (*Carrier et al.,* 2020).

If life exists or has existed, its presence may be detected in the form of biosignatures. A biosignature is any element, compound, structure, or attribute that provides evidence of life. Due to the varied possibilities of biosignatures that may arise in extraterrestrial environments, including currently uncategorized biosignatures, it is crucial to search for multiple kinds of biosignatures. Examples include biological microstructures, organic compounds, minerals, and characteristic water chemistry (*Boston et al., 2001; Carrier et al., 2020; Lanza et al., 2019*). Biosignatures may also be preserved within minerals, with silica minerals of interest for their stability over geologic time (*Carrier et al., 2020*). Microbes may inhabit minerals as a means to obtain nutrients not readily available in other regions of the cave, wherein they may deposit evidence of their habitation (*Legatzki et al., 2011*). Due to the speculative nature of these environments and their biosignatures, the study of analogous terrestrial environments may be used to more accurately inform future extraterrestrial exploratory missions. Analog-relevant aspects include the spatial extent of biogeochemical processes in the analog environment, alongside the identification of potentially high-priority features or areas.

One such terrestrial analog study is The Planetary Science and Technology from Analog Research study, BRAILLE (Biologic and Resource Analog Investigations in Low Light Environments), which seeks to characterize lava cave environments at Lava Beds National

Monument utilizing a multifaceted, multidisciplinary approach. BRAILLE fundamentally consists of two components: 1) a science team to study lava cave microorganisms, cave waters, speleothems, and biosignatures; and 2) autonomous robotics and mission simulations to test the remote sensing of biosignatures in the subsurface environment. The science team aims to characterize the caves in several avenues: the distribution, abundance, diversity, and function of microbial communities; identification of spatially identifiable biosignatures; and the determination of microbial alteration of basalt and/or microbial mediation of speleothem formation. These objectives additionally act as a ground-truth effort to provide context for measurements made by the autonomous robotics, including the prototype CaveR rover developed by the NASA Ames Intelligent Robotics Group. CaveR is equipped with a Near-InfraRed Camera capable of delineating igneous minerals and organic compounds, modified fiber-optic spectrometers (Near-InfraRed Volatile Spectrometer System) to determine secondary mineralogy (including hydrous and carbonate minerals), a suite of cameras, ultraviolet spectrometers, and more (**Fig.1.C**).

The BRAILLE project provides crucial data pertaining to the biogeochemical characterization of terrestrial lava cave environments. BRAILLE will serve to inform future extraterrestrial lava cave missions on the basis of identified biosignatures and their spatial extent, as well as the technological and analytical capabilities required to remotely assess lava cave features. This present study addresses the geochemistry of LBNM speleothems and cave waters, especially as the two may relate to biosignatures. Moreover, the data presented in this work may be considered complementary to data relating to the microbiota of the caves.

1.2. Lava Cave Secondary Mineral Deposits - Speleothems

The subterranean secondary mineral deposits formed by the combination of one or more of the interactions present within these caves can be regarded as speleothems (a term adapted from ancient Greek, literally meaning “cave deposit”). Speleothems are generally associated with karst caves and processes, but the term speleothem can be applied to any secondary mineral formation within any cave system, regardless of lithology. Lava cave speleothems exhibit morphological, mineralogical, and likely biological diversity. Observed morphologies are varied and complex, with lava caves producing speleothems of varying size and mineralogical character. Identified categories of speleothems observed in lava caves include coralloid-like features, polyp-like protrusions, finger-like growths, gours (also identified as rimstone), crusts, cauliflower structures (named for their resemblance to the eponymous vegetable), and others (**Fig. 2**) (*Lopez-Martinez et al., 2016; Miller et al., 2013; Northup and Lavoie, 2001; Swartzlow and Keller, 1937*). Traditional speleothems observed in limestone caves consisting of calcite stalagmites, stalactites, and soda straws have also been noted to occur in lava caves (*Woo et al., 2008*). It is worth noting that these identified morphological classifications are not strict categories but possibly different expressions of similar mineralogical phenomena, making it possible that some morphologies are simply either less developed or more developed instances of the same feature. For example, cauliflower structures often appear to be broader, more tightly clustered coralloids, while fingers appear to be longer and more spindly polyps. Hence, a variety of factors and processes factor into lava cave speleothem formation.

1.3. Mineralogical Variations among Speleothems

Common secondary minerals found within lava caves include amorphous and/or cryptocrystalline silica including opal and cristabolite, calcite, monohydrocalcite, gypsum, clay minerals, and Fe – hydroxides (*Forti, 2005; Lopez-Martinex et al.,2016; Rogers and Rice, 1991*).

Opal is a form of hydrous silica, where water occurs as molecular water (silanol: SiOH), and as hydroxyls bound to interstitial ions (*Webb and Finlayson, 1987*). Isolated silanol groups are capable of occurring within the broader SiO_2 framework, which compensate for charge imbalances created by the substitution of other elements for Si within opal, also acting to make opal surfaces hydrophilic. Additionally, water content in opal generally ranges from 3 – 11%. Opal most commonly occurs as amorphous opal (opal-A), which lacks crystallinity, or as microcrystalline opal CT, which consists of both cristobalite and tridymite (both polymorphs of quartz). It is worth noting that the minerals listed above do not all consistently form within all lava cave environments. Variations in host rock composition, biological activity, and environmental factors all account for the diversity in mineral formations seen across different lava caves.

Figure 2. Select morphologies of speleothems. A) Elongated features growing towards the cave roof: Fingers; B) Features resembling corals, Coralloid; C) Bird's eye view of clustered features that widen from base to tip, Polyps; D) Tightly clustered features with broad tips that form singular masses, Cauliflower.

1.4. Occurrence and Role of Water in Lava Caves

Water in cave environments can be observed to primarily exist in four forms: drips, flows / seeps, pools, and vapor. Vapor within caves (sourced from evaporation of cave waters and/or air outside the cave) may condense when saturated air interacts with a surface that has a dewpoint temperature (the temperature to which air must be cooled to become saturated with water vapor) lower than that of the cave air (*De Freitas and Schmekal, 2003*). Essentially, cave water may evaporate and later condense, resulting in more drips and ultimately a cyclical transfer of water within a subterranean environment. Cave moisture content is not consistent throughout time, with most caves receiving varying amounts of water influx throughout the year (*Baldini et al., 2006*). At Lava Beds, moisture content varies amongst separate caves, with the majority of caves belonging to the same flow (consequently approximately the same age) containing differing amounts of moisture. Some caves have numerous roof droplets and large pools (~3-6 cm depth), whereas others have few droplets and shallow pools (~1-2 cm depth). Moisture variation within individual caves closely follows the three sub-environments, with the least amount of moisture present near the cave entrance and the greatest amount in the aphotic zone (Léveillé *and Datta, 2010*). Lava cave water chemistry is typically dominated by Si, Na, Mg, and Ca, owing primarily to the dissolution of plagioclase, clinopyroxene, and basaltic glass (*De los Ríos et al., 2011; Miller et al., 2014*). Meteoric water recharge may also contribute to Cl and Na concentrations (*Kempe et al., 2019; Teehera, et al., 2018*). The interaction of water with basalt within these caves enables the precipitation of secondary minerals, including silica, clay minerals, sulfates, and carbonates (*Forti, 2005; Lopez-Martinex et al., 2016).* The study of cave water chemistry is therefore crucial for the complete understanding of the speleothems and the processes involved in their development.

1.5. Speleothem Formation Processes

There are existing controversies regarding the mechanism of speleothem formation in all cave environments. From the standpoint of this study, and the BRAILLE project, the study of life associated with mineral biosignatures is an essential component. To address this, the origin of secondary minerals will first be discussed in terms of abiotic mechanisms, and later on, biotic formation will be discussed in detail. Hence, like many natural formations, a combination of abiotic and biotic mechanisms may have helped in the formation of these secondary minerals. Speleothem formation was once considered to be entirely the result of inorganic processes, but research is evolving to assess the role of organisms in formation processes (*Du Preez et al., 2015; Forti, 2001*). However, inorganic processes must still be considered, even in the presence of biological activity. This section will describe inorganic speleothem formation processes pertinent to lava caves, while the following section will describe the importance of biological factors.

Four primary inorganic speleothem formation mechanisms can be observed to occur in lava cave environments: sublimation, vapor-based deposition, alteration and evaporation, and diffusion (*Forti, 2005*). The first two mechanisms, sublimation and vapor-based deposition, are chiefly unique to lava caves and are active only during and/or shortly after active volcanism ceases. During the solidification and cooling of cave walls, fluids can seep from fractures. These fluids subsequently cool, facilitating the deposition of predominately sulfur-based sublimate minerals. These minerals are typically unstable at post-cooling cave conditions and will not persist over geologic time (*Sauro et al., 2014*). The third mechanism, evaporation, is supported by the solubilization of the host volcanic rock by interactions with meteoric water. These interactions can result in a cave water chemistry high in dissolved silica and other dissolved species; upon evaporation, the water can become supersaturated and precipitate minerals including opal and gypsum (*Harmon et al., 1983*). Evaporation-driven secondary mineral deposition also occurs in

lava caves that are still hot, in which percolating water rapidly evaporates. The fourth mechanism, diffusion, describes the diffusion of atmospheric CO_2 into the cave environment. In combination with subsequent degassing, this is the mechanism responsible for the majority of calcite-based karst cave speleothems (*Frisia et al., 2000*). The influx of CO_2 combined with Ca/Mg ions from host rock dissolution enables the precipitation of carbonates in some lava cave environments.

1.6. Microbial Processes Influencing Speleothem Formation

Microbes can influence speleothem genesis via a variety of mechanisms: direct mineralization via enzymes, precipitation of minerals due to microbially induced change of environmental factors such as pH & Eh, and microbial colonies acting as nuclei for mineralization (*Forti, 2001*). Chemotrophic microbes are likely the strongest drivers of cave biomineralization, with sulfur oxidizing and reducing microbes being a prominent example. Sulfur oxidizing microbes can lower the pH and drive opal precipitation in silica-rich lava cave environments (*Forti, 2001*). Evidence also suggests that the precipitation of opal-A can be driven solely by microbial processes, with silicified microbes incorporated into the resulting mineral (*Peng and Jones, 2012*). In lava caves, olivine respiring bacteria may additionally contribute to the formation of certain speleothem structures (*Popa et al., 2012*). These bacteria oxidize the ferrous iron present in olivine, producing iron (III) oxide-hydroxide at near-neutral pH (*Popa et al., 2012*). The speleothems that are formed via biological pathways may be able to record this history in the form of biosignatures (Léveillé *and Datta, 2010*). Biosignatures can be biological, chemical, or morphological. Morphological examples common amongst lava tube cave speleothems are micro-stromatolites or microstromatolitic-like structures (**Fig. 3**), which typically appear as layered, hummocky structures at the micron scale (*Northup et al., 1997*). Note that these structures are not always indicative of biological activity, as mineral deposition via drips can create similar

undulating features, making other biosignatures important to confirm their origin (*Webb and Kamber, 2011).*

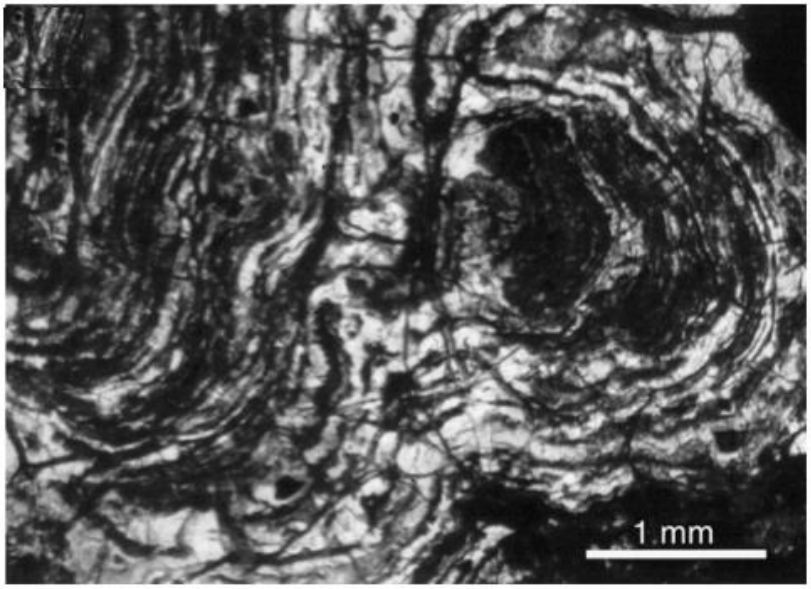

Figure 3. Calcite and kerolite (a poorly crystalline clay mineral) microstromatolite speleothem from a Hawaiian lava cave. Minerals comprising the speleothem are proposed to nucleate as the result of microbial EPS binding Mg^{2+} and silica. Figure modified from Léveillé et al., 2000.

Chemical biosignatures may occur in the form of elevated concentrations and the recorded oxidation states of known biosignature elements (Fe, Mn, V, Ba, Cu, P, and S). These characteristic elements will be included within the speleothems as they form and, therefore, can serve as elemental signatures indicative of microbial processes. For example, energy-dispersive X-ray spectroscopy (including SEM-EDS and TEM-EDS) of micro-stromatolites and biofilm in Hawaiian lava caves revealed peaks for Ca and Mg, proposed to be bound ions in bacterial extracellular material, which may act to nucleate mineral precipitation (*Léveillé et al., 2000).* Ferromanganese deposits in the carbonate cave environment of Lechuguilla have been attributed to Fe and Mn oxidizing bacteria (*Northup et al., 2003*). Similar deposits have been found in low-light volcanic environments: cryptocrystalline mineral crusts in granite tunnels deemed to be biogenic in origin have been found using FE-SEM-EDS to be comprised of Mn associated with

Ca and Fe (*Miller et al., 2012)*. Furthermore, elemental distribution maps of the mineral crusts in granite tunnels created using a combination of Scanning Transmission X-ray Microscopy (STXM) and X-ray absorption near edge structure (XANES) revealed homogenous clusters of Mn(IV) surrounded by both Fe(II) and Fe(III), which may indicate microbial oxidation of Mn(II) (*Miller et al., 2012)*. Mineral deposits enriched in V_2O_5 have been found amongst biofilms in Hawaiian lava caves, making vanadium a redox sensitive element of interest in these environments (*Spilde, et al., 2016)*. Barium may be extracted from host cave rocks by microbes to increase silica solubility, thus enabling the precipitation of amorphous silica speleothems (*Sauro et al.,* 2018). Copper is an unlikely metabolic resource, but it has been noted to be accumulated by microbes in cave environments (*Northup et al., 2011)*. Sulfur has been identified as a potentially important source of energy for chemolithoautotrophs within lava caves, making it possible that their presence is recorded in speleothems (*Northup et al., 2011*). For example, if the formation of opal in a cave is mediated by sulfur-oxidizing bacteria, it could be expected to find significant traces of oxidized sulfur species (S^0, SO_4^{2-}) within the speleothem structures. Therefore, the speciation of S may reveal microbial activity. Sulfur speciation in the form of octasulfur has been utilized as an indicator of sulfur-globule-forming microbes in sulfidic cave springs (*Engel et al., 2007*).

Although the study of lava cave environments and their associated secondary mineral structures is a relatively new field of research, most necessary techniques and principles have already been applied in other avenues. Petrographic thin section observation, Scanning Electron Microscopy (SEM) imaging, and X-Ray Diffraction (XRD) analyses have been performed on opaline speleothems in sandstone caves, as described in *Aubrecht et al. (2008)*. Morphologically, the described "doll" features are very similar to some of the features found within the LBNM lava caves, namely the sub ~1 cm polyp features, as will be shown below in chapter 4. In addition, both

cave systems shared coralloid overhang features. Most notably, the described sandstone caves seemed to lack the thicker > 5mm crust mineral deposits found within lava caves. Thin sections of the sandstone cave features revealed micro-stromatolitic layering patterns, a prominent feature also observed in lava cave samples. The authors categorize the sandstone cave speleothems as biogenic, primarily citing stromatolitic lamina and other biogenic structures. When viewed under plane-polarized light and SEM, the majority of stromatolitic speleothems exhibit peloidal layers within the cemented layers (*Aubrecht et al., 2008; Lopez-Martinez et al., 2016*). These remnants of microbial activity strongly suggest the formation of these minerals were in part influenced by biological processes.

1.7. Hypotheses and Objectives

Once thought to be primarily inorganic formations, growing evidence supports the role of microorganisms in the nucleation and growth of varied forms of speleothems in many cave environments (*Aubrecht et al., 2008; Lopez-Martinez et al., 2016; Miller et al., 2014*; *Sauro et al., 2018*). Although numerous studies have discussed the potential biogenic origin of speleothems, there is a general lack of detailed mineralogical and geochemical characterization of these features and environments, especially pertaining to lava cave speleothems.

The concentrations of potential biosignature elements in lava cave speleothems are currently a relatively unexplored avenue of investigation, making their determination a crucial objective to understand their importance in the formation of these minerals (*Boston et al., 2001*). Moreover, the relationship between lava cave speleothems and the cave waters from which they precipitate have yet to be explored – the determination of the parent solution's composition will act to aid in the determination of the origin of LBNM speleothems. For example, the determination of the saturation indices of cave waters will reveal if additional processes (including evaporation

that may be assessed by stable isotopes of hydrogen and oxygen) may be required to facilitate the mineral precipitants observed within the caves (*Forti, 2005*). Further, establishing a correlative link between morphology of speleothems and their chemical and biological characteristics can provide valuable insights for future research into extraterrestrial biomarker targets (*Lavoie et al., 2010*).

Hypotheses

1) The speleothem-forming processes are similar across sampled caves, reflected by similar mineralogy (opal and calcite), compositions, and morphologies across caves.

2) Speleothem formation is in part mediated by microbial processes, which is reflected in both elemental composition and in external and internal morphology.

3) Water availability acts as another major control on speleothem morphology and composition, with predominantly opaline speleothems suggesting wetter conditions.

4) Cave water composition is capable of supporting microbial activity (signified by high concentrations of DOC, P, S, N).

Objectives

1) Determine the mineralogy of LBNM speleothems and cave rock.

2) Characterize the elemental composition of speleothems by means of bulk and high-resolution analyses and identify compositions / distributions of potential biosignature elements.

3) Identify features relating to morphology and microstructure of speleothems via petrographic analysis that may indicate biogenic origin.

4) Determine the geochemistry of cave waters, as they relate to speleothem formation and biological processes occurring within caves.

5) Determine saturation indices of speleothem-forming minerals utilizing geochemical modeling.

6) Determine stable isotopic composition of cave waters to determine origin of water and extent of evaporation within caves.

2. Study Area

The area chosen as a terrestrial analog site for the BRAILLE project, Lava Beds National Monument (LBNM), is located in northern California near the Oregon border (**Fig. 4**). Lava Beds and most of the surrounding area was created by the Medicine Lake volcano, a relatively young (Pleistocene/Holocene) 33 km diameter shield volcano located in the eastern Cascade Range (*Donnelly-Nolan et al., 1990*). The volcano's flows cover more than 2000 km^2 of land east of the Cascade Range's main axis, and the oldest Tertiary age flows underlay more recent deposits, including those at LBNM (*Donnelly-Nolan, 2010*). The Medicine Lake volcano has produced lavas ranging from basaltic to rhyolitic, although mafic compositions are by far the dominant type produced. Basaltic flow compositions have also changed over time, with older deposits consisting of approximately 53% SiO_2, and younger deposits consisting of approximately 47% SiO_2 (*Rogers and Rice, 1991*). Most of the deposits readily accessible within Lava Beds region (located on the northern flank of the volcano) are younger than 36 ka, making the caves demonstratively recent features.

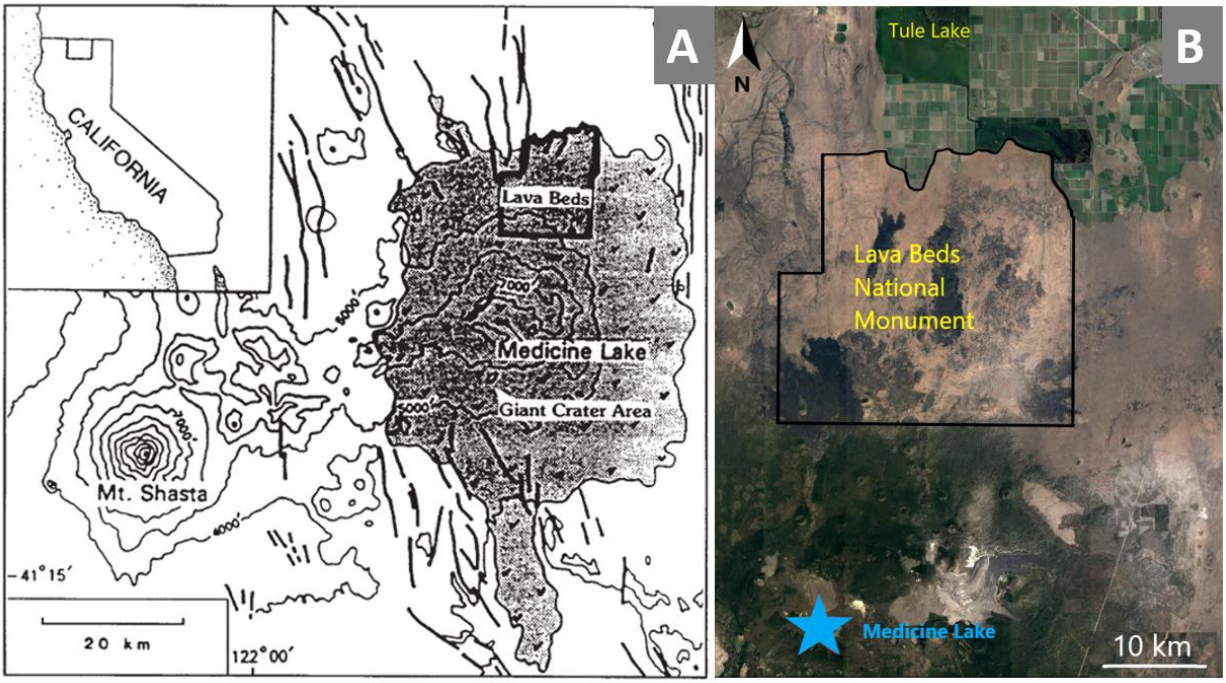

Figure 4. Location of the Medicine Lake Volcano and Lava Beds National Monument. A) LBNM is located in northern California on the north slope of the Medicine Lake shield volcano, and northeast of Mt. Shasta. Figure modified from *Rogers and Rice, 1991*. B) Satellite image of the LBNM area and Tule Lake to the north. Credit: Google Earth.

As a national monument, Lava Beds is open to the public. However, only a limited number of the more than 800 caves with 50 km total length are marked on official NPS publications and regularly visited by the public, making the majority of the caves unaffected by continuous human traffic.

2.1. Recent Medicine Lake Volcanism

The Mammoth Crater composite basalt flow, with an age of approximately 36 ± 16 ka, covers about two-thirds of the entirety of LBNM, about 250 km^2. This flow also created the majority of lava caves in the monument, including the majority of caves sampled by BRAILLE (*Donnelly-Nolan and Champion, 1987*). Approximately 12,260 years BP (before present), a series of spatter vent eruptions created a series of lava tubes comprised primarily of basaltic andesite, including those constituting Valentine Cave, one of the caves sampled by the BRAILLE study.

Another deposit of similar age exists - the Devil's Homestead. This deposit is of a more basaltic composition, and unlike the flow that produced Valentine, did not travel downslope by means of lava tubes (*Donnelly-Nolan et al., 1990*). There was a pause in volcanic activity within the Lava Beds area for 6,000 years afterwards, which resumed in the area in the form of six eruptive events (both mafic and felsic eruptions) spanning from ~1250 and ~850 years BP Two of these events are associated with the Lava Beds area: the Callahan flow and Little Glass Mountain. The Callahan flow is associated with a large cinder cone located on the southwestern outskirts of Lava Beds and is of andesitic composition (*Donnelly-Nolan et al., 1990*). Little Glass Mountain, however, is significantly different in composition compared to other deposits in the Lava Beds: it is an obsidian flow. Tephra from this event (and others), including pumice and tuff can be found scattered throughout the area, including overlying lava-tube-bearing deposits and as debris fallen and/or washed within caves. These tephra deposits contribute to the low residence times in the poorly matured soil overlaying the lava caves, and may quickly weather, influencing the chemistry of percolating waters (*Donnelly-Nolan and Grove, 2017).*

2.2. Ground Water Hydrology of Tule Lake Subbasin and LBNM

Lava Beds National Monument can be considered a semi-arid environment, with annual precipitation less than the rest of the Klamath Basin, which contains LBNM (*Applegate, 1938; Nelson and Smith, 1976*). Hydraulic head data as reported in *Gannet et al., 2007* have shown water enters the area from the north, east and west, including from the upper Klamath Basin. The inferred flow directions from well data are additionally corroborated by isotopic data consistent with recharge from the upper Klamath Basin. On the valley floor, including most of the Lava Beds area, hydraulic head gradient within Quaternary sedimentary deposits (consisting primarily of alluvial sediments, glacial deposits, and basin-filling sediments) is small at approximately 1 ft/mile

(*Gannett et al., 2007*). Within the underlying volcanic rocks, the gradient is slightly steeper at 2.5 ft/mile towards the south. As a result, groundwater flows south out of the Tule Lake subbasin and east of Medicine Lake. Aquifer tests within the Tule Lake subbasin (consisting of pumping at a constant rate, then measuring drawdown from the pumped well and nearby wells) have shown evidence of boundaries and/or double porosity. Boundaries within the aquifers in the Tule Lake subbasin may be shown by the presence of inflections in drawdown curves, which are sometimes but not always associated with faults (*Gannett et al., 2007*). These boundaries are likely indicative of a degree of local compartmentalization of the Tertiary volcanic aquifers.

Select wells in the Tule Lake agricultural region proper (near the Tule Lake National Wildlife Refuge, **Fig.4**) are relatively shallow, with depths ranging from 7-37 m, and are associated with lacustrine sediments (*Adam et al., 1989).* A 231 m deep well associated with the volcanic aquifer is used by the National Park Service as the primary water supply for the monument (*Hotchkiss et al., 1968*). For comparison, the maximum depth of Lava Beds caves ranges from approximately 6-36 m: of similar depth to agricultural wells, but shallower than the deep volcanic aquifer well (*Waters et al., 1990).*

2.3. Lava Cave Organisms

2.3.1. Prokaryotes and Archaea

The total extent and function of lava cave microorganisms is enigmatic, with an ongoing effort underway to better understand the inhabitants of these complex environments. Numerous lava caves have been found to contain large colonies of microbes, often in the form of colorful biofilms and microbial oozes (*Northup et al., 2012*). Existing in resource-restricted environments, the microbial denizens of lava caves may access nutrients by way of organic matter and other detritus entering the cave via the plethora of fractures and openings found in most lava caves.

The microbial presence within LBNM caves is readily apparent in the form of biofilm (**Fig.5.A,B**) and ooze (**Fig.5.C**). Numerous colors of biofilms have been observed: yellow, tan, white, gold, and more. The detailed study of the metagenomics and function of the cave's microbial inhabitants is still ongoing, but previous preliminary studies have noted the presence of actinobacteria, gammaproteobacteria, nitrospirae, and multiple novel candidate phyla (*Lavoie et al., 2017*). Once again, it is important to state that the precise function and nature of LBNM microorganisms, including metabolic processes, are currently poorly understood and relatively undocumented.

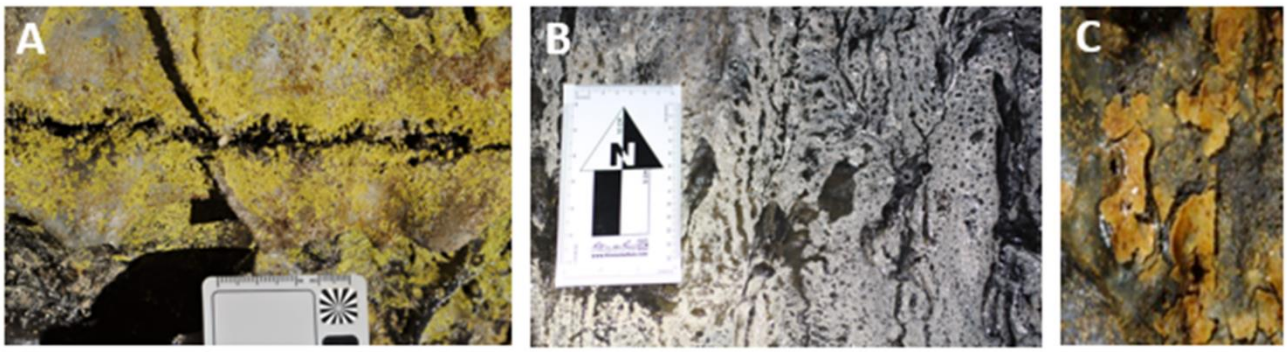

Figure 5. Microbial life within LBNM caves. A) Yellow microbial mat; B) White microbial mat; C) Microbial ooze on basalt.

2.3.2. Eukaryotes

Many of the caves host larger animals, including bats and packrats. The sampled caves were specifically chosen to not include known bat colonies, in order to reduce the potential impact on these vulnerable creatures. In addition to mammals, the caves at Lava Beds are home to a host of other fauna, including a diverse community of invertebrates. These invertebrates include arachnids, centipedes, bristletails, and springtails. Moreover, the invertebrate population includes both troglobitic organisms adapted for low-light environments, and accidentals, organisms that are typically found on the surface yet have been found in sections of caves (*Taylor and Krejca, 2006*).

2.3.3. Plants

Plant life is scarce within the caves, essentially limited to ferns nearby cave entrances where light still permeates and thin roots protruding from the surface (**Fig.6**). Plants and their roots (alongside other organisms) may serve as sources of necessary nutrients within the caves, including nitrogen and phosphorous. Some lava cave systems may experience significant root penetration through several meters of soil and rock, a feature observed in some Hawaiian lava caves.

Figure 6. Root penetration through fractured basalt in an LBNM cave. Roots are approximately 6 cm in length. White and yellow microbial biofilms are also visible on the surrounding vesicular rock.

3. Methods

3.1. Sample Collection

The samples (rock, speleothem and water) were collected in a total of eight caves: Valentine (VAL), V460 (LYO), Golden Dome (GOL), L300 (YEL), L460 (POS), and three unnamed caves (CRI, SIL and PAN) of different ages, frequency of visitation, and moisture content (three-letter names denote cave ID for use in BRAILLE studies). Two caves (VAL and LYO) belong to the Valentine flow, dated at 12,260 BP All remaining caves (YEL, POS, CRI, SIL, and PAN) belong to the Mammoth Crater flow, dated at approximately 36 ± 16 ka (*Donnelly-Nolan and Champion, 1987*). Caves designated by the National Park Service as publicly available caves (high visitation; Valentine and Golden Dome) typically have had their floors lined with crushed pumice for easier access to visitors. Water, mineral, sediment, and other samples were collected over a period of five days, from July 29th, 2018, to August 2nd, 2018. Additional targeted samples were collected during the summer of 2019. Samples were collected from shared sample sites alongside other BRAILLE Co-PIs (**Fig.7**). Sample sites were chosen based on the following parameters:

- presence of different speleothem and cave structures to obtain a representative suite of LBNM cave features, both biological and inorganic;
- presence or absence of biofilm to obtain biological samples and relatively barren samples for comparison; and
- presence of drip water and/or pools (puddle water) to obtain co-located water samples and biological / mineral samples in close proximity to the sampled water.

Sample sites were named using the following schema: three-letter cave identifier, date and year, plus an alphabetical sample site designator. For example, for LYO20180730_A_1. The

alphabetical sample site designators A represents the furthest accessible section of the cave. Letters progress towards Z as the sample sites draw nearer to the opening of the cave. Speleothem samples were collected using sterile tools and stored in sterile Whirl-Pak sampling bags for XRD/XRF analyses, and sterile O_2-impermeable Remel® bags (Mitsubishi Gas Company, Remel®, Cat no. 2019-11-02), along with O_2 absorber pouches (Mitsubishi Gas Company, AnaeroPouch® Anaero; Cat no. 23-246-379) for anaerobic storage. Tools utilized in the field (chisels, spatulas, and tweezers) were first sterilized through flaming using methanol prior to the collection of each sample. All samples were stored in a refrigerator at 2 °C. Water chemistry parameters of pH, temperature, and conductivity were measured in the field using a HACH PocketPro+ meter. Water samples intended for cation, major elements and trace elements analyses were filtered using a 0.45 µm filter (Millipore Milliex – HP) and acidified with 0.2% v/v Nitric acid. Samples intended for anion analyses were filtered through a 0.45 µm filter (Millipore Milliex – HP) and un-acidified. Additionally, at each sample site, air temperature and relative humidity were measured using a portable probe. Forty-three solid samples (including speleothems and basaltic rock) and 40 water samples (consisting of puddle water, drip water, surface water, and well water samples) were collected and considered for analysis. **Table 1** lists the sample ID of each collected sample and the analyses performed. **Table 2** details cave water samples: drip waters and puddle waters. Four nearby well waters (coordinates are stated in **Appendix A11 p.152**) were also collected for comparison with cave waters.

Table 1. Breakdown of performed analyses of Rock and Speleothem samples collected from LBNM caves. Three letter ID represents sampled cave.

Sample ID	*Cave*	*Description*	*XRF*	*XRD*	*Clay Fraction*	*Thin Section*
CRI20180731_D_12	CRI	Polyps, White	X	X	X	X
CRI20180731_D_14	CRI	Bare Basalt	X			
CRI20190803_A_3.2	CRI	Polyps, White Specks	X	X		
CRI20190804_B_01	CRI	Coralloid, Flowery, White-Tan	X			
CRI20190804_C_1.1	CRI	Cauliflower,White-Tan, Orange	X			
CRI2019081_A_4.2	CRI	Cauliflower,White-Tan,Red_Orange	X	X		
GOL20180729_B_12	GOL	Polyps, Fingers	X	X		
GOL20180729_B12_B	GOL	Bare Basalt	X			
GOL20180729_C_01	GOL	Polyps, White	X			
GOL20180729_G_02	GOL	Polyps, White	X	X	X	X
GOL20180729_G_03	GOL	Coralloid,White-Tan	X	X		X
GOL20190807_A_11	GOL	Coralloid,Brown	X	X		
GOL20190807_A_13	GOL	Coralloid, White-Tan,Gray	X	X		
GOL20190807_B_12	GOL	Coralloid,Brown	X	X		
HOP171108_08	HOP	Bare Basalt	X			
LYO20180730_A_21	LYO	Bare Basalt	X			
LYO20180730_B_07	LYO	Bare Basalt				X
LYO20180731_F_08	LYO	Polyps		X		X
LYO20180731_G_10	LYO	Cauliflower		X	X	
LYO20180731_H_06	LYO	Gour	X	X	X	X
LYO20180731_H_15	LYO	Coralloid		X		
LYO20180731_H_19	LYO	Mineral Crust, White	X	X	X	
LYO20180731_I_11	LYO	Cauliflower,Brown	X	X	X	X
LYO20180731_J_14	LYO	Coralloid, White-Tan	X	X	X	X
LYO20180731_J_18	LYO	Cauliflower, Brown (Knob)	X	X	X	
LYO20190730_A_44	LYO	Gour	X	X		
LYO20190810_A_19	LYO	Coralloid, White-Tan,Gray	X			
PAN20190808_B_06	PAN	Polyps, White	X			
PAN20190808-B-03	PAN	Coralloid, Gray	X			
POS20180801_D_09	POS	Polyps, White	X	X	X	
POS20180801_E_16	POS	Cauliflower,White-Tan	X	X	X	X
POS20180801_I_08	POS	Mineral Crust, Orange	X	X		
POS20190806_A_13	POS	Cauliflower,White-Tan	X	X		
POS20190806_B_06	POS	Coralloid, Yellow White Tip	X			
POS20190806_B_08	POS	Bare Basalt	X	X		
POS20190806_D_03	POS	Polyps, White	X			
POS20190806_D_04	POS	Polyps, Orange	X			
POS20190806_D_05	POS	Polyps, Orange	X			
POS20190806_F_02	POS	Mineral Crust, Orange	X			
SIL20180802_A_14	SIL	Bare Basalt	X			X
SIL20180802_C_01	SIL	Polyps, White	X	X		X
SIL20190808_A_03	SIL	Coralloid, White + Basalt	X			
SIL20190808_D_01	SIL	Coralloid,Brown	X			
VAL20171109_14	VAL	Bare Basalt	X	X		
VAL20190805_D_02	VAL	Cauliflower,White-Tan,Brown	X			
YEL171111_4	YEL	Bare Basalt (Oxidized)	X			
YEL20180802_B_06_A	YEL	Polyps White-Tipped		X		
YEL20180802_B_06_B	YEL	Polyps White-Tipped		X		
YEL20180802_B_06_C	YEL	Polyps White-Tipped	X	X	X	X
YEL20190804_Ac_02	YEL	Polyps, Fingers	X			

Table 2. Breakdown of performed analyses of LBNM cave water samples and well waters. Three letter ID represents sampled cave.

Sample ID	*Cave*	*Description*	*IC*	*HR-ICPMS*	*Stable Isotopes*	*DOC*	*Alkalinity*
CRI20180731-Backroom	CRI	Dripwater	X	X	X	X	X
CRI20180731-C-05	CRI	Dripwater	X	X	X	X	X
CRI20180731-D-13	CRI	Dripwater	X	X	X	X	X
GOL20180729-C-15	GOL	Puddle	X	X	X	X	X
GOL20180729-D-51	GOL	Puddle	X	X	X	X	X
GOL20180729-F-87	GOL	Puddle	X	X	X	X	X
LYO20180730-A-06	LYO	Dripwater	X	X	X	X	X
LYO20180730-B-51	LYO	Dripwater	X	X	X	X	X
LYO20180731-H-01	LYO	Dripwater	X	X	X	X	X
LYO20180731-J-13	LYO	Dripwater	X	X	X	X	X
LYO20180731-H-01	LYO	Puddle	X	X	X	X	X
POS20180801-D-01	POS	Dripwater	X	X	X	X	X
POS20180801-E-04	POS	Dripwater	X	X	X	X	X
POS20180801-F-07	POS	Dripwater	X	X	X	X	X
POS20180801-F-12	POS	Dripwater	X	X	X	X	X
POS20180801-B-14	POS	Puddle	X	X	X	X	X
POS20180801-D-01	POS	Puddle	X	X	X	X	X
POS20180801-I-10	POS	Puddle	X	X	X	X	X
SIL20180802-A-15	SIL	Dripwater	X	X	X	X	X
SIL20180802-C-14	SIL	Puddle	X	X	X	X	X
VAL20180803-A-01	VAL	Dripwater	X	X	X	X	X
VAL20180803-B-02	VAL	Dripwater	X	X	X	X	X
VAL20180803-C-02	VAL	Dripwater	X	X	X	X	X
VAL20180803-D-02	VAL	Dripwater	X	X	X	X	X
VAL20180803-E-01	VAL	Dripwater	X	X	X	X	X
VAL20180803-A-02	VAL	Puddle	X	X	X	X	X
VAL20180803-B-01	VAL	Puddle	X	X	X	X	X
VAL20180803-C-01	VAL	Puddle	X	X	X	X	X
VAL20180803-D-01	VAL	Puddle	X	X	X	X	X
YEL20180802-A-05	YEL	Dripwater	X	X	X	X	X
YEL20180802-B-02	YEL	Dripwater	X	X	X	X	X
YEL20180802-C-02	YEL	Dripwater	X	X	X	X	X
YEL20180802-D-02	YEL	Dripwater	X	X	X	X	X
YEL20180802-A-01	YEL	Puddle	X	X	X	X	X
YEL20180802-B-01	YEL	Puddle	X	X	X	X	X
YEL20180802-C-01	YEL	Puddle	X	X	X	X	X
YEL20180802-D-01	YEL	Puddle	X	X	X	X	X
Tule Lake		Surface	X	X	X	X	X
WEL20180803-1	Depth: 231 m	Deep Well	X	X	X	X	X
WEL20180803-2	Depth: 37 m	Shallow Well	X	X	X	X	X
WEL20180803-3	Depth: 23 m	Shallow Well	X	X	X	X	X
WEL20180804-4	Depth: 8 m	Shallow Well	X	X	X	X	X

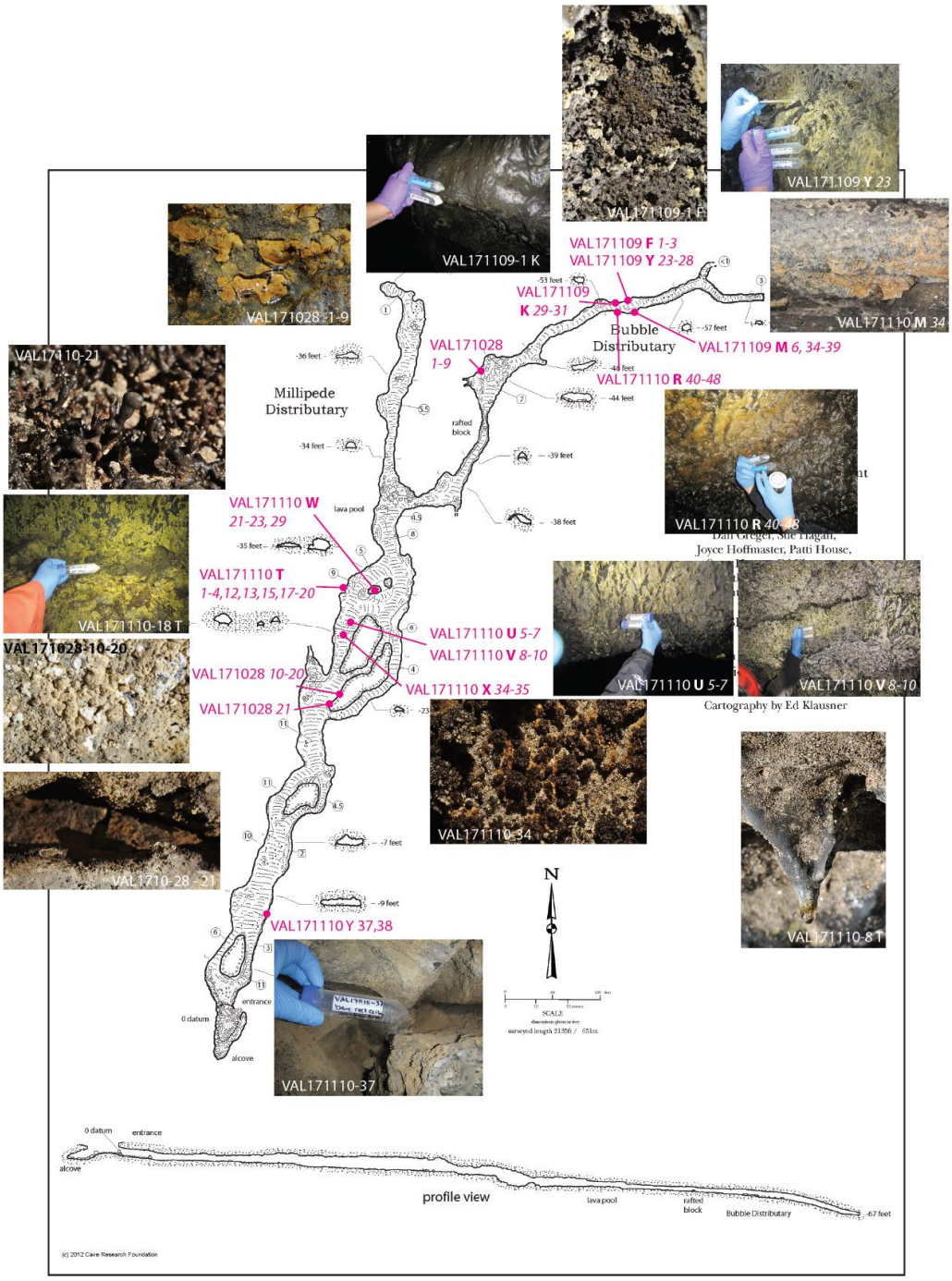

Figure 7. Cave sampling strategy example at LBNM. Caves were first scouted for relevant microbial features, speleothems, and other sites of interest. Sample locations were marked, and samples were collected moving from the end of the cave towards to entrance. Sample sites were named starting with "A" at the sample site furthest from the cave entrance. Credit: Braille team.

3.2. Sample Preparation and X-Ray Diffraction Analysis

Preparation for both XRD and XRF analyses consisted of crushing the selected speleothem/rock material and grinding via agate mortar and pestle to achieve a non-granular consistency (roughly silt sized, ~ 55 µm). Numerous samples consisted of secondary mineral growth atop a basalt nucleus. This secondary precipitant material was separated for analysis. Moreover, in the case XRD/XRF analyses performed on samples stored in anaerobic conditions, portions of the targeted samples were removed in a nitrogen glove box and subsequently resealed. XRD analyses were accomplished using a Malvern Panalytical Empyrean with a PIXcel 3D scanning line detector. X-rays were generated with a Cu tube and Ni-filter at a setting of 45 kV, 40 mA from a range of 2.5 ° -70 ° (2θ). The powdered samples were tightly packed into 16mm holders for use with the Empyrean's spinner sample stage. Panalytical's HighScore software suite (version 4.8) was subsequently utilized for analysis of peaks and mineral identification.

3.3. Clay Fraction

Clay fraction analyses of speleothem samples were completed in accordance with the in-house procedure adapted by Kansas State University based on the following works: *Moore and Reynolds (1989), Poppe et al. (2001), and Lacroix et al. (2012).* 1 g of sample was gently crushed to a gravel-sand size so as to preserve the clay textures and crystallinity. A decarbonation protocol was followed for samples exhibiting carbonates: sample was placed in a boiling flask with 100 ml of 10% HCL and stirred for 10 minutes. Immediately after, another 100 ml of 10% HCL was added and the solution was stirred for another 10 minutes. The supernatant liquid and suspended particles were subsequently transferred to a 400 ml centrifuge bottle. Following decarbonation, an acid wash via centrifuge cycling (10 minutes at 5000 rpm each cycle, supernatant liquid disposed of and bottle filled with DI water to 200 ml after each cycle) was performed to achieve a pH of 7-8. Clays were separated into <2 µm and 2-16 µm categories and placed onto glass slides: <2 µm clays were

separated by centrifuging the near-neutral solution in 50 ml tubes at 1000 rpm for 58 seconds, then the sample was syringed down to the 45 ml reference line. The 2-16 μm clays were separated by actively shaking the near-neutral solution 50 ml tube, and then standing the tube upright for 97 seconds. Immediately after, the clay fraction was collected by syringing below the 45 ml reference line to the 25 ml reference line. Both clay fractions were syringed onto separate glass slides and left to dry for 24 hours. Glass slides were analyzed using XRD, including with saturation with ethylene glycol to determine mineral identity.

3.4. X-Ray Fluorescence

Sample preparation for XRF analysis consisted of the following procedure: 0.25 g of each powdered sample (roughly silt sized, ~ 55 μm, crushed using agate pestle and mortar) was packed into *PrepCorp* 30 mm boric acid shells, then pressed at 10 tons for 60 seconds using a *Dake* 972200 B-10 10 Ton Hydraulic Bench Press. The pressed samples were mounted on sample holders with 10 mm sample masks.

Loss on Ignition (LOI) values were calculated using the following procedure: Empty porcelain crucibles were weighed (Crucible empty - Ce), 0.5 g of each powdered sample (non-pressed) was transferred to a crucible and weighed (Crucible full - Cf). Full crucibles were then transferred to a *Blue M* Lab-Heat box-type muffle furnace, at 1000° C for 2 hours. Afterwards, the crucibles were removed to cool for approximately 15 minutes and weighed (Crucible Calcinated – Cc). Finally, LOI was calculated using the following formula:

$$\text{LOI} = \frac{Cf - (Cc - Ce)}{Cf} \text{ X } 100$$

LOI values are used to measure the amount of volatiles present within a given sample, including but not limited to carbonate present within calcite and water present within opal.

X-Ray fluorescence analyses were performed using a Rigaku Primus II Wavelength Dispersive XRF spectrometer, with an overall X-ray beam power of 3.6 kW and beam diameter of 10 mm. A quantification method was designed using eight standards from the U.S. Geological Survey (BIR-1a, COQ-1, DNC-1a, GSP-2, RGM-2, SBC-1, STM-2, W-2a). Amperage ranged between 40-60 kV and 90 mA, depending on the atomic number of the element analyzed: 40kV below Ti, 50kV from Ti to Rb, and 60kV for elements heavier than Rb (Department of Geosciences, University of Texas at San Antonio).

3.5. Thin Sections and Petrography

Thin sections (17 in total, representative of varying speleothem morphologies and basalt samples) were created by Spectrum Petrographics, Inc. Samples were embedded in epoxy, cut to 30 microns in thickness, and were polished in accordance to microprobe-quality standards, enabling the use of the slides for future microprobe analyses. Petrographic analyses of thin sections were performed using a Nikon polarizing microscope (Department of Geology, Kansas State University).

3.6. Electron Microprobe

Quantitative Electron Microprobe analyses were performed at the Texas A&M University Materials Characterization Facility using a Cameca SXFive electron microprobe equipped with a LaB_6 source, a thermos EDS system, and a CL (Cathodoluminescence) detector. The scan area consisted of a rectangular 2568 by 996 μm section within a polyp speleothem thin section, chosen to be representative of the various lamina observed within LBNM speleothems. The area was analyzed with a beam voltage of 15 kV and beam current of 50 nA. A beam size of 3 μm was used with a step size of 3 μm and a count time of 80 ms per pixel. The following elements expressed as elemental oxides were detected: SiO_2, CaO, MgO, FeO, Al_2O_3, K_2O, SO_3, P_2O_5, SrO, and Cu_2O.

These data were used to construct quantitative raster elemental maps to delineate variability in elemental concentration throughout the scan area. A Gaussian kernel smoothing algorithm was applied to the Cu_2O, K_2O, SO_3, and P_2O_5 data sets to improve resolution.

3.7. Water Chemistry

Cave water samples were analyzed for the following parameters: major cations, major anions, alkalinity, major elements, trace elements, TOC, DOC and TDN, as well as $\delta^{18}O$ and $\delta^{2}H$.

3.7.1. Ion Chromatography

Major cations (Ca^{2+}, K^+, Na^+, NH_4^+, Mg^{2+}), using 0.45 µm filtered and acidified samples, and anions (Cl^-, Br^-, F^-, SO_4^{2-}, NO_3^-, NO_2^-, PO_4^{3-}), using 0.45 µm filtered and un-acidified samples were measured using ion chromatography (Dionex ICS-1100) at the Department of Geology in Kansas State University.

3.7.2. Alkalinity

Alkalinity measurements of water samples were performed using a lab pH probe, utilizing the Gran Function Plot Method. Post titration, data were inputted into the online USGS Oregon Water Science Center Alkalinity Calculator, version 2.22.

3.7.3. HR-ICP-MS

Major elements (Ca, K, Mg, Na, P, S, Si) and trace element composition (Al, Ti, V, Cr, Ga, Rb, Sr, Sb, W, Hg, Pb, U, Li, B, Mn, Fe, Ba, Co, Ni, Cu, Zn, As, Se, Mo, Cd) were determined using high resolution ICP-MS (University of Nebraska Lincoln).

3.7.4. TOC, DOC, and TDN

Samples that had been filtered (0.45 µm) and acidified with 0.2% v/v reagent grade HCl were measured for non-purgable organic carbon (NPOC or DOC) and TDN content by thermic oxidation using a Shimadzu TOC/TN analyzer (Department of Geology, Kansas State University).

3.7.5. $\delta^{18}O$ and $\delta^{2}H$ Stable Isotopes

Un-filtered, un-acidfied water samples were analyzed for stable isotopic content (δ^{18}O and δ^{2}H) using a PICARRO Cavity Ring Down Spectrometer in the Department of Geological Sciences at the University of Texas at San Antonio. Data collected were standardized to the Vienna Standard Mean Ocean Water (VSMOW) reference material.

3.8. Geochemical Modeling

Geochemical modeling work, including the calculation of saturation indices and speciation of dissolved components, was performed using the Geochemist's Workbench suite of software, version 10.0. Programs utilized within Geochemist's workbench include SpecE8 and Gtplot. The data collected from the water chemistry analyses listed above were used for the modeling.

3.9. Scanning Electron Microscopy

Scanning electron microscopy analyses were performed on five broken and carbon coated speleothem samples. These analyses were performed on speleothem samples that had excess material. The data collected from these analyses should be regarded as secondary in importance, as most micrographs display a charging effect. Nevertheless, these analyses were included as they provide supportive evidence of speleothem composition (Department of Geosciences, University of Texas at San Antonio).

4. Results

4.1. Variations in Speleothem Morphology

The caves contain a variety of morphologically distinct secondary mineral deposits observed on the cave floor, walls, roof, crevices, and essentially any and all surfaces within the caves. Five major morphologies of speleothems are identified: crusts, polyps, cauliflower, coralloids, and gours. These morphologies and their nomenclature were chosen by the BRAILLE team as the primary speleothem forms observed in LBNM caves. In addition to the five speleothem morphologies, the host rock (cave basalt) is described and analyzed in this study.

4.1.1. Cave Basalt

The host rock in the studied caves formed as a result of lava flow crystallization and exhibited various shapes and textures, including smooth glassy-surfaces, rough aa-like surfaces, lava drips, and lavacicles (*Waters et al., 1990*) (**Fig.8**). While the majority of cave basalt surfaces display either the presence of secondary minerals or microbial habitation, samples of basalt without any obvious visible presence of secondary minerals or biological material were analyzed as representative samples of relatively unaltered host rock. However, it is unlikely that any surface within the caves are truly completely barren, with the possibility of basalt surfaces harboring effectively imperceptible mineral crusts and/or microbial colonization.

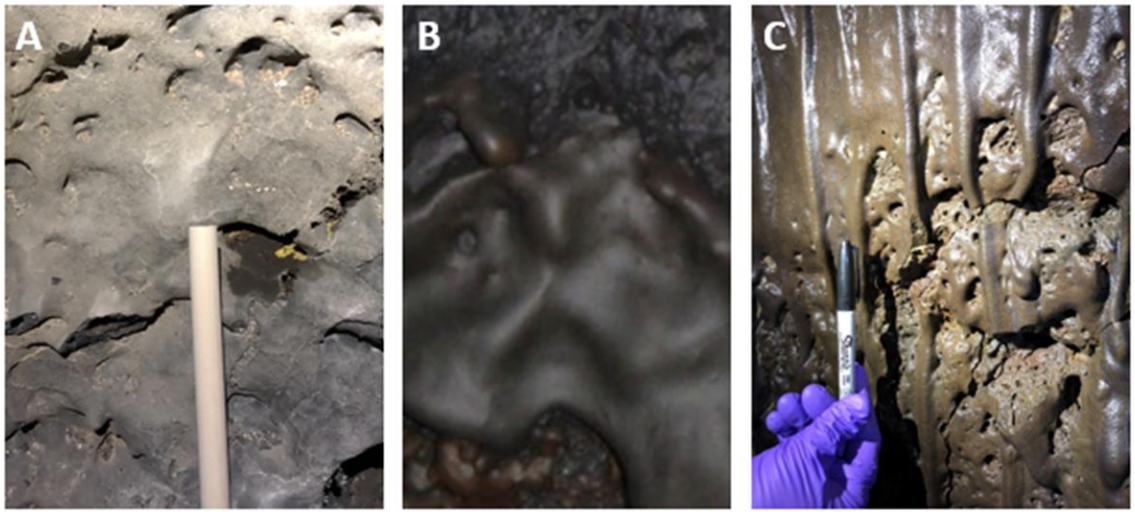

Figure 8. LBNM basalt surfaces exhibiting minimal mineral growth. A) Semi-smooth basalt wall exhibiting broken lava drips; B) Glassy basalt surface; C) Smooth lava drip basalt wall surface and underlying coarse, vesicular basalt.

4.1.2. Crusts

Crusts for the purpose of this study are defined as sub-mm to 0.5 cm thick depositions of secondary minerals that are usually white or orange in color (**Fig.9**). Crusts are ubiquitous within the sampled caves and occur primarily on collapsed cave roof surfaces and cave walls. Deposition typically spans uniformly across several meters of cave wall surfaces, or exists as patchy or semi-isolated features.

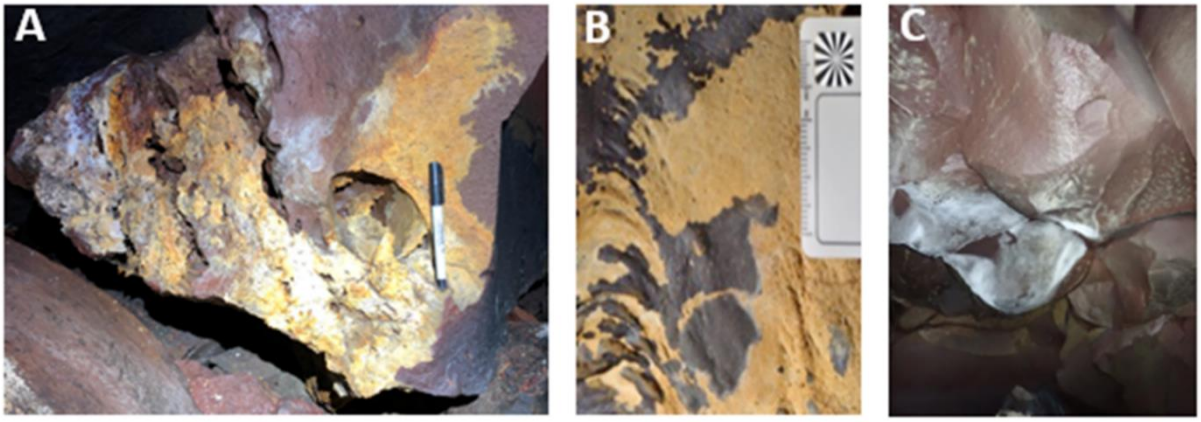

Figure 9. Crusts located on LBNM basalt surfaces. A) Orange and white crusts on reddish (oxidized) collapsed roof basalt; B) Orange crusts on cave wall; C) White crusts located on reddish cave overhang.

4.1.3. Polyps

Polyps are defined as 1-2 cm oblong upward-pointing secondary mineral growths. These secondary mineral deposits are located on collapsed roof basalt, angular aa deposits, and other irregular surfaces. Polyps are seemingly anchored to the underlying rock in a way superficially reminiscent of sea anemone polyps. Although the majority of polyps are orientated upwards against gravity, polyps are also observed to grow horizontally from overhangs and cave wall surfaces. Polyps occur in clusters of several or many individual growths, and are most commonly oriented in near-identical directions within a given polyp cluster. Polyps occur in three primary forms: 1) gray to black elongate "finger" polyps (**Fig.10.A**), 2) gray to black oblong polyps with white tips (**Fig.10.B**), and 3) orange and/or black oblong polyps (**Fig.10.C**). Furthermore, the tips of some polyps exhibited a branching structure consisting of mm-scale nodules, a morphological trait not observed elsewhere along the polyp.

Figure 10. Varieties of LBNM polyp speleothems. A) Elongate "finger" polyps; B) oblong white – tipped polyp. Note the larger, more oblong polyp on the left, compared to a cluster of relative thin polyps; C) A cluster of oblong orange polyps, with a thin white layer coating the majority of the feature.

4.1.4. Cauliflower

Cauliflower speleothems are classified as 2-5 cm diameter knob-like structures often located in clumps visually similar to heads of cauliflower (**Fig.11.A**). Cauliflower speleothems occur as relatively smooth features (**Fig.11.A**) or with closely-spaced protrusions (**Fig.11.B**).

Coloration includes one or more of the following colors: white- tan, light brown, and brown. Moreover, brown cauliflower speleothems also have been described as knobs, and may represent a separate morphology. Cauliflower structures occur primarily on cave walls and roofs.

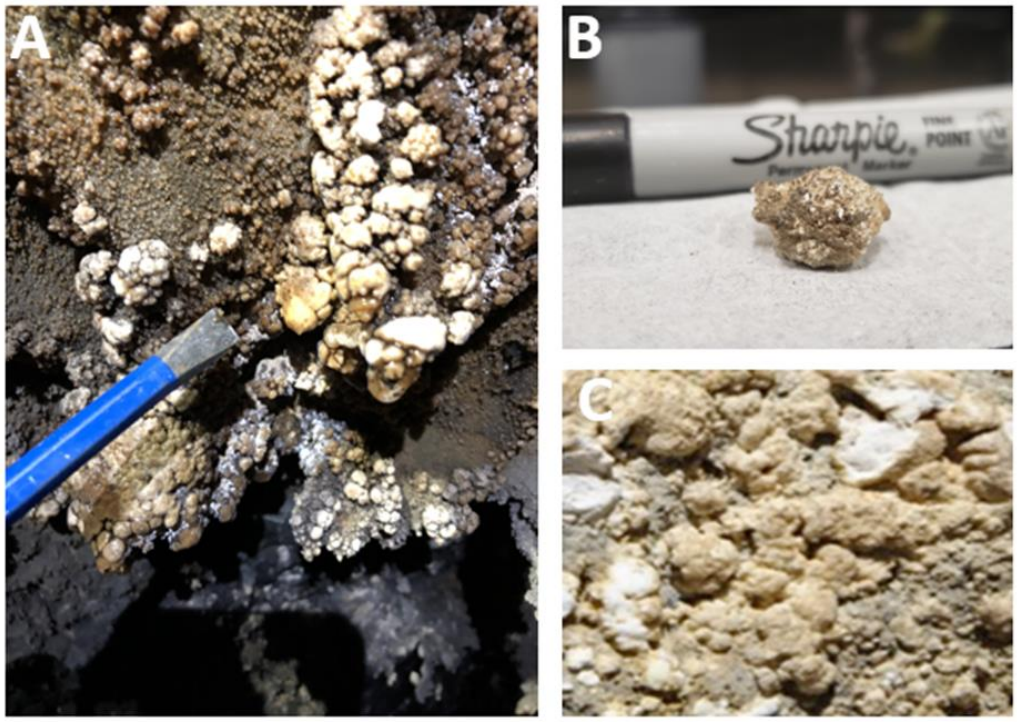

Figure 11. Examples of LBNM cauliflower speleothems. A) "Heads" of cauliflower located on a cave wall; B) Cauliflower with small spicule-like protrusions; C) Closely-spaced cauliflower forming an aggregate mass.

4.1.5. Coralloids

Coralloids are defined as mm to cm scale speleothems outwardly reminiscent of ocean coral structures. While the appearance of coralloids overlaps with that of polyps, coralloids are distinguished from polyps on the prominence of botryoidal and/or branching structures. While polyps also occurred in clusters, individual polyps are not observed to branch into additional growths. Coralloids are typically located on walls and overhangs, in comparison to polyps located on the cave floor surface and/or collapsed roof basalt. The branching pattern is observed along individual stems of the speleothem, resulting in numerous protrusions along the length of a single

feature (**Fig.12.B,C**). Closely spaced coralloids give the appearance of shrubby protrusions on cave walls (**Fig.12.A**). Coloration varies, although coralloids often are a combination of, tan, white, and gray, or as a mostly uniform vitreous brown.

Figure 12. Examples of LBNM coralloid speleothems. A) Bunched brown coralloids located on an overhang; B) Branched coralloid exhibiting a white-tan coloration with intermixed gray; C) White-tan coralloid with many branching protrusions, majority of protrusions are capped with white-colored tips.

4.1.6. Gours

Gours refer to small scale (a few cm) flow-stone like structures oriented downwards alongside gravity. Gours are often partially hollow and were typically associated with active water flow/drips, noticeably more so than other morphologies (**Fig.13.A**), with water often observed beading at the features' tips – generally cup-like protrusions (**Fig.13.B**). Coloration typically consisted of pale yellow to brown hue, and is consistent amongst all sampled gours.

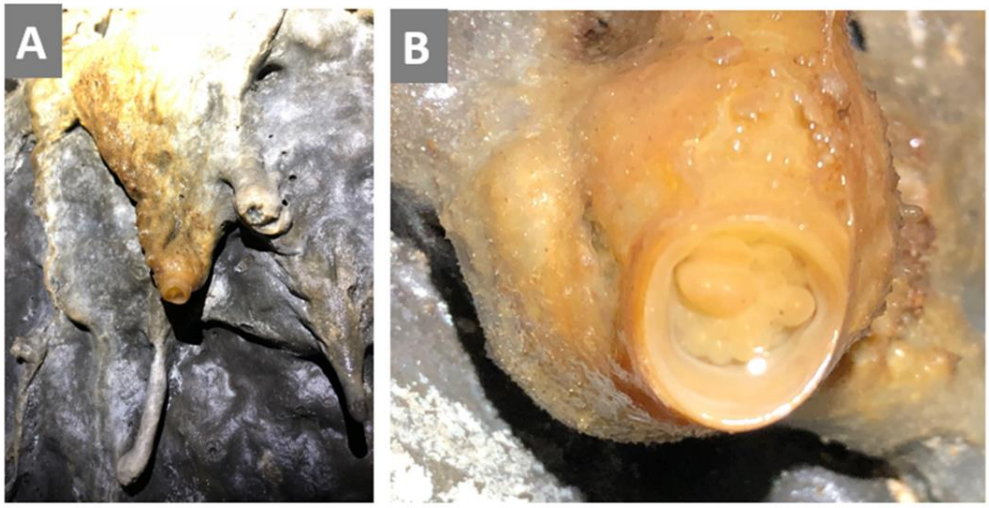

Figure 13. Gour speleothems. A) Gour growing alongside lava drip, and associated water seep; B) Close-up of gour feature. Note the cup-like appearance, beaded opal protrusions, and beaded moisture within and above the cup-like tip. Cup-like feature is approximately 4 cm across.

4.2. Speleothem and Basalt Mineralogy

4.2.1. Cave Basalt

Mineralogical analyses of basalt by X-ray diffraction indicate (**Fig.14**) that plagioclase, clinopyroxene, olivine, and oxide minerals are the predominant minerals comprising the host basaltic rock in LBNM caves. Plagioclase occurs primarily as labradorite and andesine, clinopyroxene as augite and diopside, olivine as forsterite, and oxides as magnetite and hematite. Minor mineralogical phases included apatite and orthopyroxene minerals.

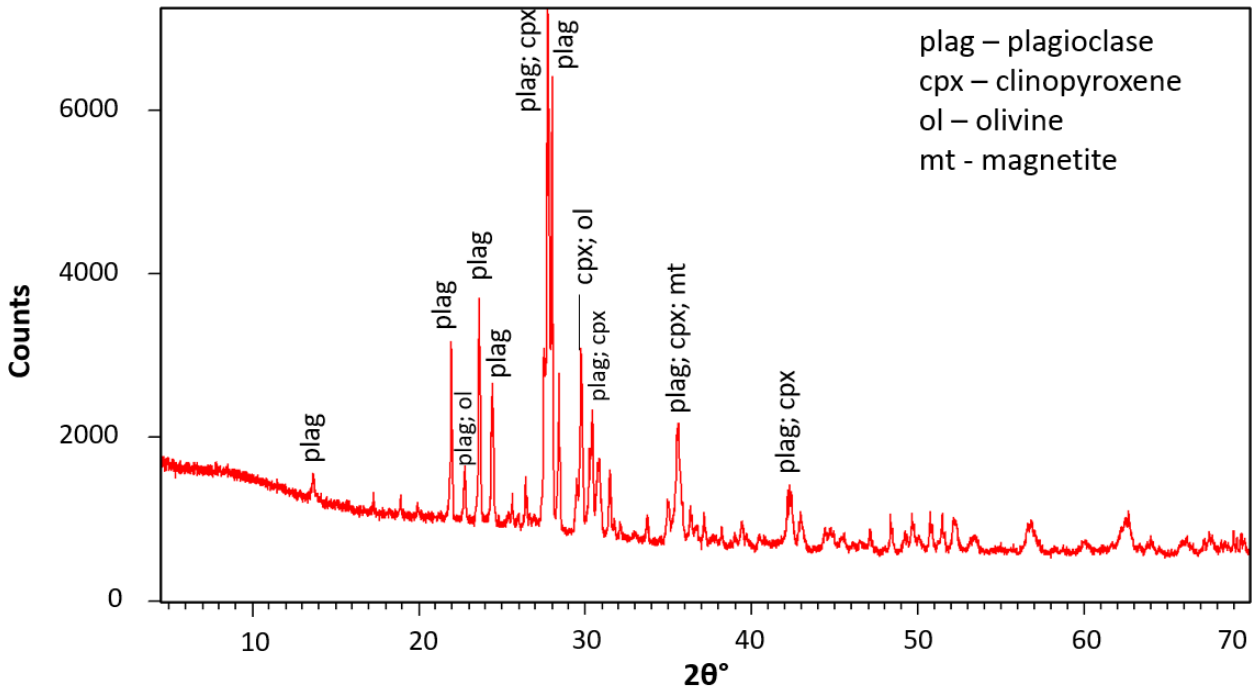

Figure 14. Diffractogram of an LBNM bare basalt cave sample. Peaks confirm presence of plagioclase (plag), clinopyroxene (cpx), olivine (ol), and magnetite (mt).

4.2.2. Speleothems

Lava Beds speleothems (crusts, cauliflower, polyps, coralloids, and gours) are comprised primarily of a combination of two minerals: amorphous opal (Opal-A: $SiO_2 \cdot nH_2O$) and calcite (often Mg-calcite: $(Ca,Mg)CO_3$). Opal is the predominant mineral. Some samples were formed entirely of opal, although calcite is present in some morphologies. X-ray Diffraction analyses performed on speleothems bearing both opal and calcite exhibit diffraction patterns with peaks ascribed to calcite (or Mg carbonate) alongside an elevated background hump from approximately 18 – 26 (2θ°). Calcite-bearing samples that contained less than 2 wt. % CaO exhibit the more strongly elevated 15 – 27 (2θ°) hump alongside calcite peaks. The mineralogy of each morphology will be presented in the following sections.

4.2.3. Museum-Grade Opal Standards

The mineralogy of opal standards were compared with LBNM speleothems to corroborate opal mineral identity. Opal standards obtained from Dr. Richard Léveillé at McGill University were analyzed by XRD to determine their mineralogical content. Minerals identified included opal CT (Opal Cristobalite-Tridymite), silica (quartz)-bearing opal, and opal-A (amorphous) opal. Opal CT included peaks for cristobalite and tridymite, while opal-A displayed a broad hump indicative of a lack of crystallinity between 15 – 27 (2θ°), with the apex at approximately 22 – 22.5 (2θ°) (**Fig.15.C,D**). These patterns are also consistent with other mineralogical studies describing amorphous opal (*Elzea and Rice, 1996*; *Sodo et. al, 2016*). Opal A proved to be the only mode of opal identified in speleothem samples.

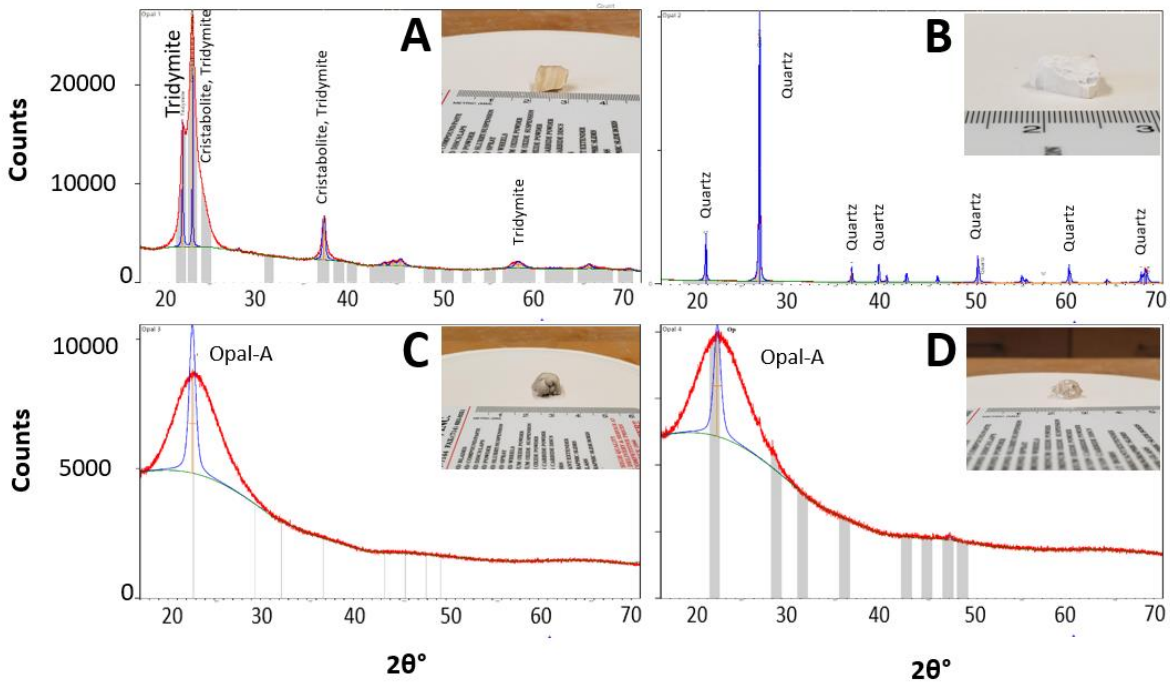

Figure 15. Diffractograms of four museum-grade opal standards. A) Diffractogram displaying peaks for opal CT; B) Diffractogram displaying peaks for quartz; C) Diffractogram exhibiting hump indicative of amorphous material: opal-A; D) Diffractogram also displaying opal-A.

4.2.4. Crusts

X-ray diffraction analysis of crust speleothems revealed the presence of two minerals: amorphous opal and calcite. Two diffractogram patterns of crust samples are observed: 1) prominent amorphous opal hump (**Fig.16.A**) and calcite peaks, and 2) relatively more intense calcite peaks (**Fig.16.B**). Note that the diffractogram associated with **Fig.16.B** was the result of an improperly prepared sample that included fragments of basalt. As a result, the diffractogram also displays peaks associated with basaltic minerals (namely plagioclase and clinopyroxene). These minerals are not secondary minerals and are as such not expected major components of speleothems.

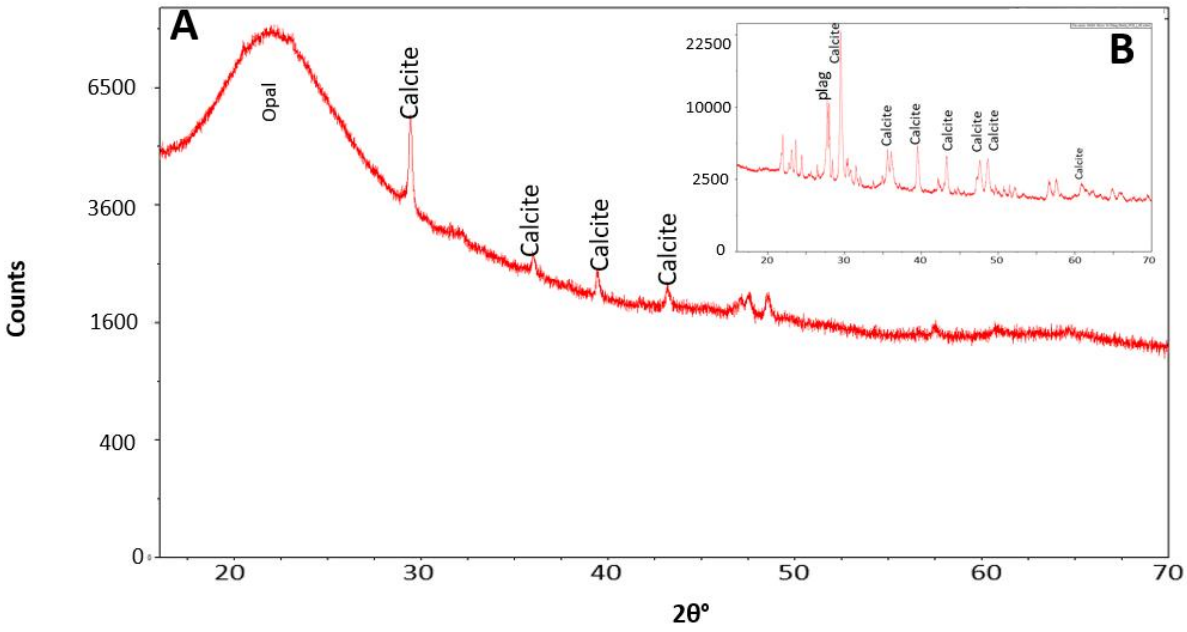

Figure 16. Diffractograms of crust speleothems. A) Opal dominant diffractogram with prominent amorphous hump; B) Calcite dominant diffractogram with plagioclase peaks not representative of speleothem composition.

4.2.5. Polyps

Mineralogical analyses revealed that polyps were primarily comprised of two mineral phases: opal and calcite (often Mg-calcite). Purely amorphous opal samples were also observed. Furthermore, three diffractogram patterns were observed: 1) strong calcite peaks and weak amorphous opal hump (**Fig.17.A**), and 2) pronounced amorphous opal hump and relatively less intense calcite peaks (**Fig.17.B**), and 3) pronounced amorphous opal hump at 22 – 22.5 (2θ°) with no calcite peaks.

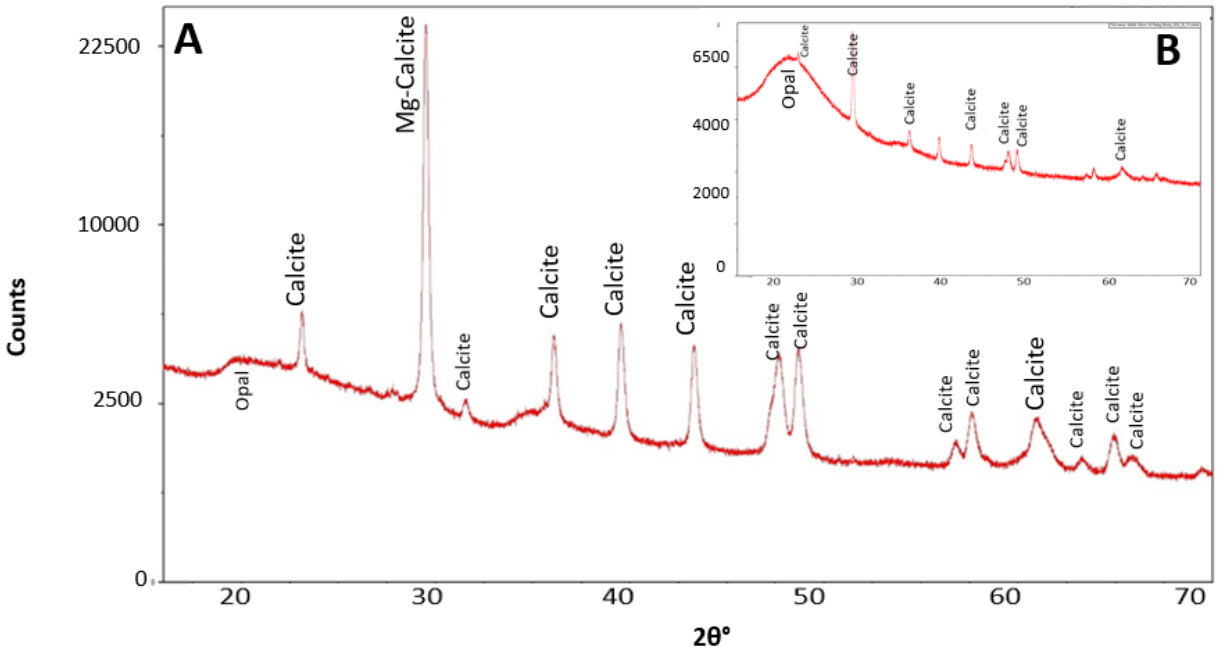

Figure 17. Diffractograms of polyp speleothems. A) Calcite dominant diffractogram with a depressed amorphous hump; B) Opal dominant diffractogram with a prominent amorphous hump.

4.2.6. Cauliflower

Mineralogical analyses of cauliflower speleothems revealed a composition comprising either of a combination of calcite (often Mg-calcite) and amorphous opal, or a composition consisting solely of amorphous opal. Two diffractogram patterns were predominantly observed: 1) strong calcite peaks and weak amorphous opal hump (depressed by the preponderance of

crystalline calcite in the sample) (**Fig.18.A**), and 2) prominent amorphous opal hump at 22 – 22.5 (2θ°) (**Fig.18.B**).

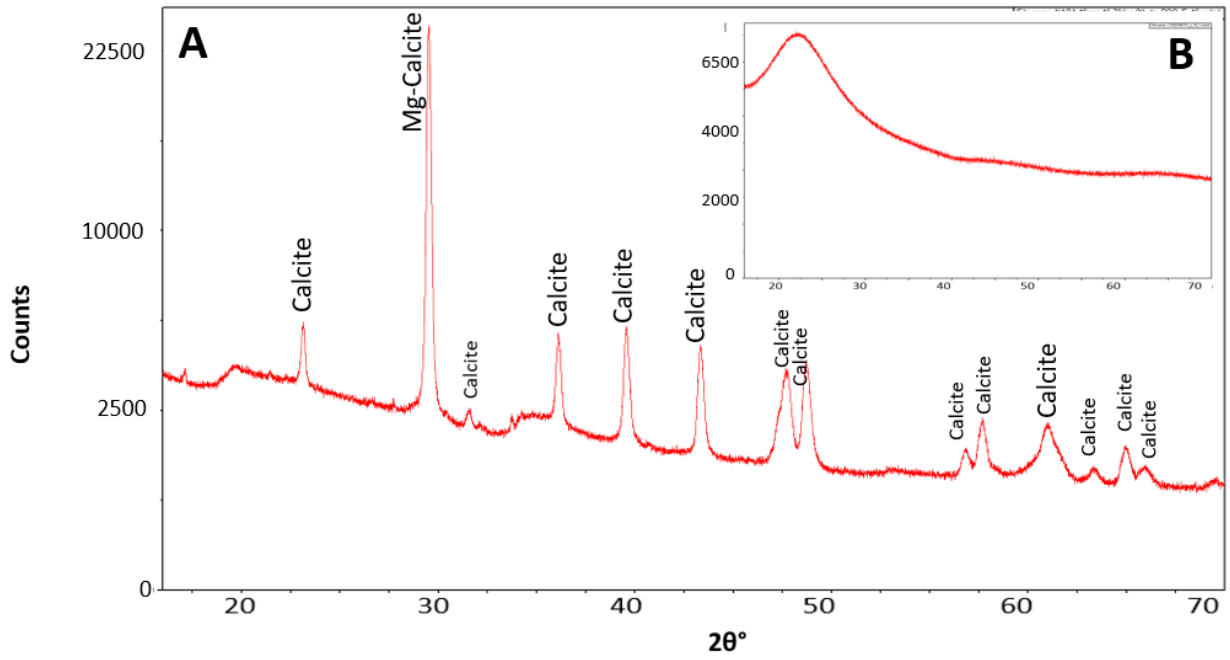

Figure 18. Diffractograms of cauliflower speleothems. A) Calcite dominant diffractogram lacking prominent opal-A hump; B) Diffractogram exhibiting opal-A hump.

4.2.7. Coralloids

Coralloids were comprised either of a combination of calcite (often Mg-Calcite) and amorphous opal or amorphous opal alone. Similar to cauliflower structures, two diffractogram patterns were predominantly observed: 1) strong calcite peaks and weak amorphous opal hump (depressed by the preponderance of crystalline calcite in the sample) (**Fig.19.A**), and 2) a prominent amorphous opal hump at 22 – 22.5 (2θ°).

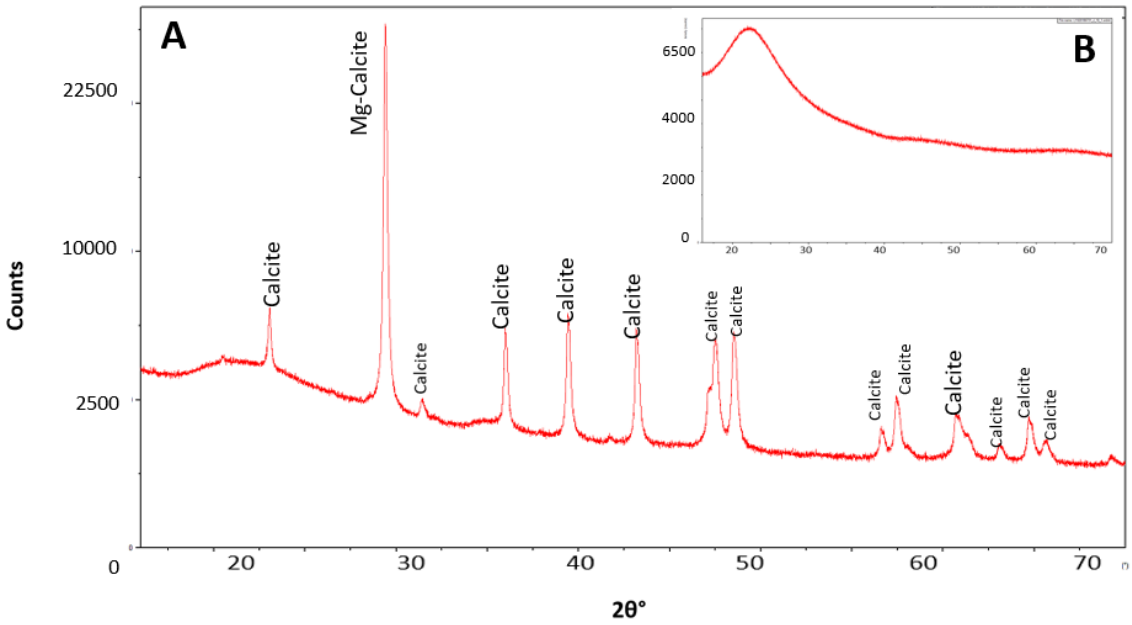

Figure 19. Diffractograms of coralloid speleothems. A) Calcite dominant diffractogram lacking prominent opal-A hump; B) Diffractogram exhibiting opal-A hump.

4.2.8. Gours

Gour speleothems displayed only a hump indicative of opal-A at 22 – 22.5 (2θ). Subsequently, no calcite peaks were present within gour speleothem diffractograms (**Fig.20**).

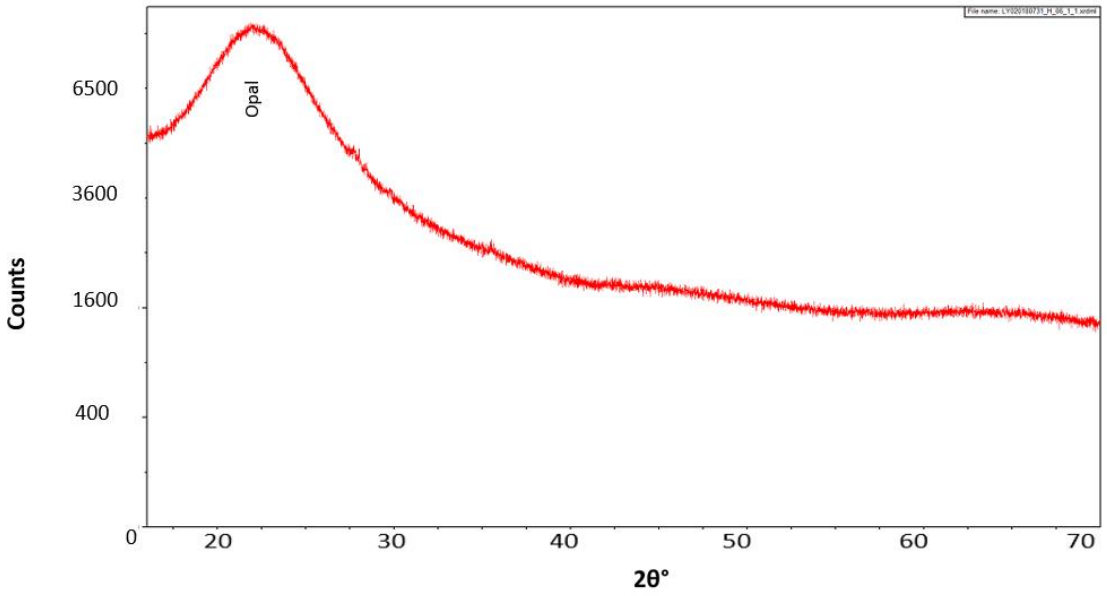

Figure 20. Diffractogram of a gour speleothem. Diffractogram displays no visible peaks, and is indicative of Opal-A.

4.3. Clay Mineralogy

Clay minerals are not observed within any analyzed basalt or speleothem samples – neither from clay fraction analysis nor petrographic analyses. However, due to the lower volume of sample collected and therefore utilized during the clay separation procedure, it is possible that some samples contained a very low volume of clay minerals not optimal for the clay fraction analysis method. Regardless, it can be stated that clay minerals are likely not a major mineralogical component of LBNM samples.

4.4. Petrographic Analysis of LBNM Speleothems and Cave Basalt

4.4.1. Cave Basalt

Cave basalts consisted predominantly of a glassy matrix, plagioclase, and clinopyroxene. Glassy textures were dominant in certain basaltic cave features, such as lava drips and lava stalactites (features associated with rapid cooling). Plagioclase grain sizes ranged from approximately 0.06 – 0.22 mm. Clinopyroxene grains were generally less than 0.15 mm (**Fig.21.A**), but larger crystals have been observed in some samples (**Fig.21.B**). Euhedral oxide crystals, representative primarily of magnetite (according to XRD analyses), were present throughout most basalts and were most highly concentrated along the peripheries of the basalt (the outermost portion the basalt sample). Moreover, many basalt peripheries were observed to be in the process of palagonite alteration, as evidenced by the characteristic yellow coloration in these samples (**Fig.21.C**). Secondary iron hydroxide minerals (likely including goethite) were noted to be present within select basalt samples, yet again exclusively along the peripheries of the sample. Palagonite alteration and iron hydroxide minerals were also observed to occur within basalt, seemingly encapsulated by secondary mineral precipitation (**Fig.21.D**), suggesting that altered basalt within caves may act as nucleation sites for secondary mineral precipitation.

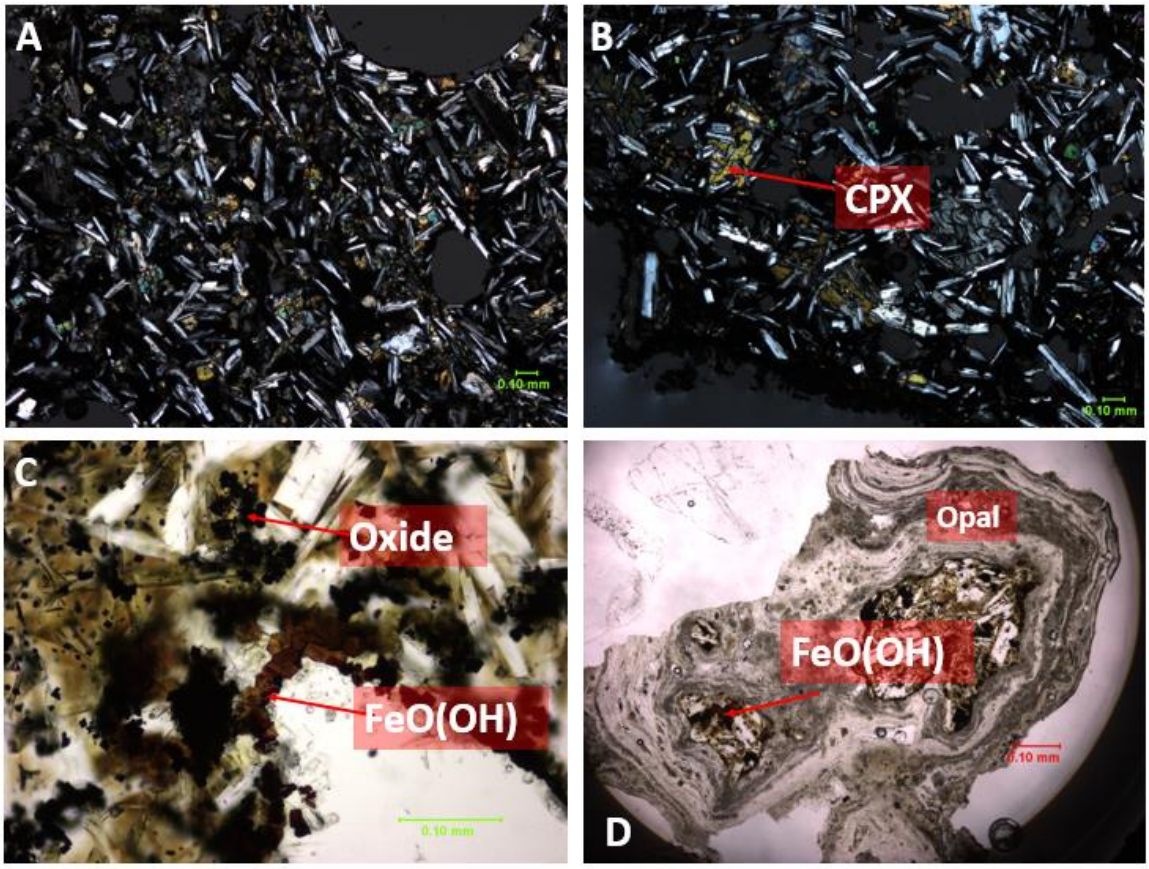

Figure 21. Basalt texture and iron hydroxide minerals. A) Glassy matrix with smaller clinopyroxene crystals – 4x, XPL; B) Glassy matrix with larger clinopyroxene crystals – 4x, XPL; C) Palagonite alteration (yellow), euhedral iron hydroxide crystals, and magnetite crystals – 20x, PPL, maximum brightness; D) Basalt exhibiting palagonite alteration (yellow) and iron hydroxide crystals, surrounded by opal precipitation in a cauliflower speleothem sample – 4x, PPL, maximum brightness. All scale bars represent 0.10 mm.

4.4.2. Crusts, Cauliflower, Polyps, Coralloids, and Gours

All five of the identified speleothem morphologies (crusts, cauliflower, polyps, coralloids, and gours) share a common internal structure: µm to mm scale, possibly microstromatolitic-like laminations of secondary mineral deposition. Depending on sample composition, the laminae consist predominantly of opal, or of alternating bands of opal and/or carbonate minerals. Opal laminae are typically massive or were porous with vesicles. Calcite infilling in opal lamina is also observed. The laminae of samples bearing both opal and calcite were not consistently ordered even within their respective morphologies. For example, polyps sampled from identical sample sites

display different orderings of opal / calcite layers. Furthermore, opal and calcite laminae do not alternate evenly; opal was observed to be deposited upon opal and calcite may be deposited on calcite.

The laminae that comprise crust speleothems largely consist of very fine (µm scale), often hummocky, layers in a coat of approximately even thickness upon a basalt surface (**Fig.22.A**). The boundary between the basalt and secondary mineral precipitant may be accompanied by iron hydroxide minerals (**Fig.22.B**), analogous to similar minerals observed along the peripheries of basalt samples. The outermost laminae display a multitude of branching and/or knoblike protrusions, likely indicative of the most recent nucleation and mineral growth. Opal coloration under plane-polarized light varied from a light tan to various shades of darker tan to brown.

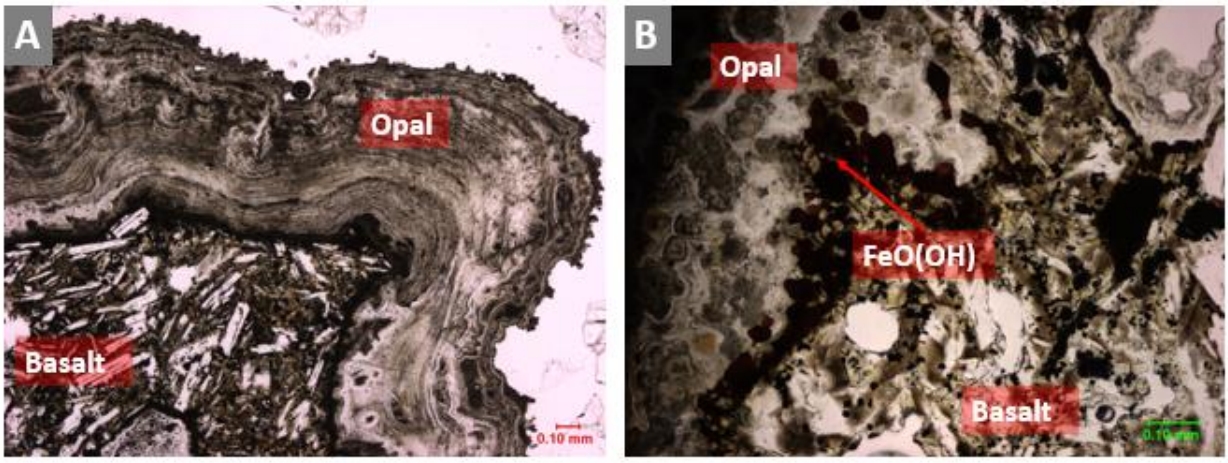

Figure 22. Crust speleothem lamina. A) Opaline crust sample and host basaltic rock – 4x, PPL; B) Iron hydroxide boundary between host basaltic rock and secondary mineral deposition (opal) – 10x, PPL, maximum brightness.

Cauliflower laminae occur in structures similar to the crust laminae, i.e. fine-scale hummocky laminae (**Fig.23.A**). These crust-like laminae were found predominantly on the outer portions of the cauliflower. Opal coloration was similar to that of other morphologies, with the addition of yellowish laminae not yet observed with crust laminae. Near the interior of cauliflower speleothems, laminae are more hummocky and/or undulating. Void spaces are also infilled with

calcite (**Fig.23.B,C**). Moreover, opal deposition tends to lack obvious laminations or occurs as nodular semi-circular structures that appear to have grown radially instead of laterally (**Fig.23.B**). Similar nodules have been noted in other basaltic lava cave speleothems, and may represent microbially-mediated concentric opal-A structures (*López-Martínez et al., 2016*). The infilled calcite is less abundant than opal. This is readily observed in thin section under crossed polars, as the opal goes to extinction and the calcite does not (**Fig.23.C**). Cauliflower laminae also exhibit microstromatolitic-like structures, with multiple growth patterns radiating from multiple positions within the speleothem (**Fig.23.D**).

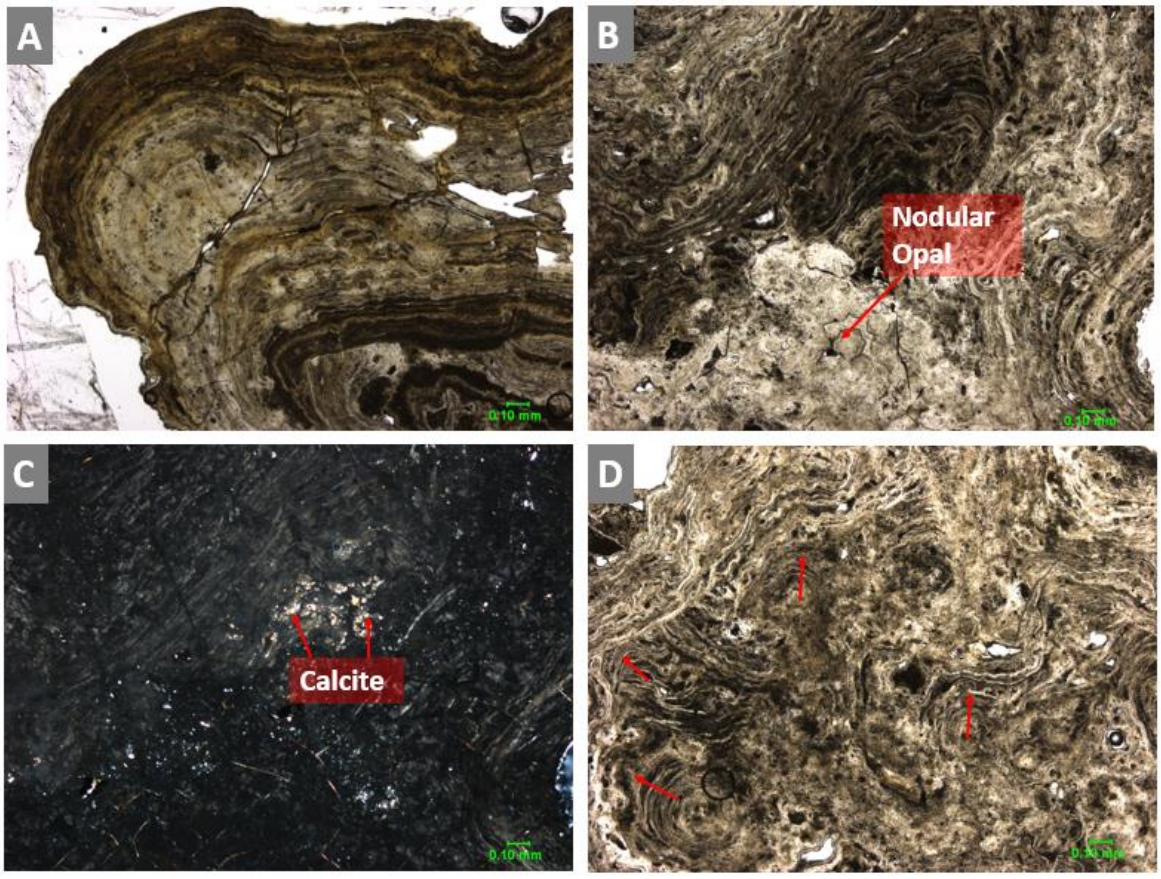

Figure 23. Internal structures of cauliflower speleothems. A) Hummocky opal laminae associated with cauliflower edge – 4x, PPL; B) Heavily undulated laminae associated with the interior of cauliflower. Note the semi-circular nodular deposition in the lower-middle portion of the image – 4x, PPL; C) Crossed-polars image of B, calcite located amongst opal – 4x, XPL; D) Chaotic and undulating laminae with multiple apparent growth directions, similar to microstramtolitc growth. Arrows represent orientation of laminae.

Polyp speleothems exhibit a wide diversity of internal structures, including distinct laminae of calcite and opal (**Fig.24.A**). Three visibly heterogeneous opal laminae are observed: a "dirty" brown and tan opal, a further laminated yellowish opal, and a mostly massive "clean" tan deposit. Calcite in polyps forms laminae that appear to be completely separate from opal deposits (**Fig.24.B**). However, intermixed laminae are also observed. Calcite occurs predominantly as a coarsely crystalline sparite, a finer micritic calcite, or as a combination of the two. Laminae thickness of both opal and calcite layers vary both inter- and intra- sample, from approximately 50 µm to excesses of 0.5 mm.

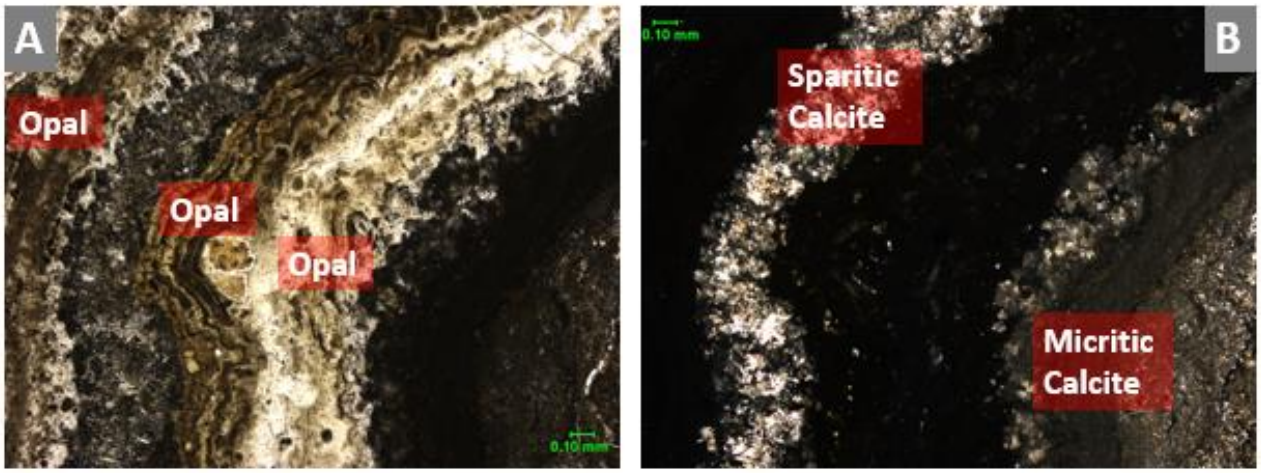

Figure 24. Internal structure and texture of a polyp speleothem. A) Three distinctive layers of opal are visible: brown and tan, yellowish, and a light tan – 4x, PPL; B) Sparitic Calcite and Micritic Calcite laminae bounding the innermost opal laminae – 4x,XPL.

Moreover, the calcite found within polyps also occurs as ordered, columnar crystals (**Fig.25**). The columnar calcite does not occur consistently between samples, occurring in basal laminae in some polyps, while other samples contain columnar calcite only towards the tip of the polyp. These laminae exist within the polyp in the same manner as the previously described forms of calcite, having been observed to straddle both opal and calcite layers.

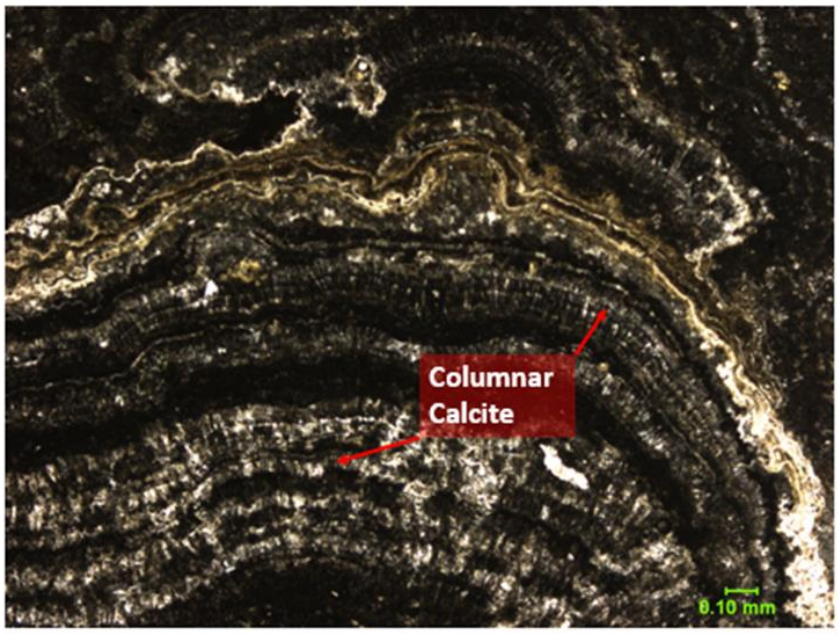

Figure 25. Columnar calcite located within a polyp speleothem. Opal laminae are also visible in-between calcite laminae, including a prominent gold-colored laminae, 4x, PPL.

Coralloid laminae outwardly appeared to be most similar to those associated with crust and cauliflower morphologies, especially in regards to opal laminae. However, calcite found within coralloids more closely resembles the textures and structures of calcite in polyp speleothems, including the presence of micritic calcite (**Fig.26.B**). The calcite displayed in **Fig.26**, located on the outward most edge of the feature, may represent the recent period of deposition that is still nested alongside previously deposited opal. Moreover, the coralloid sample depicted in **Fig.26** well illustrates the diversity of opal coloration and texture. Under plane-polarized light, the hummocky light brown laminae in the upper-center of the sample appear superficially similar to the micritic calcite. However, under crossed-polars, the light brown laminae become extinct, and is therefore likely opal (**Fig.26.B**).

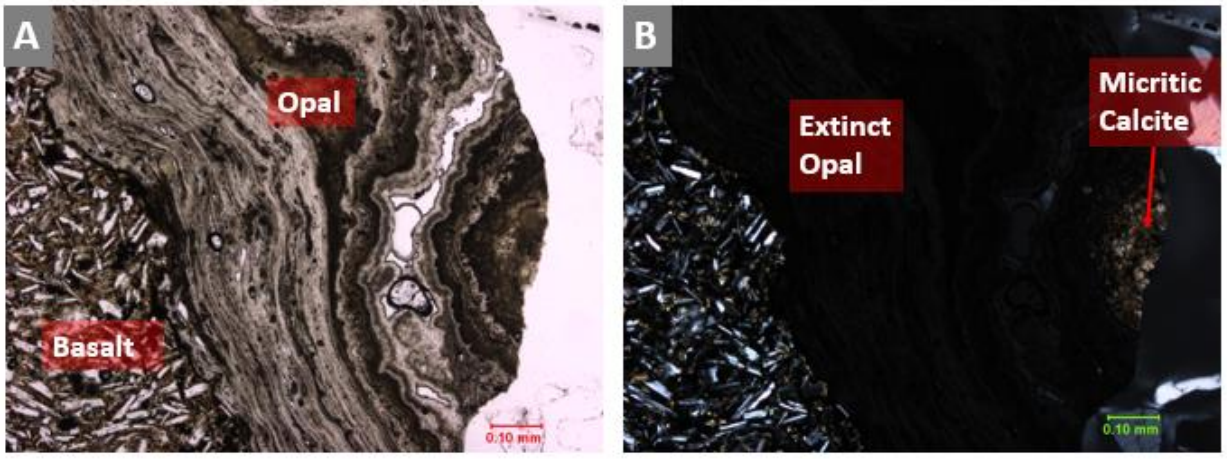

Figure 26. Opal and calcite laminae within a coralloid speleothem. A) Opal lamina may appear similar to micritic calcite, 4x,PPL; B) Calcite now distinguishable under crossed-polars, 4x,XPL.

Gour speleothem laminae consist entirely of opal; none have been noted to incorporate calcite. The individual laminae are visually similar and of similar thickness to laminae found within other morphologies, but the structure and orientation of gour laminae are noticeably different from polyp and coralloid speleothems. Gour laminae are contained within an extremely-finely laminated cup-like structure of opal, in which the laminae are concave in respect to the terminal tip of the gour speleothem (**Fig.27.A**). The cup-like structure appears to lack laminations, but the laminae are actually just closely spaced, giving the appearance of dense massive deposition. Hummocky and undulating laminae are also found within gours when viewed at higher magnifications (**Fig.27.B**).

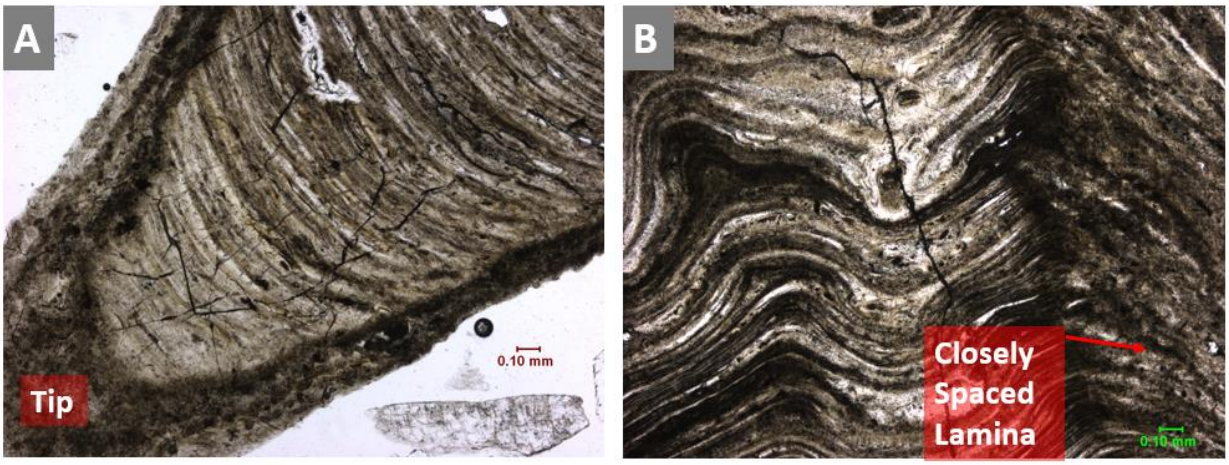

Figure 27. Internal structure of LBNM gour speleothems. A) Concave opal laminae encapsulated within cup-like tip, 4x,PPL; B) Hummocky opal laminae and closely-spaced laminae which comprise the edge of the cup-like tip feature, 4x,PPL.

4.4.3. Volcanic Fragment Inclusions within Speleothems

Lava Beds speleothems incorporate volcanic mineral fragments, glass fragments, and iron hydroxide (**Fig.28**). Moreover, the inclusions mostly occur within the matrix of opal laminae, especially thicker opal laminae equal to or approximately greater than 0.5 mm. The largest inclusions (> 0.05 mm) have been identified in polyp speleothems, and not in other morphologies of similar mineralogical and elemental composition (cauliflower, coralloids). Polyps predominantly form on or nearby the cave floor surface, making dust a likely source of these incorporated fragments. The other morphologies are primarily located in elevated positions, such as on walls and overhangs, thus perhaps lessening the opportunity for dust to settle upon the growing speleothems. Regardless, dust fragments are likely to be an expected component of opaline speleothems.

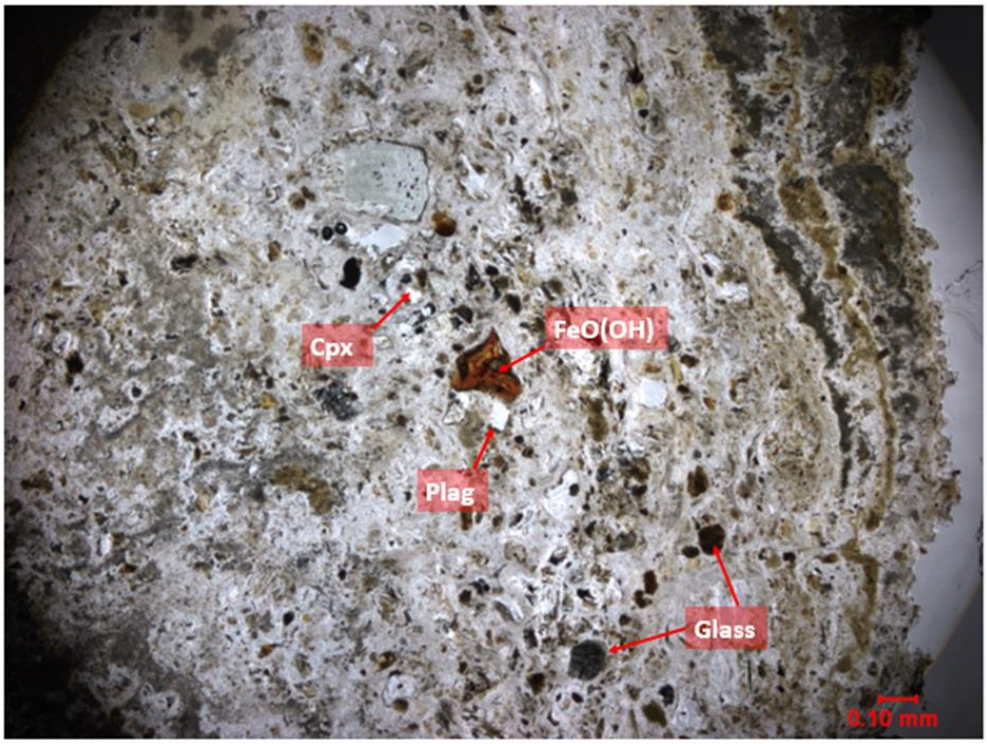

Figure 28. Volcanic glass and mineral inclusions within polyp speleothem opal matrix. Glass fragments are opaque and easily identified under plane-polarized light, while plagioclase and clinopyroxene are most easily identified under crossed-polars. The iron hydroxide in the center of the image appears to overlay weathered plagioclase grains.4x, PPL, maximum brightness.

4.5. Cave Basalt and Speleothem Elemental Composition

This study is the first of its kind at Lava Beds National Monument – an effort to understand the composition of enigmatic speleothems. However, as a result, it must be noted that the number of collected samples likely do not provide well-constrained statistics of compositional variation. Regardless, the following results represent the most comprehensive data for LBNM speleothems.

4.5.1. Cave Basalt

The host rock comprising the caves range from basalt to basaltic andesite in composition, with SiO_2 wt. % ranging from 48 – 54 wt.%. The major elemental oxide compositions determined by X-ray fluorescence varies between caves (**Table 3**), but are all consistent with previously recorded compositions of Medicine Lake basalts (*Baker et al., 1991*). Trace element concentrations (e.g. Zr, Sr, Rb, Cu, V, Ba, and Cr) are also comparable with previously analyzed Medicine Lake

basalts (**Table 3**). Sulfur concentration is below the detection limit of the XRF method used. Basalt compositions are most similar between caves that are contained in the same flow, i.e. VAL and LYO, and between GOL YEL, POS and CRI.

Table 3. Major and Trace Element Composition of LBNM Cave Basalt. Three-letter cave ID represents name of sampled cave. Major elements (presented as oxides) and LOI (Loss on Ignition) are presented in Wt.%, and trace elements are presented in ppm. All iron is given as Fe_2O_3. Values listed as bdl are below detection limits.

Cave	***SiO_2***	***CaO***	***MgO***	***Al_2O_3***	***Fe_2O_3***	***MnO***	***P_2O_5***	***K_2O***	***Na_2O***	***TiO_2***	***LOI***	***S***	***V***	***Cr***	***Co***	***Ni***	***Cu***	***Zn***	***Rb***	***Sr***	***Y***	***Zr***	***Ba***	***Pb***
	Wt. %											ppm												
VAL	51.64	9.08	4.45	16.61	10.67	0.18	0.41	1.47	3.30	1.62	0.40	bdl	199	126	39	95	83	95	49	344	43	251	338	14
LYO	52.61	7.79	4.89	15.67	9.50	0.17	0.39	1.36	3.61	1.67	2.21	bdl	182	111	36	67	68	67	36	244	37	221	343	14
GOL	53.98	8.71	5.80	17.03	8.50	0.15	0.01	1.15	2.60	0.76	1.15	bdl	145	137	42	144	220	144	36	287	26	124	250	bdl
YEL	52.07	8.92	6.10	16.79	9.34	0.16	0.07	1.29	2.97	0.84	1.30	bdl	166	162	36	150	154	150	48	304	36	144	370	1
POS	50.20	10.58	7.32	16.45	10.43	0.18	bdl	0.23	2.59	0.88	0.98	bdl	216	212	43	197	238	197	4	331	30	79	130	2
SIL	51.72	8.85	5.28	16.70	8.95	0.15	0.03	1.15	3.13	0.85	2.89	bdl	197	140	41	139	92	139	36	291	29	132	353	3
CRI	48.29	8.99	7.65	16.72	9.24	0.16	0.14	0.44	2.58	0.85	4.82	bdl	196	148	34	146	76	146	10	247	25	81	201	bdl

4.5.2. Crusts

Crust chemistry is dominated by SiO_2 (34.93 – 85.80 wt.%), CaO (2.93 – 20.23 wt.%), and MgO (0.40 – 10.92 wt.%). These elemental constituents are consistent with the observed bulk mineralogy of opal and calcite / Mg carbonate, the minerals composing most LBNM speleothems. Percentages of these elemental oxides vary, as crusts appear to incorporate varying amounts of carbonate, which is also reflected in the higher LOI values of orange crusts (**Table 4**). Samples incorporating more significant amounts of carbonate (>10 %) appear to take on an orange / tan coloration, while crusts consisting of predominantly opal appear white. Crusts contain 0.43 – 1.89 wt.% P_2O_5, with no obvious relationship between CaO content and P_2O_5 concentrations. Al_2O_3, Fe_2O_3, and Na_2O concentrations are low in crusts, with the exception of POS-I. This suggests that basaltic material may have been included in the analysis.

Trace element compositions are highly variable. Sr, Cu, V, and S occur in the highest concentrations (**Table 4**). S concentrations are highly variable among crusts, with one sample, POS-I, exhibiting 1785 ppm S; yet S is below detection limits for other samples from the same cave. The basaltic material included within this sample is unlikely to significantly contribute to the S concentration, as S was not detected in sampled basalts (**Table 3**). The variability exhibited by S in crusts is observed in the remaining trace elements.

Table 4. Major and Trace Element Composition of LBNM Crust Speleothems. Three-letter cave ID represents name of sampled cave. Major elements (presented as oxides) and LOI (Loss on Ignition) are presented in Wt.%, and trace elements are presented in ppm. All iron is given as Fe_2O_3. Values listed as bdl are below detection limits.

Cave	***Site***	***Color***	***SiO_2***	***CaO***	***MgO***	***Al_2O_3***	***Fe_2O_3***	***MnO***	***P_2O_5***	***K_2O***	***Na_2O***	***TiO_2***	***LOI***	***S***	***V***	***Cr***	***Ni***	***Cu***	***Zn***	***Sr***	***Y***	***Zr***	***Ba***	***Pb***
			Wt. %											ppm										
LYO	H	White	85.80	2.93	0.40	0.11	0.42	bdl	0.77	0.02	bdl	0.01	9.51	124	127	21	28	79	9	32	3	5	bdl	2
POS	F	Orange	51.85	13.28	8.64	0.13	0.34	bdl	0.43	0.02	bdl	bdl	25.24	bdl	595	bdl	15	16	12	65	2	2	4	2
POS	I	Orange	34.93	20.23	10.92	4.63	3.09	0.05	1.89	0.41	1.00	0.27	22.31	1785	195	42	82	80	33	230	11	43	149	2

4.5.3. Polyps

Polyp major elemental chemistry is also dominated by SiO_2 (33.9 – 77.59 wt.%), CaO (1.49 – 17.06 wt.%), and MgO (0.56 – 14.08 wt.%), indicative of the opal and calcite / Mg carbonate mineralogy of these speleothems (**Table 5**). Lesser concentrations of Al_2O_3 and P_2O_5 are also present in most polyps. Iron is present in all polyps, at a range of 0.33 – 1.53 wt. % Fe_2O_3. K_2O, and Na_2O are present in low concentrations, while MnO is below detection limits in most samples. LOI values vary, with samples incorporating higher CaO concentrations generally bearing the greatest LOI values. However, the silica-dominated YEL-Ac sample has an LOI value of 25.9 %, likely indicative of variability in opal water content between samples. Similar to crusts, select polyps were found to be comprised predominately of opal. Opal dominance (as represented by SiO_2 > 50 wt.%) is observed in the majority of samples, including all three descriptive forms (fingers, white-tipped polyps, and orange polyps). Fingers appear to be polyps that incorporate relatively small amounts of calcium (2.23 ± 1.04 CaO wt.%), white-tipped polyps with relatively high amounts of calcium (11.13 ± 4.47 CaO wt.%), and orange polyps with moderate calcium (5.82 ± 4.39 CaO %). Phosphorous occurs predominantly in carbonate-bearing polyps, ranging from 0.30 – 4.85 P_2O_5 wt. %. However, higher CaO concentrations do not correlate with greater P_2O_5 concentrations.

Sr, Cu, and S constitute the most abundant trace elements present in polyp speleothems (**Table 5**). Sr is most abundant among carbonate-bearing polyps and highest in white-tipped polyps, but concentrations are variable (7 – 784 ppm). The greatest Cu concentrations (429 and 258 ppm) are observed within opaline finger-type polyps. However, the other polyp varieties are also noted to contain relatively high Cu content, with concentrations ranging from 56 – 243 ppm. Cu content in polyps may also reflect the cave of origin and subsequently the availability of Cu in

individual cave systems: YEL 247 ± 16 ppm, GOL 297 ± 115 ppm, POS 137 ± 55 ppm, SIL 176 ppm, CRI 76 ± 6 ppm, and PAN 79 ppm. S concentrations in polyps appear to also vary amongst caves: YEL 342 ± 98, GOL 342 ± 203 ppm, POS 1549 ± 629 ppm, SIL 1601 ppm, CRI 1066 ± 458 ppm, and PAN 570 ppm. Additionally, select polyp speleothems contain moderate amounts of V (40 – 308 ppm) and Ba (14 – 221 ppm). Notably, Ba concentrations are consistently low amongst POS samples, at 32 ± 19 ppm, which may be due to POS's minimal Ba concentration in basalt at 130 ppm, nearly three times smaller than the majority of other sampled caves.

4.5.4. Cauliflower

Cauliflower speleothem major elemental composition is dominated by SiO_2 (17.13 – 85.49 wt.%), CaO (1.03 – 29.77 wt.%), MgO (0.57 – 15.62 wt.%), and lesser concentrations of P_2O_5 (**Table 6**). As compared to polyps, calcite-bearing cauliflower samples generally incorporate lesser concentrations of SiO_2. Cauliflower samples from VAL and LYO (the youngest caves sampled) are observed to be primarily opaline, while samples from POS and CRI incorporate more carbonate than the other caves, up to 29.77 wt.% CaO. Like polyps, cauliflower display a range of LOI values. Opaline cauliflower have LOI values < 15 wt.%, while carbonate-bearing cauliflower range from 18 – 38 wt.% LOI.

The three observed categories of cauliflower have markedly different compositions. The white-tan brown sample appears to be predominantly opaline (77.14 wt. % SiO_2) with a moderate incorporation of carbonate minerals (6.98 wt. % CaO), but with very little MgO (0.57 wt.%). Brown cauliflower, potentially a separate morphology altogether (knobs), is dominated by SiO_2 at 84.79 ± 1 wt.%. White-tan cauliflower incorporates less opal than brown samples, at 36.18 ± 14.62 wt.% SiO_2. However, white-tan samples incorporate higher concentrations of CaO (17.67 ± 9.34 wt.%) and MgO (12.88 ± 2.16 wt.%).

Table 5. Major and Trace Element Composition of LBNM Polyp Speleothems. Three-letter cave ID represents name of sampled cave. Major elements (presented as oxides) and LOI (Loss on Ignition) are presented in Wt.%, and trace elements are presented in ppm. All iron is given as Fe_2O_3. Values listed as bdl are below detection limits.

Cave	***Site***	***Color***	***SiO_2***	***CaO***	***MgO***	***Al_2O_3***	***Fe_2O_3***	***MnO***	***P_2O_5***	***K_2O***	***Na_2O***	***TiO_2***	***LOI***	***S***	***V***	***Cr***	***Ni***	***Cu***	***Zn***	***Sr***	***Y***	***Zr***	***Ba***	***Pb***
			Wt. %											ppm										
GOL	B	Fingers	77.59	2.96	2.76	1.66	1.04	0.01	bdl	0.17	bdl	0.07	13.65	137	40	25	23	429	bdl	81	10	15	57	4
GOL	C	White	60.67	8.13	6.27	0.39	0.45	bdl	1.48	0.05	bdl	0.02	22.43	542	41	11	17	218	15	328	10	8	104	bdl
GOL	G	White	59.65	9.14	8.48	1.70	1.03	0.01	0.30	0.22	0.08	0.07	19.18	347	77	13	36	243	12	397	12	21	168	bdl
YEL	Ac	Fingers	65.38	1.49	0.56	3.16	1.38	0.02	1.46	0.22	0.24	0.12	25.90	272	45	23	23	258	14	61	12	21	116	2
YEL	B	White	51.76	10.99	8.30	0.32	0.42	bdl	1.37	0.05	bdl	0.01	26.64	411	88	8	21	235	7	537	6	5	129	2
POS	D	Orange	74.46	2.72	4.08	0.48	0.50	bdl	0.08	0.05	bdl	0.02	17.50	619	76	18	18	176	9	7	6	5	48	bdl
POS	D	Orange	49.27	8.93	11.29	0.26	0.35	bdl	1.00	0.06	bdl	0.01	28.61	1713	120	5	16	169	6	30	4	5	17	5
POS	D	White	52.74	16.81	4.84	1.66	1.53	0.02	1.74	0.08	0.23	0.10	20.00	1905	308	36	44	56	21	136	6	10	47	bdl
POS	D	White	33.55	13.68	14.08	0.18	0.33	bdl	2.04	0.08	0.13	0.01	35.67	1959	194	4	17	146	4	105	4	4	14	3
SIL	C	White	56.91	13.02	5.39	1.31	1.08	0.01	0.73	0.12	0.03	0.07	21.09	1601	83	20	30	176	13	324	8	14	125	6
CRI	A	White	55.09	7.97	8.61	0.79	0.62	0.01	4.85	0.10	0.25	0.04	21.50	742	166	16	30	72	24	331	2	10	188	2
CRI	D	White	40.32	17.06	10.46	0.23	0.66	bdl	1.36	0.13	0.02	0.01	29.49	137	40	25	23	429	bdl	81	10	15	57	4
PAN	B	White	66.32	3.41	4.92	2.18	0.86	0.02	1.02	0.20	0.19	0.08	20.67	542	41	11	17	218	15	328	10	8	104	bdl

Cauliflower speleothems are relatively enriched in Sr, Cu, V, and S as compared to basalt composition. Sr in cauliflower samples is noticeably lower in concentration (35 – 466 ppm) than carbonate-bearing polyps, with only carbonate-bearing white-tan CRI samples significantly exceeding 100 ppm. Cu concentrations are greatest among highly opaline brown samples, notably from VAL and LYO (169 – 251 ppm). V, although present in the other morphologies, is noticeably incorporated in higher concentrations in select white-tan cauliflower samples: POS-E (239 ppm), CRI-C (350 ppm), and CRI-A (820 ppm) (**Table 6**). These samples consist of both opal and carbonate minerals and also contain the most S of all cauliflower samples (1365, 540, and 1167 ppm respectively). Ba concentrations are highest among opal-dominated samples: white-tan brown with 88 ppm, brown with 117 ± 13 ppm, and white-tan with 57 ± 49 ppm. White-tan cauliflower Ba concentrations are more variable due to lower concentrations among POS cave samples, similar to the trend observed in polyps.

4.5.5. Coralloids

Akin to the other speleothem morphologies, coralloid speleothems exhibit a variety of elemental compositions, ranging from highly opaline (>70 % wt.% SiO_2), opaline and carbonate-bearing (50 – 62 wt.% SiO_2 and > 9 wt. % CaO), and carbonate-dominated (<50 wt.% SiO_2 and > 15 wt.% CaO) (**Table 7**). MgO concentrations are notably low in comparison to the previous morphologies (4.37 ± 3.61) wt.% MgO), even among carbonate-bearing samples. Phosphorous is present at concentrations ranging from 0 – 3.02 wt.% P_2O_5. Additionally, significant concentrations of P are only present in carbonate-bearing samples, indicating that the bulk of P content may be associated with carbonate minerals. Brown coralloids, similar to brown cauliflower, are dominated by opal, with a mean of 77.82 ± 13.42 wt.% SiO_2. Consequently, brown

coralloids exhibit reduced concentrations of both CaO (3.86 ± 4.71 wt.%) and MgO (3 ± 3.42 wt.%).

Table 6. Major and Trace Element Composition of LBNM Cauliflower Speleothems. Three-letter cave ID represents name of sampled cave. Major elements (presented as oxides) and LOI (Loss on Ignition) are presented in Wt.%, and trace elements are presented in ppm. All iron is given as Fe_2O_3. Values listed as bdl are below detection limits.

Cave	***Site***	***Color***	***SiO_2***	***CaO***	***MgO***	***Al_2O_3***	***Fe_2O_3***	***MnO***	***P_2O_5***	***K_2O***	***Na_2O***	***TiO_2***	***LOI***	***S***	***V***	***Cr***	***Ni***	***Cu***	***Zn***	***Sr***	***Y***	***Zr***	***Ba***	***Pb***
			Wt. %											ppm										
VAL	D	White-tan brown	77.14	6.98	0.57	0.25	0.40	bdl	0.08	0.03	bdl	0.01	14.50	72	57	13	15	251	bdl	73	12	14	88	4
LYO	I	Brown	85.49	1.03	0.27	0.40	0.46	bdl	bdl	0.05	bdl	0.01	12.25	bdl	63	13	19	185	13	35	19	27	108	5
LYO	J	Brown	84.08	1.35	0.63	0.58	0.97	bdl	bdl	0.07	bdl	0.02	12.25	bdl	55	16	19	169	17	57	21	28	126	2
POS	A	White-tan	39.95	17.12	11.47	0.19	0.41	bdl	1.83	0.03	bdl	0.01	28.95	256	78	12	23	66	12	108	2	4	16	bdl
POS	E	White-tan	35.26	16.82	13.54	0.09	0.35	bdl	0.92	0.02	bdl	bdl	35.26	1365	239	17	26	34	9	64	2	3	18	10
CRI	A	White-tan	52.40	6.97	15.62	1.69	1.48	0.02	2.66	0.10	0.23	0.11	18.56	540	350	22	49	79	21	228	6	15	117	6
CRI	C	White-tan	17.13	29.77	10.88	0.50	0.90	0.01	2.41	0.04	0.20	0.04	37.88	1167	820	6	26	18	19	466	5	7	75	11

White-tan coralloids instead incorporate lesser concentrations of SiO_2 (59.11 ± 23.93 wt.%) and relatively greater concentrations of CaO (12.30 ± 10.52 wt.%) and MgO (6.02 ± 5.64 wt.%). However, as compared to cauliflower of similar coloration, the major element composition of coralloids is noticeably more variable.

Coralloid trace element chemistry includes higher concentrations of Sr, Cu, V, and S (**Table 7)**. Sr content correlates with calcite content, ranging from 35 – 466 ppm. Cu is observed to occur in the highest concentrations in highly opaline samples, and like polyps, Cu content may be associated with the cave of origin (which is not apparent amongst the other morphologies): GOL 257 ± 95 ppm, POS 68 ppm, LYO 79 ± 28, SIL 200 ppm, and CRI 13 ppm. GOL coralloids contain the highest Cu concentrations, similar to the trend observed amongst polyp speleothems. Additionally Cu concentrations are not significantly different between brown and white-tan coralloids. Vanadium concentrations range from 55 – 820 ppm and do not appear to correlate with S as observed in cauliflower speleothems. Rather, V and S appear to be associated with higher carbonate content, as expressed as CaO %. Sulfur concentrations are also greatest in samples with LOI > 20 wt.%, but it cannot be definitively stated that S content itself strongly influences volatile content. Ba content in coralloids is similar to that found within other morphologies, and is greatest in white-tan (106 ± 64) as opposed to brown (27 ± 15) samples. The greater concentrations of Ba within the predominantly calcite-bearing white-tan samples suggest Ba may be incorporating within the carbonate mineral structure.

Table 7. Major and Trace Element Composition of LBNM Coralloid Speleothems. Three-letter cave ID represents name of sampled cave. Major elements (presented as oxides) and LOI (Loss on Ignition) are presented in Wt.%, and trace elements are presented in ppm. All iron is given as Fe_2O_3. Values listed as bdl are below detection limits.

Cave	***Site***	***Color***	***SiO_2***	***CaO***	***MgO***	***Al_2O_3***	***Fe_2O_3***	***MnO***	***P_2O_5***	***K_2O***	***Na_2O***	***TiO_2***	***LOI***	***S***	***V***	***Cr***	***Ni***	***Cu***	***Zn***	***Sr***	***Y***	***Zr***	***Ba***	***Pb***
			Wt. %											ppm										
LYO	A	White-tan	82.27	1.53	0.42	1.08	0.53	bdl	bdl	0.13	bdl	0.03	13.95	72	57	13	15	251	bdl	73	12	14	88	4
LYO	J	White-tan	45.19	19.44	5.39	0.17	0.43	bdl	1.27	0.03	bdl	0.01	27.64	bdl	63	13	19	185	13	35	19	27	108	5
GOL	A	Brown	86.71	1.09	0.85	0.21	0.45	bdl	bdl	0.04	bdl	0.01	10.58	bdl	55	16	19	169	17	57	21	28	126	2
GOL	A	White-tan	76.38	4.68	3.48	1.63	1.61	0.02	0.03	0.15	bdl	0.11	11.79	256	78	12	23	66	12	108	2	4	16	bdl
GOL	B	Brown	62.38	9.29	6.94	0.43	0.50	bdl	0.30	0.06	bdl	0.02	19.97	1365	239	17	26	34	9	64	2	3	18	10
GOL	G	White-tan	82.22	2.34	1.28	1.66	1.30	0.02	bdl	0.20	bdl	0.10	10.83	540	350	22	49	79	21	228	6	15	117	6
POS	B	White-tan	40.20	24.44	10.88	0.13	0.47	bdl	3.02	0.04	0.07	bdl	20.67	1167	820	6	26	18	19	466	5	7	75	11
SIL	D	Brown	84.37	1.19	1.21	1.00	0.74	0.01	bdl	0.08	bdl	0.04	11.32	180	84	15	15	98	12	56	13	15	228	bdl
CRI	B	White-tan	28.40	21.36	14.66	0.12	0.38	bdl	1.88	0.04	0.03	bdl	32.94	3673	148	15	26	59	13	238	2	3	98	7

4.5.6. Gours

All analyzed gour speleothems are comprised predominantly of opal, as indicated by the predominance of SiO_2 within the samples (85.4 – 86.6 wt.% SiO_2) (**Table 8**). The LOI values are also consistent with relatively pure opal (*Webb and Finlayson, 1987*). CaO wt. % ranges from 0.81 – 0.91, although no XRD analyses indicate calcite or any other Ca-bearing mineral. Instead Ca within gour speleothems may likely be interstitial in nature (occurring as a Ca silicate phase), alongside lesser amounts of Fe, Mg, and Al.

In comparison to the previously described (and often calcite-bearing) speleothems, gours contain relatively lesser concentrations of Sr, S, and P (**Table 8**). Cu is observed to be the most abundant trace element present in gours, with a mean concentration of 404 ± 76 ppm. V concentrations are lower than in the majority of the calcite-bearing morphologies (crusts, cauliflower, polyps, and coralloids), but are still present at 61 ± 28 ppm. S is measured to be either below detection levels or present at relatively low concentrations, with only one sample exhibiting detectable S (3 ppm). Gours also have the greatest Y concentrations among speleothems, at 23 ± 6 ppm.

Table 8. Major and Trace Element Composition of LBNM Gour Speleothems. Three-letter cave ID represents name of sampled cave. Major elements (presented as oxides) and LOI (Loss on Ignition) are presented in Wt.%, and trace elements are presented in ppm. All iron is given as Fe_2O_3. Values listed as bdl are below detection limits.

Cave	***Site***	***SiO_2***	***CaO***	***MgO***	***Al_2O_3***	***Fe_2O_3***	***MnO***	***P_2O_5***	***K_2O***	***Na_2O***	***TiO_2***	***LOI***	***S***	***V***	***Cr***	***Ni***	***Cu***	***Zn***	***Sr***	***Y***	***Zr***	***Ba***	***Pb***
		Wt. %											ppm										
LYO	A	85.37	0.91	0.42	0.32	0.38	bdl	bdl	0.03	bdl	0.01	12.51	bdl	41	17	19	458	10	18	13	16	bdl	bdl
LYO	H	86.60	0.81	0.23	0.41	0.40	bdl	bdl	0.04	bdl	0.01	11.43	3	80	13	25	350	19	27	20	23	3	3

4.6. Maps of Elemental Distribution within Speleothems

Electron microprobe analyses were performed on a CRI polyp speleothem (CRI20180731-D-12) to determine the concentration and distribution of the following elements within the laminated structures at resolutions unobtainable from previous XRF analyses: Si, Ca, Mg, Al, Fe, K, Cu, P, S, and Sr (**Fig.29.A,B)**. A 996 µm by 2568 µm transect in the central region of the polyp was chosen to represent the textures and structures found within LBNM speleothems (**Fig.29.C)**.

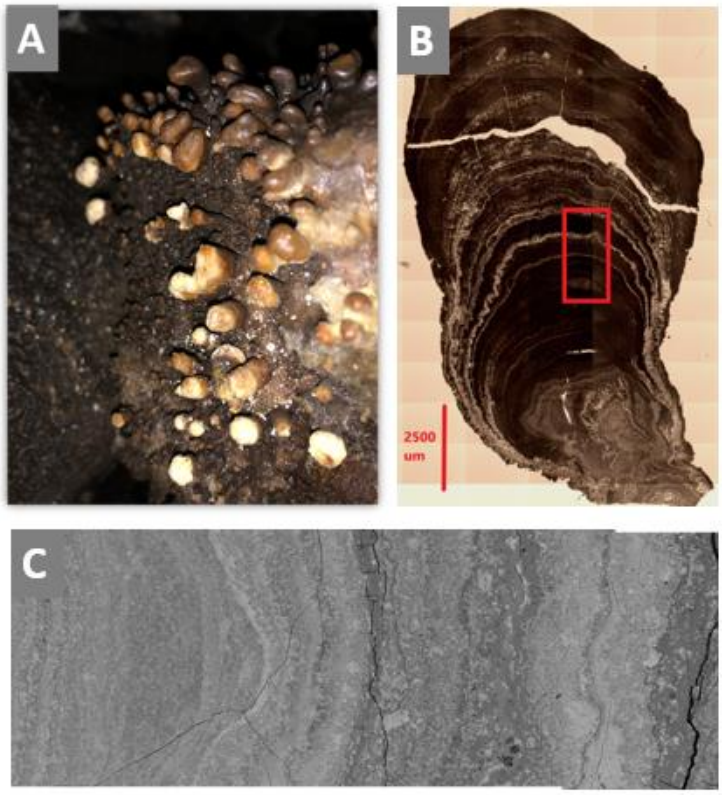

Figure 29. Polyp sample and electron microprobe map transect. A) CRI20180731_D_12 in-situ sample, representative of a white-tipped polyp; B) Location of the 996 µm by 2568 µm mapping transect within individual polyp; C) Backscatter image of map transect, leftmost portion of region represents basal region of transect, while the right represents the top of the transect, nearest to the tip of the speleothem.

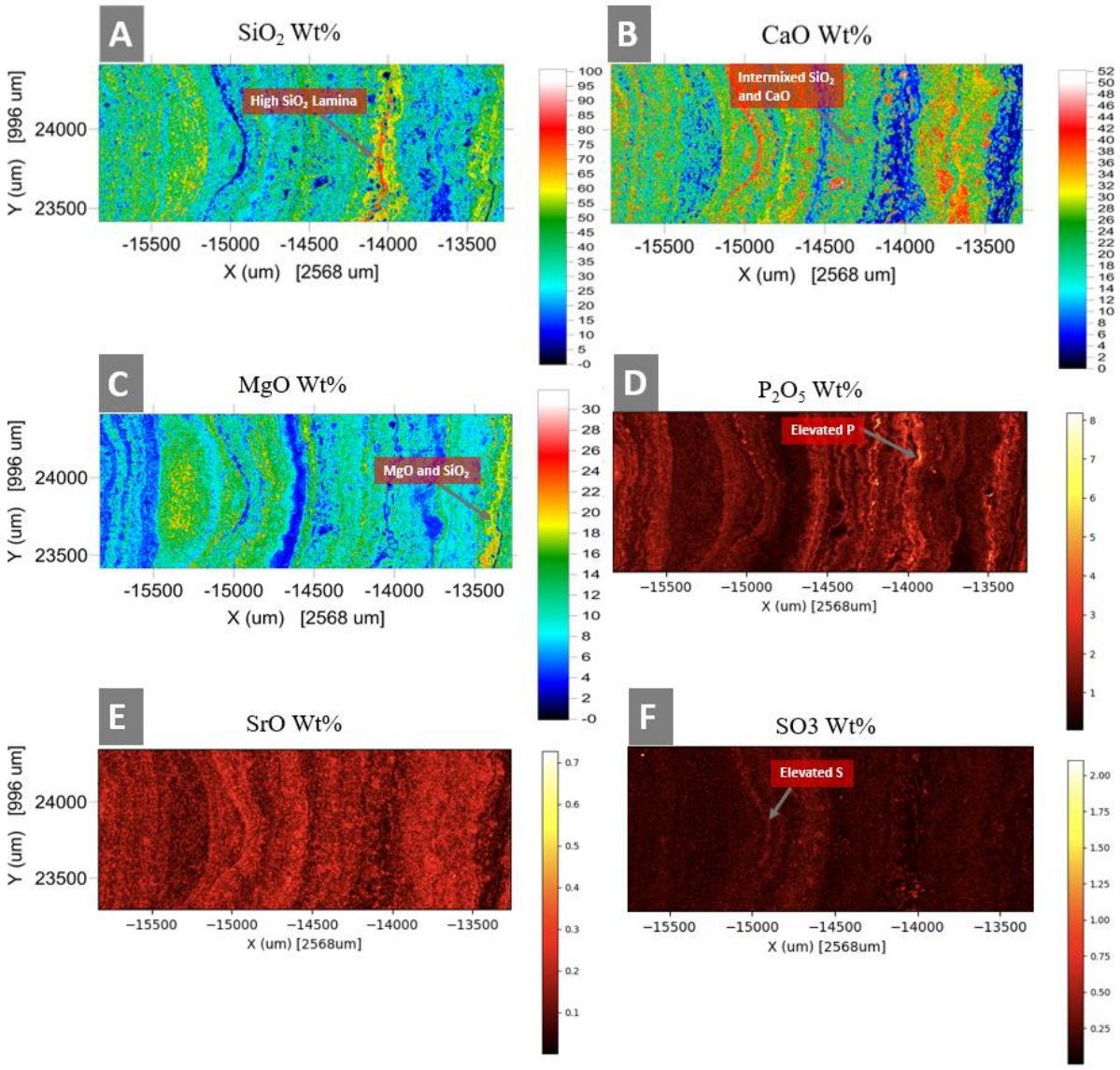

Figure 30. Elemental distribution maps of CRI20180731_D_12 polyp speleothem transect. A) SiO_2 map; B) CaO map; C) MgO map; D) P_2O_5 map; E) SrO map; F) SO_3 map. Maps A-C wt.% are represented by the following color scale: Black denotes below detection limits, while blue grading into cyan, green, yellow, orange, red, and white denotes increasing concentrations. Maps D-F are represented by the following color scale: Black denotes below detection limits, while maroon grading into red, orange, yellow, and white denote increasing concentrations.

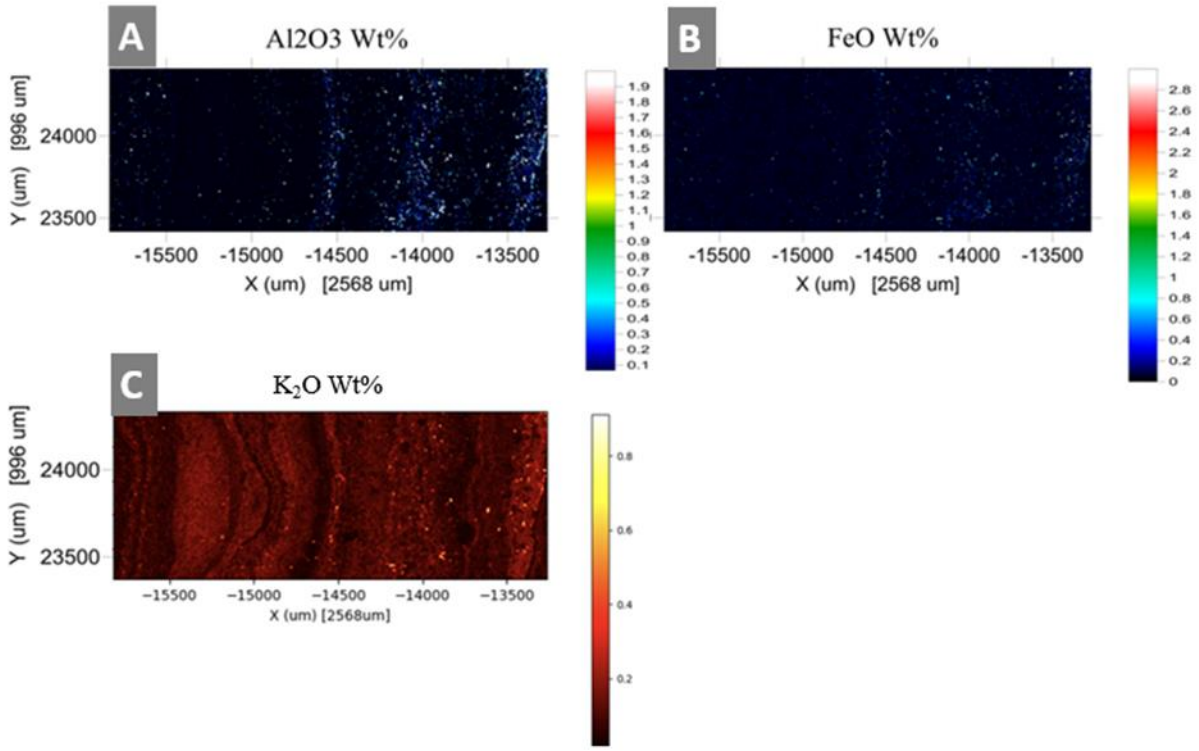

Figure 31. Additional elemental distribution maps of CRI20180731_D_12 polyp speleothem transect. A) Al_2O_3 map; B) FeO map; C) K_2O map. Maps A-B wt.% are represented by the following color scale: Black denotes below detection limits, while blue grading into cyan, green, yellow, orange, red, and white denotes increasing concentrations. Map C is represented by the following color scale: Black denotes below detection limits, while maroon grading into red, orange, yellow, and white denote increasing concentrations.

As expected from previous quantitative XRF analyses, the major elements within the mapping area were determined to be SiO_2, CaO, and MgO (**Fig.30.A,B,C).** A range of SiO_2 concentrations (representative of opal) and distributions are observed, with zones exhibiting concentrations of < 10 wt.%, ~30 wt.%, 50-60 wt.%, and a distinct laminae (approximately at -14100 X) with ~ 80 wt.% (**Fig.30.A)**. CaO concentrations (most likely indicative of calcite and/or Mg carbonate) occur at minimal levels of < 5 wt. %, 12-14 wt.%, 24-26 wt.%, 30-32 wt.%, and maximums of 40-42 wt.% (**Fig.30.B**). MgO content is the lowest amongst the three oxides, at concentrations of < 2 wt. %, 8-9 wt.%, 14-16 wt.%, and ~24 wt.% (**Fig.30.C**).

SiO_2 is the dominant oxide present within the majority of the scan area, with patches of lower concentration and a distinctive laminae of much higher concentration (apex located at approximately -14900 X, 23800 Y). The low-SiO_2 (< 10 wt.%) zones appeared to correspond with the highest CaO concentrations. Moreover, SiO_2 and CaO are intermixed in moderate concentrations (30-40 wt.% SiO_2 and 16-22 wt.% CaO) within many of the lamina, which suggests infilling of void spaces in opal laminae by calcite. Laminae consisting of predominantly either SiO_2 or CaO are observed, but are nominal in total area as compared to infilled laminae. MgO occurs alongside moderate concentrations of CaO (8-16 wt.% MgO) as well as SiO_2 (8-20 wt.% MgO) – indicating that Mg is also incorporated within opal, or as a Mg-SiO_2 phase within opal. A notably large distribution of SiO_2-rich laminae spanning ~ 800 μm is observed at approximately (-15400 X, 23750 Y), an area likely representative of a relatively large porous opal lamina with infilled calcite deposition.

Three additional elemental oxides are found to be associated with high CaO zones (and therefore calcite): P_2O_5, SrO, and SO_3 (**Fig.30.D,E,F**). SrO is distributed among the majority of CaO-bearing lamina at concentrations of approximately 0.2-0.3 wt.% (**Fig.30.E**). SO_3 is observed to be incorporated strongly within the CaO-rich laminae near the center-left of the scan area at concentrations ranging from 0.4-0.7 wt.% (**Fig.30.F**). Unlike SrO, SO_3 (0.3-0.5 wt.%) is distributed more sparsely throughout the scan area, even among laminae of similar CaO content. Phosphorous occurs in higher concentrations (1-8 wt.% P_2O_5) than SO_3, but concentrations of these two elements do not appear to be spatially correlated (**Fig.30.D**). For example, relatively thin bands with high P_2O_5 occur in the densest SO_3-bearing zones in the center-left of the scan area. The P_2O_5-rich zones are also conspicuously located atop the apex of CaO-rich lamina at the bottom region of SiO_2-rich laminae.

Concentrations of Al_2O_3 and FeO within the scan area occur in low concentration (0-1 wt.% and 0-2.5 wt.%, respectively) throughout the scan area (**Fig.31.A,B**). The highest concentrations of Al_2O_3 and FeO appear to be spatially associated in laminae at approximately (-14600 X, -14000 X, and -13250 X). These laminae are also SiO_2 rich (>50 wt.%), indicative of an opal-dominated composition. The scattered distribution and variable concentrations suggest that areas with high Al_2O_3 and FeO are representative of volcanic mineral fragments and/or dust particles trapped within the opal matrix.

K_2O concentrations appear to follow a nearly identical distribution to those of MgO, albeit at lower concentrations at 0.1-0.3 wt. % (**Fig.31.C**). In particular, K_2O concentrations are generally greatest among SiO_2 dominated lamina. However, K_2O is also distributed in a speckled pattern akin to that of Al_2O_3 and FeO, the pixels of which may also represent foreign inclusions and detrital inputs within the speleothem.

Lastly, Cu_2O concentrations range from 0.04 – 0.12 wt. %. However, the vast majority of pixels range from 0.04 – 0.09 wt. %, with the only > 0.10 wt. % pixels occurring within a circular shape along the far right region of the scan area (**Appendix E4 p.167**).

4.7. Speleothem Microstructures

Whole and broken speleothems coated with carbon and analyzed via scanning electron microscopy revealed surficial textures and microstructures associated with opal that are similar to structures noted in previous studies on opaline speleothems (*Webb and Finlayson, 1987*). Major structures as depicted in **Fig.32 A,B,C** included colloidal aggregates, colloform surfaces, and glassy conchoidal fracture surfaces. Porous opal surfaces are also observed, often associated with white-tipped polyp and coralloid speleothems (**Fig.32 D,E**). Similar porous opal surfaces (also predominantly associated with feature tips) have been observed in other lava cave speleothems

(*Romaní et al., 2010*). The micrographs in **Fig.32** may display a charging effect, creating artificial streaking patterns in the image caused by negative charge build-up.

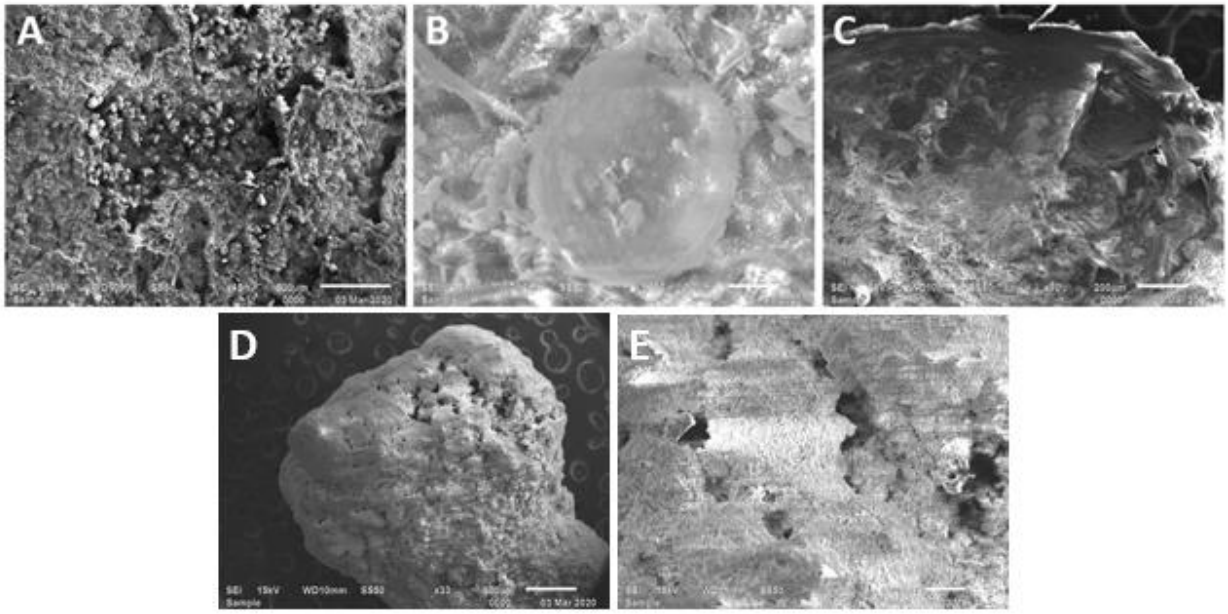

Figure 32. SEM micrographs depicting surficial microstructures of LBNM speleothems. A) Colloidal aggregate on polyp surface; B) Colloform surface on coralloid; C) Conchoidal fractures in broken polyp fragment; D) Porous opal "white tip" of a coralloid speleothem; E) Further magnification of porous opal surface. The micrographs may display a charging effect due to improper coating.

4.8. Air Temperature and Relative Humidity

Presented in **Table 9** are the air temperature and relative humidity data of co-located sample sites wherein both mineral and associated water samples were collected. Consistent with most caves, humidity was generally the highest in the earliest alphabetical sample sites (sample sites deepest within the caves). One exception exists, with YEL site A exhibiting a lower relative humidity percentage than sample sites near the cave entrance. It is unknown why this sample site is less humid, but variations in airflow and depth may play a role: warm, humid air was observed to emanate from the YEL entrance during the 2018 summer field season. Regardless, the majority of sample sites across the caves exhibit relatively high relative humidity.

Table 9. Air Temperature and Relative Humidity Data by Sample Type, Cave, and Sample Site. Three-letter IDs represent sampled caves. Sample site represents the BRAILLE nomenclature used to designate sites within caves where co-located samples were collected. Sample sites begin with A at the deepest sampled region of the cave, and progress towards Z as sample sites approach the entrance of the cave.

Water Sample	*Cave*	*Sample Site*	*Air Temperature*	*Relative Humidity*
	ID		ºC	%
Puddle	GOL	C	10	87.4
Puddle	GOL	D	10.1	80
Puddle	GOL	F	10.7	83
Puddle	LYO	H	11.08	73
Puddle	POS	B	6.85	77
Puddle	POS	I	6.85	77
Puddle	SIL	C	10.3	91.5
Puddle	VAL	A	14.94	86.6
Puddle	VAL	B	11.42	81.54
Puddle	VAL	C	16.37	73.34
Puddle	VAL	D	9.37	74.65
Puddle	YEL	A	19.38	56.1
Puddle	YEL	B	19.38	56.1
Puddle	YEL	C	14.14	92.17
Puddle	YEL	D	10.2	91
Drip	CRI	C	n/a	88
Drip	CRI	D	n/a	57
Drip	LYO	B	9.9	86.3
Drip	LYO	H	11.08	73
Drip	LYO	J	11.95	89
Drip	POS	E	4.84	75
Drip	POS	F	5.74	86.1
Drip	POS	F	5.74	86.1
Drip	SIL	A	10.6	87.4
Drip	VAL	A	14.94	86.6
Drip	VAL	B	11.42	81.54
Drip	VAL	C	16.37	73.34
Drip	VAL	D	9.37	74.65
Drip	YEL	A	19.38	56.1
Drip	YEL	B	19.38	56.1
Drip	YEL	C	14.14	92.17
Drip	YEL	D	10.2	91

4.9. Cave Water Chemistry

Many of the water data presented in this work were produced by K-State (and later University of Texas at San Antonio) postdoctoral research fellow Dr. Harshad Kulkarni. These data are crucial for a complete discussion of speleothems, formation processes, and the specifically the water-rock interaction, and will be presented in this section. With due acknowledgement to Dr.

Kulkarni, some of the figures that appear in this work are modified from Kulkarni et al. (in prep.). The figures were created from the same data set, but do not represent duplications of the work.

4.9.1. Cave Waters – Drip and Puddle Waters

Percolating water entering LBNM caves, after interacting with basalt, soil, and tephra, can be observed in situ primarily as drip waters or puddle waters. Major element concentrations of the two varieties of cave water samples, drips and puddles, are shown in **Fig.33**. Puddle water was collected from depressions in the cave floor and/or collapsed roof basalt. Drip water was collected from drips and/or beads of water condensed on wall and roof surfaces of caves. **Fig.33** shows that the two sample types do not differ significantly in composition and, therefore, will be presented in aggregate in following general chemistry sections.

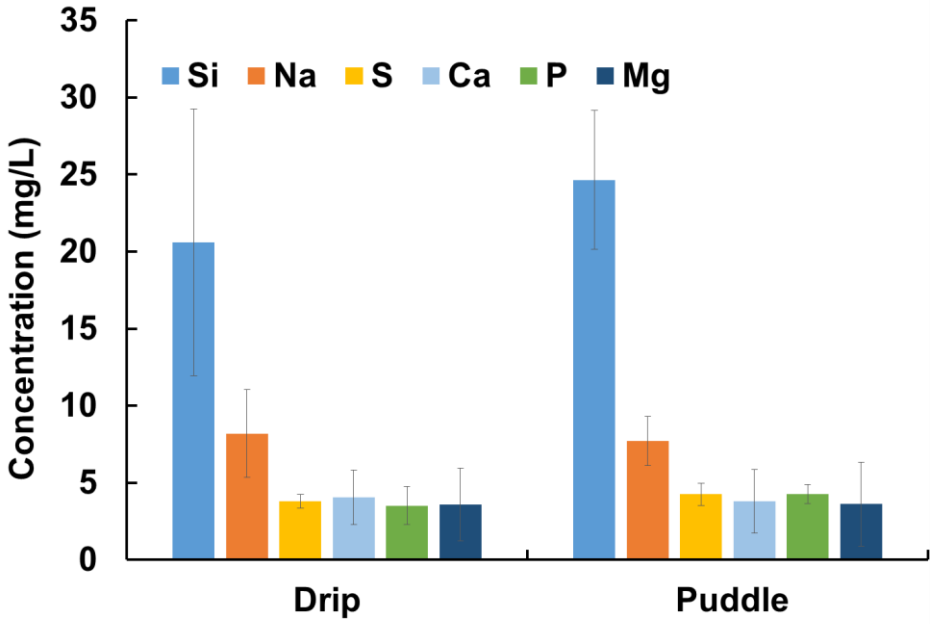

Figure 33. Major elements composition as measured by ICP-MS comparison of LBNM cave drip and puddle waters, showing that the two water types are similar in composition.

4.9.2. Inorganic Water Chemistry

4.9.2.1. pH, Conductivity, and Alkalinity

Conductivity values across all caves are 117 ± 76 µS/cm and pH is neutral to slightly basic 7.6 ± 0.3 (**Fig.34**). Nearby well waters exhibited higher conductivity values than LBNM caves, up to 2700 µS/cm, with the disparity revealing relatively low total dissolved solids in cave waters.

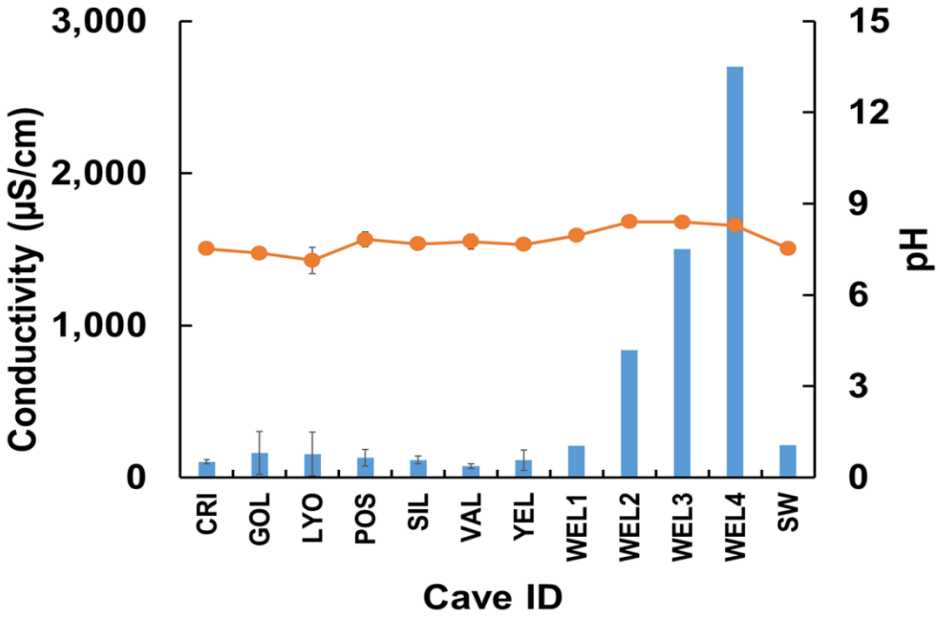

Figure 34. Conductivity (bar graph, µS/cm) and pH values (dotted line) of cave waters and nearby well and surface water samples. Cave IDs represent the sampled caves. Well waters 2-4 exhibited conductivity values much greater than any cave water. pH of cave waters is a consistent neutral to mostly basic.

Alkalinity as represented by HCO_3^- varies amongst caves, with a mean concentration of 34 ± 23 mg/L. Additionally, HCO_3^- concentrations are lowest in the cave waters in VAL and LYO, the youngest caves sampled (**Fig.35**).

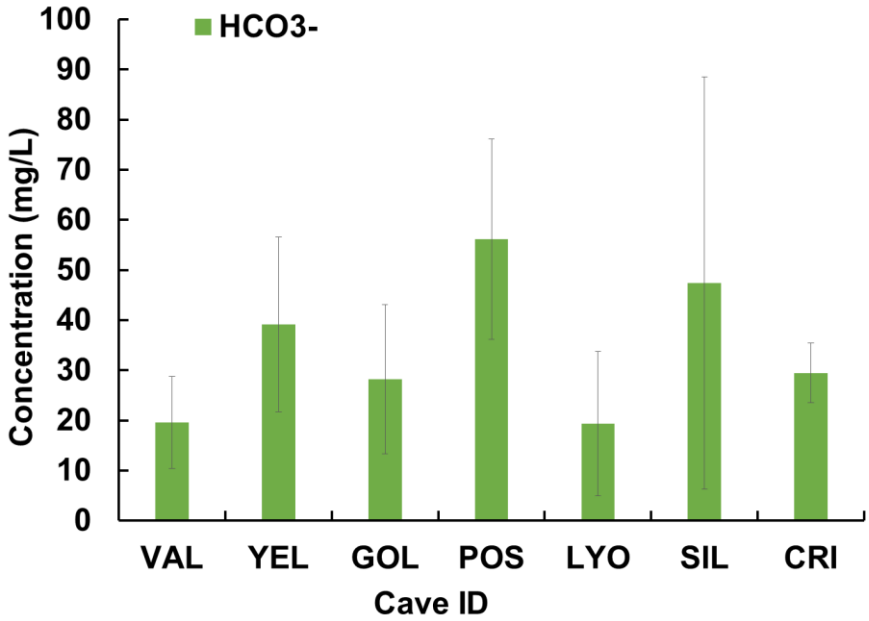

Figure 35. Alkalinity of LBNM cave waters expressed as HCO_3^- (mg/L). Cave IDs represent the sampled caves.

4.9.2.2. Major Elements and Anions

The cave waters are dominated by Si (23 ± 1 mg/L) followed by Na (8 ± 3 mg/L) and Ca (4 ± 2 mg/L); concentrations vary within and among the caves (**Fig.36.A**). Variable levels of NO_3^- (9 ± 8 mg/L), SO_4^{2-} (2.4 ± 1), PO_4^{3-} (2.5 ± 1), and Cl^- (3.8 ± 1) are also observed (**Fig.36.B**). Additionally, SO_4^{2-} and PO_4^{3-} do not constitute the entirety of total S (4 ± 0.4) and total P (3.9 ± 1) concentrations, with the deficit estimated as organic species. Lesser concentrations of several other trace elements include Fe (63.4 ± 66 µg/L) and Al (92.1 ± 69 µg/L) (**Fig.37**).

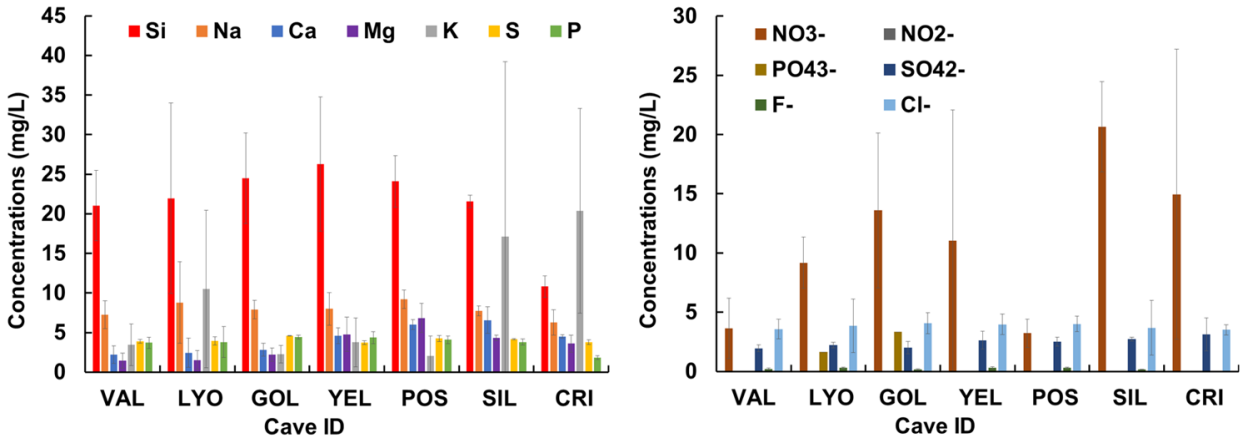

Figure 36. Major element (measured by ICP-MS) and anion (measured by IC) component concentrations of LBNM cave water chemistry. A) Major elements; B) Anions. Cave IDs represent the sampled caves.

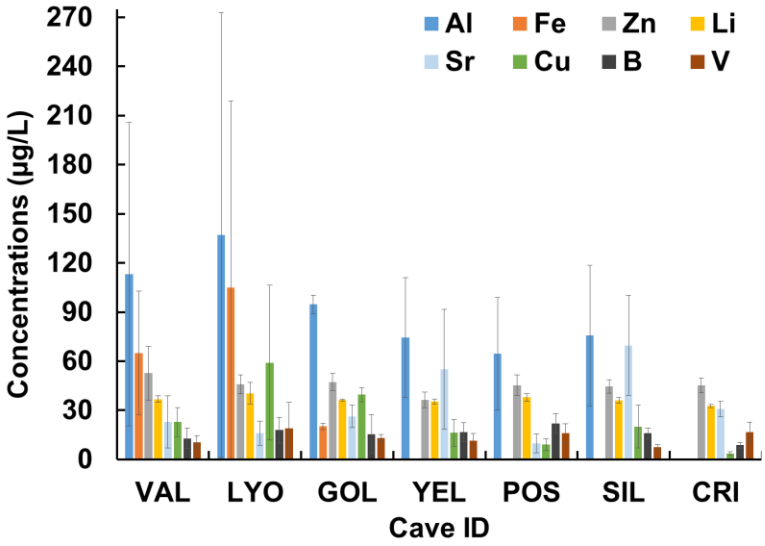

Figure 37. Trace element (measured by ICP-MS) concentrations of LBNM cave waters. Cave IDs represent sampled caves.

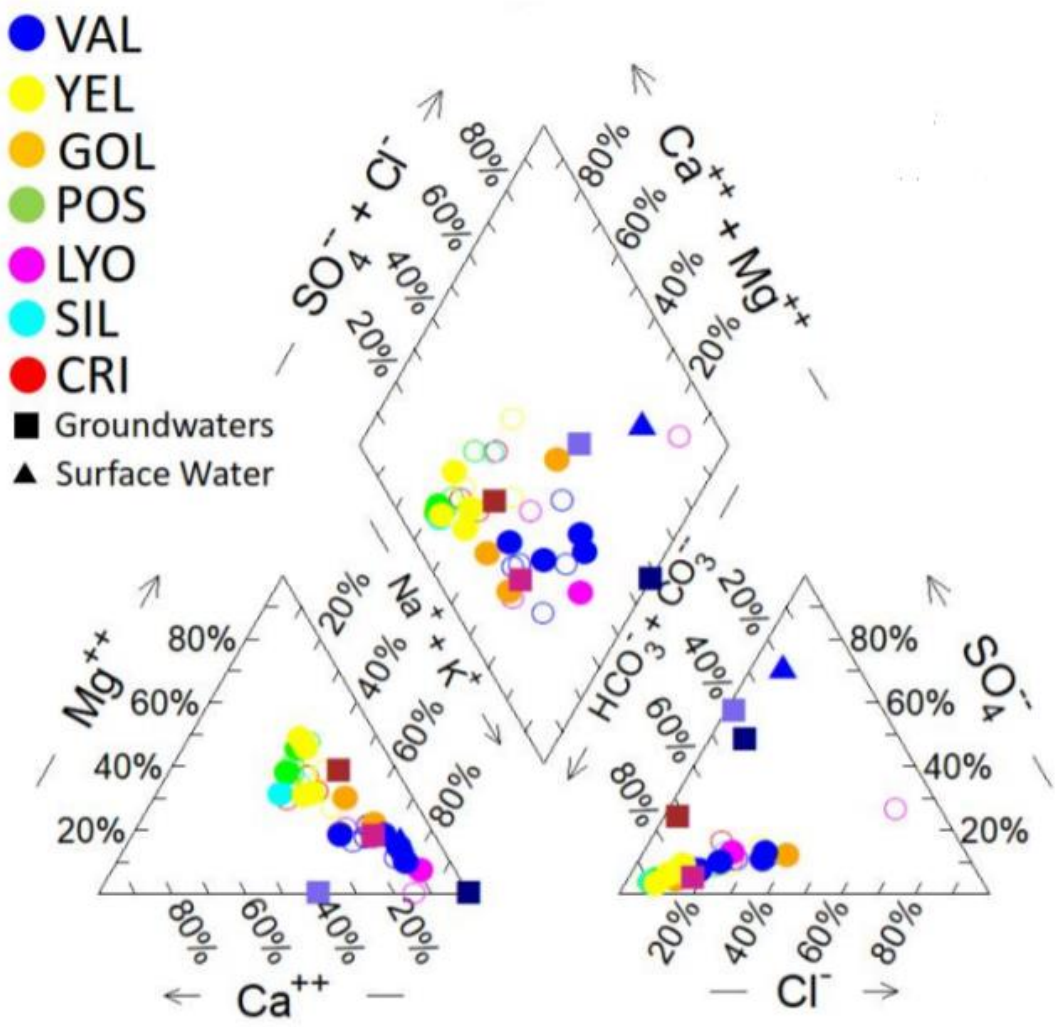

Figure 38. Piper diagram illustrating major water chemistry components of all cave waters. (Puddle: solid circle, Drip: open circle), groundwater (squares: blue - 231 m well, maroon - 37 m well, pink - 23 m well, lavender – 8 m well) and surface water (blue tringle: Tule Lake).

Water samples plotted along a Piper diagram (**Fig.38**) indicate that the cave waters predominately plot within two hydrochemical facies: Mixed Type and Magnesium Bicarbonate Type. Two of the three shallow well groundwater samples and the deep well groundwater sample (represented in pink, lavender, maroon, and blue) plot strongly within the Mixed Type facies; the final shallow groundwater sample (most proximal to Tule Lake agriculture, represented as a dark blue triangle) belongs to the Sodium Chloride facies.

4.9.3. Organic Water Chemistry – DOC, DON, DOS, and DOP

Cave waters are enriched in dissolved organic carbon (DOC), at 11.8 ± 8 mg/L, and vary among caves (**Fig.39.A**). Concentrations of Dissolved Organic Nitrogen (DON) (0.64 ± .90 mg/L), Dissolved Organic Sulfur (DOS) (3.24 ± .43 mg/L), and Dissolved Organic Phosphorous (DOP) (3.64 ± .92 mg/L) were not directly measured, but their concentrations were estimated by subtracting the major respective inorganic species (NO_3^-, SO_4^{2-}, PO_4^{3-}) from the total concentration values (Total Dissolved Nitrogen (TDN), Total S, and Total P respectively) of those elements (**Fig.39.B**).

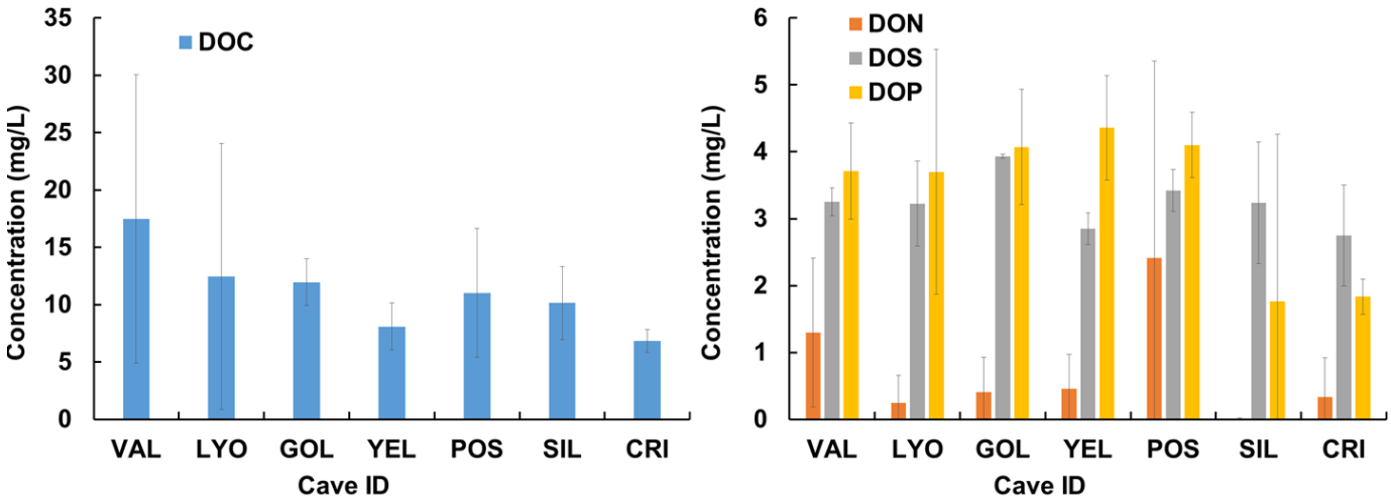

Figure 39. Organic water chemistry of LBNM cave waters. A) Dissolved organic carbon content in mg/L variation amongst LBNM caves. B) Dissolved organic nitrogen, sulfur, and phosphorous variability between caves.

DOC plotted against total dissolved inorganic carbon (DIC) (**Fig. 40. A**) reveals a relative enrichment of DOC as compared to DIC. Similar to DOC, cave waters are enriched in dissolved organic sulfur relative to dissolved inorganic sulfur (**Fig. 40. B**). Nitrate represents a major inorganic species that is not a readily explainable product of volcanic material dissolution. N-bearing minerals were not identified in any host rock (or secondary mineral) material. Nitrate, instead, must be generated within the caves, or transferred into caves from an external source, i.e.

agriculturally affected groundwater. The caves do not exhibit a consistent preponderance of inorganic nitrogen over organic nitrogen (or vice versa), suggesting that multiple processes, including microbial processes, are likely influencing the N chemistry of cave waters (**Fig.40.C**).

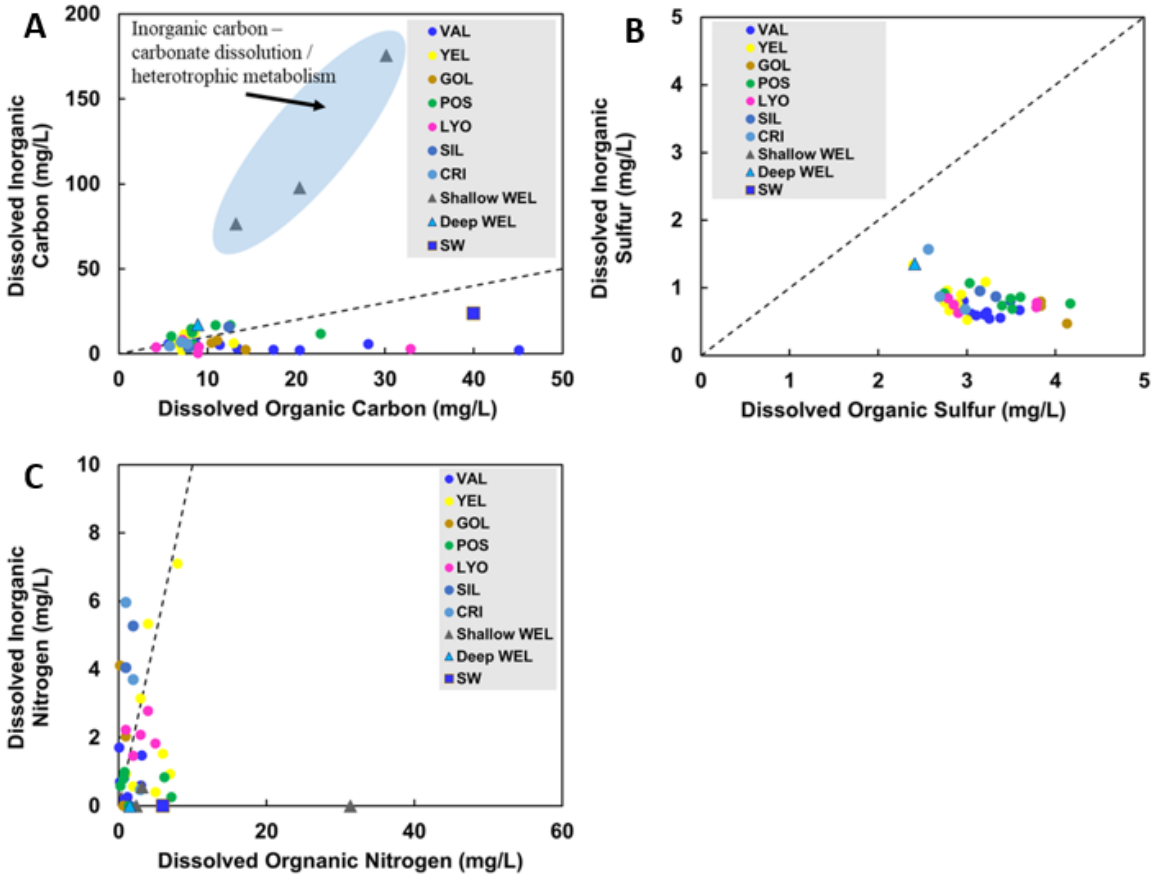

Figure 40. Dissolved organic constituent concentrations (C, S, N) of cave, well, and surface waters plotted alongside respective inorganic constituent concentrations. A) Cave waters enriched in DOC; B) Cave waters enriched in DOS; C) No enrichment of organic N relative to inorganic N. Dashed lines indicate a 1:1 line.

4.9.4. Relationships between Dissolved Components

The three dissolved components exhibiting the strongest correlations with dissolved Si are P, F-, and Na+ (**Fig.41**). These components therefore most likely represent components associated with basalt dissolution or potentially other processes associated with silica solubilization in the cave environment. Phosphorous has the strongest correlation, at an R^2 value of 0.8842 (**Fig.41.A**).

A strong P correlation (greater than 6 mg/L in select samples) between P and Si is not necessarily expected from basalt dissolution, given the low concentration of P_2O_5 in cave basalts (BDL – 0.37 wt.%). Na^+ and F^- are likely the result of basalt dissolution and/or additional water-rock interactions between overlying tephra and soils (**Fig.41.B,C**).

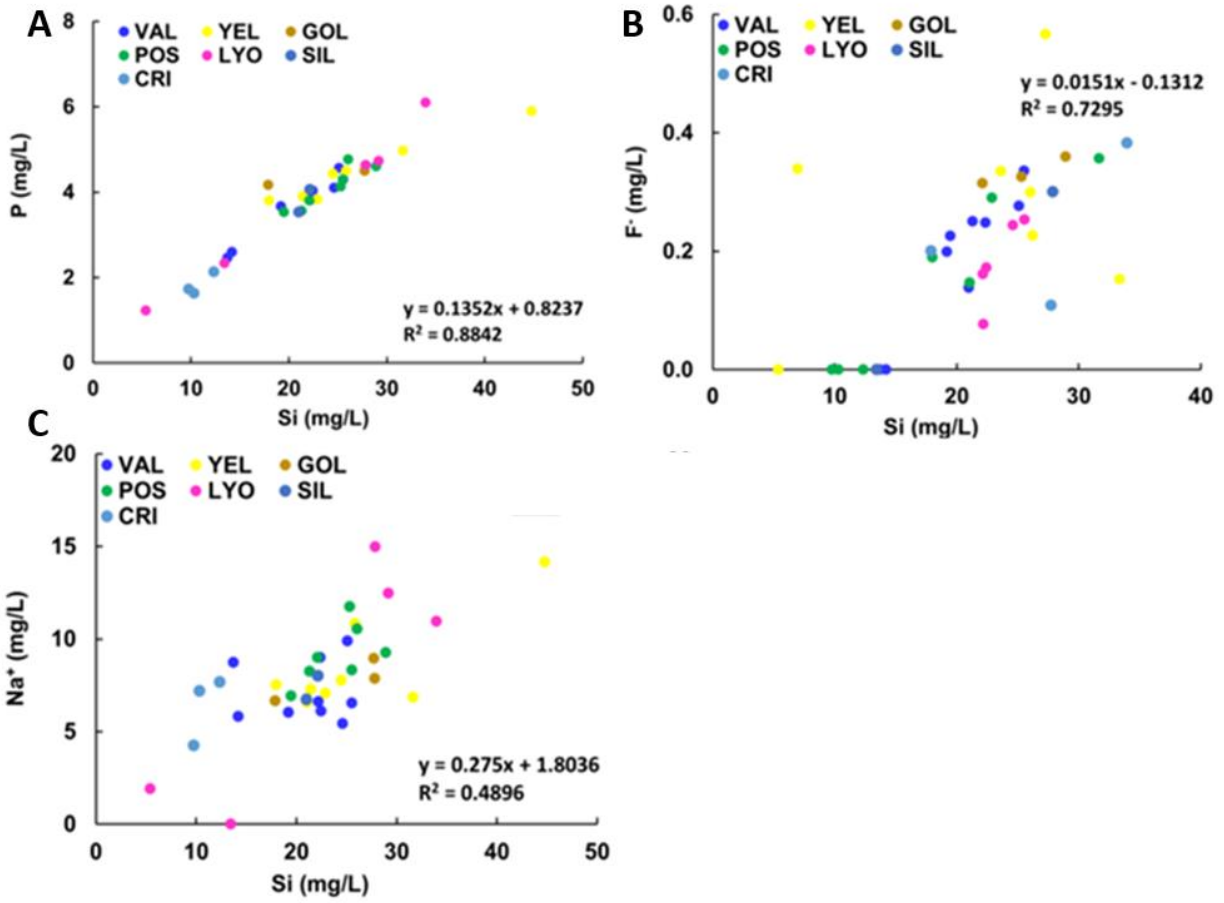

Figure 41. Relationships among select dissolved species with Si (mg/L). A) P (mg/L); B) F^- (mg/L); C) Na^+ (mg/L). R^2 values are provided within each graph.

4.9.5. Cave Water Stable Isotopes

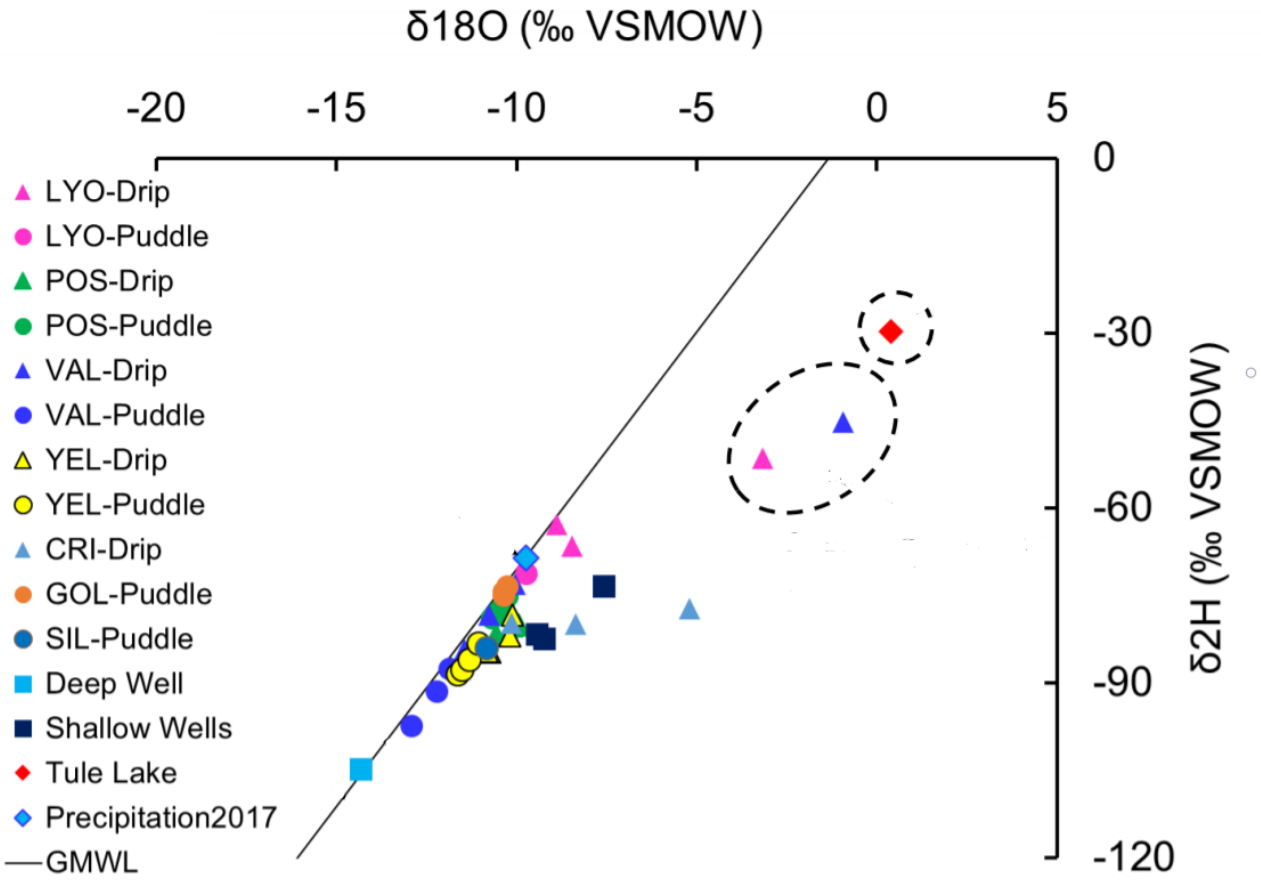

Figure 42. Oxygen and hydrogen isotopic composition of LBNM cave water, well water, local precipitation, and surface water samples plotted alongside the Global Meteoric Water Line (GMWL). Triangle symbols represent drip water samples, circles represent puddle water samples, squares represent well water samples, and diamonds represent surficial water. Dashed oval and circle indicate most highly evaporated water samples.

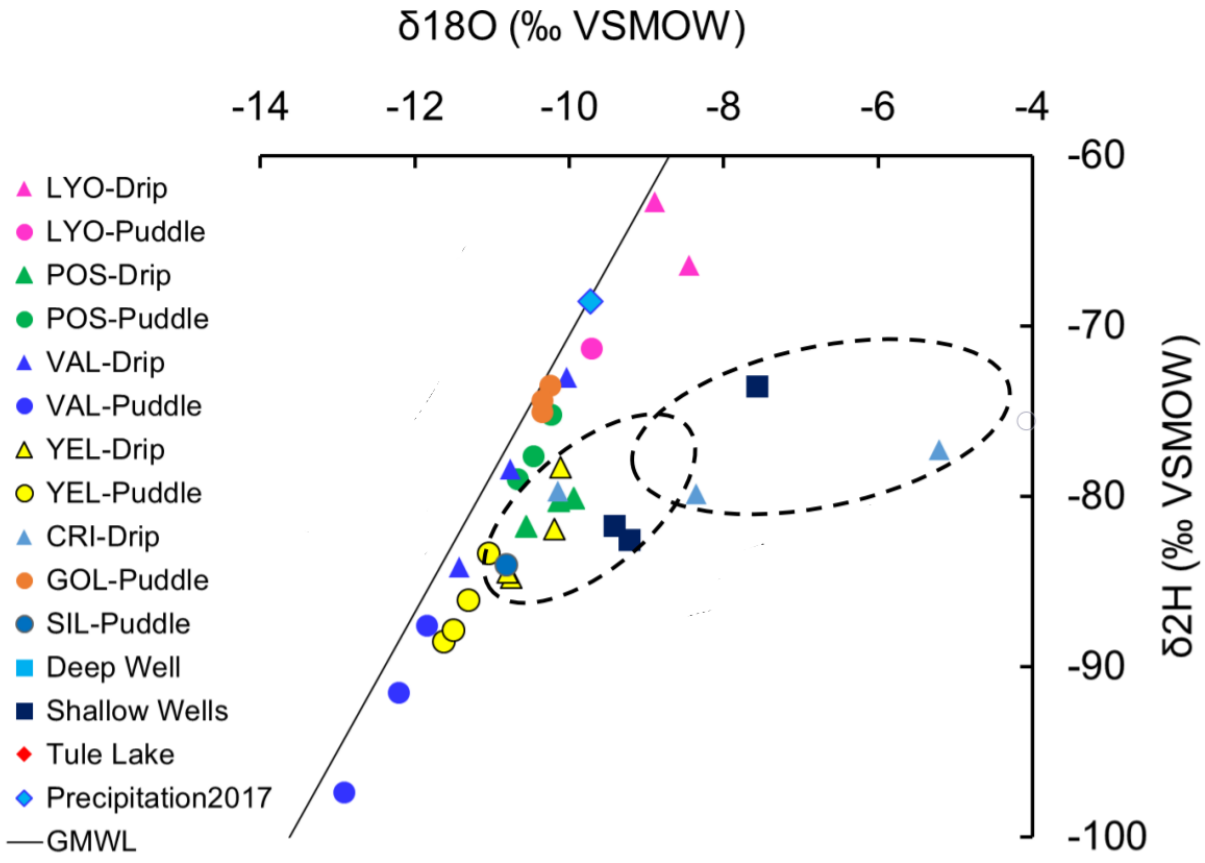

Figure 43. Zoomed-in view of Fig. 42. Oxygen and hydrogen isotopic composition to highlight relative enrichment of select of LBNM cave drip waters and shallow well samples plotted alongside the Global Meteoric Water Line (GMWL). Triangle symbols represent drip water samples, circles represent puddle water samples, squares represent well water samples, and diamonds represent surficial water. Dashed ovals indicate most highly evaporated water samples.

4.9.5.1. Meteoric Water Influx

The oxygen and hydrogen stable isotopic composition of water molecules provides a signature indicative of that water molecule's phase in the water cycle. Meteoric water is depleted in the heavier isotopes of oxygen and hydrogen relative to ocean water, while evaporated water is relatively enriched in the heavier isotopes relative to ocean water (*Gat, 1996*). Condensation will initially result in an isotopic composition identical to that of the water vapor, but further condensation of vapor will result in more depleted values for $\delta^{18}O$ and $\delta^{2}H$ (*Dansgaard, 1964*). The puddle waters in a majority of the sampled caves (VAL, GOL, LYO, POS, YEL) and drip

waters in VAL, LYO plot parallel to the Global Meteoric Water Line (GMWL) (**Fig. 43**). These samples have an isotopic composition consistent with meteoric water (water derived from precipitation), indicating that these cave waters most likely are sourced from precipitation events (*Gat, 1996*) (**Fig.42**). The meteoric origin within these five caves does not appear to correlate with cave age, as two of the age endmembers were present (VAL: 12 ka, YEL: 36 ka). This lack of correlation with age suggests that meteoric water is the primary source of water influx among all sampled LBNM caves.

4.9.5.2. Evaporation of Cave Waters

Drip water samples collected from YEL, POS, and CRI are all enriched in $\delta^{18}O$ and $\delta^{2}H$ relative to both the GMWL and their associated puddle water samples. Two CRI drips exhibit larger $\delta^{18}O$ enrichment than the others **(Fig.43)**. This enrichment suggests a cycle of evaporation and condensation (found within the caves in the form of drips on roofs without any obvious seep and/or other moist surfaces including speleothems) within the caves. Not all cave waters are enriched $\delta^{18}O$ and $\delta^{2}H$, suggesting that certain caves and specific localities within caves may experience more evaporation relative to others.

4.9.5.3. Well and Surface Water

The surface water sample collected at the nearby Tule Lake (**Fig.42**) has high $\delta^{18}O$ for a given $\delta^{2}H$, plotting to the right of the GMWL, indicating a composition consistent with a highly evaporated residual surface water (*Gat, 1996*). Shallow well waters collected in the Tule Lake region also plot off of the GMWL, but did not exhibit the same degree of enrichment as the surface water. The deep well sample plots on the GMWL, suggesting that the deep groundwater in the region (below the caves) is the result of precipitation-induced recharge.

4.10. Geochemical Calculations

4.10.1. Saturation Indices

Modeled saturation indices calculated using Geochemist's Workbench reveal a consistent undersaturation of the dominant secondary mineral phases: amorphous silica (representative of opal-A) and calcite, which is observed in all cave waters (**Table 10**.) Calcite is found to be supersaturated in well water samples. Basaltic minerals, including plagioclase minerals, are saturated and/or supersaturated, consistent with a water chemistry evolved primarily from the dissolution of basaltic rock. Clay minerals (gibbsite, illite, beidellite, etc) are supersaturated in all cave waters. However, no clay minerals were definitively identified within any speleothems. The consistent undersaturation of both opal and calcite suggests that additional processes are likely required to enable the precipitation of the two minerals comprising the bulk of speleothems. As seen in **Fig.43**, cave waters experience evaporation (and subsequent condensation), a process that likely plays a role in the precipitation of these minerals.

Table 10. Saturation Indices of Select Mineral Phases. Three-letter IDs represent the sampled caves and SW surface water. Orange coloration indicates the presence of the mineral has been verified in solid cave samples (speleothems, basalt). Amrph ^ silica is representative of opal-A.

	VAL	YEL	GOL	POS	LYO	SIL	CRI	SW	WELL
Albite	0.00	0.64	0.80	0.83	0.06	-0.07	n/a	-0.97	0.74
Amrph^silica	-0.71	-0.55	-0.57	-0.56	-0.72	-0.69	-0.95	-1.23	-0.65
Chalcedony	0.35	0.54	0.53	0.56	0.37	0.36	0.14	-0.21	0.37
Cristobalite	0.06	0.25	0.24	0.26	0.08	0.07	-0.16	-0.49	0.09
Tridymite	0.45	0.65	0.64	0.66	0.48	0.46	0.24	-0.11	0.47
Quartz	0.62	0.82	0.81	0.84	0.65	0.63	0.42	0.06	0.64
Calcite	-2.07	-1.47	-2.16	-1.00	-2.87	-1.20	-1.71	-0.62	0.64
Aragonite	-2.23	-1.63	-2.32	-1.16	-3.04	-1.36	-1.88	-0.78	0.47
Hematite	11.99	n/a	11.54	n/a	12.45	n/a	n/a	0.00	13.02
Goethite	5.52	n/a	5.31	n/a	5.76	n/a	n/a	0.00	6.03
Gibbsite	1.20	1.41	1.95	1.45	2.12	1.15	n/a	0.76	0.15
Kaolinite	4.10	4.84	5.94	4.97	5.93	4.03	n/a	2.13	2.07
Illite	3.97	5.14	6.01	5.22	6.27	4.07	n/a	1.70	3.23
Beidellite-Mg	4.32	5.42	6.52	5.62	6.98	4.34	n/a	1.47	2.73
Muscovite	5.89	7.07	8.50	7.02	8.10	5.86	n/a	3.68	4.28
Nontronite-Mg	15.94	n/a	16.29	n/a	18.99	n/a	n/a	0.00	16.75
Clinoptilolite-K	5.71	8.02	8.76	7.94	6.59	5.90	n/a	0.75	6.71

4.10.2. Dissolved Components Speciation

Additional modeling was also performed to ascertain the speciation of the major dissolved components in cave and surrounding waters (Si, Ca, Mg, and SO_4^{2-}). SiO_2 is the dominant form of Si (>98%) in all waters (**Fig.44.A**). Ca^{2+} predominates (>95%) in cave waters with $CaSO_4$ and $CaCO_3$ as comparatively minor phases (**Fig.44.B**). In surface and well waters, $CaSO_4$ contributes in addition to Ca^{2+} as a major Ca species (>35%). In cave waters, Mg^{2+} is the primary species (>96%), with $MgSO_4$ and $MgHCO_3$ existing as minor phases (**Fig.44.C**). Lastly, in both cave and surface/well waters, SO_4^{2-} exists as the primary phase of inorganic sulfur (>90%) alongside $CaSO_4$ and $MgSO_4$ as minor species (**Fig.44.D**).

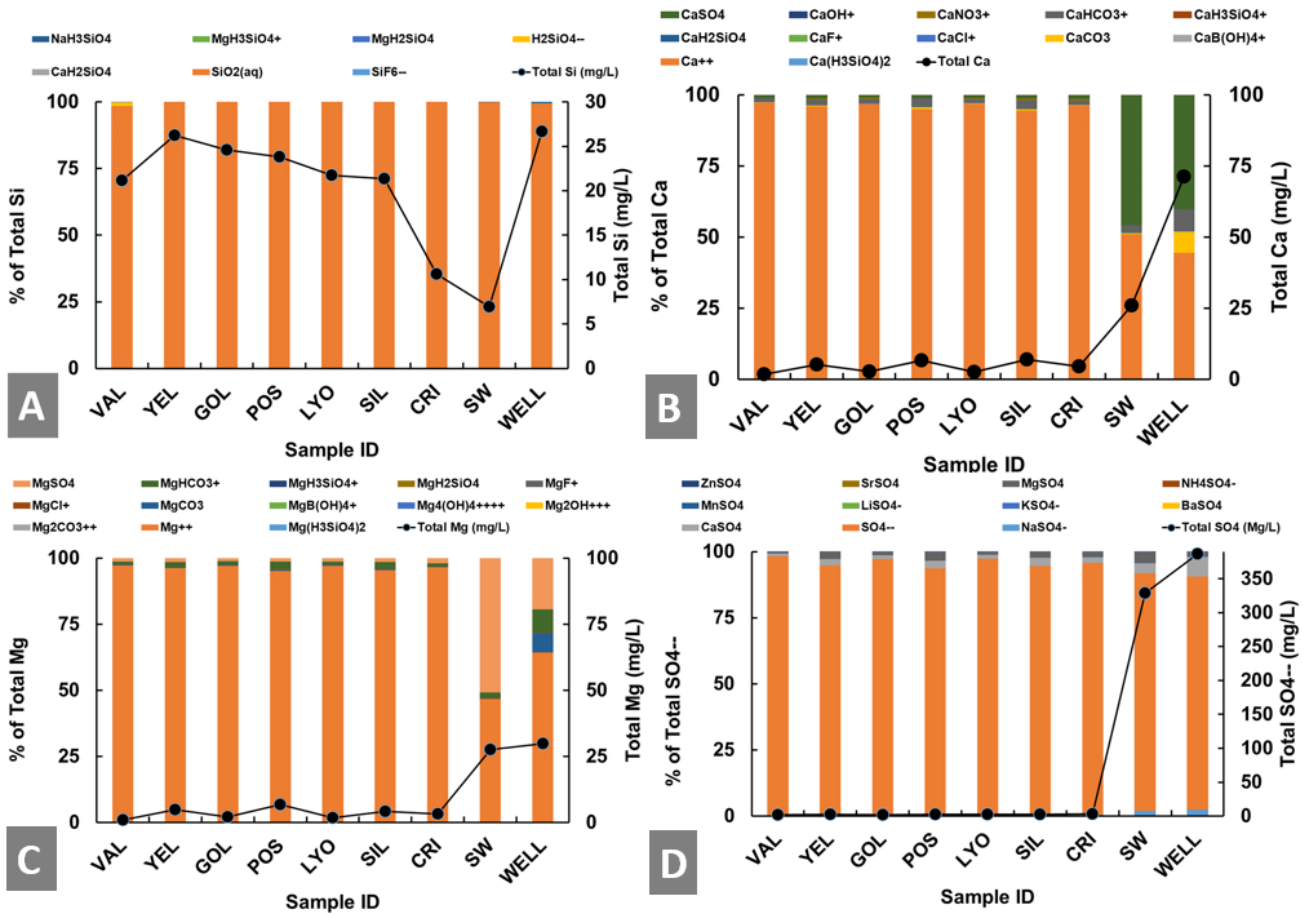

Figure 44. Chemical speciation of cave waters. A) Si speciation – SiO_2 (aq) dominant in caves; B) Ca speciation – Ca^{2+} dominant in caves; C) Mg speciation – Mg^{2+} dominant in caves; D) SO_4 speciation – SO_4^{2-} dominant in caves. Dotted line represents total concentration of the modeled species (e.g. total Si Mg/L).

4.10.3. Evaporation Factor Reverse Modeling

Reverse modeling was performed using PHREEQC Version 3 to assess the number of times cave waters must be evaporated in order to achieve supersaturation of opal-A (represented by amorphous silica) and calcite: the evaporation factor. Individual cave water samples were used as the initial composition of the parent solution, and were compared to the respective co-located bulk SiO_2 or CaO speleothem / basalt sample composition. As seen in **Fig. 45.A,B**, the evaporation factor of amorphous silica is consistently lower than the evaporation factor of calcite. This relationship suggestions that in order for calcite to become supersaturated, more evaporation than

what is required for amorphous silica saturation must occur. Hence, amorphous silica is expected to precipitate prior to calcite. Moreover, the dissolved concentrations of Si and Ca can be observed to not correlate with solid SiO_2 and CaO composition – sample sites in the caves with CaO-rich speleothems do not necessarily contain the greatest dissolved Ca concentrations in water, and vice-versa. Such sample sites therefore may be expected to require more evaporation to precipitate higher proportions of calcite.

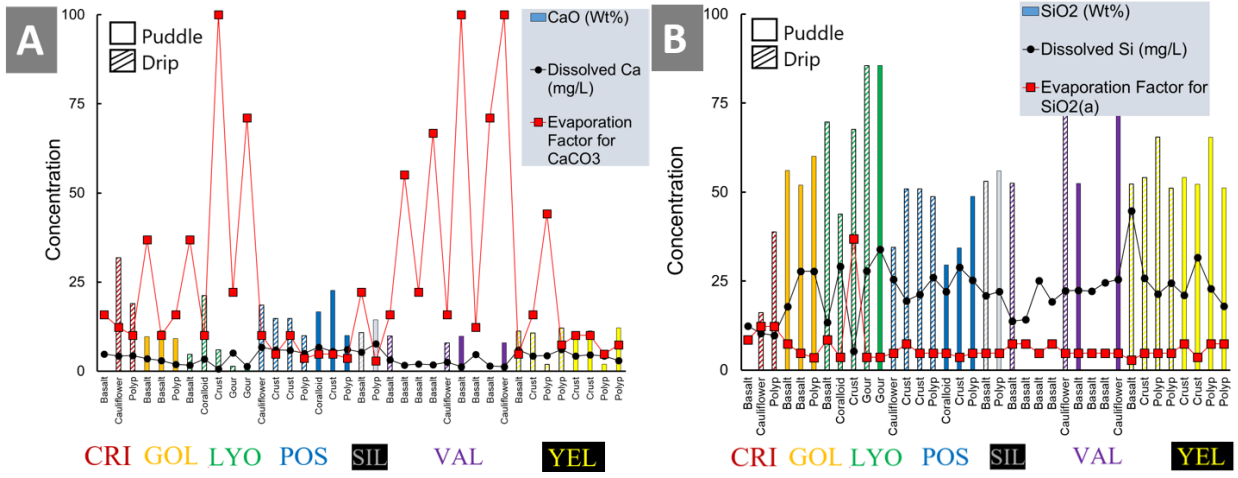

Figure 45. Evaporation factors of calcite (A) and amorphous silica (B) for co-located sample sites. A greater evaporation factor indicates increased evaporation is required to supersaturate the mineral. Bar graphs indicate speleothem/basalt CaO or SiO_2 concentration in wt.%, with solid bars indicating puddle waters and hashed bars indicating drip waters. Morphology of sample indicated on the x-axis below each bar. Black circle points indicate dissolved Ca or Si concentrations in mg/L. Red square points indicate evaporation factor. Colors indicate the cave each sample was collected from: red=CRI, orange=GOL, green=LYO, blue=POS, gray=SIL, purple=VAL, and yellow=YEL. Figure adapted from Kulkarni et al. (In Prep).

4.10.4. Geochemical Correlations

Presented in **Table 11** is a correlation matrix displaying Pearson correlation coefficients for 1) Geochemical parameters of cave water samples (pH, Na, K, Ca, Mg, Sr, Si, HCO_3^-, F^-, Cl^-, NO_3^-, SO_4^{2-}, DOC, TDN, P, S Al, V, Cr, Mn, Cu, Zn, and stable isotopes), 2) Major elemental composition of water sample - correlated speleothem samples (SiO_2 wt.% and CaO wt.%), 3) Cave environment parameters (air temperature and humidity), and 4) Evaporation factors of amorphous

silica (SiO_2(a) in table) and calcite (Calcite in table). Evaporation factor data were calculated by Harshad Kulkarni using PHREEQC and are to be fully published in *Kulkarni et al. (In Prep)*. Evaporation factors represent the degree of evaporation that must occur to precipitate a given mineral - the greater the evaporation factor, the greater the evaporation that must occur prior to precipitation. Cells highlighted in orange represent positive correlation coefficients ($R > 0.5$) and those in blue represent negative correlation coefficients ($R < -0.5$).

Dissolved Ca concentrations correlate strongly (R=0.81) with dissolved Mg, most likely indicative of a shared source of the two elements, possibly basalt dissolution. Ca and Mg also both correlate positively (R=0.69 and R = 0.76) with HCO_3^-, consistent with the hydrochemical facies exhibited by cave waters (**Fig. 35**). Dissolved P concentrations (indicative of mostly organic P, **Fig.39**), correlate strongly with dissolved Si (R=0.95),

CaO wt.% negatively correlates with SiO_2 wt.% (R=-0.89), indicative of the reduced calcite content frequently observed in silica-rich speleothems. SiO_2 content in speleothems positively correlates with dissolved Cu in cave waters (R=0.61). XRF data also suggest greater concentrations of Cu in silica-rich speleothems (**Tables 3-8**), suggesting that greater dissolved Cu concentrations are associated with predominantly opaline speleothems. Interestingly, dissolved Si did not share as strong a correlation (R=0.34) as that observed between speleothem SiO_2 wt.% and dissolved Cu. However, comparisons of speleothems with modern cave waters may not yield identical correlations, as speleothems essentially represent records of prior conditions.

Humidity correlates negatively (R=-0.55) with air temperature, a trend indicative of the deeper, cooler recesses of caves bearing more moisture. Additionally, humidity positively correlates with nitrate concentrations (R=0.53), suggesting that nitrification processes (should they occur) are occurring in more humid regions of caves. The evaporation factor for amorphous silica

correlates negatively with dissolved Si (R=-0.67). This relationship is due to the fact that increasingly greater Si concentrations require less evaporation (and hence a lower evaporation factor) to precipitate amorphous silica. A similar relationship is observed between dissolved Ca and the evaporation factor for calcite (R=-0.75). Other dissolved species, including P and Na, correlate negatively with amorphous silica's evaporation factor. This behavior results from the increased concentrations of both P and Na within Si-rich water samples.

Table 11. Geochemical Correlations of Cave Water Major Elements, Speleothem Major Elements, Evaporation Factors, and Other Geochemical Parameters. Orange cells represent positive correlations (R>0.51), while blue cells represent negative correlations (R<-0.51). SiO_2 and CaO wt.% represent major elemental components of speleothems, RH = relative humidity of caves, DOC = dissolved organic carbon, TDN = total dissolved nitrogen, SiO_2(a) = evaporation factor of amorphous silica, Cal = evaporation factor of calcite. Table adapted from Kulkarni et al. (In Prep).

	SiO2 wt %	CaO wt %	Air Temp.	RH	pH	Na	K	Ca	Mg	Sr	Si	HCO3-	F-	NO3-	DOC	TDN	P	S	d18O	d2H	SiO2(a)	Cal	Al	V	Cr	Mn	Cu
SiO2 wt %	1.00																										
CaO wt %	-0.89	1.00																									
Air Temp.	0.23	-0.45	1.00																								
Humidity	-0.14	0.23	-0.55	1.00																							
RH	-0.18	0.16	-0.08	-0.04	1.00																						
Na	0.06	-0.01	-0.18	0.07	0.41	1.00																					
K	0.11	-0.06	-0.03	-0.07	0.01	0.07	1.00																				
Ca	-0.49	0.39	-0.30	0.02	0.69	0.41	0.12	1.00																			
Mg	-0.43	0.24	-0.29	0.02	0.59	0.44	-0.05	0.81	1.00																		
Sr	0.00	-0.03	0.49	-0.33	0.26	-0.09	0.01	0.19	-0.02	1.00																	
Si	0.16	-0.15	-0.14	0.11	0.23	0.70	-0.26	0.21	0.41	-0.01	1.00																
HCO3-	-0.42	0.31	-0.21	0.00	0.63	0.45	-0.21	0.69	0.76	0.11	0.31	1.00															
F-	0.01	-0.08	-0.12	-0.17	0.19	0.52	-0.07	0.21	0.50	-0.30	0.69	0.25	1.00														
NO3-	0.01	0.09	-0.21	0.53	0.19	0.15	0.35	0.22	0.18	0.13	0.22	-0.04	0.18	1.00													
SO42-	-0.22	0.19	-0.10	0.08	0.44	0.39	0.41	0.50	0.54	0.11	0.21	0.26	0.53	0.64													
DOC	0.30	-0.24	-0.11	0.12	-0.24	-0.03	-0.29	-0.31	-0.26	-0.11	0.08	-0.20	-0.02	-0.13	1.00												
TDN	-0.04	0.03	-0.28	0.34	0.25	0.19	-0.13	0.22	0.31	-0.12	0.18	0.26	0.14	0.23	0.42	1.00											
P	0.25	-0.24	-0.06	0.01	0.22	0.66	-0.33	0.15	0.30	0.06	0.95	0.26	0.64	0.10	0.16	0.21	1.00										
S	-0.06	-0.02	-0.28	0.12	-0.01	0.09	-0.17	0.08	0.07	-0.28	0.06	0.26	-0.02	-0.01	0.14	0.08	0.15	1.00									
d18O	0.14	-0.05	-0.05	0.06	0.04	0.12	0.52	-0.14	-0.13	-0.27	-0.19	-0.13	0.23	0.10	-0.34	-0.10	-0.20	0.05	1.00								
d2H	0.31	-0.21	-0.20	0.09	-0.09	0.15	0.35	-0.25	-0.21	-0.40	-0.11	-0.14	0.26	-0.03	-0.22	-0.08	-0.09	0.24	0.87	1.00							
SiO2(a)	0.02	-0.01	0.08	0.02	-0.28	-0.62	0.05	-0.31	-0.29	-0.09	-0.67	-0.30	-0.46	-0.03	-0.09	-0.20	-0.69	0.08	0.15	0.25	1.00						
Cal	0.48	-0.40	0.14	-0.01	-0.55	-0.48	-0.13	-0.75	-0.64	-0.21	-0.19	-0.70	-0.08	-0.14	0.42	-0.20	-0.13	-0.02	-0.08	0.02	0.37	1.00					
Al	0.35	-0.29	0.16	-0.12	-0.33	-0.24	-0.33	-0.44	-0.40	0.09	0.12	-0.28	-0.06	-0.03	0.43	-0.16	0.24	0.16	-0.30	-0.26	-0.05	0.61	1.00				
V	0.05	0.04	-0.17	-0.06	0.18	0.78	0.20	0.25	0.25	-0.17	0.42	0.26	0.48	0.16	0.02	0.11	0.38	0.18	0.18	0.19	-0.35	-0.28	0.11	1.00			
Cr	0.22	-0.25	0.03	0.13	-0.46	-0.55	-0.13	-0.43	-0.34	-0.36	-0.56	-0.31	0.45	-0.03	0.02	-0.18	-0.53	0.30	0.43	0.51	0.93	0.47	-0.02	-0.33	1.00		
Mn	-0.31	0.40	-0.14	0.09	0.03	-0.13	0.15	0.11	0.06	-0.03	-0.25	-0.12	0.04	0.18	-0.11	-0.05	-0.27	-0.30	0.20	0.06	0.05	-0.06	-0.25	-0.26	-0.11	1.00	
Cu	0.61	-0.45	0.01	-0.01	-0.07	0.47	0.12	-0.20	-0.29	-0.03	0.34	-0.22	0.09	0.11	0.23	0.06	0.40	0.10	0.08	0.28	-0.15	0.16	0.53	0.61	-0.04	-0.27	1.00

5. Discussion

5.1. Mineralogy of LBNM Speleothems as Compared to Other Cave Environments

Opaline speleothems have been observed in other lava cave environments (*Brunet and Revuelta, 2014; Gonzalez-Pimentel et al., 2018*; *Luis-Vargas et al.,2019*; *Miller et al.,2014; Webb and Finlayson, 1987*), as well as in sandstone and quartzite caves (*Aubrecht et al., 2008; Melim and Spilde, 2018*). LBNM speleothems are predominantly opaline but are also observed to incorporate calcite (including Mg carbonate). A 1937 LBNM cave study by *Swartzlow and Keller (1937)* was perhaps the earliest study detailing the secondary mineral deposits found in the lava caves. The authors used the term "coralloidal opal" to describe much of what are interpreted as polyps and coralloids in this present study. The presence of carbonates was noted in the form of weak effervescent reactions in a minority of the tested samples. It is, however, now known that, although primarily comprised of opal, the speleothems are observed to incorporate significant amounts of carbonate, as shown by speleothem samples displaying upwards of 24 wt.% CaO.

Interestingly, another study at Lava Beds (*Rogers and Rice, 1991*) described gypsum mineral crusts in select caves. However, gypsum was not identified in any of the samples collected as a part of the BRAILLE study. Sulfate minerals in lava caves are typically the result of wind-blown sulfur-bearing aerosols and dust particles, which tend to accumulate to the point at which sulfate minerals can form in relatively older caves *(Sauro et al., 2014*). The gypsum deposits identified at Lava Beds are in different caves from those sampled by BRAILLE; although they are of similar age (36 ± 16 ka), they occur upland, closer to the shield volcano. It is currently unknown whether sulfate-mineral-bearing features were simply missed during sampling, or whether sulfate minerals only form in certain caves with potentially distinct water chemistry, such as the higher

elevation caves at Lava Beds. Extent of evaporation may also be a factor, which has not been properly documented across all caves.

5.2. Role of Cave Water in the Formation of LBNM Speleothems

The finely laminated opal and carbonate-bearing speleothem morphologies (polyps, crusts, coralloids, and cauliflower) are likely the result of variable yet somewhat cyclical shifts in environmental parameters (availability of water, pH, etc.) inside the caves, alongside interactions with microbial life present therein (*Gonzalez-Pimentel et al., 2018*; *Lopez-Martinex et al.,2016; Woo et al., 2008;*). The processes associated with opal precipitation are likely the dominant and most widely occurring within the caves, as indicated by the high wt % silica across all speleothems and the dominance of dissolved Si in cave waters. Consequently, carbonate mineral precipitation appears to occur as a process secondary to that of opal precipitation. The conditions leading to precipitation of opal and those leading to precipitation of carbonate minerals are likely different, with water and its mode of occurrence within caves acting as a major control on these conditions. These conditions will be discussed in the following sections.

5.2.1. Evolution of LBNM Cave Water Chemistry

Cave water chemistry plays an important role in the formation of speleothems, as well as the evolution of that chemistry within the context of the cave environment. Most inorganic cave water chemistry constituents (Si, Na, Ca, Mg, Fe, Al, etc.) are likely derived from interactions between percolating water, cave basalt, and overlying soil and volcanic materials - including Si-rich tephra (*Donnelly-Nolan et al., 1990*) (**Fig.46**). These water-rock interactions occur primarily between meteoric water and the host rock, as shown by the propensity for cave waters to plot on or near the Global Meteoric Water Line (**Fig.43**). Moreover, the sampled well waters (one deep well and three shallow lacustrine Tule Lake area wells) display similar isotopic signatures as

compared to drip waters (**Fig.42**). The isotopic composition of the deep well water suggests it is less evaporated than the shallow well water (**Fig.43**). Consequently, the extent of shallow groundwater influence on cave water chemistry is unknown.

Inorganic constituents in the cave waters are ultimately sourced from easily-leachable volcanic glass (including overlying tephra and glassy lava cave interior), as well as dissolution of other silicate minerals in the basalt, including plagioclase, clinopyroxene, and olivine. Water enters the caves in forms of drips, seeps, puddles, and films on rocks and speleothems. Furthermore, this water likely cycles throughout caves via repetitions of evaporation and condensation wherein puddles and films become vapor that may later become drips, serving to both evolve cave water chemistry through evaporative concentration and greatly increase the contact between water and secondary mineral deposits (*De Freitas and Schmekal, 2003*).

Dissolved inorganic carbon concentrations of LBNM cave waters (34 ± 23 mg/L) are lower than lava cave waters found in wetter climates, including Hawaiian lava caves, which have recorded concentrations upwards of 120 mg/L DIC (*Howarth et al., 2007;Teehera et al., 2018*). The tropical Hawaiian climate begets well-developed soil horizons, which provide a source of both dissolved inorganic and organic carbon to underlying caves. Soils located above LBNM caves however, are relatively thin and poorly developed, reflective of the arid climate (*Lavoie et al., 2017*). Hence, LBNM caves are more carbon-restricted than lava caves situated in other wetter climates.

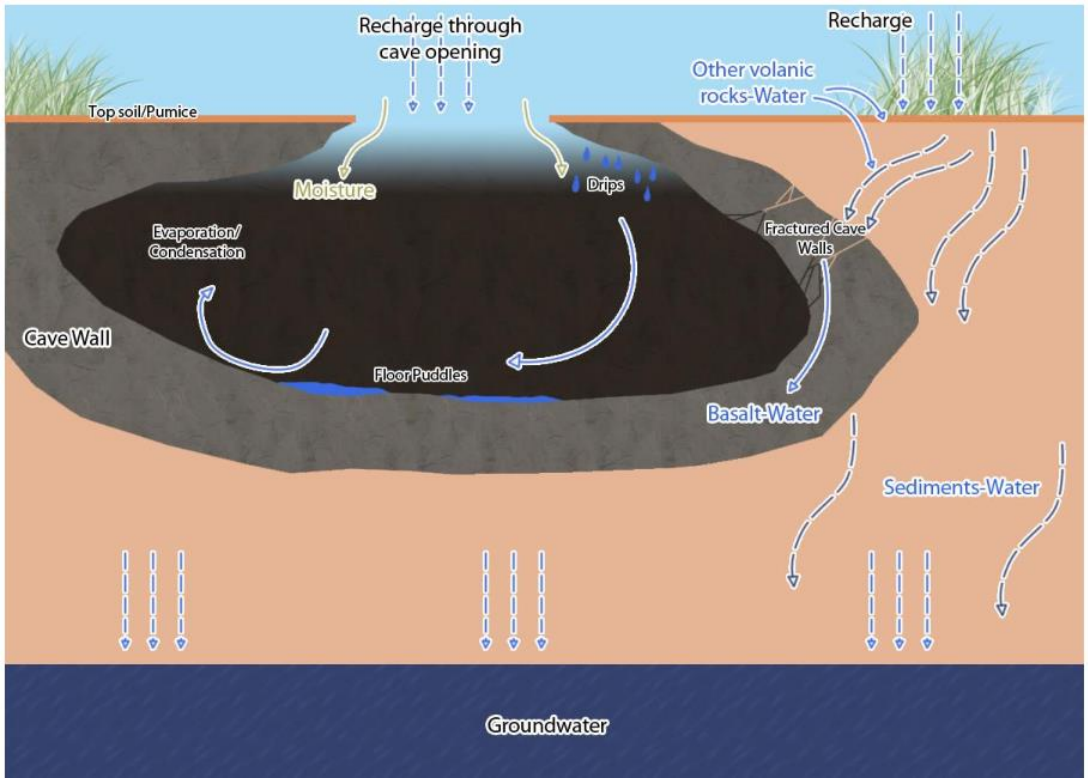

Figure 46. Conceptual cross-sectional model of water-rock interaction within caves at LBNM. Meteoric recharge enters the cave through large openings and/or through smaller fractures after interacting with basalt, tephra, and thin soil horizons. Figure modified from Kulkarni et al., in preparation.

5.2.2. Wet / Dry periods as Controls on Opal and Calcite Precipitation

One potential major mechanism for the cyclical variation of environmental parameters resulting in shifts in mineral deposition may be local climatic successions of wet and dry periods (*Fairchild and McMillan, 2007*). There are several lines of evidence observed within the speleothems and cave systems that support this mechanism, including the presence of concentric opal laminae and the presence of carbonate minerals within predominantly opaline speleothems.

5.2.2.1. Opaline Concentric Laminated Structures as Indicators of Environmental Change

First described in **Fig 23**, the nodular opal found within speleothems may represent microbially-mediated opal deposition in the form of a botyroidal structure. Concentric lamina are observed within cauliflower, polyps, and coralloids (**Fig.47.A,B**). Concentric opal laminae have

previously been described to represent structures that may form similarly to ooids (*Aubrecht et al.*, 2008; *López-Martínez et al.,* 2016) Ooids typically refer to spherical carbonate grains composed of laminae surrounding a nucleus often comprised of both inorganic and organic materials (*Diaz and Eberli et al., 2019*). In LBNM cave speleothems, only opaline concentric lamina are observed, not carbonate. Concentric opal laminae may suggest biofilm volume variation, as caused by multiple occurrences of desiccation followed by rehydration of the biofilm, ultimately driven by changes in climatic conditions (*López-Martínez et al., 2016*). Additionally, concentric laminae in lava cave environments may form in a similar manner to pedogenetic ooids in calcic soil (*Robins et al., 2015*). In calcic soils, ooids primarily form during periods of increased rainfall and porosity, in which a small particle acting as a nucleus can become coated to form the spherical laminated structures. During periods of increased moisture (e.g. a period of relatively increased rainfall), a microbial biofilm coating a nucleation particle will receive a more consistent supply of silica-saturated water, favoring the precipitation of silica in extracellular polymeric substances (EPS) (*López-Martínez et al., 2016*). Conversely, during drier periods the supply of water, and consequently dissolved silica to the biofilm, is lessened, reducing the favorability of opal to precipitate.

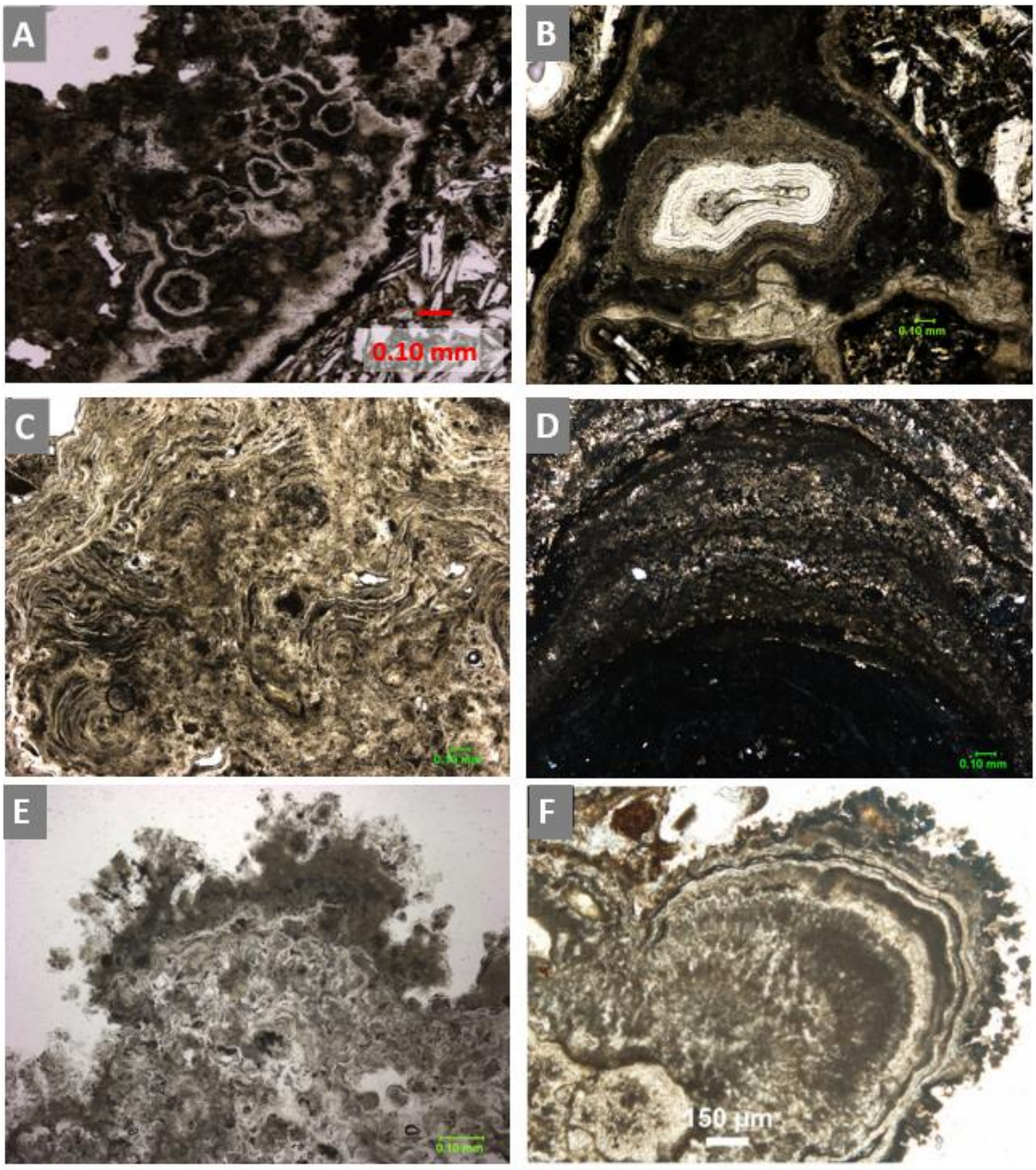

Figure 47. Structural features within speleothems. A) Concentric lamina within a cauliflower speleothem, 4x, PPL; B) Concentric lamina exhibiting a distinct partitioning between clear and brown opal, 4x, PPL; C) Hummocky, undulating stromatolite-like laminae within a cauliflower speleothem 4x, PPL; D) Porous opal exhibiting calcite-infilling. Note the extinct, dense opal laminae directly below the calcite-bearing lamina. 4x, XPL; E) and F) Comparison of E) potentially peloid-bearing LBNM cauliflower speleothem and F) Peloid-bearing opaline speleothem from the Chimalacatepec lava tube system, figure modified from López-Martínez et al., 2016.

The inclusion of volcanic mineral fragments as seen in **Fig.28** and **Fig.31** may also support the conclusion that the opal within the caves is precipitating during wet periods. Droplets or small streams of water flow within caves have been observed to transport mineral grains (*Aubrecht et al., 2008*). Increased rainfall (indicative of a wetter climate) may tend to produce more continuous droplets and streams, increasing the capability of water to deliver mineral grains and fragments to speleothem surfaces. Moreover, a more continuously moistened speleothem surface will act to adhere foreign particles.

5.2.2.2. Speleothem Mineralogy and Magnesium Content as an Indicator of Dry/Wet Conditions in LBNM Caves

The presence of carbonate minerals within this lava cave environment may also indicate a history of alternating wet and dry periods. The chemistry of LBNM cave waters alone isn't suitable for the precipitation of calcite, as all analyzed cave waters modeled using Geochemist's Workbench are consistently undersaturated with respect to calcite and other carbonates (**Table 10**). In order for calcite to become supersaturated in cave waters, and consequently capable of precipitating, it is necessary for the ionic components of calcite (Ca^{2+}, Mg^{2+}, dissolved carbonate species) to become further concentrated. A possible explanation for the required increase in concentration is by the action of evaporation, likely of surficial water films on speleothem surfaces (*López-Martínez et al., 2016*). Evaporative concentration of solutes also augments carbonate precipitation driven by degassing CO_2 (*Fairchild et al., 2000*). Evaporative concentration of water films would be most active during drier periods, as a less consistent water supply generally enhances evaporation (*Atkinson, 1983*).

Evaporative concentration as the driving mechanism responsible for carbonate precipitation can also be observed in the elemental composition of speleothems. The consistent incorporation of Mg carbonate throughout most of the morphological forms strongly indicates

evaporative concentration as a dominant process throughout all sampled caves (*Tremaine and Froelich, 2013*). Increased Mg content in cave speleothems has been noted to correlate with periods of drier climate and subsequently evaporative concentration of Mg^{2+} in solution, facilitating the incorporation of elevated concentrations of Mg into calcite (*Fairchild et al., 2000; Tremaine and Froelich, 2013*). Previous precipitation of carbonates (low-Mg) can also increase the Mg/Ca ratio of the solution, further increasing the proportion of Mg carbonate to precipitate. Normalizing CaO and MgO to SiO_2 (the most prevalent component in all speleothems) reveals a strong correlation between CaO/SiO_2 and MgO/SiO_2 (**Fig.48.B,** R^2=0.75), indicating that an increase of CaO generally entails an increase in MgO. As a result, greater SiO_2 concentrations beget lower MgO concentrations (**Fig.48.A**, R^2=0.79). Lesser incorporation of carbonate minerals in speleothems likely entails a lesser extent of parent solution evaporation, and therefore the reduction of Mg availability in carbonate precipitation.

All MgO concentrations however do not appear to be strictly associated with carbonate: electron microprobe analyses of a polyp speleothem (CRI20180731_D_12) reveal MgO weight percentages of up to 24% in silica-dominated regions, which can be observed at approximately the coordinates of (-13600 X, 23500 Y) in **Fig30.C**. Additionally, a broad band containing elevated MgO content (18-20 wt.%) is visible at approximately (-15250 X, 23750 Y) in **Fig.30.C**. This general region of the speleothem contains elevated SiO_2 concentrations as well as pockets of CaO throughout, indicative of a porous opal laminae with infilled calcite (**Fig.30.A, B).** The co-occurrence of SiO_2 and MgO often also precede thicker laminae of (once porous) infilled calcite laminae. These SiO_2 and MgO dominant laminae represent poorly ordered $MgSiO_2$ phases within opal, or as interstitially-bonded Mg^{2+} in a disordered opal-A matrix (*Cody, 1980; Webb and Finlayson, 1987*). Furthermore, interstitial incorporation of Mg^{2+} creates a charge imbalance,

which is often accommodated by the introduction of OH^- groups bonded directly to the interstitial ions (*Webb and Finlayson, 1987*). Interstitial Mg bonded in the described manner is not an entirely unexpected component of amorphous opal, as $Mg(OH)_2$ bears a positive surface charge, enabling the neutralization of negatively charged silica particles, and consequently the precipitation of Mg alongside silica (*Williams and Crerar, 1985*).

Magnesium content in speleothems, and therefore likely in opal, is highest among crusts, cauliflower, polyps, and coralloids (5-14 wt.% MgO in carbonate-bearing samples). However, the most highly opaline speleothem morphology, gours, consistently incorporate low concentrations of Mg in comparison to other speleothems, i.e. less than 1 wt.% MgO (**Fig.48.A**). This suggests a significantly different formation mechanism for gours than other morphologies. A possible explanation is water availability, where speleothems receiving limited water supply will experience more evaporative concentration. Gours appear to be predominately associated with active drips and consequently less evaporative concentration of the parent solution, resulting in relatively rapid opal precipitation fed by a steady supply of dissolved silica. Due to a more stable supply of silica, it is likely that Mg is not favored to precipitate alongside opal in high concentrations (*Miller et al., 2014*); in solutions experiencing less evaporative concentration, Mg is less likely to become saturated in the solution relative to Si. Moreover, dissolved Si does not correlate with dissolved Mg (**Fig.48.C**, R^2=0.16), with POS and YEL waters displaying the greatest Mg concentrations. This behavior may be due to the host rock composition, as POS (7.3 wt.%) and YEL (6.1 wt.%) have the second and third highest MgO wt.%. Additionally, the lowest Mg concentration cave waters, LYO and VAL, also have the lowest MgO wt.% in basalt (4.9 and 4.5 wt.%). Many POS and YEL speleothems have high MgO contents (>8 wt.%), while LYO and VAL speleothems have less than 5 wt.%. This relationship among caves may be suggestive of host

rock composition influencing speleothem composition, but due to the limited number of samples, it may be difficult to eliminate sampling bias as a factor.

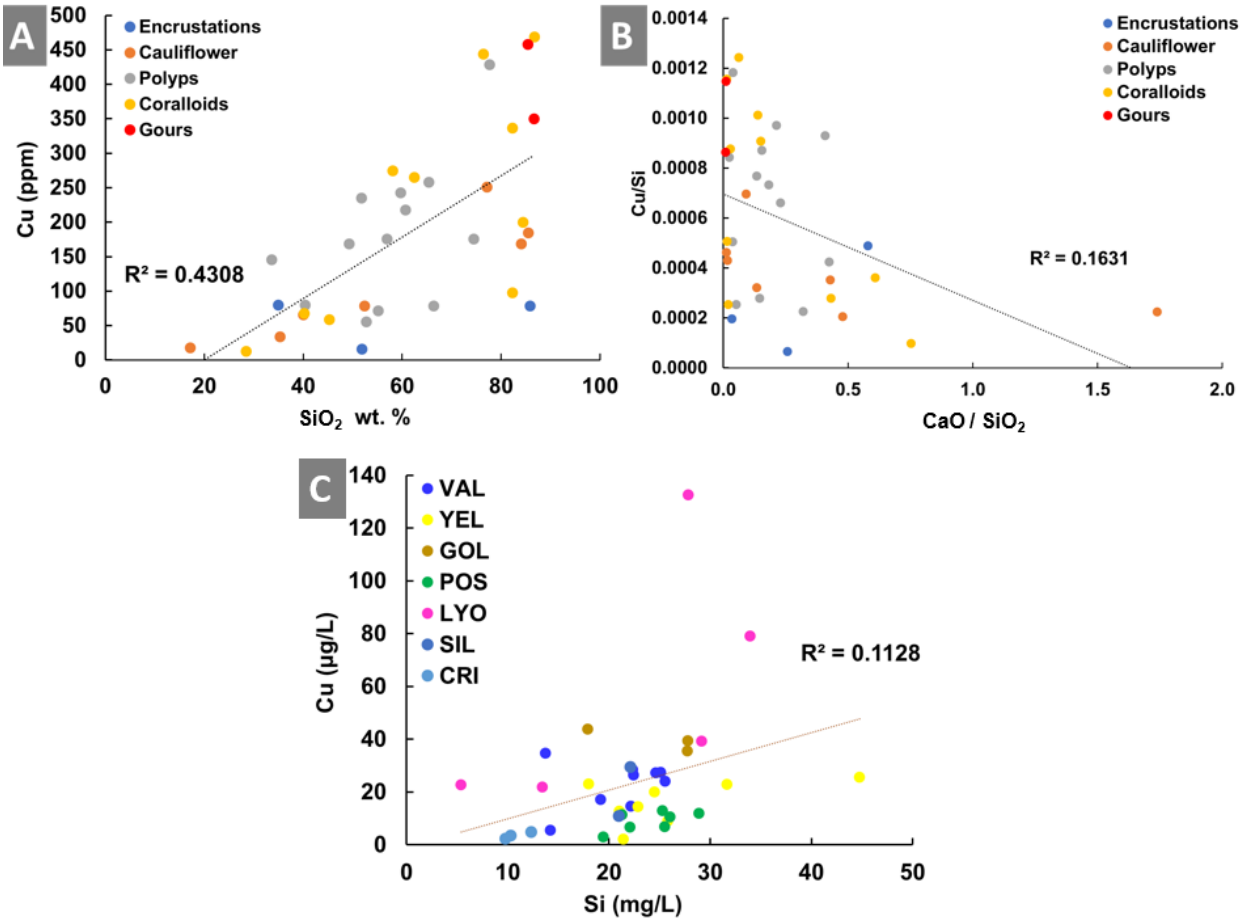

Figure 48. Mg content in speleothems and cave waters, comparing speleothem morphologies. A) MgO wt.% vs SiO_2 wt.% R^2= 0.79; B) MgO/SiO_2 vs CaO/SiO_2, R^2=0.75; C) Mg (mg/L) vs Si (mg/L), R^2= 0.16. Dotted line represents trend line. A-B: Blue = crusts, Orange = cauliflower, Gray = polyps, Yellow = coralloids, Red = gours. C: Colors represent Cave IDs.

The variations in calcite texture observed in speleothems (bladed columnar, sparitic, micritic) may also further indicate depositional differences caused by climatic conditions. Sparitic calcite is more likely to form during relatively wetter periods, where a greater flow of water acts to limit the entry of organic colloids onto speleothem surfaces (*Vanghi et al., 2017*). Micritic calcite is associated with drier periods, wherein the lack of water flow facilitates the incorporation of particulates and other irregularities, including organic particles (*Frisia et al., 2014*). Columnar

calcite fabrics in speleothems have been interpreted as the product of several environmental factors, including low Mg in solution and relatively constant flow of thin water films over the speleothem surface (*Frisia, 2014; Kendall and Broughton, 1978*).

5.2.2.3. Possible Role of Magnesium in the Formation of Poorly-Ordered Clay Minerals in Speleothems

Although the identity of clay minerals was not directly ascertained via clay separation and subsequent XRD analysis (potentially due to low volume), there are several lines of evidence that may suggest the limited presence of Mg-rich clay in select LBNM speleothems: 1) MgO is associated with SiO_2 in laminae containing up to 24 wt.% MgO (**Fig. 30**), 2) the highest concentrations of K_2O up to 0.5 wt.% are in Mg-SiO_2 laminae, 3) broad hump at low angles (19 – 20 (2θ°) in a polyp diffractogram (**Fig.17**, likely masked by amorphous opal hump), and 4) a sharp peak at low angles (approximately 17 2θ°) in a cauliflower diffractogram (**Fig.18**). These results may be consistent with a poorly-ordered (or pontentially amorphous) mixed-layer Mg-rich clay mineral(s), such as kerolite, sepiolite, or saponite, Such clay minerals have been identified in other lava cave speleothems, and likely represent low temperature precipitation via dehydration of hydrous Si-Mg gels (*Miller et al., 2014; Léveillé et al., 2002; Webb and Finlayson, 1987*; *Woo et al., 2008).* Clays formed in low temperature, humid environments in the presence of microbes are often impure, taking in cations such as K^+ (*Eick et al., 1990; Léveillé et al.,* 2002). Moreover, the relative lack of Al-oxides in these speleothems and clays strongly suggest that the clays are not detrital (*Léveillé et al., 2002*). Future analyses of clays in LBNM speleothems will be crucial to discern the role of Mg in the formation and extent of clay minerals in lava caves.

5.2.3. Water Availability and Transport as Factors in the Formation of Varied Speleothem Morphologies

The variations in speleothem morphology and appearance are due to complex interactions between physical, inorganic and microbial processes. A predominant control appears to be availability of water, how that water is transported (including by drips, air flux, and capillary action), and the ability of the water to transport impurities. These factors will control mineralogy, morphology and, potentially, the extent of microbial influence.

5.2.3.1. Availability of Water and Speleothem Composition / Morphology

An active continuous drip/flow of water appears to fulfill the conditions for gour (speleothem) formation, as gours and flowstone speleothems in caves have been previously noted to occur where active water flows are observed (*Brunet and Revuelta, 2014*; *Cuevas-González et al., 2010; Varnedoe 1965*). The continuous transport of water supplies dissolved Si and supports precipitation of opal. Gour speleothems for instance lack some of the previously identified biosignature features, including opaline concentric lamina. However, hummocky microstromatolite-like laminae and porous opal (non calcite-infilled) laminae can be observed within gours, making the possibility of the involvement of microbial activities in their formation difficult to completely disregard (*Aubrecht et al., 2008*).

Conversely, the carbonate-bearing morphologies (crusts, cauliflower, polyps, and coralloids) likely represent more ephemeral water sources, with opal precipitation occurring during wet periods and carbonate primarily during dry periods. The carbonate bearing samples have the following concentrations of CaO: crusts (18.7 ± 5.7 wt.% CaO); cauliflower (17.1 ± 9.9 wt.% CaO); polyps (fingers: 2.8 ± 1.2 wt.% CaO, white-tipped: 11.9 ± 4.5 wt.% CaO, orange-tipped: 6.7 ± 4.7 wt.% CaO); coralloids (14.9 ± 4.7 wt. % CaO). Significant differences can be observed among the speleothem morphologies, but the majority of samples range from approximately 7.0 –

15.0 wt. % CaO. Crusts and cauliflower speleothems incorporate the greatest CaO wt. %, but the two are the same within one standard deviation of the mean. Coralloids contain moderate concentrations of calcium (as shown by 14.9 ± 4.7 wt. % CaO) content, and polyps consistently contain the lowest CaO wt.%. (11.9 ± 4.5 and lesser wt.% CaO). Should the carbonate content in speleothems be associated with availability of water, crusts and cauliflower represent the most restricted contact with water, coralloids moderately restricted, and polyps the least restricted.

5.2.3.2. Variations in Speleothem Morphology and Transport of Cave Water

Although water availability is an important control on secondary mineral deposition, it is not the only parameter of interest, as it can be shown that water availability alone cannot explain the variation in secondary mineral deposition. For example, finger polyps are nearly pure opal, which suggests a more constant water supply, similar to gour speleothems. However, these opaline polyps are distinct in morphology, coloration, and composition from gours, implying that the formation of speleothems with similar mineralogical composition may be the result of a combination of different processes. One important factor to consider is the location(s) within the cave in which secondary minerals nucleate / precipitate, and consequently, where the speleothems form. Foremost, polyp speleothems are predominantly, but not exclusively, found on angular cave floors (including aa lava flow deposits) and/or collapsed roof basalt surfaces, and oriented upwards at various angles that do not seem to be associated with any active overlying drips (**Fig.49**). Moreover, individual polyps amongst a cluster are generally oriented similarly (**Fig. 49**).

Figure 49. Polyps located on cave surfaces. Note the concentration and similar orientation of polyps on the left-most side of the collapsed roof basalt.

Therefore it follows that the polyp formations (and likely other morphologies) are greatly influenced by the directionality of water transport within a cave. The shared orientation and sub-90 degree angularity of many polyp speleothems indicate that the water from which they precipitated was likely transported to the nucleation site via air flux. Speleothem formation supported by the transport of dispersed water particles has been documented in karst cave systems (*Vanghi et al., 2017*). The *Vanghi et al. (2017)* study described the formation of protruding coralloid calcite speleothems by action of a hydroaerosol effect, wherein water droplets impacting the cave floor are mechanically dispersed into smaller particles, which are then capable of being transported further within the cave. The above study noted the abundance of high surface area bone fragments within the cave as nucleation sites for speleothem growth. The highly irregular basaltic LBNM cave surfaces are analogous as relatively high surface area features. Additionally, droplets of water strengthen the outgassing of CO_2, which may act to encourage calcite precipitation in

cave environments (*Chen et al., 2004*). Flux of vapor-saturated air within cave environments alone may act as a source of water to speleothems and/or nucleation surfaces, as water saturated air moving into deeper cooler parts of a cave loses its ability to hold moisture, forcing condensation to occur (*De Freitas and Schmekal, 2003*). Warm air interacting with relatively cooler rock and/or speleothem surfaces will also result in condensation, and thus additional water supplying dissolved solutes necessary for mineral precipitation.

5.2.3.3. Influence of Capillary Action of Cave Water in Speleothem Formation

Capillary action, the ability of water to flow against gravity - is yet another process that may help explain the morphological diversity of these speleothems. A plethora of speleothems (especially polyps and coralloids) grow upwards and/or exhibit branching features. This requires that the solution from which the minerals are precipitating also progresses upward during the growth of the speleothem. The speleothems' surfaces and tips also appear moistened in many cases, which suggests capillary forcing. Moreover, water supplied from air flux alone may not be suitable to generate distinct upward-oriented speleothems, since evaporation and subsequent condensation is likely to occur consistently throughout caves (**Fig.43**). As observed in **Fig 49,** the darker surface near the polyps is moistened, which may act as a condensation-fueled reservoir for capillary action to supply water to the protruding speleothems. This effect of capillary action in upward-oriented porous opaline speleothems has been measured to draw water up to ~10 cm, indicating the power of capillary action to propagate speleothem growth (*Aubrecht et al., 2008; Sauro et al., 2018*).

5.2.3.4. *Foreign Bodies and Impurities Indicative of Water Availability*

The introduction of dust particles, organic matter, and other impurities carried by cave waters (and air flux) may also influence the growth patterns and, therefore, morphology of speleothems. Such impurities (including organic colloids) are potentially capable of acting as nucleation sites for future mineral precipitation, which may result in the irregular, dendritic structures observed in coralloids and other morphologies (*Vanghi et al., 2017*). Furthermore, decreased water availability appears to act as a major control upon the rate at which impurities are included in speleothems. A lower water supply will concentrate impurities and more easily facilitate the incorporation of organic colloids within speleothems (*Vanghi et al., 2017*).

5.3. Microbial Influence in LBNM Speleothem Formation

5.3.1. Capability of LBNM Cave Waters to Support Microbial Metabolism

In accordance with the prominent biofilms observed within the caves (**Fig.5**), cave waters exhibit an accumulation of dissolved organic carbon (DOC), at a mean of 11.8 ± 8.0 mg/L. DOC plotted against total dissolved inorganic carbon (DIC) (**Fig. 40. A**) shows enrichment of DOC relative to DIC. As mentioned previously, the caves are inhabited by colonies of microbes, visibly apparent through the presence of biofilm. Cave microbes are generally highly efficient nutrient scavengers, as resources are restricted in caves and analogous environments. The accumulation of DOC in lieu of DIC suggests that (litho)autotrophy, not heterotrophy, may be the predominant metabolic pathway utilized by microbes (*Stevens, 1997*). If heterotrophy were the dominant process, the cave waters would be expected to show accumulation of DIC, as represented by the following simple acetotrophic metabolic reaction:

$$\mathbf{CH_3COO^- + 4H_2O = 2HCO_3^- + 9H^+ + 8e^-}$$

This reaction shows the fundamental process of heterotrophy: an organic carbon electron donor (such as acetate) is consumed, forming an inorganic carbon compound (such as bicarbonate). Eight electrons must also be products to maintain charge balance. Since DOC is prevalent throughout the various caves and DIC is consistently lower in concentration than DOC, it can be presumed that heterotrophy as a whole may not be a major contributor to cave water chemistry.

Similar to DOC, cave waters are enriched in dissolved organic sulfur relative to dissolved inorganic sulfur (**Fig. 40. B**). The accumulation of dissolved inorganic sulfur may indicate a lack of (litho)autotrophic sulfur oxidation metabolic processes utilized by cave microbes, i.e. sulfate would be expected to accumulate over dissolved organic sulfur, which is not observed (*Macalady et al., 2008*).

Nitrate represents a major inorganic species that is not a readily explained product of volcanic material dissolution, since N-bearing minerals were not identified in any host rock (or secondary mineral) material. Nitrate, instead, must be generated within the caves or transferred into caves from an external source, i.e. groundwater. Shallow groundwater contamination in LBNM caves is possible, as stable isotopic data for O and H were similar for shallow wells and drip waters. However, further investigations into N stable isotopes may be required to discount outside sources of N within caves. The cave waters do not exhibit a consistent preponderance of inorganic nitrogen over organic nitrogen (or vice versa), suggesting that multiple processes are likely influencing the N chemistry of cave waters. Nitrifying microorganisms may play a pivotal role in the generation of nitrate. Soil organic matter, animal waste (i.e guano), and the dissolution of the cave basalt itself may provide ammonium and other forms of N utilized by microbial processes. Likewise, the equal accumulation of inorganic nitrate does not discount denitrification as a potential process within the caves. Nitrification, nitrate oxidation, and other N-focused

metabolic activities have been associated with bacterial phyla (including nitrospirae) previously reported in lava cave environments, including LBNM caves (*Gonzalez-Pimentel et al., 2018*; *Lavoie et al., 2017*). N-cycling organisms are also crucial for the supply of nutrients in resource-limited environments, acting to support the growth of diverse microbial communities (*Lavoie et al., 2017*).

The elevated concentrations of dissolved organic phosphorous (DOP: 3.64 ± .92 mg/L) in cave waters may also be indicative of microbial activity. Furthermore, the strong correlation between dissolved P and Si (r=0.95, **Table 11**) is likely not the sole result of inorganic basalt dissolution. The strong correlation between P and Si may rather be indicative of biologically mediated silica solubilization. Increased concentrations of dissolved P (especially organic) may represent the byproducts of relatively heightened biological influence responsible for the acceleration of silica dissolution (*Mapelli et al., 2012*). One likely agent of dissolution are microbes capable of mediating the dissolution of silicate minerals. This phenomenon has been documented in several cave systems, including in granitic caves, orthoquartzite caves, and basaltic caves (*Aubrecht et al., 2008; Barton et al., 2009; Dontsova et al., 2014 Romani et al., 2010;*). Microbially produced low-molecular weight organic acids in particular may greatly mediate the dissolution of volcanic minerals (*Romani et al., 2010*). Weathered basalt, as observed in LBNM cave basalt palagonite and Fe-hydroxide mineral alteration, may be a product of DOC-enhanced weathering (*Dontsova et al., 2014*). It is not definitive that microorganisms are the only biological agents that can dissolve silica. Other factors, such as pedogenic organic acids, have been demonstrated to effectively increase the rate of silica dissolution in basaltic environments (*Bennett, 1991*). The poorly developed soil horizons above LBNM caves however may not strongly contribute pedogenic organic acids to the cave environment (*Lavoie et al., 2017*). Nevertheless,

biological processes likely act to increase silica availability in cave systems. However, to further understand the relationship between P and Si, further characterization of the dissolved P content is required. The identities of the P-bearing compounds and processes associated with the organic P content are currently poorly understood.

5.3.2. Speleothem Microstructures and Fabrics Indicative of Microbial Mediation

The internal structures, texture, and morphology of LBNM speleothems exhibit similarities to those found in previously-described lava cave and select karst speleothems (*López-Martínez et al., 2016, Melim and Spilde, 2018, Melim et al., 2016; Swartzlow and Keller, 1937; Vanghi et al., 2017*). The aforementioned concentric opal laminae may be microbial in origin (*Diaz and Eberli et al., 2019*). However, concentric lamina in other environments are often the product of both organic and inorganic processes, making it difficult to discern the ultimate extent of microbial action involved with their formation (*Robins et al., 2015*). Dissolution of microbially-mediated secondary minerals and subsequent abiotic precipitation may also occur, but can be challenging to establish a definitive timeline of microbial mediation in speleothem formation (*Jones, 2010*).

A noteworthy yet potentially contentious feature that may indicate the role of microbial mediation in secondary mineral precipitation are the microstromatolite-like laminae present throughout the various cave speleothem morphologies. Microstromatolites are often characterized by irregular and/or wavy laminae that tend to conform to dome-like structures indicative of lithified microbial mats and/or biofilm (*Jones, 2010; Léveillé et al., 2002; López-Martínez et al., 2016*). Many LBNM speleothems appear to embody the characteristics associated with microstromatolites (**Fig.47.C**). However, laminae produced by inorganic mechanisms may also exhibit hummocky and irregular structures, making their origins ambiguous.

Present within some terrestrial microstromatolites are dark peloid-like particles within the opal matrix (*Aubrecht et al., 2008; López-Martínez et al., 2016*). These particles may represent basal components of microbial communities and, therefore, microbial habitation of affected speleothems. The peloids appear distinct from the mineral fragments (glass, plagioclase, pyroxene) found within speleothems and appear to be preferentially oriented perpendicular to their respective laminae (**Fig.47.E,F**). Additionally, the peloid-like particles may consist primarily of silicified organic particles, since they become extinct along with the surrounding opal under crossed polarized light.

Porous opal laminae may also be consistent with microbially-mediated precipitation. Experiments show that inorganic silica precipitation produces a dense matrix via continual infilling of pores by subsequent opal deposition (*Orange et al., 2013).* In comparison, microbially-mediated silica precipitation may produce silica precipitated in extracellular polymeric substances, which generates a porous sinter (*Orange et al., 2013, Sauro et al., 2018*). Porous opal speleothems may act as a pseudokarst system wherein microbial life is related to the distribution and circulation of water throughout the microsystem (*Romaní et al., 2010*). Furthermore, autotrophic inhabitants of porous opal may mediate the precipitation of carbonate minerals through the metabolic fixation of CO_2 and/or N, which acts to raise the pH of the system and increase the proportion of carbonate ions (*Diaz and Eberli et al., 2019*; *Jones, 2010; López-Martínez et al., 2016*). Degassing of CO_2 would also result in a similar outcome (*Forti, 2001*). Moreover, a pH rise is also favorable for silica amorphization, as silica solubility rises, resulting locally in more dissolved SiO_2 (*Konhauser et al., 2004*). However, the increase in silica solubility must be paired with a nucleating process to precipitate amorphous silica phases such as opal-A (e.g. microbial cell surfaces, ultrastructures, and EPS) (*Sauro et al., 2018*). Acidification of high-pH cave waters may also drive opal

precipitation (Forti, *2001*). Infilled-carbonate (including calcite present within what was presumably a pore within opal) may therefore act as a possible biosignature. Both dense and porous opal are seen within LBNM speleothems, including calcite-infilling of porous opal (**Fig. 47.D**). The occurrence of both dense and porous opal within the speleothems may indicate inconsistent microbial habitation throughout the development of a speleothem.

5.3.3. Exterior Colorations of Speleothems Indicative of Microbes

The sampled speleothems often exhibit a dark brown to gray coloration, most commonly amongst coralloids and polyps of all three types (fingers, white-tipped, and orange-tipped). *Swartzlow and Keller* (1937) concluded the color was due to dust particles adhering to a moistened opal surface. Trapping of mineral grains has also been attributed to filamentous microbes in the formation of bulbous speleothems (*Jones, 2010*). Additionally, the darker colorations are also observed in samples without obvious volcanic mineral fragment inclusions. Therefore, other factors may be responsible for brown/gray coloration. Opal free from impurities takes on a clear (colorless) coloration. With impurities of Ca, it becomes milky-white; Fe, Al, and Pb impart a black/gray coloration, and non-substitutional Al produces a brown coloration (*Makreski et al., 2004).* Additionally, the common incorporation of calcite within speleothems may also contribute to white and tan colorations, two common calcite colors.

Dark gray speleothem coloration may also indicate incorporation of organic matter (*Urbani et al., 2005; Zupancic et al., 2011*). It is, therefore, possible that gray opal coloration indicates a more active role of biological mineral precipitation. Other colorations, such as the light brown to muted yellow color observed in some LBNM speleothems, may also be the product of microbial pigments (*Gonzalez-Pimentel et al., 2018*). Yellow pigments can be produced by actinobacteria, a major phylotype in LBNM caves (*Lavoie et al., 2017*). However, a more detailed organics-focused

study of these laminae is required to confirm pigmentation in speleothems. Coloration may also be controlled by a combination of inorganic factors (including presence of Fe-containing dust and calcite infilling) in tandem with the inclusion of organic matter.

5.3.4. Similarities between Polyps and Microbially-Mediated Sinter Deposits

Speleothems (especially polyps and cauliflower) bear an outward morphological resemblance to sinter deposits: siliceous (including opal-A) hot spring deposits that are associated with and often entrap thermophilic microorganisms. Sinter deposits are morphologically diverse, with several lithofacies arising from variations in temperature gradient of parent fluids, biological activity, and more (*Cady and Farmer, 1996; Jones and Renaut, 2003; Guido and Campbell, 2014*). Nodular geyserite deposits, sinter deposits associated with the proximal area surrounding vents, are a category of sinter deposit exhibiting characteristics that are strikingly similar to polyp speleothems. Nodular geyserite describes an aggregate of <1 cm clustered rounded nodules, composed by fine columnar lamina (**Fig**.**50.A,D**). Furthermore, nodular geyserite forms along relatively dry portions of a vent that receive less water splash than other surrounding areas (*Hamilton et al., 2019*). The water-limited nature of nodular geyserite is comparable to polyp speleothems, which likely do not receive constant direct drips. The upward orientation of nodular geyserite and elongate rounded form of individual nodules are outwardly analogous to the similar structures observed in polyp speleothem deposits (**Fig.50.B,C,E**).

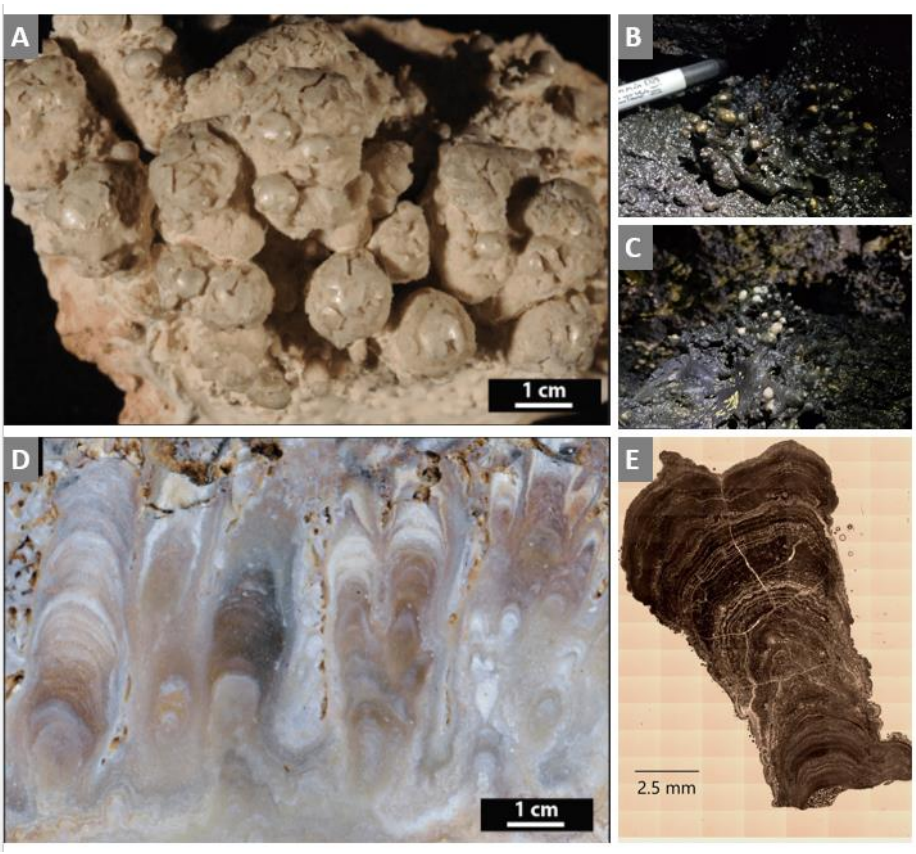

Figure 50. Comparison of nodular geyserite and polyp speleothem features. A) Nodular geyserite exhibiting clustered oblong growths; B) and C) clustered LBNM polyp speleothems; D) Cross-section of nodular geyserite exhibiting columnar lamina; E) Single polyp speleothem cross-section. A) and D) are modified from *Hamilton et al., 2019.*

The involvement of microbes in the formation of sinter deposits, including nodular geyserite, is well-documented (*Campbell et al., 2015; Renaut and Jones, 2011; Urusov et al., 2008*). In the case of nodular geyserite, microbial communities (often biofilm) colonizing the mineral surface grow upwards as a method to escape complete silica entombment. This upward growth acts to guide further mineral precipitation, and ultimately results in the upward-growing nodular features after repeated cycles of silica deposition, and subsequent silicification of microbes. Although sinter deposits and LBNM speleothems exist in two distinctly different environments, especially regarding temperature, their similarities may suggest a similar role of microbial activity in upward-growing polyp speleothems. Similar to nodular geyserite, the

prominent upward trajectory of polyps (and other speleothems) may be also controlled by consistent microbial habitation of mineral surfaces.

5.4. Potential Biosignature Elements within LBNM Speleothems

Speleothem compositions may provide evidence for microbial mediation of speleothem growth, be it by passive or active influence (i.e. microbial processes changing environmental conditions vs. direct precipitation by microbial process, e.g. silica shells created by diatoms). The following sections will discuss speleothem chemistry regarding Cu, Ba, V, S, and P. These elements were selected for their known roles in microbial processes, including microbial pathways noted to occur in cave environments (**Table 12**). The majority of the above elements have been observed to accumulate within microbial EPS, which then may act as nucleation points for mineral precipitation, or otherwise become entombed in later precipitation. **Table 12** below summarizes these elements and references thereof where these are specifically cited to be related to microbial biosignatures.

Table 12. Potential Biosignature Elements and Their Possible Functions in Cave Environments. Included elements: Cu, Ba, V, S, P

Element	***Microbial Function / Interaction***	***References***
Cu	Bioaccumulation, Capture within EPS, Toxicity Resistant	*Northup et al., 2011*
Ba	Bioaccumulation, Increase of silica solubility	*Sanchez-Moral et al., 2004 Sauro et al., 2018*
V	Metabolism, Bioaccumulation, Nitrogen Fixation Enzyme	*Huang et al., 2015; McRose et al.,2017; Spilde, et al., 2016*
S	Metabolism, Bioaccumulation	*Boston et al., 2001; Northup et al., 2011*
P	Metabolism, P precipitants, Essential Nutrient	*Jones 2009;Jones 2010*

5.4.1. Copper Content in Speleothems and Cave Waters

Copper within the speleothems is predominately sourced from the cave basalt itself, with Cu mobilized during dissolution of the host rock. Copper content correlates most strongly with increasing silica content in the speleothems, upwards of 500 ppm in samples with silica weight percentages in excess of 88% (**Fig.51.A**, R^2= 0.43). Accordingly, samples with lower silica weight percentages (and consequently greater CaO and MgO values indicative of carbonate) generally have lower concentrations of Cu (**Fig.51.B,** R^2= 0.16). Host rock composition may influence the concentration of Cu in speleothems, as Cu content in speleothems varies amongst caves. The greatest non-gour speleothem Cu concentrations (> 400 ppm Cu) belong to GOL speleothems. This cave is older (36 ± 16 ka) than those in LYO and VAL (12,260 BP), and has the second highest Cu concentrations among the sampled cave basalt at 220 ppm (compared to VAL: 83 ppm and LYO: 68 ppm). However, higher host cave basalt Cu concentrations may not necessarily indicate increased Cu mobility and availability, as the greatest dissolved Cu concentrations analyzed are seen in LYO cave waters; yet, LYO basalt has a low Cu concentration at 68 ppm. Moreover, LYO housed the >400 ppm gour speleothems, suggesting that bulk basalt chemistry alone is likely not sufficient to explain both Cu mobility and subsequent incorporation within speleothems.

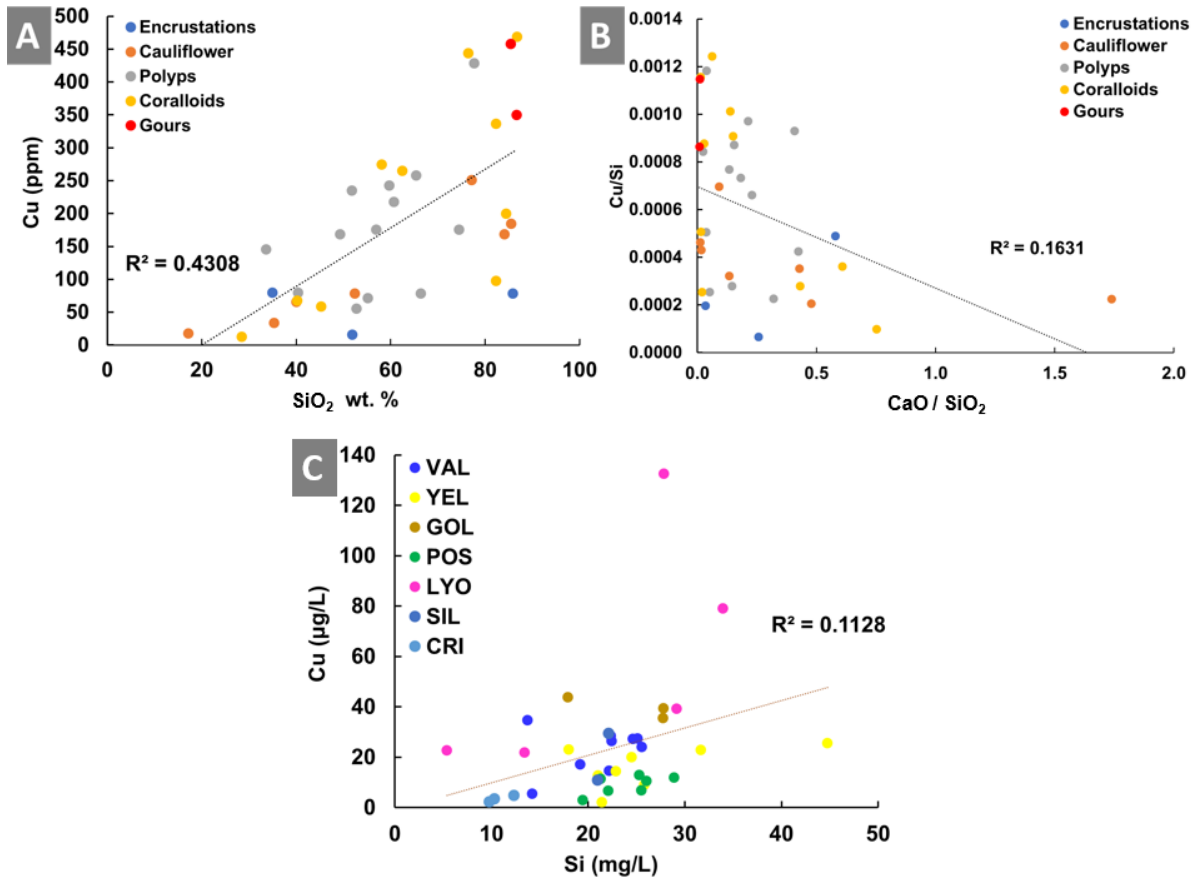

Figure 51. Cu content in speleothems and cave waters, comparing speleothem morphologies. A) Cu (ppm) vs SiO_2 wt.%, R^2 = 0.43; B) Cu/Si vs CaO/SiO_2, R^2=0.16; C) Cu (µg/L) vs Si (mg/L), R^2=0.11. Dotted line represents trend line. A-B: Blue = crusts, Orange = cauliflower, Gray = polyps, Yellow = coralloids, Red = gours. C: Colors represent cave IDs.

Copper in opaline speleothems occurs interstitially rather than as a substitution in silica, as Cu has a greater ionic radius and lower charge than Si. Additionally, Cu is known to incorporate into karst cave calcite speleothems as an exchange between Ca^{2+} and Cu^{2+} in the calcium carbonate lattice (*Turner, 2002*). Copper-bearing calcite speleothems typically take on a blue coloration, which has not been observed in any LBNM speleothems, neither in situ nor in thin section. The preferential presence of Cu in opal at LBNM (as represented by the correlation between Cu and SiO_2) suggests that Cu is primarily removed from solution during periods of opal precipitation, which likely occur prior to calcite precipitation. The resultant solution post opal precipitation consequently contains a lower Cu concentration, which is subsequently no longer available to

readily precipitate alongside calcite and/or Mg carbonate. Copper concentrations and distribution measured by electron microprobe appear to follow the general trend set forth in **(Appendix E4 p.167) –** Cu_2O concentrations are highest within regions of elevated SiO_2. Furthermore, laminae with >0.08 wt.% Cu_2O have >50 wt.% SiO_2 . Cu_2O exists within CaO-dominated regions, but at noticeably lower concentrations <0.04 wt.%). However, the resolution achieved for Cu is lower in comparison to the other analyzed elements, making it difficult to confirm the distribution of Cu in these speleothems.

Dissolved Cu is present in the cave waters, albeit at relatively low and highly variable concentrations (23.3 ± 24 µg/L), with dissolved Cu not correlating with dissolved Si (**Fig.51.C**, R^2=0.11). The large standard deviation value is due to the presence of a 132.6 µg/L drip water sample, which was by far the greatest concentration of Cu recorded. This high Cu content water sample was directly associated with an opaline gour speleothem in LYO, which contains a Cu concentration of 350 ppm, one of the highest Cu concentrations among the speleothems. Copper isn't commonly utilized in microbial metabolic processes and is generally toxic to microbes, but it has been noted to occur in extracellular products (*Miranda and Rojas, 2006; Samanovic et al., 2012*). Copper-bearing silica speleothems comprised of poorly crystalline chrysocolla have also been observed: blue-green speleothems in Hawaiian lava caves were found to contain microbes, but their formation mechanism, abiotic or otherwise, is currently unknown (*Northup et al., 2011*). One possible explanation is that microbial EPS may bind cations, which then act as nucleation points for mineral precipitation (*Diaz and Eberli et al., 2019*). The low concentrations of dissolved copper in LBNM cave waters and >400 ppm Cu concentrations among high silica speleothems suggests a role for microbial Cu accumulation during opal precipitation, although the degree of concentration is likely limited to the point such that Cu minerals do not precipitate.

5.4.2. Barium Content in Speleothems and Cave Waters

Barium represents an element of interest with regard to microbial influence during speleothem genesis. Firstly, dissolved barium enhances availability of silica (*Dove and Nix, 1997*). At near neutral pH, low concentrations (including microgram magnitude) of Ba^{2+} in solution increase both the dissolution rate and solubility of silica up to 40 times that of deionized water (*Dove and Nix, 1997).* Secondly, some microbes mobilize and precipitate barium, including bioaccumulation in EPS and cell wall nucleation sites (*Gonzalez-Muñoz et al., 2003; Gonzalez-Muñoz et al., 2012).*

Consequently, bioaccumulation of barium within cave environments may enhance silica saturation in cave waters, which enables precipitation of opal (*Sauro et al., 2018*), as seen in the Venezuelan orthoquartzite cave Imawarì Yeuta. Imawari Yeuta is home to massive opaline deposits, including meter-high columnar stromatolite-like formations. These bulbous speleothems contain up to 75 ppm Ba, and associated cave waters have Ba^{2+} concentrations of up to 5 μg/L (*Sauro et al., 2018*). These authors hypothesize that microbes drive silica dissolution, in part by drawing Ba out of host rock, and that opal nucleates upon microbial membranes and EPS, resulting in biogenic speleothems that contain trace amounts of barium.

LBNM speleothems contain barium concentrations comparable to those found in Imawari Yeuta speleothems. However, approximately half of the analyzed (18) LBNM speleothems yield concentrations over 80 ppm Ba and 14 contain < 50 ppm Ba, indicating large variability in Ba content even within samples of the same morphology and no apparent relationship with silica content (**Fig.52.A**, R^2=0.0001). Elevated Ba concentrations occur in all morphologies besides gours, with polyps and coralloids most consistently exhibiting non-zero concentrations. Barium concentrations in the cave waters are also comparable to those found within the Imawari Yeuta

waters. Concentrations range from 0.9 – 14.1 µg/L, but show no correlation with dissolved Si (**Fig.52.C**, R^2=0.02). Dissolved Ba does not vary greatly among caves, with the exception of a limited collection of samples from CRI, LYO, GOL, AND SIL.

The lack of a correlation between dissolved Ba and dissolved Si may indicate a limited (or non-existent) involvement of Ba mobilization in basalt dissolution. Similarly, the lack of correlation between Ba and the elemental composition of LBNM speleothems does not strongly indicate microbial processes. Based on the available data, it is nearly impossible to disregard a primarily abiotic origin for Ba within speleothems.

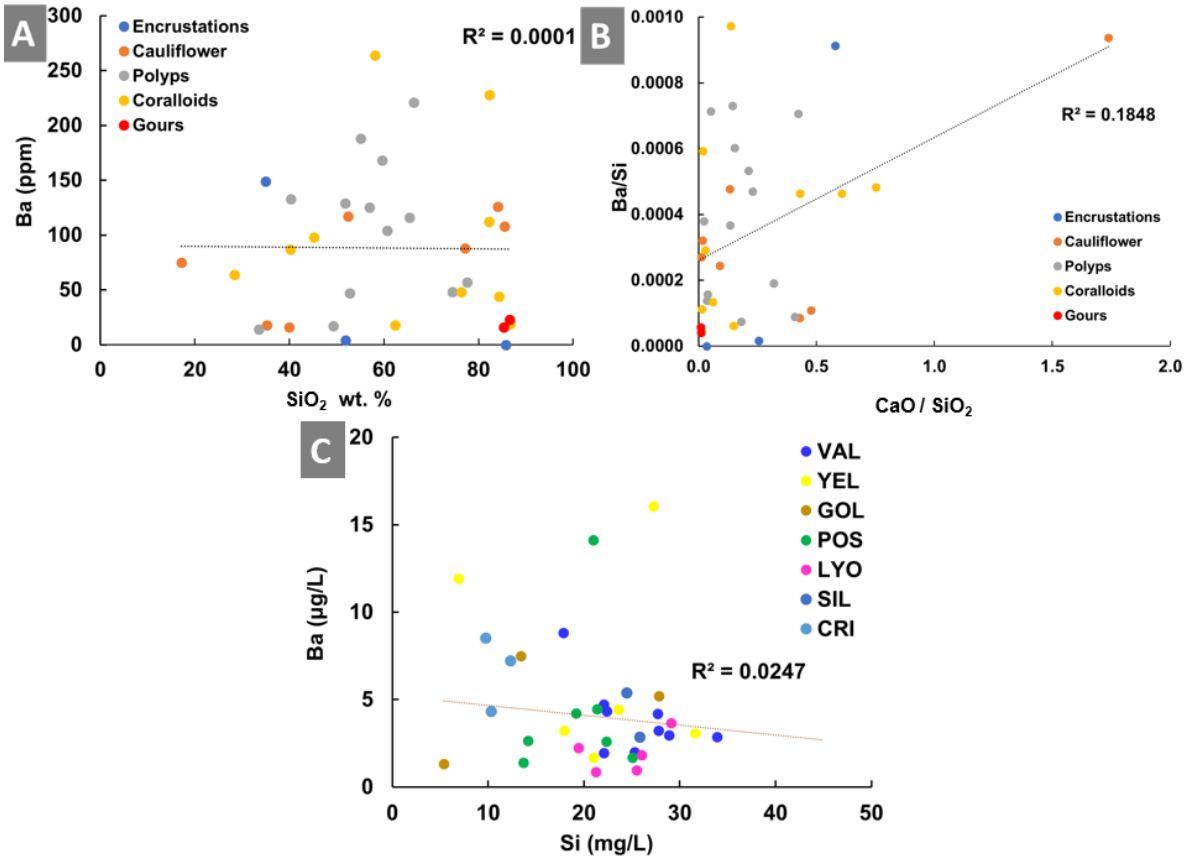

Figure 52. Ba content in speleothems and cave waters, comparing speleothem morphologies. A) Silica wt. % vs Ba (ppm), R^2 = 0.0001; B) Ba/ Si vs CaO/SiO_2. R^2= 0.18; C) Dissolved Si (mg/L) vs Ba (µg/L) among cave waters. R^2 = 0.02. A-B: Blue = crusts, Orange = cauliflower, Gray = polyps, Yellow = coralloids, Red = gours. C: Colors represent cave IDs.

5.4.3. Vanadium Content in Speleothems and Cave Waters

Vanadium is a common trace element in basaltic rocks, as V readily substitutes for Fe in in most mafic minerals. Weathering of the host basalt releases V into cave waters, at concentrations of 16.8 ± 6 μg/L (see **Fig. 37**). V is a redox-sensitive element (generally in the form of +3, +4, and +5) that is widely utilized by microbes in a variety of environments, typically for metabolic reactions. V is also observed to sorb strongly onto microbial surfaces, therefore resulting in microbial uptake of V and subsequent V concentration in associated sediments (*Huang et al., 2015*). Vanadium will commonly sorb to organic and inorganic surfaces as the oxyanion vanadate (V), rather than as a cation (*Larsson et al., 2013*). Microbes are also capable of leaching V from minerals via oxidation (*Huang et al., 2015*). Similarly, V may be incorporated into speleothems by means of V accumulators inhabiting speleothems becoming entombed. Hence, V content in secondary mineral deposits may be regarded as a potential biomarker element (*Spilde, et al., 2016*).

In speleothems, V shows a weak negative correlation with SiO_2 (**Fig.53.A,** R^2=0.40). It correlates most strongly with CaO, with the V / Si ratio increasing as the CaO / SiO_2 ratio increases (**Fig.53.B,** R^2=0.80). This relationship suggests that V is predominantly deposited during periods of calcite precipitation, likely within calcite. This, however, cannot yet be confirmed. Similar relationships are not observed between V / Si and other elements associated with basalt dissolution, including Fe, Zn, and Ti (**Table 11**). Since V is in greater concentrations than these other various elements, it is probable that some degree of accumulation (either inorganic or biogenic) is occurring within speleothems. Moreover, despite being present at relatively high concentrations compared to other trace elements within speleothems, V concentration in cave waters is low as compared to other dissolved species (**Fig.37**) and shows no correlation with Si (**Fig.53.C**, R^2=0.18). Dissolved V does not vary significantly between caves, and similarly is not reflected in

speleothem concentrations. These results can neither prove nor disprove whether V content in speleothems is due to inorganic or microbial processes.

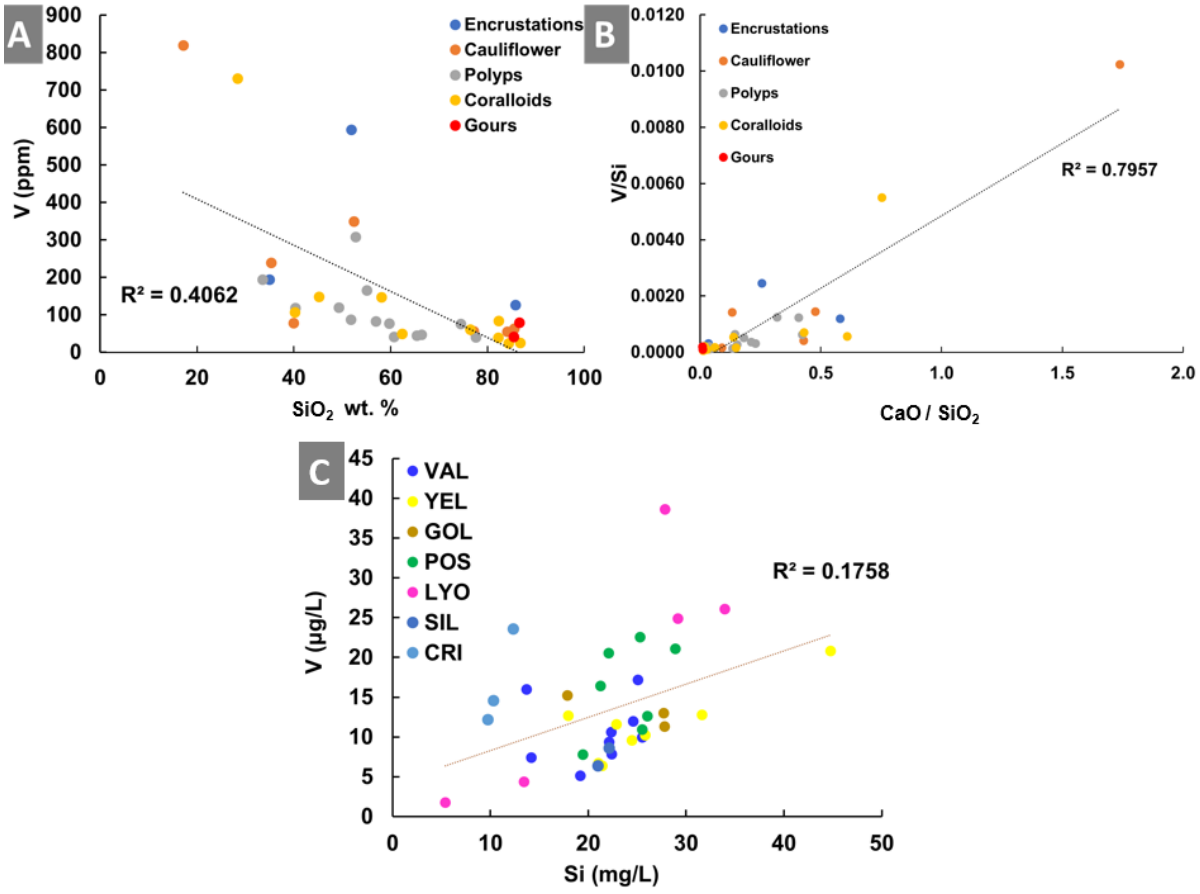

Figure 53. V content in speleothems and cave waters, comparing speleothem morphologies. A) V (ppm) vs SiO_2 wt.%, R^2=0.40; B) V/Si vs CaO/SiO_2. R^2=0.80; C) V (µg/L) vs Si (mg/L), R^2=0.18. Dotted line represents trend line. A-B: Blue = crusts, Orange = cauliflower, Gray = polyps, Yellow = coralloids, Red = gours. C: colors represent cave IDs.

5.4.4. Sulfur and Phosphorous Content in Speleothems and Cave Waters

Sulfur and phosphorous are perhaps the two elements that may most obviously be regarded as potential biosignatures, as they represent elements that are nearly ubiquitous and necessary for life. In the speleothems, sulfur shows a weak positive correlation with CaO (**Fig.54.C**, R^2=0.46) and a similarly weak negative correlation with SiO_2 (**Fig.54.A**, R^2=0.34). In accordance with their carbonate content, S concentration is highest in polyps, coralloids, and cauliflower (300-1500 ppm

in the majority of samples). Phosphorous correlates positively with CaO as shown in **Fig.54.D (**R^2=0.72), but only weakly with SiO_2 (**Fig.54.B**, R^2=0.45). The positive relationships between S vs CaO and P vs CaO are likely due to the inclusion of these two elements in calcite, as S and P (in the form of ions including SO_4^{2-} and PO_4^{3-}) can substitute for the carbonate component of calcite. During the mineralization process of carbonate speleothems, S can be oxidized to SO_4^{2-} (*Wynn et al., 2013*). Carbonate speleothems may also incorporate other forms of S, including sulfide and elemental S (*Frisia et al.,* 2012). The exact speciation of S within LBNM speleothems, however, cannot be ascertained with current data.

Dissolved S in cave waters does not correlate with dissolved Si (**Fig.54.E**, R^2=0.005), but dissolved P shows a strong positive correlation with dissolved Si (**Fig.54.F**, R^2=0.90). As mentioned previously, the majority of dissolved P likely represents organic species, as inorganic P is low in sampled waters (**Fig.39**). Therefore, the correlation between dissolved P and Si may represent microbially mediated silica dissolution of cave basalts (*Fisk et al., 1998*). However, the relationship may also represent mostly inorganic dissolution of P-bearing volcanic glass and subsequent organic transformation. As a product of late-stage mesostasis, the volcanic glass within the basalt has a greater concentration of SiO_2 and weathers more easily than the whole basalt (*Brunet and Chazot, 2001; Long and Wood, 1986; Tarrago et al., 2018*) Moreover, the concentrations of both dissolved S and P in water do not appear to vary greatly among caves, and further do not correlate with S and P_2O_5 concentrations in speleothems.

The electron microprobe data for polyp sample CRI20180731_D_12 are consistent with the above findings for sulfur: SO_3 is present in most laminae, but the highest concentrations (0.4 – 0.6 wt.%) occur primarily in laminae with high CaO contents (**Fig.30.F,B**). However, the highest CaO concentrations (> 40 wt.%) do not necessarily correlate with the highest SO_3 concentration

(> 0.4 wt.%), as can be seen by the low SO_3 concentrations in the rightmost portion of the scan area (approximately perpendicular along -13750 x) where CaO concentration is > 40 wt%. Instead, SO_3 is most prominently associated with the hummocky CaO-rich lamina near the center-left of the scan area (approximately perpendicular along both -15000 X and -14700 X). These hummocky lamina are morphologically most similar to microstromatolitic laminae, suggesting that these laminae in particular may be indicative of microbial activity. Alternatively, the sulfur content in LBNM speleothems may indicate inorganic carbonate-associated sulfate, which can come from a variety of sources, including atmospheric pollution and volcanic emissions (*Wynn et al., 2014*). Therefore, high S concentrations in hummocky lamina may be coincidental.

Interestingly, the electron microprobe data for polyp sample CRI20180731_D_12 for phosphorous do not appear to show the same correlation between P_2O_5 and CaO as shown by **Fig.53.D**. Rather than the highest P_2O_5 concentrations (4-8 wt.%) occurring throughout high CaO regions, P_2O_5 is distributed within relatively thin, discrete laminae associated with elevated SiO_2 (and often further alongside heightened MgO) (**Fig.30.D,A,C**). These P_2O_5-rich laminae predominantly occur at sharp CaO / SiO_2 boundaries—boundaries indicative of a shift between calcite and opal deposition. Furthermore, the P_2O_5-rich laminae occur at the top of CaO-rich laminae and the base of SiO_2-rich laminae, suggesting that the phosphorous deposition occurred prior to and/or during early phases of opal deposition. The P_2O_5-rich laminae may, therefore, represent corrosion surfaces indicative of lapses of mineral precipitation, upon which microbes colonized and facilitated the precipitation of phosphorous (potentially as phosphates) prior to or during the next stage of opal deposition (*Frisia et al., 2012, Jones 2009; Jones 2010; Melim et al.,2016*). The source of P precipitated within speleothems may be from the cave water itself and/or P liberated from carbonate minerals via condensation corrosion, where a moistened speleothem tip

is subject to dissolution, a process that may be most pronounced when water flow into the cave is limited (*Jones, 2009*).

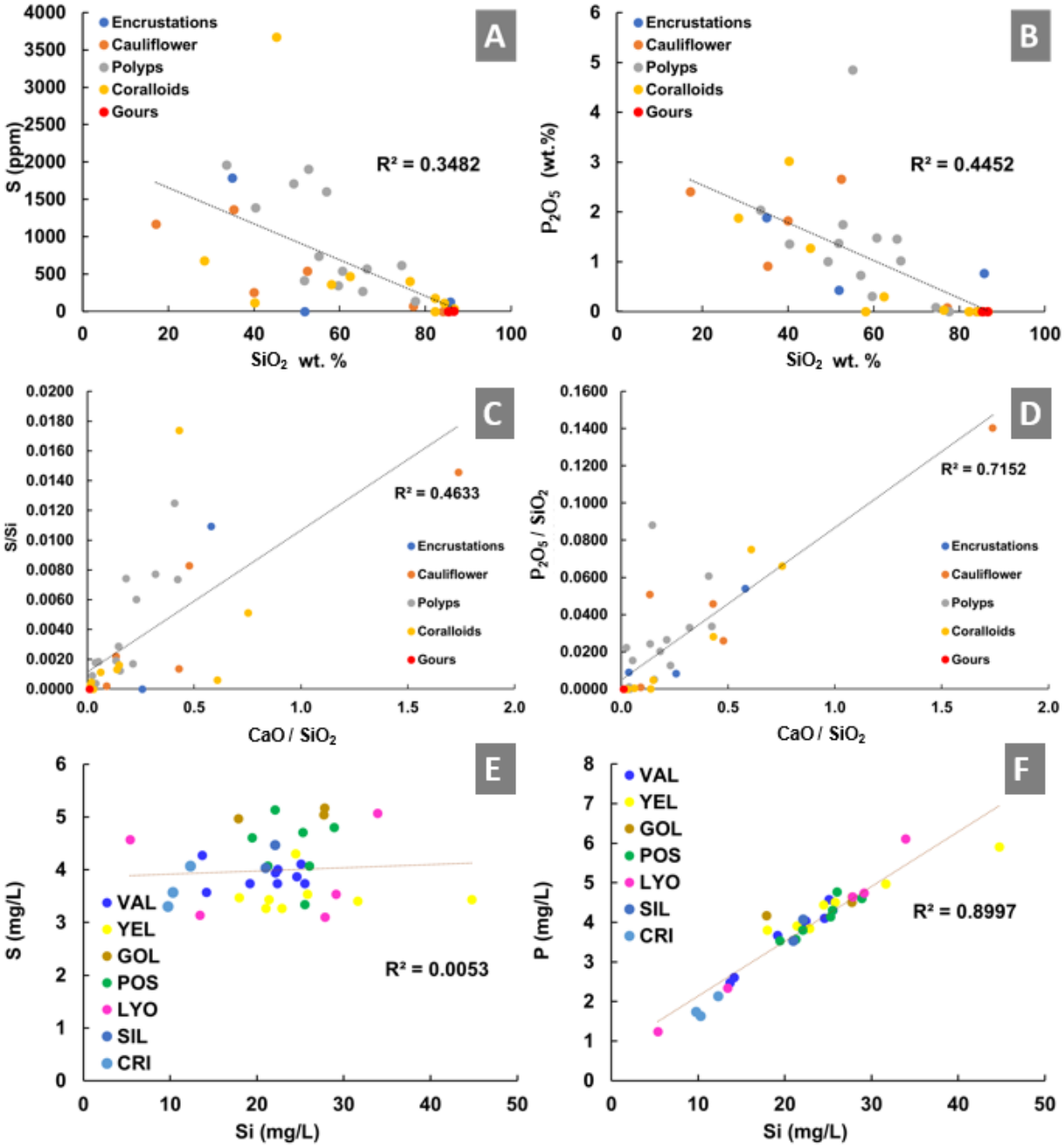

Figure 54. P and S content in speleothems and cave waters, comparing speleothem morphologies. A) S (ppm) vs SiO_2 wt.%, R^2=0.35; B) P_2O_5 wt.% vs SiO_2 wt.%, R^2=0.45; C) S/Si vs CaO/SiO_2, R^2= 0.46; D) P_2O_5/SiO_2 vs CaO/SiO_2, R^2=0.72; E) S (mg/L) vs Si (mg/L), R^2=0.005; F) P (mg/L) vs Si (mg/L); R^2=0.90. Dotted line represents trend line. A-D:Blue = crusts, Orange = cauliflower, Gray = polyps, Yellow = coralloids, Red = gours. E-F: Colors represent Cave IDs.

5.5. Relevance of Speleothem Research to the Exploration of Mars and other Planetary Bodies

Lava caves on Mars and other planetary bodies may be regarded as extreme environments: low temperatures combined with restricted energy sources (including limited light penetration), suggest that extant organisms would be akin to extremophiles (*Boston et al., 2001; Carrier et al., 2020).* The possibility also exists that Mars had an earth-like atmosphere in the past, wherein microorganisms similar to those observed in terrestrial caves may have existed (*Kite, 2019;* Fairén, *2010; McKay and Stoker, 1989*). Hence, extraterrestrial lava caves may contain speleothems, and as discussed in previous sections, may represent features mediated by passive or active microbial intervention. In regards to finding biosignatures that represent organisms that are millions of years old, the mineralogy of speleothems is important. Carbonate minerals are seen in some LBNM speleothems (crusts, cauliflower, polyps, and coralloids). Research suggests that carbonates are relatively unstable over geologic time and are prone to dissolution (*Boston et al., 2001).* Silica minerals, including opal-A, however, are far more stable than carbonate minerals and are capable of preserving biosignatures over geologic time, even if the minerals themselves are not produced by microbes (*Ehrenfreund et al., 2011; Léveillé and Datta, 2010).* The finding that LBNM speleothems are silica-dominated may therefore provide additional evidence that lava caves are capable of recording evidence of life that span over many millions of years.

6. Conclusions

Speleothems collected at Lava Beds National Monument exhibit a diverse range of morphologies, including thin crusts, bulbous cauliflower, elongate polyps, branched coralloids, and rimstone-like gours. Speleothem morphologies are similar across caves, with most morphologies represented in each cave. LBNM speleothems are predominantly comprised of amorphous opal (opal-A), and calcite (including Mg carbonate). The speleothems range from purely opaline varieties to incorporating varying amounts of calcite, as shown by varying concentrations of CaO. Speleothem composition is dominated by SiO_2, CaO, and lesser concentrations of MgO. Magnesium concentrations are greatest among CaO-rich speleothems, indicative of their Mg carbonate composition. The speleothems contain varying concentrations of the following potential biomarker elements: Cu, Ba, V, S, and P. Cu is concentrated in predominantly opaline samples, while V, S, and P increase with increasing CaO concentrations.

Microstromatolitic laminae of opal and calcite are observed in most speleothems, being most pronounced in cauliflower, polyp, and coralloid morphologies. Speleothems also exhibit porous opal laminae infilled with calcite, and concentric opal laminae. These features indicate potential microbial activity. Polyp laminae analyzed using electron microprobe confirm the presence of porous opal laminae infilled with calcite by the co-occurrence of CaO and SiO_2 concentrations within micron-scale lamina. In addition to moderate MgO concentrations within CaO-dominant lamina, elevated MgO concentrations also occur within SiO_2-dominant lamina, indicative of Mg incorporation within opal.

In addition to dissolved concentrations of Si, Na, Ca, and Mg consistent with basalt dissolution, cave waters exhibit elevated concentrations of both dissolved organic carbon, nitrate, and dissolved organic phosphorous, suggesting the prevalence of microbial processes, including

autotrophy and nitrification. Stable isotopes of cave waters also confirm the process of evaporation (and subsequent condensation) in LBNM caves, a process that may be crucial for the formation of the speleothems.

LBNM speleothems, according to the geochemical and structural evidence presented in this work, may most likely be regarded as biologically-influenced speleothems. Their formation relies on both inorganic and biological factors, with interactions between cave water, biofilms, and basalt leading to the genesis of these unique features.

Speleothem formation begins when moderately evaporated meteoric recharge water infiltrates into the caves through cave overburden, fractured basaltic cave walls and cave openings. During this process, the chemical interaction of water with the volcanic rock material results in basalt weathering and mobilizes elements such as Si, Na, K, Ca and Mg. Water then reaches a nucleation site through a combination of drips and condensation, likely an angular floor surface, collapsed roof basalt, or similar high surface-area locality. Prior to secondary mineral precipitation, weathering of the basalt nucleation surface, likely mediated by microbes, frees additional Ca, Mg, Si, and other elements into solution. During relatively wet conditions, the biofilm receives elevated concentrations of Si, binding silanol groups to cell surfaces and facilitating the precipitation of porous opal. Continuing to receive water through condensation and capillary action, microbial processes including autotrophic carbon fixation may induce carbonate mineral precipitation via an increase in pH and CO_3^{2-}. Condensative corrosion during dry periods frees P, which is precipitated prior to additional opal precipitation, possibly by microbes. The speleothems, their formation guided both by successions of wet/dry periods and repeated microbial habitation, will eventually come to appear as they are observed today.

Although the evidence presented is strongly suggestive of microbial influence in LBNM speleothem formation, further research and correlations between geochemical data and the caves' microbial inhabitants are required to more precisely determine the exact nature of the microbial processes affecting secondary mineral precipitation. Several further research directions exist to achieve these goals: analysis of speleothem organic content, acid-etching of thin sections to reveal possible microbial structures, and analysis by synchrotron-aided spectroscopy to determine speciation and coordination chemistry of potential biomarker elements, including V, S, and P. Speciation and coordination chemistry of P in speleothems in particular will provide valuable insights into the microbial processes potentially responsible for precipitating P atop calcite-dominant lamina. These findings will be crucial to more definitively classify LBNM speleothems as biosignature features, and will contribute to the understanding of biological phenomena that may be identified in resource-restricted cave environments.

References

Adam, D.P., Sarna-Wojcicki, A.M., Rieck, H.J., Bradbury, J.P., Dean, W.E. and Forester, R.M., 1989. Tulelake, California: the last 3 million years. *Palaeogeography, Palaeoclimatology, Palaeoecology*, *72*, pp.89-103.

Applegate, E.I., 1938. Plants of the Lava Beds National Monument, California. *American Midland Naturalist*, *19*(2), pp.334-368.

Atkinson, T.C., 1983. Growth mechanisms of speleothems in castleguard cave, Columbia Icefields, Alberta, Canada. *Arctic and Alpine Research*, *15*(4), pp.523-536

Aubrecht, R., Brewer-Carías, C., Šmída, B., Audy, M. and Kováčik, Ľ., 2008. Anatomy of biologically mediated opal speleothems in the World's largest sandstone cave: Cueva Charles Brewer, Chimantá Plateau, Venezuela. *Sedimentary Geology*, *203*(3-4), pp.181-195. http://doi.org/10.1016/j.sedgeo.2007.10.005

Baker, M.B., Grove, T.L., Kinzler, R.J., Donnelly-Nolan, J.M. and Wandless, G.A., 1991. Origin of compositional zonation (high-alumina basalt to basaltic andesite) in the Giant Crater Lava Field, Medicine Lake Volcano, northern California. *Journal of Geophysical Research: Solid Earth*, *96*(B13), pp.21819-21842.

Baldini, J.U.L., McDermott, F. and Fairchild, I.J., 2006. Spatial variability in cave drip water hydrochemistry: Implications for stalagmite paleoclimate records. *Chemical Geology*, *235*(3-4), pp.390-404.

Barton, H., 2009. Surface analysis of the role of pyoverdin siderophores in Pseudomonas aeruginosa biofilm formation on metal oxides.

Bennett, P.C., 1991. Quartz dissolution in organic-rich aqueous systems. *Geochimica et Cosmochimica Acta*, *55*(7), pp.1781-1797.

Blank, J.G., Agha-mohammadi, A., Bell, E.R., Crown, D.A., Morrell, B., Patterson, C.J.S., Uckert, K., Whelley, P.L., 2020. Volcanic Caves as Priority Sites for Astrobiology Science. Submitted to *the Decadal Survey on Planetary Science & Astrobiology*.

Boston, P.J., Spilde, M.N., Northup, D.E., Melim, L.A., Soroka, D.S., Kleina, L.G., Lavoie, K.H., Hose, L.D., Mallory, L.M., Dahm, C.N. and Crossey, L.J., 2001. Cave biosignature suites: microbes, minerals, and Mars. *Astrobiology*, *1*(1), pp.25-55.

Brunet, D.R. and Revuelta, M.Á., 2014. Exceptional silica speleothems in a volcanic cave: A unique example of silicification and sub-aquatic opaline stromatolite formation (T erceira, A zores). *Sedimentology*, *61*(7), pp.2113-2135.

Brunet, F. and Chazot, G., 2001. Partitioning of phosphorus between olivine, clinopyroxene and silicate glass in a spinel lherzolite xenolith from Yemen. *Chemical Geology*, *176*(1-4), pp.51-72.

Cady, S.L. and Farmer, J.D., 1996, January. Fossilization processes in siliceous thermal springs: trends in preservation along thermal gradients. In *Ciba Foundation Symposium* (pp. 150-173). John Wiley & Sons Ltd.

Campbell, K.A., Guido, D.M., Gautret, P., Foucher, F., Ramboz, C. and Westall, F., 2015. Geyserite in hot-spring siliceous sinter: Window on Earth's hottest terrestrial (paleo) environment and its extreme life. *Earth-Science Reviews*, *148*, pp.44-64.

Carrier, B.L., Beaty, D.W., Meyer, M.A., Blank, J.G., Chou, L., DasSarma, S., Des Marais, D.J., Eigenbrode, J.L., Grefenstette, N., Lanza, N.L. and Schuerger, A.C., 2020. Mars Extant Life: What's Next? Conference Report.

Chen, J., Zhang, D.D., Wang, S., Xiao, T. and Huang, R., 2004. Factors controlling tufa deposition in natural waters at waterfall sites. *Sedimentary Geology*, *166*(3-4), pp.353-366.

Cody, A., 1980. Stalagmitic deposits in Auckland lava caves. N.Z. Speleol. Bull., vol. 6, pp. 337-343.

Cuevas-González, J., Fernández-Cortés, A., Muñoz-Cervera, M.C., Benavente, D., del Cura, M.G., Andreu, J.M. and Cañaveras, J.C., 2010. Mineral-forming processes at Canelobre cave (Alicante, SE Spain). In *Advances in Research in Karst Media* (pp. 503-508). Springer, Berlin, Heidelberg.

Cushing, G.E., 2012. Candidate cave entrances on Mars. *Journal of Cave and Karst Studies, 74*(1), pp. 33-47.

Dansgaard, W., 1964. Stable isotopes in precipitation. *Tellus, 16*(4), pp.436-468.

De Freitas, C.R. and Schmekal, A., 2003. Condensation as a microclimate process: measurement, numerical simulation and prediction in the Glowworm Cave, New Zealand. *International Journal of Climatology: A Journal of the Royal Meteorological Society*, *23*(5), pp.557-575.

De los Ríos, A., Bustillo, M.A., Ascaso, C. and Carvalho, M.D.R., 2011. Bioconstructions in ochreous speleothems from lava tubes on Terceira Island (Azores). *Sedimentary Geology*, *236*(1-2), pp.117-128.

Diaz, M.R. and Eberli, G.P., 2019. Decoding the mechanism of formation in marine ooids: A review. *Earth-Science Reviews, 190*, pp.536-556.

Donnelly-Nolan, J.M. and Champion, D.E., 1987. *Geologic map of Lava Beds National Monument, northern California* (No. 1804).

Donnelly-Nolan, J.M., Champion, D.E., Miller, C.D., Grove, T.L. and Trimble, D.A., 1990. Post-11,000-year volcanism at Medicine Lake Volcano, Cascade Range, northern California. *Journal of Geophysical Research: Solid Earth, 95*(B12), pp.19693-19704.

Donnelly-Nolan, J.M. and Grove, T.L., 2017. *Geologic field-trip guide to Medicine Lake Volcano, northern California, including Lava Beds National Monument* (No. 2017-5022-K1). US Geological Survey.

Donnelly-Nolan, J.M., 2010, Geologic map of Medicine Lake volcano, northern California: U.S. Geological Survey Scientific Investigations Map 2927, pamphlet 48 p., 2 sheets, scale 1:50,000, https://pubs.usgs.gov/sim/2927/.

Dontsova, K., Zaharescu, D., Henderson, W., Verghese, S., Perdrial, N., Hunt, E. and Chorover, J., 2014. Impact of organic carbon on weathering and chemical denudation of granular basalt. *Geochimica et Cosmochimica Acta*, *139*, pp.508-526.

Dove, P.M. and Nix, C.J., 1997. The influence of the alkaline earth cations, magnesium, calcium, and barium on the dissolution kinetics of quartz. *Geochimica et Cosmochimica Acta*, *61*(16), pp.3329-3340.

Du Preez, G.C., Jacobs, G., Jordaan, A., Tiedt, L.R. and Forti, P., 2015. Hairy Stalagmites, a new biogenic root speleothem from Botswana.

Ehrenfreund, P., Thiel, C.S., Quinn, R., Sephton, M.A., Stoker, C., Kotler, J.M., Direito, S.O.L., Martins, Z., Orzechowska, G.E., Kidd, R.D. and van Sluis, C.A., 2011. Astrobiology and habitability studies in preparation for future Mars missions: trends from investigating minerals, organics and biota. *International Journal of Astrobiology*, *10*(3), p.239.

Eick, M.J., Sparks, D.L., Bar-Tal, A. and Feigenbaum, S., 1990. Analyses of Adsorption Kinetics Using a Stirred-Flow Chamber: II. Potassium-Calcium Exchange on Clay Minerals. *Soil Science Society of America Journal*, *54*(5), pp.1278-1282.

Elzea, J.M. and Rice, S.B., 1996. TEM and X-ray diffraction evidence for cristobalite and tridymite stacking sequences in opal. *Clays and Clay Minerals*, *44*(4), pp.492-500.

Engel, A.S., Lichtenberg, H., Prange, A. and Hormes, J., 2007. Speciation of sulfur from filamentous microbial mats from sulfidic cave springs using X-ray absorption near-edge spectroscopy. *FEMS microbiology letters*, *269*(1), pp.54-62. http://doi.org/10.1111/j.1574-6968.2006.00600.x

Engel, A.S., Megan L. Porter, Brian K. Kinkle, Thomas C. Kane, A., 2001. Ecological assessment and geological significance of microbial communities from Cesspool Cave, Virginia. *Geomicrobiology Journal*, *18*(3), pp.259-274.

Fairchild, I.J. and McMillan, E.A., 2007. Speleothems as indicators of wet and dry periods. *International Journal of Speleology*, *36*(2), p.2.

Fairchild, I.J., Baker, A., Borsato, A., Frisia, S., Hinton, R.W., McDERMOTT, F.R.A.N.K. and Tooth, A.F., 2001. Annual to sub-annual resolution of multiple trace-element trends in speleothems. *Journal of the Geological Society*, *158*(5), pp.831-841.

Fairchild, I.J., Borsato, A., Tooth, A.F., Frisia, S., Hawkesworth, C.J., Huang, Y., McDermott, F. and Spiro, B., 2000. Controls on trace element (Sr–Mg) compositions of carbonate cave waters: implications for speleothem climatic records. *Chemical Geology*, *166*(3-4), pp.255-269.

Fairén, A.G., 2010. A cold and wet Mars. *Icarus*, *208*(1), pp.165-175

Fisk, M.R., Giovannoni, S.J. and Thorseth, I.H., 1998. Alteration of oceanic volcanic glass: textural evidence of microbial activity. *Science*, *281*(5379), pp.978-980.

Forti, P., 2001. Biogenic speleothems: an overview. *International Journal of Speleology*, *30*(1), p.4.

Forti, P., 2005. Genetic processes of cave minerals in volcanic environments: an overview. *Journal of cave and Karst Studies*, *67*(1), pp.3-13.

Frisia, S., 2014. Microstratigraphic logging of calcite fabrics in speleothems as tool for palaeoclimate studies. *International Journal of Speleology*, *44*(1), p.1.

Frisia, S., Borsato, A., Drysdale, R.N., Paul, B., Greig, A. and Cotte, M., 2012. A re-evaluation of the palaeoclimatic significance of phosphorus variability in speleothems revealed by high-resolution synchrotron micro XRF mapping. *Climate of the Past*, *8*(6).

Frisia, S., Borsato, A., Fairchild, I.J. and McDermott, F., 2000. Calcite fabrics, growth mechanisms, and environments of formation in speleothems from the Italian Alps and southwestern Ireland. *Journal of Sedimentary Research*, *70*(5), pp.1183-1196.

Gannett, M.W., Lite, K.E., La Marche, J.L., Fisher, B.J. and Polette, D.J., 2007. *Ground-water hydrology of the upper Klamath basin, Oregon and California*. U. S. Geological Survey.

Gat, J.R., 1996. Oxygen and hydrogen isotopes in the hydrologic cycle. *Annual Review of Earth and Planetary Sciences*, *24*(1), pp.225-262.

González-Munoz, M.T., Fernández-Luque, B., Martínez-Ruiz, F., Chekroun, K.B., Arias, J.M., Rodríguez-Gallego, M., Martínez-Canamero, M., De Linares, C. and Paytan, A., 2003. Precipitation of barite by Myxococcus xanthus: possible implications for the biogeochemical cycle of barium. *Appl. Environ. Microbiol.*, *69*(9), pp.5722-5725.

Gonzalez-Muñoz, M.T., Martinez-Ruiz, F., Morcillo, F., Martin-Ramos, J.D. and Paytan, A., 2012. Precipitation of barite by marine bacteria: a possible mechanism for marine barite formation. *Geology*, *40*(8), pp.675-678.

Gonzalez-Pimentel, J.L., Miller, A.Z., Jurado, V., Laiz, L., Pereira, M.F. and Saiz-Jimenez, C., 2018. Yellow coloured mats from lava tubes of La Palma (Canary Islands, Spain) are dominated by metabolically active Actinobacteria. *Scientific reports*, *8*(1), pp.1-11.

Gounelle, M., Chaussidon, M., Morbidelli, A., Barrat, J.A., Engrand, C., Zolensky, M.E. and McKeegan, K.D., 2009. A unique basaltic micrometeorite expands the inventory of solar system planetary crusts. *Proceedings of the National Academy of Sciences*, *106*(17), pp.6904-6909.

Greeley, R. and Hyde, J.H., 1972. Lava tubes of the cave basalt, Mount St. Helens, Washington. *Geological Society of America Bulletin*, *83*(8), pp.2397-2418.

Guido, D.M. and Campbell, K.A., 2014. A large and complete Jurassic geothermal field at Claudia, Deseado massif, Santa Cruz, Argentina. *Journal of Volcanology and Geothermal Research*, *275*, pp.61-70.

Haberle, R.M., McKay, C.P., Schaeffer, J., Cabrol, N.A., Grin, E.A., Zent, A.P. and Quinn, R., 2001. On the possibility of liquid water on present-day Mars. *Journal of Geophysical Research: Planets*, *106*(E10), pp.23317-23326.

Hamilton, A.R., Campbell, K.A., Guido, D.M., 2019. Atlas of siliceous hot spring deposits (sinter) and other silicified surface manifestations in epithermal environments. Lower Hutt (NZ): *GNS Science*. 56 p. (GNS Science report; 2019/06). doi: 10.21420/BQDR-XQ16.

Harmon, R.S., Atkinson, T.C. and Atkinson, J.L., 1983. The mineralogy of Castleguard Cave, Columbia Icefields, Alberta, Canada. *Arctic and Alpine Research*, *15*(4), pp.503-516.

Hotchkiss, W.R., 1968. *A geologic and hydrologic reconnaissance of Lava Beds National Monument and vicinity, California* (No. 68-140). US Dept. of the Interior, Geological Survey, Water Resources Division.

Howarth, F.G., James, S.A., McDowell, W., Preston, D.J. and Imada, C.T., 2007. Identification of roots in lava tube caves using molecular techniques: implications for conservation of cave arthropod faunas. *Journal of Insect Conservation*, *11*(3), pp.251-261.

Huang, J.H., Huang, F., Evans, L. and Glasauer, S., 2015. Vanadium: Global (bio) geochemistry. *Chemical Geology*, *417*, pp.68-89.

Jones, B. and Renaut, R.W., 2003. Hot spring and geyser sinters: the integrated product of precipitation, replacement, and deposition. *Canadian Journal of Earth Sciences*, *40*(11), pp.1549-1569.

Jones, B., 2009. Phosphatic precipitates associated with actinomycetes in speleothems from Grand Cayman, British West Indies. *Sedimentary Geology*, *219*(1-4), pp.302-317.

Jones, B., 2010. Speleothems in a wave-cut notch, Cayman Brac, British West Indies: the integrated product of subaerial precipitation, dissolution, and microbes. *Sedimentary Geology*, *232*(1-2), pp.15-34.

Kempe, S., 2019. Volcanic rock caves. In *Encyclopedia of Caves* (pp. 1118-1127). Academic Press.

Kendall, A.C. and Broughton, P.L., 1978. Origin of fabrics in speleothems composed of columnar calcite crystals. *Journal of Sedimentary Research*, *48*(2), pp.519-538.

Keszthelyi, L., Jaeger, W., McEwen, A., Tornabene, L., Beyer, R.A., Dundas, C. and Milazzo, M., 2008. High Resolution Imaging Science Experiment (HiRISE) images of volcanic terrains from the first 6 months of the Mars Reconnaissance Orbiter primary science phase. *Journal of Geophysical Research: Planets*, *113*(E4). http://doi.org/10.1029/2007JE002968

Kite, E.S., 2019. Geologic constraints on early Mars climate. *Space Science Reviews*, *215*(1), p.10.

Konhauser, K.O., Jones, B., Phoenix, V.R., Ferris, G. and Renaut, R.W., 2004. The microbial role in hot spring silicification. *AMBIO: A Journal of the Human Environment*, *33*(8), pp.552-558.

Lacroix, B., Charpentier, D., Buatier, M., Vennemann, T., Labaume, P., Adatte, T., Travé, A. and Dubois, M., 2012. Formation of chlorite during thrust fault reactivation. Record of fluid origin and P–T conditions in the Monte Perdido thrust fault (southern Pyrenees). *Contributions to Mineralogy and Petrology*, *163*(6), pp.1083-1102. https://doi.org/10.1007/s00410-011-0718-0

Lanza, N.L., Fischer, W.W., Yeager, C., Lingappa, U., Ollila, A.M., Gasda, P.J., Lamm, S.N., Salvatore, M., Clegg, S.M., and Wiens, R.C. (2019) Targeting manganese minerals on Mars as potential biosignatures [abstract 5035]. In *Mars Extant Life: What's Next? Conference Abstracts*, Lunar and Planetary Institute, Houston. Available online at https://www.hou.usra.edu/meetings/lifeonmars2019/pdf/5035.pdf

Larsson, M.A., Baken, S., Gustafsson, J.P., Hadialhejazi, G. and Smolders, E., 2013. Vanadium bioavailability and toxicity to soil microorganisms and plants. *Environmental toxicology and chemistry*, *32*(10), pp.2266-2273.

Lavoie, K.H., Northup, D.E. and Barton, H.A., 2010. Microbe–mineral interactions: cave geomicrobiology. *Geomicrobiology*, pp.1-45.

Lavoie, K.H., Winter, A.S., Read, K.J., Hughes, E.M., Spilde, M.N. and Northup, D.E., 2017. Comparison of bacterial communities from lava cave microbial mats to overlying surface soils from Lava Beds National Monument, USA. *PloS one*, *12*(2).

Legatzki, A., Ortiz, M., Neilson, J.W., Dominguez, S., Andersen, G.L., Toomey, R.S., Pryor, B.M., Pierson III, L.S. and Maier, R.M., 2011. Bacterial and archaeal community structure of two adjacent calcite speleothems in Kartchner Caverns, Arizona, USA. *Geomicrobiology Journal*, *28*(2), pp.99-117.

Léveillé, R.J, 2010. A half-century of terrestrial analog studies: from craters on the Moon to searching for life on Mars. *Planetary and Space Science*, *58*(4), pp.631-638.

Léveillé, R.J. and Datta, S., 2010. Lava tubes and basaltic caves as astrobiological targets on Earth and Mars: a review. *Planetary and Space Science*, 58(4), pp.592-598. https://doi.org/10.1016/j.pss.2009.06.004

Léveillé, R.J., Fyfe, W.S. and Longstaffe, F.J., 2000. Geomicrobiology of carbonate–silicate microbialites from Hawaiian basaltic sea caves. *Chemical Geology*, *169*(3-4), pp.339-355. https://doi.org/10.1016/S0009-2541(00)00213-8

Léveillé, R.J., Longstaffe, F.J. and Fyfe, W.S., 2002. Kerolite in carbonate-rich speleothems and microbial deposits from basaltic caves, Kauai, Hawaii. *Clays and Clay Minerals*, *50*(4), pp.514-524.

Long, P.E. and Wood, B.J., 1986. Structures, textures, and cooling histories of Columbia River basalt flows. *Geological Society of America Bulletin*, *97*(9), pp.1144-1155.

López-Martínez, R., Barragán, R., Beraldi-Campesi, H., Lánczos, T., Vidal-Romaní, J.R., Aubrecht, R., Bernal Uruchurtu, J.P., Pi Puig, T. and Espinasa-Pereña, R., 2016. Morphological and mineralogical characterization of speleothems from the Chimalacatepec lava tube system, Central Mexico. *International Journal of Speleology*, *45*(2), p.2.

Luis-Vargas, M.N., López-Martínez, R.A., Vilchis-Nestor, A.R., Daza, R. and Alcántara-Hernández, R.J., 2019. Bacterial Insights into the Formation of Opaline Stromatolites from the Chimalacatepec Lava Tube System, Mexico. *Geomicrobiology Journal*, *36*(8), pp.694-704.

Macalady, J.L., Dattagupta, S., Schaperdoth, I., Jones, D.S., Druschel, G.K. and Eastman, D., 2008. Niche differentiation among sulfur-oxidizing bacterial populations in cave waters. *The ISME Journal*, *2*(6), pp.590-601.

Makreski, P., Jovanovski, G., Stafilov, T. and Boev, B., 2004. Minerals from Macedonia XII. The dependence of quartz and opal color on trace element composition-AAS, FT IR and MICRO-RAMAN spectroscopy study. *Bulletin of the Chemists and Technologists of Macedonia*, *23*(2), pp.171-184.

Mapelli, F., Marasco, R., Balloi, A., Rolli, E., Cappitelli, F., Daffonchio, D. and Borin, S., 2012. Mineral–microbe interactions: biotechnological potential of bioweathering. *Journal of Biotechnology*, *157*(4), pp.473-481.

Martin-Torres, F.J., Zorzano, M.P., Valentín-Serrano, P., Harri, A.M., Genzer, M., Kemppinen, O., Rivera-Valentin, E.G., Jun, I., Wray, J., Madsen, M.B. and Goetz, W., 2015. Transient liquid water and water activity at Gale crater on Mars. *Nature Geoscience*, *8*(5), pp.357-361.

McKay, C.P. and Stoker, C.R., 1989. The early environment and its evolution on Mars: Implication for life. *Reviews of Geophysics*, *27*(2), pp.189-214.

McRose, D.L., Zhang, X., Kraepiel, A.M. and Morel, F.M., 2017. Diversity and activity of alternative nitrogenases in sequenced genomes and coastal environments. *Frontiers in microbiology*, *8*, p.267.

Melim, L.A. and Spilde, M.N., 2018. A New Unified Model For Cave Pearls: Insights from Cave Pearls in Carlsbad Cavern, New Mexico, USA. *Journal of Sedimentary Research*, *88*(3), pp.344-364.

Melim, L.A., Northup, D.E., Boston, P.J. and Spilde, M.N., 2016. Preservation of fossil microbes and biofilm in cave pool carbonates and comparison to other microbial carbonate environments. *Palaios*, *31*(4), pp.177-189.

Miller, A.Z., Dionísio, A., Braga, M.S., Hernández-Mariné, M., Afonso, M.J., Muralha, V.S.F., Herrera, L.K., Raabe, J., Fernandez-Cortes, A., Cuezva, S. and Hermosin, B., 2012. Biogenic Mn oxide minerals coating in a subsurface granite environment. *Chemical Geology*, *322*, pp.181-191. http://doi.org/10.1016/j.chemgeo.2012.07.005

Miller, A.Z., Pereira, M.F., Calaforra, J.M., Forti, P., Dionísio, A. and Saiz-Jimenez, C., 2014. Siliceous speleothems and associated microbe-mineral interactions from Ana Heva Lava Tube in Easter Island (Chile). *Geomicrobiology Journal*, *31*(3), pp.236-245.

Miranda, C.D. and Rojas, R., 2006. Copper accumulation by bacteria and transfer to scallop larvae. *Marine pollution bulletin*, *52*(3), pp.293-300.

Moore, D.M. and Reynolds, R.C., 1989. *X-ray Diffraction and the Identification and Analysis of Clay Minerals* (Vol. 322, p. 321). Oxford: Oxford university press.

Nelson, B.C. and Smith, C.R., 1976. Ecological effects of a plague epizootic on the activities of rodents inhabiting caves at Lava Beds National Monument, California. *Journal of Medical Entomology*, *13*(1), pp.51-61.

Northup, D.E. and Lavoie, K.H., 2001. Geomicrobiology of caves: a review. *Geomicrobiology journal*, 18(3), pp.199-222. http://doi.org/10.1080/01490450152467750

Northup, D.E., Barns, S.M., Yu, L.E., Spilde, M.N., Schelble, R.T., Dano, K.E., Crossey, L.J., Connolly, C.A., Boston, P.J., Natvig, D.O. and Dahm, C.N., 2003. Diverse microbial communities inhabiting ferromanganese deposits in Lechuguilla and Spider Caves. *Environmental Microbiology*, *5*(11), pp.1071-1086. http://doi.org/10.1046/j.1462-2920.2003.00500.x

Northup, D.E., Hathaway, J.J., Snider, J.R., Balasch, M.M., Garcia, M.G., Dapkevicius, M.L.E., Gabriel, C.R., Stone, F.D., Spilde, M.N. and Boston, P.J., 2012. Life in Earth's lava caves: implications for life detection on other planets. In *Life on Earth and other Planetary Bodies* (pp. 459-484). Springer, Dordrecht.

Northup, D.E., Hathaway, J.J.M., Spilde, M.N., Moser, D.P., and Blank, J.G., 2019. Investigating the mineral:microbe continuum in lava caves to enhance selection of life detection targets [abstract 5037]. In *Mars Extant Life: What's Next? Conference Abstracts*, Lunar and Planetary Institute, Houston. Available online at https://www.hou.usra.edu/meetings/ lifeonmars2019/pdf/5037.pdf

Northup, D.E., Melim, L.A., Spilde, M.N., Hathaway, J.J.M., Garcia, M.G., Moya, M., Stone, F.D., Boston, P.J., Dapkevicius, M.L.N.E. and Riquelme, C., 2011. Lava cave microbial communities within mats and secondary mineral deposits: implications for life detection on other planets. *Astrobiology*, *11*(7), pp.601-618. http://doi.org/10.1089/ast.2010.0562

Northup, D.E., Reysenbach, A.L. and Pace, N.R., 1997. Microorganisms and speleothems. *Cave minerals of the world*, pp.261-266.

Orange, F., Lalonde, S.V. and Konhauser, K.O., 2013. Experimental simulation of evaporation-driven silica sinter formation and microbial silicification in hot spring systems. *Astrobiology*, *13*(2), pp.163-176.

Peng, X. and Jones, B., 2012. Rapid precipitation of silica (opal-A) disguises evidence of biogenicity in high-temperature geothermal deposits: case study from Dagunguo hot spring, China. *Sedimentary Geology*, *257*, pp.45-62. http://doi.org/10.1016/j.sedgeo.2012.01.013

Pontefract, A., Zhu, T.F., Walker, V.K., Hepburn, H., Lui, C., Zuber, M.T., Ruvkun, G. and Carr, C.E., 2017. Microbial diversity in a hypersaline sulfate lake: a terrestrial analog of ancient Mars. *Frontiers in microbiology*, *8*, p.1819.

Popa, R., Smith, A.R., Boone, J. and Fisk, M., 2012. Olivine-respiring bacteria isolated from the rock-ice interface in a lava-tube cave, a Mars analog environment. *Astrobiology*, *12*(1), pp.9-18. http://doi.org/10.1089/ast.2011.0639

Poppe, L.J., Paskevich, V.F., Hathaway, J.C. and Blackwood, D.S., 2001. A laboratory manual for X-ray powder diffraction. *US Geological Survey Open-File Report*, *1*(041), pp.1-88. https://doi.org/10.3133/ofr0141

Prieto-Ballesteros, O., Rodríguez, N., Kargel, J.S., Kessler, C.G., Amils, R. and Remolar, D.F., 2003. Tirez lake as a terrestrial analog of Europa. *Astrobiology*, *3*(4), pp.863-877.

Robins, C.R., Deurlington, A., Buck, B.J. and Brock-Hon, A.L., 2015. Micromorphology and formation of pedogenic ooids in calcic soils and petrocalcic horizons. *Geoderma*, *251*, pp.10-23.

Renaut, R.W. and Jones, B., 2011. Hydrothermal environments, terrestrial. In *Encyclopedia of geobiology*.

Rogers, B.W. and Rice, P.H., 1991. Geology and Mineralogy of Lava Tube Caves in Medicine Lake Volcano, California. *Cave Research Foundation Annual Report*, pp.25-31.

Romaní, J., Sanjurjo Sánchez, J., Rodríguez, M. and Fernández Mosquera, D., 2010. Speleothem development and biological activity in granite cavities. *Geomorphologie: relief, processus, environnement*, *16*(4), pp.337-346.

Samanovic, M.I., Ding, C., Thiele, D.J. and Darwin, K.H., 2012. Copper in microbial pathogenesis: meddling with the metal. *Cell host & microbe*, *11*(2), pp.106-115.

Sanchez-Moral, S., Luque, L., Cañaveras, J.C., Laiz, L., Jurado, V., Hermosin, B. and Saiz-Jimenez, C., 2004. Bioinduced barium precipitation in St. Callixtus and Domitilla catacombs. *Annals of Microbiology*, *54*(1), pp.1-12.

Sauro, F., Tisato, N., De Waele, J., Bernasconi, S.M., Bontognali, T.R. and Galli, E., 2014. Source and genesis of sulphate and phosphate–sulphate minerals in a quartz-sandstone cave environment. *Sedimentology*, *61*(5), pp.1433-1451.

Sauro, F., Cappelletti, M., Ghezzi, D., Columbu, A., Hong, P.Y., Zowawi, H.M., Carbone, C., Piccini, L., Vergara, F., Zannoni, D. and De Waele, J., 2018. Microbial diversity and biosignatures of amorphous silica deposits in orthoquartzite caves. *Scientific reports*, *8*(1), pp.1-14.

Sodo, A., Casanova Municchia, A., Barucca, S., Bellatreccia, F., Della Ventura, G., Butini, F. and Ricci, M.A., 2016. Raman, FT-IR and XRD investigation of natural opals. *Journal of Raman Spectroscopy*, *47*(12), pp.1444-1451.

Spilde, M.N., Northup, D.E., Caimi, N.A., Boston, P.J., Stone, F.D. and Smith, S., 2016. Microbial mats communities in Hawaiian lava caves. In *Proc 16th Int Symp Vucanospeleo*. http://doi.org/ 10.1130/abs/2016AM-283965

Spilde, M.N., Medley, J.J., Northup, D.E., and Boston, P.J., 2019. Biomarkers in lava caves: an analog for the search for life on Mars [abstract 5036]. In *Mars Extant Life: What's Next? Conference Abstracts*, Lunar and Planetary Institute, Houston. Available online at https://www.hou.usra.edu/meetings/ lifeonmars2019/pdf/5036.pdf

Stevens, T., 1997. Lithoautotrophy in the subsurface. *FEMS Microbiology Reviews*, *20*(3-4), pp.327-337.

Swartzlow, C.R. and Keller, W.D., 1937. Coralloidal opal. *The Journal of Geology*, *45*(1), pp.101-108.

Tarrago, M., Garcia-Valles, M., Martínez, S. and Neuville, D.R., 2018. Phosphorus solubility in basaltic glass: Limitations for phosphorus immobilization in glass and glass-ceramics. *Journal of environmental management*, *220*, pp.54-64.

Taylor, S.J. and Krejca, J.J., 2006. *A biological assessment of caves in Lava Beds National Monument*. Illinois Natural History Survey.

Teehera, K.B., Jungbluth, S.P., Onac, B.P., Acosta-Maeda, T.E., Hellebrand, E., Misra, A.K., Pflitsch, A., Rappé, M.S., Smith, S.M., Telus, M. and Schorghofer, N., 2018. Cryogenic minerals in Hawaiian Lava Tubes: a geochemical and microbiological exploration. *Geomicrobiology Journal*, *35*(3), pp.227-241.

Tremaine, D.M. and Froelich, P.N., 2013. Speleothem trace element signatures: A hydrologic geochemical study of modern cave dripwaters and farmed calcite. *Geochimica et Cosmochimica Acta*, *121*, pp.522-545.

Turner, K., 2002. Chromophores producing blue speleothems at Cliefden, NSW. *Helictite*, *38*(1), pp.3-6.

Urbani, F., Compère, P. and Willems, L., 2005. Opal-A speleothems of Wei-Assipu-tepui, Roraima Province, Brazil. *Boletín de la Sociedad Venezolana de Espeleología*, *39*.

Urusov, V.S., Shvanskaya, L.V., Bychkov, A.Y., Mokhov, A.V. and Labutova, E.A., 2008. Microstructure investigations of Kamchatka geyserites. *Moscow University Geology Bulletin*, *63*(5), p.311.

Vanghi, V., Frisia, S. and Borsato, A., 2017. Genesis and microstratigraphy of calcite coralloids analysed by high resolution imaging and petrography. *Sedimentary Geology*, *359*, pp.16-28.

Varnedoe Jr, W.W., 1965. A hypothesis for the formation of rimstone dams and gours. *Bulletin of the National Speleological Society*, *27*(4), pp.151-152.

Walker, D., Stolper, E.M. and Hays, J.F., 1979. Basaltic volcanism-The importance of planet size. In *Lunar and Planetary Science Conference Proceedings* (Vol. 10, pp. 1995-2015).

Waters, A.C., Donnelly-Nolan, J.M. and Rogers, B.W., 1990. Selected caves and lava-tube systems in and near Lava Beds National Monument, California.

Webb, G.E. and Kamber, B.S., 2011. Trace element Geochemistry as a tool for interpreting microbialites. In *Earliest Life on Earth: Habitats, Environments and Methods of Detection* (pp. 127-170). Springer, Dordrecht. https://doi.org/10.1007/978-90-481-8794-2_6

Webb, J.A. and Finlayson, B.L., 1987. Incorporation of Al, Mg, and water in opal-A; evidence from speleothems. *American Mineralogist*, *72*(11-12), pp.1204-1210.

Williams, L.A., Parks, G.A. and Crerar, D.A., 1985. Silica diagenesis; I, Solubility controls. *Journal of Sedimentary Research*, *55*(3), pp.301-311.

Woo, K.S., Choi, D.W. and Lee, K.C., 2008. Silicification of cave corals from some lava tube caves in the Jeju Island, Korea: implications for speleogenesis and a proxy for paleoenvironmental change during the Late Quaternary. *Quaternary International*, *176*, pp.82-95.

Woo, K.S., Kim, J.C., Choi, D.W., Kim, J.K., Kim, R. and Nehza, O., 2008. The origin of erratic calcite speleothems in the Dangcheomul Cave (lava tube cave), Jeju Island, Korea. *Quaternary International*, *176*, pp.70-81.

Wynn, P.M., Borsato, A., Baker, A., Frisia, S., Miorandi, R. and Fairchild, I.J., 2013. Biogeochemical cycling of sulphur in karst and transfer into speleothem archives at Grotta di Ernesto, Italy. *Biogeochemistry*, *114*(1-3), pp.255-267.

Wynn, P.M., Fairchild, I.J., Spötl, C., Hartland, A., Mattey, D., Fayard, B. and Cotte, M., 2014. Synchrotron X-ray distinction of seasonal hydrological and temperature patterns in speleothem carbonate. *Environmental Chemistry*, *11*(1), pp.28-36.

Zupančič, N., Šebela, S. and Miler, M., 2011. Mineralogical and chemical characteristics of black coatings in Postojna Cave System. *Acta Carsologica*, *40*(2).

This page is left intentionally blank.

Appendix A - Water Chemistry

Appendix A1: Field Parameters – Cave waters and Well water

Sample ID	Sample Type	pH	T	Conductivity	TDS	Salinity	Alkalinity
			°C	µs/cm	mg/L	g/L	(mg/L) as HCO_3^-
CRI20180731-Backroom	Dripwater	7.18		110	78	0.06	23
CRI20180731-C-05	Dripwater	6.6		88	62	0.04	30
CRI20180731-D-13	Dripwater	6.62		114	81	0.06	35
GOL20180729-C-15	Puddle	6.5	12.7	72	51	0.04	33
GOL20180729-D-51	Puddle	6.17	15.6	325	214	0.15	12
GOL20180729-F-87	Puddle	6.45	12.4	87	62	0.04	40
LYO20180730-A-06	Dripwater	5.84	15.6	411	293	0.21	2
LYO20180730-B-51	Dripwater	6.04		95	68	0.05	20
LYO20180731-H-01	Dripwater	6.89		101	72	0.05	20
LYO20180731-J-13	Dripwater	6.9		90	64	0.04	41
LYO20180731-H-01	Puddle	6.26	12.7	77	56	0.04	15
POS20180801-D-01	Dripwater	7.81		118	83	0.06	85
POS20180801-E-04	Dripwater	7.2		121	87	0.06	28
POS20180801-F-07	Dripwater	7.02		91	65	0.05	52
POS20180801-F-12	Dripwater	6.56	6.2	82	59	0.05	60
POS20180801-B-14	Puddle	6.73	6.2	113	81	0.06	74
POS20180801-D-01	Puddle	6.81	6.6	251	179	0.13	85
POS20180801-I-10	Puddle	6.82	6.7	133	95	0.07	63
SIL20180802-A-15	Dripwater	6.27		98	70	0.05	18
SIL20180802-C-14	Puddle	9.01		132	17	0.01	77
VAL20180803-A-01	Dripwater	6.38		91	65	0.05	29
VAL20180803-B-02	Dripwater	6.36		77	54	0.04	13
VAL20180803-C-02	Dripwater	6.87		78	56	0.04	29
VAL20180803-D-02	Dripwater	6.58		80	57	0.04	32
VAL20180803-E-01	Dripwater	6.2		72	51	0.04	11
VAL20180803-A-02	Puddle	6.05		41	14	0.01	11
VAL20180803-B-01	Puddle	6.56		69	15	0.01	26
VAL20180803-C-01	Puddle	6.04		99	17	0.01	15
VAL20180803-D-01	Puddle	6.02		77	15	0.01	10
YEL20180802-A-05	Dripwater	7.31		95	67	0.05	11
YEL20180802-B-02	Dripwater	6.85		92	66	0.05	49
YEL20180802-C-02	Dripwater	6.21		83	59	0.04	25
YEL20180802-D-02	Dripwater	7.16		101	72	0.05	61
YEL20180802-A-01	Puddle	6.99		279	206	0.15	59
YEL20180802-B-01	Puddle	6.39		81	58	0.04	46
YEL20180802-C-01	Puddle	6.45	14.7	74	52	0.04	32
YEL20180802-D-01	Puddle	6.7	12.7	115	80	0.06	31
Tule Lake	Surface	7.53		214	15	0.11	120
WEL20180803-1	Well	7.4		210	20	0.01	87
WEL20180803-2	Well	8.18		837	24	0.02	387
WEL20180803-3	Well	8.27		1500	20	0.01	493
WEL20180804-4	Well	7.84		2700	32	0.02	890

Appendix A2: Cations Analysis of Cave and Well Water

Sample ID	Sample Type	Na^+	$NH4^+$	K^+	Mg^{2+}	Ca^{2+}	Sr^{2+}
		mg/L	mg/L	mg/L	mg/L	mg/L	mg/L
CRI20180731-Backroom	Dripwater	7.18	7.67	BDL	1.56	4.40	4.88
CRI20180731-C-05	Dripwater	6.6	7.20	BDL	1.64	3.23	4.07
CRI20180731-D-13	Dripwater	6.62	4.26	BDL	1.36	2.17	4.15
GOL20180729-C-15	Puddle	6.5	7.87	BDL	1.96	1.64	1.79
GOL20180729-D-51	Puddle	6.17	6.66	BDL	4.04	1.62	3.50
GOL20180729-F-87	Puddle	6.45	8.97	BDL	1.57	3.03	3.02
LYO20180730-A-06	Dripwater	5.84	1.92	BDL	2.80	BDL	0.53
LYO20180730-B-51	Dripwater	6.04	BDL	BDL	BDL	BDL	BDL
LYO20180731-H-01	Dripwater	6.89	14.98	BDL	1.64	3.04	5.53
LYO20180731-J-13	Dripwater	6.9	12.48	0.52	1.87	1.91	3.00
LYO20180731-H-01	Puddle	6.26	10.95	BDL	1.49	0.56	1.14
POS20180801-D-01	Dripwater	7.81	10.55	BDL	1.43	8.51	5.70
POS20180801-E-04	Dripwater	7.2	8.34	BDL	1.00	5.98	6.55
POS20180801-F-07	Dripwater	7.02	6.92	BDL	1.05	4.12	6.00
POS20180801-F-12	Dripwater	6.56	8.25	BDL	0.48	4.99	6.26
POS20180801-B-14	Puddle	6.73	9.01	BDL	0.47	5.81	7.53
POS20180801-D-01	Puddle	6.81	11.75	BDL	1.29	9.69	7.21
POS20180801-I-10	Puddle	6.82	9.28	BDL	0.46	7.34	6.21
SIL20180802-A-15	Dripwater	6.27	6.75	BDL	1.59	3.70	5.10
SIL20180802-C-14	Puddle	9.01	8.01	BDL	1.80	4.50	8.36
VAL20180803-A-01	Dripwater	6.38	8.73	BDL	1.14	1.34	3.10
VAL20180803-B-02	Dripwater	6.36	5.82	0.82	1.30	0.53	1.06
VAL20180803-C-02	Dripwater	6.87	9.90	BDL	0.87	0.89	1.39
VAL20180803-D-02	Dripwater	6.58	9.01	BDL	1.45	1.80	2.25
VAL20180803-E-01	Dripwater	6.2	6.03	BDL	1.08	0.97	1.73
VAL20180803-A-02	Puddle	6.05	6.10	BDL	1.30	0.46	0.92
VAL20180803-B-01	Puddle	6.56	6.62	BDL	0.94	1.24	2.84
VAL20180803-C-01	Puddle	6.04	5.43	BDL	1.10	0.86	1.05
VAL20180803-D-01	Puddle	6.02	6.56	BDL	1.37	0.76	1.01
YEL20180802-A-05	Dripwater	7.31	7.30	BDL	1.22	4.19	4.65
YEL20180802-B-02	Dripwater	6.85	7.77	BDL	1.91	4.60	6.41
YEL20180802-C-02	Dripwater	6.21	10.83	BDL	1.48	3.33	4.73
YEL20180802-D-02	Dripwater	7.16	14.17	BDL	3.29	7.78	6.51
YEL20180802-A-01	Puddle	6.99	7.07	BDL	1.53	5.76	4.41
YEL20180802-B-01	Puddle	6.39	7.53	BDL	1.68	3.39	4.58
YEL20180802-C-01	Puddle	6.45	6.60	BDL	1.16	2.92	4.49
YEL20180802-D-01	Puddle	6.7	6.86	BDL	1.57	6.60	4.71
Tule Lake	Surface	7.53	132.33	0.42	10.57	15.91	17.12
WEL20180803-1	Well	7.4	25.70	BDL	1.90	3.94	5.99
WEL20180803-2	Well	8.18	79.63	1.42	16.36	39.67	26.96
WEL20180803-3	Well	8.27	157.52	1.16	19.92	BDL	100.67
WEL20180804-4	Well	7.84	238.19	1.98	15.24	BDL	BDL

Appendix A3: Anions Analysis of Cave and Well Water

Sample ID	Sample Type	F^-	Cl^-	NO_2^-	Br^-	NO_3^-	PO_4^{3-}	PO_4-P	SO_4^{2-}	SO_4-S	NO_3-N
		mg/L	mg/L	mg/L	mg/L	mg/L	mg/L	mg/L	mg/L	mg/L	mg/L
CRI20180731-Backroom	Dripwater	BDL	4.13	BDL	BDL	26.41	BDL	BDL	4.71	1.57	5.96
CRI20180731-C-05	Dripwater	BDL	3.07	BDL	BDL	16.40	BDL	BDL	2.61	0.87	3.70
CRI20180731-D-13	Dripwater	BDL	3.33	BDL	BDL	2.06	BDL	BDL	2.05	0.68	0.47
GOL20180729-C-15	Puddle	0.21	3.06	BDL	BDL	BDL	BDL	BDL	1.41	0.47	BDL
GOL20180729-D-51	Puddle	0.20	5.73	BDL	BDL	18.21	3.33	1.09	2.40	0.80	4.11
GOL20180729-F-87	Puddle	0.11	3.40	BDL	BDL	8.97	BDL	BDL	2.20	0.73	2.03
LYO20180730-A-06	Dripwater	BDL	3.67	BDL	BDL	8.07	BDL	BDL	2.14	0.71	1.82
LYO20180730-B-51	Dripwater	BDL	4.41	BDL	BDL	6.46	BDL	BDL	1.89	0.63	1.46
LYO20180731-H-01	Dripwater	0.30	4.47	BDL	BDL	9.21	BDL	BDL	2.54	0.85	2.08
LYO20180731-J-13	Dripwater	0.23	3.47	BDL	BDL	12.30	BDL	BDL	2.24	0.75	2.78
LYO20180731-H-01	Puddle	0.38	3.23	BDL	BDL	9.83	1.63	0.53	2.33	0.78	2.22
POS20180801-D-01	Dripwater	0.30	4.45	BDL	BDL	3.67	BDL	BDL	3.20	1.07	0.83
POS20180801-E-04	Dripwater	0.34	5.00	BDL	BDL	4.09	BDL	BDL	2.76	0.92	0.92
POS20180801-F-07	Dripwater	0.23	4.85	BDL	BDL	BDL	BDL	BDL	2.06	0.69	BDL
POS20180801-F-12	Dripwater	0.25	3.35	BDL	BDL	1.13	BDL	BDL	2.21	0.74	0.25
POS20180801-B-14	Puddle	0.31	3.39	BDL	BDL	2.59	BDL	BDL	2.30	0.77	0.58
POS20180801-D-01	Puddle	0.33	3.72	BDL	BDL	3.48	BDL	BDL	2.58	0.86	0.79
POS20180801-I-10	Puddle	0.36	3.27	BDL	BDL	4.38	BDL	BDL	2.51	0.84	0.99
SIL20180802-A-15	Dripwater	0.14	3.59	BDL	BDL	23.35	BDL	BDL	2.85	0.95	5.27
SIL20180802-C-14	Puddle	0.16	3.77	BDL	BDL	17.95	BDL	BDL	2.61	0.87	4.05
VAL20180803-A-01	Dripwater	BDL	3.43	BDL	BDL	6.52	BDL	BDL	2.01	0.67	1.47
VAL20180803-B-02	Dripwater	BDL	3.29	BDL	BDL	3.65	BDL	BDL	1.78	0.59	0.82
VAL20180803-C-02	Dripwater	0.28	3.40	BDL	BDL	1.14	BDL	BDL	2.42	0.81	0.26
VAL20180803-D-02	Dripwater	0.25	4.27	BDL	BDL	BDL	BDL	BDL	2.41	0.80	BDL
VAL20180803-E-01	Dripwater	0.20	4.09	BDL	BDL	2.61	BDL	BDL	1.85	0.62	0.59
VAL20180803-A-02	Puddle	0.17	3.81	BDL	BDL	BDL	BDL	BDL	1.67	0.56	BDL
VAL20180803-B-01	Puddle	0.08	3.59	BDL	BDL	0.82	BDL	BDL	1.92	0.64	0.19
VAL20180803-C-01	Puddle	0.24	2.79	BDL	BDL	3.08	BDL	BDL	1.64	0.55	0.69
VAL20180803-D-01	Puddle	0.25	3.45	BDL	BDL	7.52	BDL	BDL	1.81	0.60	1.70
YEL20180802-A-05	Dripwater	0.33	3.69	BDL	BDL	1.76	BDL	BDL	2.35	0.78	0.40
YEL20180802-B-02	Dripwater	0.26	5.65	BDL	BDL	6.74	BDL	BDL	3.25	1.08	1.52
YEL20180802-C-02	Dripwater	0.25	5.51	BDL	BDL	4.10	BDL	BDL	2.69	0.90	0.93
YEL20180802-D-02	Dripwater	0.52	4.53	BDL	BDL	31.44	BDL	BDL	4.01	1.34	7.10
YEL20180802-A-01	Puddle	0.29	3.14	BDL	BDL	4.18	BDL	BDL	1.58	0.53	0.94
YEL20180802-B-01	Puddle	0.19	3.13	BDL	BDL	2.54	BDL	BDL	2.30	0.77	0.57
YEL20180802-C-01	Puddle	0.15	3.21	BDL	BDL	13.89	BDL	BDL	1.99	0.66	3.14
YEL20180802-D-01	Puddle	0.36	2.96	BDL	BDL	23.58	BDL	BDL	2.87	0.96	5.33
Tule Lake	Surface	0.34	30.99	BDL	2.69	BDL	BDL	BDL	320.9	107.00	BDL
WEL20180803-1	Well	0.33	11.63	BDL	0.43	BDL	BDL	BDL	4.07	1.36	BDL
WEL20180803-2	Well	0.57	11.37	BDL	BDL	BDL	BDL	BDL	102.3	34.11	BDL
WEL20180803-3	Well	0.23	17.42	BDL	BDL	BDL	BDL	BDL	556.1	185.40	BDL
WEL20180804-4	Well	0.15	120.60	BDL	BDL	2.48	BDL	BDL	805.2	268.40	0.56

Appendix A4: DOC and TN of Cave and Well Waters

Sample ID	Sample Type	DOC	TN	Org. N
		mg/L	mg/L	mg/L
CRI20180731-Backroom	Dripwater	5.77	1.93	BDL
CRI20180731-C-05	Dripwater	7.72	2.02	BDL
CRI20180731-D-13	Dripwater	7.03	1.48	1.01
GOL20180729-C-15	Puddle	10.45	0.66	0.66
GOL20180729-D-51	Puddle	14.29	4.34	0.23
GOL20180729-F-87	Puddle	11.12	3.02	1.00
LYO20180730-A-06	Dripwater	8.95	0.62	BDL
LYO20180730-B-51	Dripwater	4.23	1.20	BDL
LYO20180731-H-01	Dripwater	9.03	1.93	BDL
LYO20180731-J-13	Dripwater	7.20	1.78	BDL
LYO20180731-H-01	Puddle	32.90	3.17	0.95
POS20180801-D-01	Dripwater	10.92	7.04	6.21
POS20180801-E-04	Dripwater	8.43	1.68	0.75
POS20180801-F-07	Dripwater	5.91	1.35	1.35
POS20180801-F-12	Dripwater	22.79	7.38	7.13
POS20180801-B-14	Puddle	8.18	0.86	0.28
POS20180801-D-01	Puddle	12.58	1.42	0.64
POS20180801-I-10	Puddle	8.28	1.78	0.79
SIL20180802-A-15	Dripwater	7.89	2.01	BDL
SIL20180802-C-14	Puddle	12.40	3.77	BDL
VAL20180803-A-01	Dripwater	28.14	4.61	3.14
VAL20180803-B-02	Dripwater	7.12	1.56	0.73
VAL20180803-C-02	Dripwater	5.61	1.47	1.21
VAL20180803-D-02	Dripwater	8.60	1.61	1.61
VAL20180803-E-01	Dripwater	45.12	3.61	3.02
VAL20180803-A-02	Puddle	17.47	0.93	0.93
VAL20180803-B-01	Puddle	11.40	0.92	0.74
VAL20180803-C-01	Puddle	13.39	0.91	0.21
VAL20180803-D-01	Puddle	20.43	1.77	0.07
YEL20180802-A-05	Dripwater	7.07	1.38	0.99
YEL20180802-B-02	Dripwater	7.28	1.69	0.17
YEL20180802-C-02	Dripwater	7.30	1.51	0.58
YEL20180802-D-02	Dripwater	8.53	2.88	BDL
YEL20180802-A-01	Puddle	7.39	0.97	0.03
YEL20180802-B-01	Puddle	7.58	1.07	0.49
YEL20180802-C-01	Puddle	6.57	2.60	BDL
YEL20180802-D-01	Puddle	12.96	6.72	1.40
Tule Lake	Surface	39.97	5.96	5.96
WEL20180803-1	Well	8.89	1.48	1.48
WEL20180803-2	Well	13.20	2.39	2.39
WEL20180803-3	Well	20.37	31.34	31.34
WEL20180804-4	Well	30.15	3.73	3.16

Appendix A5: ICP-MS Data for Cave and Well Waters

Sample ID	Sample Type	Si/29	Na/23	K/39	Ca /44	Mg / 24	P /31	S /33	S /34
		mg/L	mg/L	mg/L	µg/L	µg/L	mg/L	mg/L	mg/L
CRI20180731-Backroom	Dripwater	12	7.9	29.3	4764.3	4621.0	2.1	4.1	4.1
CRI20180731-C-05	Dripwater	10	6.1	5.5	4321.3	3675.3	1.6	3.6	3.6
CRI20180731-D-13	Dripwater	10	4.8	26.2	4432.0	2492.0	1.7	3.3	3.7
GOL20180729-C-15	Puddle	28	7.7	1.6	1952.7	1727.3	4.6	5.2	4.6
GOL20180729-D-51	Puddle	18	6.8	3.5	3504.3	1712.7	4.2	5.0	4.6
GOL20180729-F-87	Puddle	28	9.1	1.6	3042.0	3177.0	4.5	5.0	4.6
LYO20180730-A-06	Dripwater	5	1.8	2.5	605.1	418.4	1.2	4.6	4.5
LYO20180730-B-51	Dripwater	13	5.4	16.9	1736.0	1060.3	2.3	3.1	3.5
LYO20180731-H-01	Dripwater	28	13.9	24.4	5138.3	3178.0	4.6	3.1	3.6
LYO20180731-J-13	Dripwater	29	12.9	7.6	3425.3	2350.7	4.7	3.5	3.6
LYO20180731-H-01	Puddle	34	10.0	1.1	1344.0	646.7	6.1	5.1	4.6
POS20180801-D-01	Dripwater	26	10.0	4.4	4999.3	8943.7	4.8	4.1	4.1
POS20180801-E-04	Dripwater	26	9.3	1.1	6748.0	6842.3	4.3	3.3	3.7
POS20180801-F-07	Dripwater	19	7.5	6.8	5945.0	4510.3	3.5	4.6	4.2
POS20180801-F-12	Dripwater	21	8.4	0.3	5846.0	5055.7	3.6	4.1	4.1
POS20180801-B-14	Puddle	22	8.7	0.3	6745.3	5964.0	3.8	5.1	4.9
POS20180801-D-01	Puddle	25	11.1	1.1	6079.7	9243.0	4.1	4.7	4.5
POS20180801-I-10	Puddle	29	9.4	0.4	5559.0	7359.3	4.6	4.8	4.3
SIL20180802-A-15	Dripwater	21	7.3	32.7	5374.7	4081.3	3.5	4.0	4.1
SIL20180802-C-14	Puddle	22	8.2	1.5	7749.7	4590.0	4.1	4.5	4.2
VAL20180803-A-01	Dripwater	14	9.1	5.1	3241.7	1509.7	2.5	4.3	4.3
VAL20180803-B-02	Dripwater	14	5.8	5.8	1740.0	854.9	2.6	3.6	3.7
VAL20180803-C-02	Dripwater	25	10.1	7.4	2007.0	1187.0	4.6	4.1	4.3
VAL20180803-D-02	Dripwater	22	9.3	6.1	2564.7	2182.0	3.8	3.7	3.8
VAL20180803-E-01	Dripwater	19	6.0	2.4	1763.3	1246.7	3.7	3.7	3.7
VAL20180803-A-02	Puddle	22	5.6	0.9	1239.3	610.7	4.0	4.0	3.9
VAL20180803-B-01	Puddle	22	6.8	1.2	4663.0	3677.7	3.8	3.9	3.9
VAL20180803-C-01	Puddle	25	5.9	1.0	1478.0	1061.0	4.1	3.9	3.8
VAL20180803-D-01	Puddle	26	6.6	1.0	1268.7	911.5	4.3	3.7	3.8
YEL20180802-A-05	Dripwater	21	7.2	3.6	4340.3	4411.7	3.9	3.4	3.5
YEL20180802-B-02	Dripwater	25	7.9	7.5	6065.7	4989.0	4.4	4.3	4.3
YEL20180802-C-02	Dripwater	26	8.8	7.4	4234.3	3476.3	4.5	3.5	3.8
YEL20180802-D-02	Dripwater	45	12.6	7.2	5971.3	8115.7	5.9	3.4	3.7
YEL20180802-A-01	Puddle	23	7.3	1.4	4266.3	5836.7	3.8	3.3	3.5
YEL20180802-B-01	Puddle	18	6.9	0.8	3030.0	1416.7	3.8	3.5	3.7
YEL20180802-C-01	Puddle	21	6.0	0.8	4268.7	3028.7	3.5	3.3	3.5
YEL20180802-D-01	Puddle	32	7.2	1.4	4585.7	6855.0	5.0	3.4	3.7
Tule Lake	Surface	7	118.3	10.6	14643.3	15100.0	1.5	70.0	73.6
WEL20180803-1	Well	24	24.1	1.7	5435.0	4107.7	4.1	3.8	3.8
WEL20180803-2	Well	27	75.3	14.9	26520.0	37640.0	4.7	27.2	29.3
WEL20180803-3	Well	26	142.1	17.4	85383.3	72516.7	5.0	113.2	122.9
WEL20180804-4	Well	33	225.4	13.9	182666.7	126400.0	6.1	153.7	167.3

Appendix A6: ICP-MS Data for Cave and Well Waters Cont.

Sample ID	Sample Type	Al/27	Ti/47	V/51	Cr/52	Ga/71	Rb/85	Sr / 88	Sb /121
		µg/L	µg/L	µg/L	µg/L	µg/L	µg/L	µg/L	µg/L
CRI20180731-Backroom	Dripwater	BDL	0.7	23.6	BDL	BDL	4.6	28.7	BDL
CRI20180731-C-05	Dripwater	BDL	0.2	14.6	BDL	BDL	3.0	27.2	BDL
CRI20180731-D-13	Dripwater	BDL	0.3	12.2	1.6	BDL	4.2	36.2	BDL
GOL20180729-C-15	Puddle	89.0	4.4	11.3	1.7	0.5	3.6	18.3	0.5
GOL20180729-D-51	Puddle	100.3	3.6	15.2	1.1	0.3	10.9	29.6	0.5
GOL20180729-F-87	Puddle	94.6	3.3	13.0	0.3	BDL	4.0	30.8	0.3
LYO20180730-A-06	Dripwater	82.4	1.1	1.7	10.7	BDL	4.7	6.9	BDL
LYO20180730-B-51	Dripwater	BDL	1.2	4.4	BDL	BDL	19.0	14.7	0.1
LYO20180731-H-01	Dripwater	BDL	2.2	38.6	0.3	BDL	8.9	24.8	0.2
LYO20180731-J-13	Dripwater	37.4	1.3	24.9	BDL	BDL	10.4	21.9	0.2
LYO20180731-H-01	Puddle	291.6	5.6	26.1	3.2	0.6	5.8	11.2	0.3
POS20180801-D-01	Dripwater	36.4	0.4	12.6	BDL	BDL	4.5	10.7	0.2
POS20180801-E-04	Dripwater	35.1	0.6	10.9	BDL	BDL	2.6	19.7	0.3
POS20180801-F-07	Dripwater	42.2	0.6	7.8	BDL	BDL	3.3	7.8	BDL
POS20180801-F-12	Dripwater	38.5	0.8	16.4	BDL	BDL	1.5	4.3	BDL
POS20180801-B-14	Puddle	90.3	2.3	20.5	2.0	BDL	2.1	2.8	0.1
POS20180801-D-01	Puddle	91.3	1.4	22.5	0.6	0.4	4.3	13.8	0.2
POS20180801-I-10	Puddle	117.9	2.1	21.1	0.6	BDL	2.2	9.7	0.1
SIL20180802-A-15	Dripwater	45.3	0.6	6.4	0.6	BDL	5.5	48.0	0.2
SIL20180802-C-14	Puddle	106.1	1.3	8.6	BDL	BDL	4.1	91.2	0.1
VAL20180803-A-01	Dripwater	62.9	1.2	15.9	1.6	BDL	6.5	15.7	0.2
VAL20180803-B-02	Dripwater	38.6	0.8	7.4	BDL	BDL	4.3	7.7	0.1
VAL20180803-C-02	Dripwater	38.7	0.6	17.1	BDL	BDL	5.7	7.8	0.1
VAL20180803-D-02	Dripwater	48.0	1.1	10.6	BDL	BDL	8.7	17.4	0.3
VAL20180803-E-01	Dripwater	105.7	1.9	5.1	BDL	BDL	3.8	35.4	0.1
VAL20180803-A-02	Puddle	320.8	5.7	7.8	1.1	BDL	4.7	35.1	0.2
VAL20180803-B-01	Puddle	69.1	2.6	9.4	0.4	BDL	3.1	54.4	BDL
VAL20180803-C-01	Puddle	159.5	2.6	12.0	0.3	BDL	6.0	9.3	BDL
VAL20180803-D-01	Puddle	175.1	3.4	9.9	0.9	BDL	4.8	23.5	0.2
YEL20180802-A-05	Dripwater	42.8	0.2	6.4	BDL	BDL	2.9	46.1	BDL
YEL20180802-B-02	Dripwater	96.1	0.9	9.5	1.0	BDL	4.7	59.4	BDL
YEL20180802-C-02	Dripwater	51.1	0.6	10.2	BDL	BDL	3.5	34.4	BDL
YEL20180802-D-02	Dripwater	37.3	0.8	20.8	BDL	BDL	6.7	45.6	0.1
YEL20180802-A-01	Puddle	88.9	1.0	11.6	BDL	BDL	3.7	55.1	BDL
YEL20180802-B-01	Puddle	129.9	2.2	12.7	BDL	BDL	4.7	141.1	0.2
YEL20180802-C-01	Puddle	BDL	0.7	6.7	BDL	BDL	2.9	33.9	BDL
YEL20180802-D-01	Puddle	BDL	1.9	12.8	1.0	BDL	3.2	24.5	BDL
Tule Lake	Surface	38.9	0.4	11.9	0.5	BDL	6.4	206.3	0.2
WEL20180803-1	Well	62.9	0.7	22.6	0.3	BDL	8.1	32.0	0.2
WEL20180803-2	Well	63.4	0.6	1.7	3.0	BDL	8.1	292.2	0.5
WEL20180803-3	Well	36.9	0.3	32.0	BDL	BDL	8.1	762.4	BDL
WEL20180804-4	Well	44.8	0.6	47.2	0.5	BDL	7.8	1423.3	BDL

Appendix A7: ICP-MS Data for Cave and Well Waters Cont.

Sample ID	Sample Type	Ba/135	W/182	Hg/200	Pb/208	U/238	Li /7	B /11
		µg/L	µg/L	µg/L	µg/L	µg/L	µg/L	µg/L
CRI20180731-Backroom	Dripwater	7.2	1.5	6.6	BDL	BDL	33806.7	8509.0
CRI20180731-C-05	Dripwater	4.3	1.4	3.9	BDL	0.8	32326.7	7055.3
CRI20180731-D-13	Dripwater	8.5	1.1	6.1	BDL	BDL	31903.3	10405.0
GOL20180729-C-15	Puddle	3.2	16.7	29.6	0.3	14.7	36906.7	9514.7
GOL20180729-D-51	Puddle	8.8	9.6	24.5	BDL	9.8	35663.3	29016.7
GOL20180729-F-87	Puddle	4.2	6.6	9.5	BDL	12.4	36110.0	7834.7
LYO20180730-A-06	Dripwater	1.3	0.6	2.0	BDL	2.6	35020.0	20926.7
LYO20180730-B-51	Dripwater	7.5	1.3	4.4	BDL	1.7	32946.7	15086.7
LYO20180731-H-01	Dripwater	5.2	1.0	4.8	BDL	10.7	49146.7	27173.3
LYO20180731-J-13	Dripwater	3.6	2.3	25.3	BDL	4.2	44010.0	20303.3
LYO20180731-H-01	Puddle	2.8	5.5	6.9	BDL	44.6	40723.3	6165.3
POS20180801-D-01	Dripwater	1.8	0.5	2.9	BDL	2.8	35376.7	28366.7
POS20180801-E-04	Dripwater	0.9	1.7	8.8	BDL	0.7	37986.7	25106.7
POS20180801-F-07	Dripwater	2.2	1.5	9.6	BDL	0.6	36773.3	23923.3
POS20180801-F-12	Dripwater	0.8	1.3	4.6	BDL	1.9	37503.3	20280.0
POS20180801-B-14	Puddle	1.9	4.1	6.0	BDL	8.9	40663.3	13090.0
POS20180801-D-01	Puddle	2.0	3.4	5.6	BDL	60.4	36006.7	28166.7
POS20180801-I-10	Puddle	2.9	3.2	4.8	BDL	3.3	41036.7	14573.3
SIL20180802-A-15	Dripwater	14.1	1.2	11.0	BDL	0.8	34790.0	18240.0
SIL20180802-C-14	Puddle	4.7	2.5	4.3	BDL	3.6	37373.3	13546.7
VAL20180803-A-01	Dripwater	1.4	1.1	6.5	BDL	4.8	37593.3	20510.0
VAL20180803-B-02	Dripwater	2.6	1.3	6.1	BDL	BDL	35586.7	8344.0
VAL20180803-C-02	Dripwater	1.7	0.9	4.7	BDL	2.3	40200.0	19730.0
VAL20180803-D-02	Dripwater	2.6	0.9	4.6	BDL	2.4	36086.7	21686.7
VAL20180803-E-01	Dripwater	4.2	0.7	3.9	BDL	4.3	33150.0	10314.7
VAL20180803-A-02	Puddle	4.3	2.0	2.8	0.2	15.0	36663.3	5135.7
VAL20180803-B-01	Puddle	4.9	1.7	2.7	BDL	4.7	36663.3	13660.0
VAL20180803-C-01	Puddle	2.0	1.5	2.2	BDL	13.9	39023.3	8426.0
VAL20180803-D-01	Puddle	5.1	1.5	2.5	BDL	12.6	36566.7	8046.3
YEL20180802-A-05	Dripwater	4.4	0.7	3.8	BDL	BDL	35176.7	21003.3
YEL20180802-B-02	Dripwater	5.4	0.8	4.2	BDL	1.1	34990.0	21203.3
YEL20180802-C-02	Dripwater	2.8	1.8	3.5	BDL	0.8	37096.7	15960.0
YEL20180802-D-02	Dripwater	4.7	0.7	3.6	BDL	3.6	33030.0	19690.0
YEL20180802-A-01	Puddle	5.3	1.3	2.7	BDL	10.9	35210.0	16106.7
YEL20180802-B-01	Puddle	3.2	1.2	2.0	BDL	7.9	37546.7	6131.7
YEL20180802-C-01	Puddle	1.7	1.8	1.9	BDL	4.3	35846.7	11250.0
YEL20180802-D-01	Puddle	3.1	1.6	2.0	BDL	8.9	33976.7	22533.3
Tule Lake	Surface	11.9	0.6	3.3	1.8	29.5	32560.0	68280.0
WEL20180803-1	Well	4.4	1.2	2.7	BDL	37.7	84363.3	295466.7
WEL20180803-2	Well	16.0	0.6	2.7	BDL	32.5	39646.7	131566.7
WEL20180803-3	Well	50.3	0.6	2.3	BDL	125.6	39310.0	170233.3
WEL20180804-4	Well	95.6	0.6	4.6	BDL	390.8	31410.0	87556.7

Appendix A8: ICP-MS Data for Cave and Well Waters Cont.

Sample ID	Sample Type	Mn/55	Fe /56	Co / 59	Ni / 60	Cu / 63	Zn / 66	As / 75
		µg/L	µg/L	ng/L	ng/L	µg/L	µg/L	ng/L
CRI20180731-Backroom	Dripwater	0.8	BDL	211.7	BDL	4.8	41.9	BDL
CRI20180731-C-05	Dripwater	7.0	BDL	443.1	BDL	3.5	50.2	BDL
CRI20180731-D-13	Dripwater	0.2	BDL	304.2	BDL	2.3	43.5	BDL
GOL20180729-C-15	Puddle	0.5	18.8	BDL	BDL	39.4	45.4	BDL
GOL20180729-D-51	Puddle	0.6	21.6	88.9	BDL	43.9	53.2	700.2
GOL20180729-F-87	Puddle	0.3	BDL	BDL	BDL	35.5	43.2	BDL
LYO20180730-A-06	Dripwater	0.5	BDL	BDL	BDL	22.8	40.7	BDL
LYO20180730-B-51	Dripwater	3.0	24.5	306.0	BDL	21.9	42.9	BDL
LYO20180731-H-01	Dripwater	0.4	BDL	909.3	BDL	132.6	44.1	825.1
LYO20180731-J-13	Dripwater	1.0	BDL	250.7	BDL	39.2	55.6	650.8
LYO20180731-H-01	Puddle	0.7	185.6	178.5	BDL	79.1	46.1	723.4
POS20180801-D-01	Dripwater	1.6	BDL	BDL	BDL	10.6	41.1	BDL
POS20180801-E-04	Dripwater	2.9	BDL	BDL	BDL	6.8	54.9	BDL
POS20180801-F-07	Dripwater	3.0	BDL	BDL	BDL	2.9	49.5	BDL
POS20180801-F-12	Dripwater	0.9	BDL	247.6	BDL	11.4	49.5	BDL
POS20180801-B-14	Puddle	0.4	BDL	BDL	BDL	6.7	36.6	BDL
POS20180801-D-01	Puddle	0.2	BDL	BDL	BDL	12.8	42.5	746.3
POS20180801-I-10	Puddle	0.4	BDL	BDL	BDL	11.8	42.9	BDL
SIL20180802-A-15	Dripwater	2.8	BDL	BDL	BDL	10.8	47.5	728.1
SIL20180802-C-14	Puddle	0.6	BDL	BDL	BDL	29.4	41.7	BDL
VAL20180803-A-01	Dripwater	0.4	BDL	385.3	BDL	34.7	51.9	BDL
VAL20180803-B-02	Dripwater	0.9	BDL	619.4	BDL	5.4	51.4	BDL
VAL20180803-C-02	Dripwater	0.5	BDL	380.2	BDL	27.5	54.7	BDL
VAL20180803-D-02	Dripwater	2.8	BDL	BDL	1543.0	28.4	85.8	BDL
VAL20180803-E-01	Dripwater	2.1	BDL	BDL	BDL	17.1	29.4	BDL
VAL20180803-A-02	Puddle	1.4	91.7	222.0	BDL	26.4	53.6	BDL
VAL20180803-B-01	Puddle	0.5	BDL	BDL	BDL	14.6	34.8	BDL
VAL20180803-C-01	Puddle	0.4	BDL	BDL	BDL	27.2	65.9	BDL
VAL20180803-D-01	Puddle	0.7	38.4	111.0	BDL	24.0	46.4	BDL
YEL20180802-A-05	Dripwater	2.3	BDL	BDL	BDL	2.1	31.9	BDL
YEL20180802-B-02	Dripwater	3.1	BDL	759.4	BDL	19.9	36.2	BDL
YEL20180802-C-02	Dripwater	BDL	BDL	608.6	BDL	9.0	34.5	BDL
YEL20180802-D-02	Dripwater	BDL	BDL	607.2	BDL	25.5	35.3	673.7
YEL20180802-A-01	Puddle	0.2	BDL	BDL	BDL	14.4	46.6	BDL
YEL20180802-B-01	Puddle	0.4	BDL	BDL	BDL	23.0	31.4	BDL
YEL20180802-C-01	Puddle	0.2	BDL	BDL	BDL	12.7	36.4	BDL
YEL20180802-D-01	Puddle	0.8	BDL	BDL	BDL	22.9	38.9	538.9
Tule Lake	Surface	1.5	BDL	523.0	971.5	2.7	33.9	5596.0
WEL20180803-1	Well	BDL	BDL	BDL	BDL	BDL	56.1	18223.3
WEL20180803-2	Well	126.5	120.2	BDL	BDL	0.7	49.6	4357.7
WEL20180803-3	Well	277.0	BDL	298.6	2676.3	4.1	56.3	42600.0
WEL20180804-4	Well	2526.7	323.3	2582.0	12456.7	2.8	49.4	23140.0

Appendix A9: ICP-MS Data for Cave and Well Waters Cont.

Sample ID	Sample Type	Se / 78	Mo / 95	Cd / 111
		ng/L	ng/L	ng/L
CRI20180731-Backroom	Dripwater	BDL	BDL	BDL
CRI20180731-C-05	Dripwater	BDL	BDL	BDL
CRI20180731-D-13	Dripwater	BDL	BDL	BDL
GOL20180729-C-15	Puddle	358.6	BDL	BDL
GOL20180729-D-51	Puddle	BDL	BDL	BDL
GOL20180729-F-87	Puddle	BDL	BDL	BDL
LYO20180730-A-06	Dripwater	BDL	BDL	BDL
LYO20180730-B-51	Dripwater	BDL	BDL	BDL
LYO20180731-H-01	Dripwater	BDL	BDL	BDL
LYO20180731-J-13	Dripwater	571.8	1778.3	BDL
LYO20180731-H-01	Puddle	339.3	BDL	BDL
POS20180801-D-01	Dripwater	BDL	BDL	BDL
POS20180801-E-04	Dripwater	BDL	510.0	BDL
POS20180801-F-07	Dripwater	BDL	BDL	BDL
POS20180801-F-12	Dripwater	BDL	BDL	BDL
POS20180801-B-14	Puddle	BDL	BDL	BDL
POS20180801-D-01	Puddle	353.9	801.4	BDL
POS20180801-I-10	Puddle	BDL	BDL	BDL
SIL20180802-A-15	Dripwater	BDL	BDL	BDL
SIL20180802-C-14	Puddle	BDL	BDL	BDL
VAL20180803-A-01	Dripwater	BDL	BDL	BDL
VAL20180803-B-02	Dripwater	BDL	BDL	BDL
VAL20180803-C-02	Dripwater	407.0	BDL	BDL
VAL20180803-D-02	Dripwater	BDL	BDL	BDL
VAL20180803-E-01	Dripwater	BDL	BDL	BDL
VAL20180803-A-02	Puddle	BDL	BDL	BDL
VAL20180803-B-01	Puddle	BDL	BDL	BDL
VAL20180803-C-01	Puddle	BDL	BDL	BDL
VAL20180803-D-01	Puddle	BDL	BDL	BDL
YEL20180802-A-05	Dripwater	BDL	BDL	BDL
YEL20180802-B-02	Dripwater	BDL	BDL	BDL
YEL20180802-C-02	Dripwater	BDL	BDL	BDL
YEL20180802-D-02	Dripwater	BDL	989.9	BDL
YEL20180802-A-01	Puddle	BDL	BDL	BDL
YEL20180802-B-01	Puddle	BDL	BDL	BDL
YEL20180802-C-01	Puddle	BDL	BDL	BDL
YEL20180802-D-01	Puddle	BDL	736.5	BDL
Tule Lake	Surface	BDL	8275.0	BDL
WEL20180803-1	Well	BDL	1778.7	BDL
WEL20180803-2	Well	BDL	6259.0	BDL
WEL20180803-3	Well	908.6	13596.7	BDL
WEL20180804-4	Well	BDL	25330.0	BDL

Appendix A10: Stable Isotopes Data for Cave and Well Waters

Sample ID	Sample Type	δ 18O (‰)	δ D (‰)
		ng/L	ng/L
CRI20180731-Backroom	Dripwater	-5.20	-77.23
CRI20180731-C-05	Dripwater	-8.36	-79.86
CRI20180731-D-13	Dripwater	-10.14	-79.71
GOL20180729-C-15	Puddle	-10.24	-73.51
GOL20180729-D-51	Puddle	-10.34	-75.07
GOL20180729-F-87	Puddle	-10.34	-74.39
LYO20180730-A-06	Dripwater	-8.89	-62.72
LYO20180730-B-51	Dripwater	-3.18	-51.39
LYO20180731-H-01	Dripwater	-8.45	-66.45
LYO20180731-J-13	Dripwater	-9.70	-71.36
LYO20180731-H-01	Puddle	-	-
POS20180801-D-01	Dripwater	-10.66	-78.99
POS20180801-E-04	Dripwater	-10.46	-77.69
POS20180801-F-07	Dripwater	-10.14	-80.24
POS20180801-F-12	Dripwater	-	-
POS20180801-B-14	Puddle	-9.95	-80.11
POS20180801-D-01	Puddle	-10.56	-81.74
POS20180801-I-10	Puddle	-10.23	-75.22
SIL20180802-A-15	Dripwater	-	-
SIL20180802-C-14	Puddle	-10.81	-84.01
VAL20180803-A-01	Dripwater	-11.43	-84.17
VAL20180803-B-02	Dripwater	-12.77	-94.99
VAL20180803-C-02	Dripwater	-12.91	-97.40
VAL20180803-D-02	Dripwater	-10.77	-78.41
VAL20180803-E-01	Dripwater	-12.21	-91.57
VAL20180803-A-02	Puddle	-0.93	-45.23
VAL20180803-B-01	Puddle	-11.84	-87.61
VAL20180803-C-01	Puddle	-10.04	-73.00
VAL20180803-D-01	Puddle	-	-
YEL20180802-A-05	Dripwater	-11.62	-88.54
YEL20180802-B-02	Dripwater	-10.75	-84.78
YEL20180802-C-02	Dripwater	-11.49	-87.87
YEL20180802-D-02	Dripwater	-10.80	-84.48
YEL20180802-A-01	Puddle	-11.30	-86.10
YEL20180802-B-01	Puddle	-10.11	-78.29
YEL20180802-C-01	Puddle	-11.04	-83.35
YEL20180802-D-01	Puddle	-10.19	-81.89
Tule Lake	Surface	0.40	-29.68
WEL20180803-1	Well	-14.30	-104.87
WEL20180803-2	Well	-7.56	-73.59
WEL20180803-3	Well	-9.40	-81.77
WEL20180804-4	Well	-9.21	-82.57

Appendix A11: Coordinates and depth of Well Waters and Surface Waters

Sample ID	Sample Type	Latitude	Longitude	Depth
				m
Tule Lake	Surface	N 41.9074 °	W 121.5628 °	-
WEL20180803-1	Well	N 41.7174 °	W 121.5075 °	231
WEL20180803-2	Well	N 41.8813 °	W 121.3313 °	37
WEL20180803-3	Well	N 41.9225 °	W 121.3597 °	23
WEL20180804-4	Well	N 41.9893 °	W 121.5063 °	8

Appendix B - XRF Data

Appendix B1: Major Elements and LOI.

Note: App. B1-B3 contain corrected speleothem data for Na_2O, Cu, and Ba.

Sample ID	Sample Type	SiO_2	CaO	MgO	Al_2O_3	Fe_2O_3	MnO	P_2O_5	K_2O	Na_2O	TiO_2	LOI
		Wt.%	Wt %	Wt.%	Wt.%	Wt.%	Wt.%	Wt.%	Wt.%	Wt.%	Wt.%	Wt.%
LYO20180731_J_18	Cauliflower, Brown (Knob)	84.1	1.4	0.6	0.6	1.0	0.0	0.0	0.1	0.0	0.0	12.2
LYO20180731_I_11	Cauliflower,Brown	85.5	1.0	0.3	0.4	0.5	0.0	0.0	0.0	0.0	0.0	12.2
POS20180801_E_16	Cauliflower,White-Tan	35.3	16.8	13.5	0.1	0.3	0.0	0.9	0.0	0.0	0.0	32.8
POS20190806_A_13	Cauliflower,White-Tan	39.9	17.1	11.5	0.2	0.4	0.0	1.8	0.0	0.0	0.0	28.9
CRI20190804_C_1.1	Cauliflower,White-Tan, Orange	17.1	29.8	10.9	0.5	0.9	0.0	2.4	0.0	0.2	0.0	37.9
VAL20190805_D_02	Cauliflower,White-Tan,Brown	77.1	7.0	0.6	0.2	0.4	0.0	0.1	0.0	0.0	0.0	14.5
CRI2019081_A_4.2	Cauliflower,White-Tan,Red_Orange	52.4	7.0	15.6	1.7	1.5	0.0	2.7	0.1	0.2	0.1	18.6
CRI20190804_B_01	Coralloid, Flowery, White-Tan	28.4	21.4	14.7	0.1	0.4	0.0	1.9	0.0	0.0	0.0	32.9
LYO20180731_J_14	Coralloid, White-Tan	45.2	19.4	5.4	0.2	0.4	0.0	1.3	0.0	0.0	0.0	27.6
GOL20190807_A_13	Coralloid, White-Tan,Gray	76.4	4.7	3.5	1.6	1.6	0.0	0.0	0.2	0.0	0.1	11.8
LYO20190810_A_19	Coralloid, White-Tan,Gray	82.3	1.5	0.4	1.1	0.5	0.0	0.0	0.1	0.0	0.0	13.9
POS20190806_B_06	Coralloid, Yellow White Tip	40.2	24.4	10.9	0.1	0.5	0.0	3.0	0.0	0.1	0.0	20.7
GOL20190807_A_11	Coralloid,Brown	86.7	1.1	0.8	0.2	0.5	0.0	0.0	0.0	0.0	0.0	10.6
GOL20190807_B_12	Coralloid,Brown	62.4	9.3	6.9	0.4	0.5	0.0	0.3	0.1	0.0	0.0	20.0
SIL20190808_D_01	Coralloid,Brown	84.4	1.2	1.2	1.0	0.7	0.0	0.0	0.1	0.0	0.0	11.3
GOL20180729_G_03	Coralloid,White-Tan	82.2	2.3	1.3	1.7	1.3	0.0	0.0	0.2	0.0	0.1	10.8
LYO20180731_H_06	Gour	86.6	0.8	0.2	0.4	0.4	0.0	0.0	0.0	0.0	0.0	11.4
LYO20190730_A_44	Gour	85.4	0.9	0.4	0.3	0.4	0.0	0.0	0.0	0.0	0.0	12.5
POS20180801_I_08	Mineral Crust, Orange	34.9	20.2	10.9	4.6	3.1	0.0	1.9	0.4	1.0	0.3	22.3
POS20190806_F_02	Mineral Crust, Orange	51.9	13.3	8.6	0.1	0.3	0.0	0.4	0.0	0.0	0.0	25.2
LYO20180731_H_19	Mineral Crust, White	85.8	2.9	0.4	0.1	0.4	0.0	0.8	0.0	0.0	0.0	9.5
GOL20180729_B_12	Polyps, Fingers	77.6	3.0	2.8	1.7	1.0	0.0	0.0	0.2	0.0	0.1	13.7
YEL20190804_Ac_02	Polyps, Fingers	65.4	1.5	0.6	3.2	1.4	0.0	1.5	0.2	0.2	0.1	25.9
POS20190806_D_05	Polyps, Orange	74.5	2.7	4.1	0.5	0.5	0.0	0.1	0.0	0.0	0.0	17.5
POS20190806_D_04	Polyps, Orange	49.3	8.9	11.3	0.3	0.4	0.0	1.0	0.1	0.0	0.0	28.6
CRI20180731_D_12	Polyps, White	40.3	17.1	10.5	0.2	0.7	0.0	1.4	0.1	0.0	0.0	29.5
GOL20180729_C_01	Polyps, White	60.7	8.1	6.3	0.4	0.4	0.0	1.5	0.1	0.0	0.0	22.4
GOL20180729_G_02	Polyps, White	59.6	9.1	8.5	1.7	1.0	0.0	0.3	0.2	0.1	0.1	19.2
PAN20190808_B_06	Polyps, White	66.3	3.4	4.9	2.2	0.9	0.0	1.0	0.2	0.2	0.1	20.7
POS20180801_D_09	Polyps, White	52.7	16.8	4.8	1.7	1.5	0.0	1.7	0.1	0.2	0.1	20.0
POS20190806_D_03	Polyps, White	33.6	13.7	14.1	0.2	0.3	0.0	2.0	0.1	0.1	0.0	35.7
SIL20180802_C_01	Polyps, White	56.9	13.0	5.4	1.3	1.1	0.0	0.7	0.1	0.0	0.1	21.1
CRI20190803_A_3.2	Polyps, White Specks	55.1	8.0	8.6	0.8	0.6	0.0	4.9	0.1	0.2	0.0	21.5
YEL20180802_B_06C	Polyps,White	51.8	11.0	8.3	0.3	0.4	0.0	1.4	0.0	0.0	0.0	26.6

Appendix B2: Trace Elements

Sample ID	Sample Type	S	V	Cr	Co	Ni	Cu	Zn	Ga	As	Rb	Sr
		ppm	ppm	ppm	ppm	ppm	ppm	ppm	ppm	ppm	ppm	ppm
LYO20180731_J_18	cauliflower, brown (knob)	0	55	16	6	19	169	17	4	0	4	57
LYO20180731_I_11	cauliflower,brown	0	63	13	5	19	185	13	7	0	2	35
POS20180801_E_16	cauliflower,white-tan	1365	239	17	3	26	34	9	0	7	3	64
POS20190806_A_13	cauliflower,white-tan	256	78	12	3	23	66	12	1	3	2	108
CRI20190804_C_1.1	cauliflower,white-tan, orange	1167	820	6	9	26	18	19	1	8	1	466
VAL20190805_D_02	cauliflower,white-tan,brown	72	57	13	0	15	251	0	3	0	0	73
CRI2019081_A_4.2	cauliflower,white-tan,red_orange	540	350	22	9	49	79	21	4	1	5	228
CRI20190804_B_01	Coralloid, flowery, white-tan	679	731	0	2	15	13	11	2	7	3	414
LYO20180731_J_14	Coralloid, white-tan	3673	148	15	3	26	59	13	1	0	1	238
GOL20190807_A_13	Coralloid, white-tan,gray	402	61	30	3	48	444	2	4	0	4	79
LYO20190810_A_19	Coralloid, white-tan,gray	180	84	15	0	15	98	12	8	1	7	56
POS20190806_B_06	Coralloid, yellow white tip	114	107	19	9	20	68	13	0	8	1	280
GOL20190807_A_11	Coralloid,brown	32	25	19	3	24	469	0	3	0	1	20
GOL20190807_B_12	Coralloid,brown	469	49	9	2	15	265	10	1	1	1	369
SIL20190808_D_01	Coralloid,brown	111	24	11	5	24	200	13	3	0	3	30
GOL20180729_G_03	Coralloid,white-tan	0	39	29	8	48	337	2	5	1	4	68
LYO20180731_H_06	Gour	3	80	13	5	25	350	4	12	0	1	19
LYO20190730_A_44	Gour	0	41	17	6	19	458	0	5	1	0	10
POS20180801_I_08	Mineral Crust, orange	1785	195	42	10	82	80	33	7	3	13	230
POS20190806_F_02	Mineral Crust, orange	0	595	0	4	15	16	12	0	0	2	65
LYO20180731_H_19	mineral crust, white	124	127	21	3	28	79	9	5	0	0	32
GOL20180729_B_12	Polyps, fingers	137	40	25	5	23	429	0	4	0	5	81
YEL20190804_Ac_02	Polyps, fingers	272	45	23	6	23	258	14	4	1	6	61
POS20190806_D_05	Polyps, Orange	619	76	18	3	18	176	9	2	1	0	7
POS20190806_D_04	polyps, orange	1713	120	5	3	16	169	6	1	1	4	30
CRI20180731_D_12	Polyps, white	1390	118	10	1	22	80	12	1	1	1	784
GOL20180729_C_01	Polyps, white	542	41	11	3	17	218	15	0	2	1	328
GOL20180729_G_02	Polyps, white	347	77	13	2	36	243	12	5	3	7	397
PAN20190808_B_06	Polyps, white	570	47	26	6	22	79	70	4	0	4	194
POS20180801_D_09	Polyps, white	1905	308	36	7	44	56	21	2	2	3	136
POS20190806_D_03	polyps, white	1959	194	4	6	17	146	4	2	4	4	105
SIL20180802_C_01	Polyps, white	1601	83	20	5	30	176	13	4	0	4	324
CRI20190803_A_3.2	Polyps, white specks	742	166	16	3	30	72	24	3	1	6	331
YEL20180802_B_06_C	Polyps,white	411	88	8	2	21	235	7	0	1	0	537

Appendix B3: Trace Elements Cont.

Sample ID	Sample Type	Y	Zr	Nb	Mo	Ba	Pb	Th	U
		ppm	ppm	ppm	ppm	ppm	ppm	ppm	ppm
LYO20180731_J_18	cauliflower, brown (knob)	21	28	0	2	126	2	2	1
LYO20180731_I_11	cauliflower,brown	19	27	0	2	108	5	0	1
POS20180801_E_16	cauliflower,white-tan	2	3	0	1	18	10	4	1
POS20190806_A_13	cauliflower,white-tan	2	4	0	1	16	0	0	1
CRI20190804_C_1.1	cauliflower,white-tan, orange	5	7	0	1	75	11	4	0
VAL20190805_D_02	cauliflower,white-tan,brown	12	14	0	1	88	4	0	1
CRI2019081_A_4.2	cauliflower,white-tan,red_orange	6	15	0	1	117	6	0	0
CRI20190804_B_01	Coralloid, flowery, white-tan	3	2	0	1	64	7	0	1
LYO20180731_J_14	Coralloid, white-tan	2	3	0	1	98	7	4	1
GOL20190807_A_13	Coralloid, white-tan,gray	11	23	0	1	48	2	4	2
LYO20190810_A_19	Coralloid, white-tan,gray	13	15	0	1	228	0	0	2
POS20190806_B_06	Coralloid, yellow white tip	4	2	0	1	87	5	0	2
GOL20190807_A_11	Coralloid,brown	7	5	0	2	19	0	0	0
GOL20190807_B_12	Coralloid,brown	16	10	0	1	18	0	3	2
SIL20190808_D_01	Coralloid,brown	14	10	0	1	44	0	0	2
GOL20180729_G_03	Coralloid,white-tan	24	23	0	1	112	4	1	2
LYO20180731_H_06	Gour	27	20	0	2	23	3	2	2
LYO20190730_A_44	Gour	18	13	0	2	16	0	1	0
POS20180801_I_08	Mineral Crust, orange	11	43	1	1	149	2	2	1
POS20190806_F_02	Mineral Crust, orange	2	2	0	1	4	2	1	0
LYO20180731_H_19	mineral crust, white	3	5	0	2	0	2	2	0
GOL20180729_B_12	Polyps, fingers	10	15	0	1	57	4	0	2
YEL20190804_Ac_02	Polyps, fingers	12	21	0	1	116	2	3	0
POS20190806_D_05	Polyps, Orange	6	5	0	1	48	0	1	1
POS20190806_D_04	polyps, orange	4	5	0	1	17	5	4	0
CRI20180731_D_12	Polyps, white	5	6	0	1	133	4	1	0
GOL20180729_C_01	Polyps, white	10	8	0	1	104	0	2	2
GOL20180729_G_02	Polyps, white	12	21	0	1	168	0	2	0
PAN20190808_B_06	Polyps, white	14	14	0	1	221	2	4	1
POS20180801_D_09	Polyps, white	6	10	0	1	47	0	5	2
POS20190806_D_03	polyps, white	4	4	0	1	14	3	1	0
SIL20180802_C_01	Polyps, white	8	14	0	1	125	6	1	0
CRI20190803_A_3.2	Polyps, white specks	2	10	0	1	188	2	0	0
YEL20180802_B_06_C	Polyps,white	6	5	0	1	129	2	0	1

Appendix C – XRF Data Cont.

Appendix C1: Major Elements and LOI. Note: this data set (Appendix C) represents XRF measurements where Cu, Ba, and Na_2O were not optimized. These data were not utilized in the text. The above XRF data (Appendix B) represent the corrected data set for speleothems and bare rock samples.

Sample ID	Sample Type	SiO_2	CaO	Fe_2O_3	MgO	Al_2O_3	P_2O_5	K_2O	MnO	Na_2O	TiO_2
		Wt.%	Wt.%	Wt.%	Wt.%	Wt.%	Wt.%	Wt.%	Wt.%	Wt.%	Wt.%
20190813_A_01	Devil's Homestead	48.57	11.13	13.08	5.14	17.61	0.20	0.88	0.41	0.00	1.20
CRI20180729_D_14	Bare Basalt	49.11	10.89	11.09	7.37	14.72	0.10	0.48	0.30	0.00	0.93
CRI20190804_B_01	Coralloid, Flowery	23.34	18.52	0.29	11.92	0.12	1.53	0.03	0.00	0.00	0.00
CRI20190804_C_1.1	Cauliflower	16.18	31.88	0.93	9.94	0.44	2.37	0.04	0.01	0.00	0.04
CRI20190804_A_4.2	Cauliflower	52.25	8.06	1.65	14.74	1.51	2.75	0.12	0.04	0.00	0.12
CRI20190804_A_3.2	Polyps	54.89	9.06	0.66	7.89	0.69	4.92	0.10	0.01	0.02	0.04
CRI20180731_C_10	Crust Basalt	52.31	11.68	12.13	5.89	14.60	0.00	0.57	0.33	0.00	0.95
CRI20180731_D_12	Polyps, White	38.82	18.93	0.69	9.98	0.23	1.39	0.14	0.00	0.00	0.01
GOL20180729_G_02	Polyps, White	59.47	10.07	1.07	7.94	1.45	0.27	0.22	0.02	0.00	0.08
GOL20180729_G_03	Coralloid	81.98	2.87	1.33	1.07	1.42	0.00	0.21	0.02	0.00	0.09
GOL20180729_B_12	Polyps, Fingers	77.21	3.59	1.11	2.49	1.43	0.00	0.19	0.02	0.00	0.07
GOL20180729_B12B	Bare Basalt	54.77	10.64	10.28	5.57	14.85	0.00	1.29	0.29	0.00	0.84
GOL20180729_C_01	Polyps	60.02	9.15	0.46	5.84	0.35	1.47	0.06	0.00	0.00	0.02
GOL20180729_D_67	Mat Basalt, White	56.11	9.66	9.38	5.46	14.60	0.00	1.54	0.26	0.00	0.84
GOL20180729_F_85	Mat Basalt, Tan	51.96	11.42	11.73	5.44	14.75	0.00	1.54	0.34	0.00	1.02
GOL20190807_A_11	Coralloid	86.31	1.53	0.44	0.66	0.20	0.00	0.05	0.00	0.00	0.02
GOL20190807_A_12	Turdite	63.24	6.74	10.14	1.86	10.33	0.12	2.71	0.28	0.00	1.71
GOL20190807_A_13	Coralloid	70.73	5.10	1.60	2.90	1.33	0.00	0.15	0.03	0.00	0.10
GOL20190807_B_12	Coralloid	61.57	10.50	0.52	6.43	0.43	0.27	0.06	0.00	0.00	0.02
HOP171108_08	Bare Basalt	57.13	9.85	9.54	5.71	12.96	0.00	1.27	0.27	0.00	0.82
LYD20180730_A_16	Soda Straw	57.70	8.95	11.59	3.32	11.86	0.38	1.81	0.31	0.00	2.00
LYD20180730_B_29	Cave Sediment	69.74	4.73	4.40	1.16	10.40	0.20	2.38	0.13	0.00	0.58
LYD20180730_C_47	Crust Basalt	52.75	11.17	13.11	3.74	13.59	0.32	1.64	0.35	0.00	1.88
LYD20180731_F_09	Crust Basalt	55.53	10.26	12.06	3.86	12.70	0.21	1.42	0.32	0.00	1.61
LYD20180731_H_06	Gour	86.09	1.29	0.42	0.11	0.40	0.00	0.05	0.00	0.00	0.01
LYO20180730_B_61	Mat Basalt,Yellow	54.09	9.75	11.77	3.70	14.38	0.40	1.54	0.32	0.00	1.71
LYO20180731_J_18	Cauliflower	83.76	1.82	0.98	0.48	0.52	0.00	0.08	0.00	0.00	0.02
LYO20180731_E_10	Cave Sediment	70.33	3.67	4.35	0.20	11.36	0.31	4.83	0.12	0.00	0.50
LYO20180731_H_01	Gour	85.55	1.36	0.45	0.23	0.21	0.00	0.05	0.00	0.00	0.01
LYO20180731_H_19	Crust	85.37	3.53	0.41	0.24	0.13	0.71	0.03	0.00	0.00	0.01
LYO20180731_I_11	Cauliflower	85.10	1.50	0.46	0.13	0.38	0.00	0.05	0.00	0.00	0.01
LYO20180731_J_14	Coralloid	43.87	21.20	0.44	4.89	0.18	1.25	0.04	0.00	0.00	0.01
LYO20180730_A_21	Bare Basalt	54.24	9.50	11.33	4.68	13.81	0.37	1.50	0.31	0.00	1.79
LYO20190730_A_44	Gour	84.95	1.38	0.38	0.24	0.28	0.00	0.04	0.00	0.00	0.01
LYO20190803_F_02	Surface Soil	71.68	3.50	4.22	0.00	10.98	0.00	5.37	0.10	0.00	0.50
LYO20190810_A_19	Coralloid, Black	81.93	2.06	0.56	0.27	0.95	0.00	0.14	0.00	0.00	0.03
LYO20190810_A_35	Crust Basalt	67.62	6.03	10.08	1.65	6.85	0.34	1.55	0.27	0.00	1.99
LYO20190810_H_01	Crust Basalt	53.87	11.83	10.80	4.15	11.50	0.60	1.58	0.30	0.00	1.76
PAN20190808_B_03	Coralloids	53.48	12.86	0.64	6.22	0.57	0.88	0.06	0.00	0.00	0.03
PAN20190808_B_06	Polyps, White	67.52	3.74	0.79	4.68	1.08	1.09	0.15	0.02	0.00	0.06
POS20180801_D_07	Tan Mat	51.37	11.27	9.82	8.06	13.59	0.34	0.22	0.28	0.00	0.81
POS20180801_E_16	Cauliflower	48.57	11.13	13.08	5.14	17.61	0.20	0.88	0.41	0.00	1.20

Appendix C2: Major Elements Cont.

Sample ID	Sample Type	SiO_2	CaO	Fe_2O_3	MgO	Al_2O_3	P_2O_5	K_2O	MnO	Na_2O	TiO_2
		Wt.%	Wt.%	Wt.%	Wt.%	Wt.%	Wt.%	Wt.%	Wt.%	Wt.%	Wt.%
POS20180801_D_09	Polyps	44.17	1.23	1.25	3.88	14.79	0.00	0.07	0.08	1.42	0.03
POS20180801_H_11	Ooze-Covered Basalt	45.64	16.92	12.84	6.28	11.85	0.00	0.31	0.95	0.03	0.34
POS20180801_I_08	Mineral Crust	34.28	3.89	3.47	10.27	22.72	0.00	0.43	0.28	1.92	0.08
POS20180806_D_05	Polyps, Orange	74.23	0.44	0.52	3.71	3.31	0.00	0.05	0.02	0.04	0.00
POS20190806_A_13	Cauliflower	38.70	0.30	0.44	10.76	18.87	0.00	0.04	0.02	1.84	0.00
POS20190806_B_06	Coralloid	29.53	0.10	0.27	7.41	16.62	0.00	0.03	0.00	1.91	0.00
POS20190806_B_08	Bare Basalt	49.47	15.01	12.49	7.32	12.92	0.00	0.26	0.96	0.00	0.36
POS20190806_D_03	Polyps	32.87	0.18	0.34	13.31	15.15	0.00	0.08	0.01	2.06	0.00
POS20190806_D_04	Polyps	48.76	0.26	0.36	10.65	10.00	0.00	0.06	0.01	1.00	0.00
POS20190806_F_02	Mineral Crust	50.88	0.26	0.37	7.96	14.74	0.00	0.03	0.01	0.41	0.00
POS20190810_C_02	Cave Sediment	50.26	15.13	14.96	3.31	9.99	0.00	1.61	1.67	0.41	0.37
SIL20180802_A_14	Bare Basalt	53.07	14.61	10.67	5.07	10.77	0.00	1.29	0.92	0.00	0.29
SIL20180802_B_14	Mat Basalt,Yellow	51.35	14.74	11.86	5.06	11.90	0.00	1.36	1.09	0.00	0.34
SIL20180802_C_01	Polyps, White	55.98	1.12	1.15	4.97	14.44	0.00	0.13	0.07	0.70	0.02
SIL20180802_C_03	Mat Basalt, Yellow	60.28	12.03	8.35	5.12	8.62	0.00	1.05	0.72	0.00	0.23
SIL20190808_A_03	Coralloid, White	59.01	12.76	9.34	5.31	9.52	0.00	0.85	0.75	0.00	0.26
SIL20190808_D_01	Coralloid	84.09	0.87	0.77	1.01	1.67	0.00	0.08	0.04	0.00	0.01
SIL20190808_E_02	Surface Soil	64.32	13.66	5.80	0.55	4.50	0.00	3.40	0.71	0.20	0.18
VAL171109_14	Bare Basalt	52.66	14.61	12.69	4.24	11.03	0.00	1.63	1.72	0.37	0.35
VAL20190802_A_07	Cave Sediment	38.28	8.69	5.19	0.80	7.21	0.57	1.00	0.57	9.06	0.37
VAL20190802_A_10	Mat Basalt,Yellow	52.45	14.22	11.28	4.43	9.82	0.00	1.57	1.58	0.97	0.31
VAL20190805_D_02	Cauliflower	76.26	0.24	0.40	0.39	7.97	0.00	0.03	0.01	0.04	0.00
VAL20190805_D_09	Surface Soil	62.38	10.23	3.38	0.08	2.95	0.00	4.26	0.40	0.00	0.09
YEL171027_10	Mat Basalt,Yellow	56.34	13.23	9.29	5.06	10.26	0.00	1.28	0.84	0.55	0.27
YEL171111_4	Bare Basalt Oxidized	53.22	14.79	11.09	5.81	10.84	0.00	1.43	0.90	0.01	0.31
YEL20190804_A_02	Mat Basalt, Yellow	60.36	12.40	8.22	4.93	8.79	0.00	1.11	0.74	0.01	0.23
YEL20190804_Ac_02	Polyps	65.48	2.68	1.49	0.44	1.94	0.00	0.24	0.12	1.50	0.03
YEL20190804_C_02	Crust Basalt	54.12	11.84	7.59	7.80	10.71	0.00	1.06	0.67	0.57	0.21
YEL20190804_D_05	Ooze Covered Basalt	52.24	16.07	11.30	5.23	11.27	0.00	1.26	0.97	0.00	0.32
YEL20180802_B_06_C	Polyp	51.16	0.37	0.43	7.61	12.12	0.00	0.05	0.02	1.35	0.00

Appendix C3: Trace Elements

Sample ID	Sample Type	Y	Zr	Nb	Ba	Ni	Cu	Zn	Cr	Co	Rb
		ppm	ppm	ppm	ppm	ppm	ppm	ppm	ppm	ppm	ppm
20190813_A_01	Devil's Homestead	60	257	14	292	132	531	70	262	0	153
CRI20180729_D_14	Bare Basalt	47	140	5	214	174	361	62	234	2	62
CRI20190804_B_01	Coralloid, Flowery	0	14	0	1	0	28	10	6	2	10
CRI20190804_C_1.1	Cauliflower	4	30	0	6	0	88	16	5	3	14
CRI20190804_A_4.2	Cauliflower	3	32	0	185	48	352	20	44	2	34
CRI20190804_A_3.2	Polyps	2	27	0	221	11	326	20	12	3	37
CRI20180731_C_10	Crust Basalt	67	171	8	212	190	593	67	263	0	84
CRI20180731_D_12	Polyps, White	0	39	0	128	0	389	13	0	2	20
GOL20180729_G_02	Polyps, White	16	42	0	88	16	1101	13	22	0	37
GOL20180729_G_03	Coralloid	40	30	0	71	45	1531	8	22	2	33
GOL20180729_B_12	Polyps, Fingers	14	21	0	0	7	2040	9	29	3	35
GOL20180729_B12B	Bare Basalt	33	206	9	516	178	1117	62	250	5	248
GOL20180729_C_01	Polyps	17	20	0	8	1	1082	16	5	3	7
GOL20180729_D_67	Mat Basalt, White	32	180	4	398	138	1462	52	222	0	240
GOL20180729_F_85	Mat Basalt, Tan	47	243	10	423	179	1879	69	279	0	267
GOL20190807_A_11	Coralloid	7	6	0	0	8	2039	2	17	3	3
GOL20190807_A_12	Turdite	66	430	19	860	0	1783	60	27	0	569
GOL20190807_A_13	Coralloid	17	29	0	18	31	1951	11	39	3	29
GOL20190807_B_12	Coralloid	34	27	0	1	10	1229	11	4	2	5
HOP171108_08	Bare Basalt	38	206	8	467	160	1072	61	207	0	242
LYD20180730_A_16	Soda Straw	77	468	24	623	40	682	74	148	0	351
LYD20180730_B_29	Cave Sediment	30	355	4	1024	42	683	61	7	0	345
LYD20180730_C_47	Crust Basalt	85	474	26	433	62	624	87	186	0	298
LYD20180731_F_09	Crust Basalt	68	385	16	399	80	611	82	210	0	293
LYD20180731_H_06	Gour	56	28	0	0	27	1705	10	2	0	13
LYO20180730_B_61	Mat Basalt,Yellow	72	370	19	494	76	711	77	178	0	234
LYO20180731_J_18	Cauliflower	36	38	0	61	3	730	15	15	0	30
LYO20180731_E_10	Cave Sediment	0	482	17	1472	0	135	60	8	0	1098
LYO20180731_H_01	Gour	54	36	0	0	13	2184	5	16	2	17
LYO20180731_H_19	Crust	4	5	0	0	9	357	10	15	3	2
LYO20180731_I_11	Cauliflower	35	37	0	37	12	868	16	0	3	11
LYO20180731_J_14	Coralloid	0	13	0	19	4	290	12	3	2	6
LYO20180730_A_21	Bare Basalt	68	356	19	596	62	340	72	178	0	241
LYO20190730_A_44	Gour	32	16	0	0	11	2121	2	5	1	13
LYO20190803_F_02	Surface Soil	0	534	12	1657	0	86	64	12	0	1280
LYO20190810_A_19	Coralloid, Black	17	20	0	272	3	442	12	18	5	49
LYO20190810_A_35	Crust Basalt	78	453	24	552	0	750	74	17	0	318
LYO20190810_H_01	Crust Basalt	64	381	23	569	62	913	70	144	0	275
PAN20190808_B_03	Coralloids	11	18	0	59	0	165	13	12	0	12
PAN20190808_B_06	Polyps, White	17	24	0	302	3	348	52	18	2	32
POS20180801_D_07	Tan Mat	47	99	5	155	198	393	53	287	0	14
POS20180801_E_16	Cauliflower	0	5	0	0	7	159	10	7	1	17

Appendix C4: Trace Elements Cont.

Sample ID	Sample Type	Y	Zr	Nb	Ba	Ni	Cu	Zn	Cr	Co	Rb
		ppm	ppm	ppm	ppm	ppm	ppm	ppm	ppm	ppm	ppm
POS20180801_D_09	Polyps	5	15	0	24	18	207	16	51	3	19
POS20180801_H_11	Ooze-Covered Basalt	52	144	7	161	245	1015	77	769	3	56
POS20180801_I_08	Mineral Crust	10	73	1	139	83	345	30	94	0	85
POS20180806_D_05	Polyps, Orange	12	6	0	0	8	832	10	7	3	8
POS20190806_A_13	Cauliflower	0	7	0	0	2	287	12	2	3	23
POS20190806_B_06	Coralloid	0	9	0	0	0	175	9	0	0	9
POS20190806_B_08	Bare Basalt	61	140	10	164	234	619	70	349	3	18
POS20190806_D_03	Polyps	3	8	0	4	0	680	10	12	1	27
POS20190806_D_04	Polyps	3	4	0	0	0	796	8	8	1	19
POS20190806_F_02	Mineral Crust	0	4	0	0	0	65	12	11	2	12
POS20190810_C_02	Cave Sediment	70	493	34	1135	111	495	119	182	0	299
SIL20180802_A_14	Bare Basalt	46	217	10	458	156	430	66	256	0	228
SIL20180802_B_14	Mat Basalt,Yellow	56	284	12	475	279	409	75	269	0	283
SIL20180802_C_01	Polyps, White	13	33	0	127	10	816	13	25	2	23
SIL20180802_C_03	Mat Basalt, Yellow	31	159	6	321	120	626	53	223	2	196
SIL20190808_A_03	Coralloid, White	36	156	4	326	155	1388	51	224	0	144
SIL20190808_D_01	Coralloid	25	11	0	24	7	927	11	16	2	15
SIL20190808_E_02	Surface Soil	0	404	9	1454	7	153	70	42	0	885
VAL171109_14	Bare Basalt	74	400	20	495	89	419	93	254	0	299
VAL20190802_A_07	Cave Sediment	36	195	1	1906	49	2159	316	65	0	217
VAL20190802_A_10	Mat Basalt,Yellow	62	323	16	570	75	864	89	210	0	223
VAL20190805_D_02	Cauliflower	25	17	0	0	0	1201	10	12	4	4
VAL20190805_D_09	Surface Soil	0	387	14	1298	0	93	47	4	0	946
YEL171027_10	Mat Basalt,Yellow	41	205	8	495	187	689	59	188	1	221
YEL171111_4	Bare Basalt Oxidized	51	237	18	479	173	770	66	250	1	304
YEL20190804_A_02	Mat Basalt, Yellow	35	160	5	288	123	801	49	189	1	181
YEL20190804_Ac_02	Polyps	21	31	0	119	13	1205	14	27	1	39
YEL20190804_C_02	Crust Basalt	26	158	7	259	103	641	44	162	3	176
YEL20190804_D_05	Ooze Covered Basalt	62	244	11	529	185	733	66	242	0	208
YEL20180802_B_06_C	Polyp	8	28	0	42	7	1155	10	6	2	12

Appendix C5: Trace Elements Cont.

Sample ID	Sample Type	Sr	Th	U	V	As	S	Mo	Ga	Pb
		ppm	ppm	ppm	ppm	ppm	ppm	ppm	ppm	ppm
20190813_A_01	Devil's Homestead	226	14	5	342	0	0	2	22	25
CRI20180729_D_14	Bare Basalt	259	5	5	311	0	0	1	22	9
CRI20190804_B_01	Coralloid, Flowery	287	1	3	693	8	589	0	3	35
CRI20190804_C_1.1	Cauliflower	424	5	5	1073	13	1273	1	5	54
CRI20190804_A_4.2	Cauliflower	217	4	4	466	2	652	1	7	20
CRI20190804_A_3.2	Polyps	310	1	4	208	0	871	1	6	18
CRI20180731_C_10	Crust Basalt	312	7	6	353	0	0	1	28	25
CRI20180731_D_12	Polyps, White	724	0	5	129	2	1662	1	5	23
GOL20180729_G_02	Polyps, White	357	2	4	101	1	491	1	6	14
GOL20180729_G_03	Coralloid	60	1	5	50	0	0	1	6	19
GOL20180729_B_12	Polyps, Fingers	75	2	5	27	2	231	1	5	15
GOL20180729_B12B	Bare Basalt	309	20	7	279	3	0	1	26	34
GOL20180729_C_01	Polyps	302	0	5	49	0	651	1	6	11
GOL20180729_D_67	Mat Basalt, White	237	21	6	262	4	0	2	19	65
GOL20180729_F_85	Mat Basalt, Tan	330	18	7	326	2	0	2	25	50
GOL20190807_A_11	Coralloid	16	2	6	0	0	156	1	1	15
GOL20190807_A_12	Turdite	193	26	6	396	6	0	3	21	47
GOL20190807_A_13	Coralloid	66	1	5	61	0	404	1	7	20
GOL20190807_B_12	Coralloid	343	2	4	55	2	592	1	4	17
HOP171108_08	Bare Basalt	285	16	6	253	2	0	1	22	19
LYD20180730_A_16	Soda Straw	266	19	6	419	6	0	2	26	69
LYD20180730_B_29	Cave Sediment	687	4	7	104	7	124	2	26	44
LYD20180730_C_47	Crust Basalt	359	17	8	409	9	0	3	31	51
LYD20180731_F_09	Crust Basalt	349	22	7	376	7	0	2	29	52
LYD20180731_H_06	Gour	19	7	6	79	0	54	1	9	0
LYO20180730_B_61	Matbasalt,Yellow	335	21	7	419	3	0	2	28	26
LYO20180731_J_18	Cauliflower	46	0	6	68	0	50	1	10	10
LYO20180731_E_10	Cave Sediment	202	30	7	55	15	0	3	26	78
LYO20180731_H_01	Gour	24	0	5	102	0	0	1	4	11
LYO20180731_H_19	Crust	29	1	4	137	0	188	1	7	9
LYO20180731_I_11	Cauliflower	29	0	6	40	0	34	1	12	9
LYO20180731_J_14	Coralloid	218	1	5	173	2	4148	1	4	22
LYO20180730_A_21	Bare Basalt	256	14	5	421	2	0	2	23	43
LYO20190730_A_44	Gour	9	1	5	63	0	0	1	4	3
LYO20190803_F_02	Surface Soil	183	28	9	28	16	0	3	37	84
LYO20190810_A_19	Coralloid, Black	50	2	5	98	2	276	1	9	7
LYO20190810_A_35	Crust Basalt	161	16	6	431	6	0	2	25	33
LYO20190810_H_01	Crust Basalt	274	15	5	369	4	423	2	22	44
PAN20190808_B_03	Coralloids	249	3	4	221	0	1634	1	6	13
PAN20190808_B_06	Polyps, White	167	3	5	49	0	825	1	8	13
POS20180801_D_07	Tan Mat	257	2	5	345	0	0	1	23	21
POS20180801_E_16	Cauliflower	59	2	4	315	11	1533	1	3	44

Appendix C6: Trace Elements Cont.

Sample ID	Sample Type	Sr	Th	U	V	As	S	Mo	Ga	Pb
		ppm	ppm	ppm	ppm	ppm	ppm	ppm	ppm	ppm
POS20180801_D_09	Polyps	93	2	3	318	2	1834	1	5	17
POS20180801_H_11	Ooze-Covered Basalt	349	16	7	413	3	3624	1	23	25
POS20180801_I_08	Mineral Crust	223	2	4	245	5	2042	1	11	46
POS20180806_D_05	Polyps, Orange	4	0	5	87	0	797	1	6	7
POS20190806_A_13	Cauliflower	99	0	3	74	1	339	1	3	19
POS20190806_B_06	Coralloid	143	2	3	71	5	68	0	3	22
POS20190806_B_08	Bare Basalt	346	20	6	366	0	0	1	21	23
POS20190806_D_03	Polyps	98	2	3	239	7	2263	1	2	28
POS20190806_D_04	Polyps	26	0	4	141	2	1960	1	5	18
POS20190806_F_02	Mineral Crust	61	4	4	804	0	0	1	5	9
POS20190810_C_02	Cave Sediment	829	24	9	353	0	0	3	42	54
SIL20180802_A_14	Bare Basalt	302	13	5	284	2	1688	2	22	34
SIL20180802_B_14	Mat Basalt,Yellow	400	14	10	389	2	0	2	31	19
SIL20180802_C_01	Polyps, White	299	3	4	117	0	1821	1	5	18
SIL20180802_C_03	Mat Basalt, Yellow	223	6	4	220	4	62	1	18	32
SIL20190808_A_03	Coralloid, White	254	16	7	260	3	435	1	19	39
SIL20190808_D_01	Coralloid	26	1	5	43	0	245	1	7	10
SIL20190808_E_02	Surface Soil	335	27	8	119	13	166	3	30	75
VAL171109_14	Bare Basalt	351	11	8	410	9	0	2	29	34
VAL20190802_A_07	Cave Sediment	504	8	5	136	5	4213	2	32	35
VAL20190802_A_10	Mat Basalt,Yellow	374	19	6	337	7	0	2	26	69
VAL20190805_D_02	Cauliflower	66	0	5	34	1	142	1	7	16
VAL20190805_D_09	Surface Soil	146	24	6	33	10	50	2	25	66
YEL171027_10	Mat Basalt,Yellow	291	11	5	292	5	0	1	22	38
YEL171111_4	Bare Basalt Oxidized	312	20	8	289	5	0	2	22	53
YEL20190804_A_02	Mat Basalt, Yellow	217	14	4	256	3	0	1	17	33
YEL20190804_Ac_02	Polyps	56	0	4	59	1	371	1	6	13
YEL20190804_C_02	Crust Basalt	275	12	6	223	3	683	1	15	15
YEL20190804_D_05	Ooze Covered Basalt	350	22	8	275	1	0	1	25	49
YEL20180802_B_06_C	Polyp	493	1	4	85	3	531	1	3	19

Appendix D – Handheld XRF Data

Appendix D1: Major Elements

The following XRF data was collected utilizing a hand-held Bruker instrument. None of these data were utilized in the text – their inclusion here is meant to illustrate the limitations of hand-held XRF analyses in speleothem characterization. The measurement of many elements resulted in poor accuracy, including Mg, P, and the majority of trace elements. While not intended as a methods development study, it can be nevertheless stated that traditional application of hand-held XRF instruments is better suited as a field tool, rather than as a laboratory method. A subset of samples analyzed via this technique are included.

Sample ID	Sample Type	SiO_2	CaO	Fe_2O_3	MgO	Al_2O_3	P_2O_5	K_2O	MnO	Na_2O	TiO_2
		Wt.%	Wt.%	Wt.%	Wt.%	Wt.%	Wt.%	Wt.%	Wt.%	Wt.%	Wt.%
CRI20180731_B_13	Crust Basalt	69.16	0.57	0.00	0.00	0.40	0.07	0.00	0.05	0.80	0.05
CRI20180731_Backroom	Cauliflower	50.35	8.81	0.00	5.19	0.00	0.99	0.00	0.03	0.79	0.02
CRI20180731_C_10	Crust Basalt: Popcorn	37.14	7.58	7.55	2.06	11.77	0.05	0.27	0.09	0.56	0.70
CRI20180731_C_11	Crust Basalt	44.45	6.97	7.31	2.44	10.84	0.07	0.25	0.09	0.51	0.68
CRI20180731_D_12	Polyps	31.41	19.16	0.41	3.79	0.00	0.66	0.04	0.02	0.71	0.03
GOL20180729_B_13	Polyps	66.30	3.34	0.00	1.03	0.00	0.09	0.00	0.04	0.81	0.00
GOL20180729_C_02	Crust Basalt	41.27	4.61	4.65	0.66	7.17	0.03	0.65	0.08	0.72	0.44
GOL20180729_E_14	Tan Ooze Basalt Chips	36.56	7.15	7.02	1.66	12.66	0.08	1.05	0.09	0.58	0.68
GOL20180729_G_02	Polyps	47.82	8.39	0.46	2.33	0.75	0.12	0.03	0.03	0.83	0.07
GOL20180729_G_03	Coralloid	72.06	1.67	0.91	0.00	1.18	0.10	0.00	0.05	0.70	0.09
LYO20180730_A_16	Sodastraw	42.72	5.49	3.58	1.14	9.77	0.17	1.62	0.10	0.54	1.73
LYO20180730_B_12	Yellow Mat Basalt	36.98	7.48	5.77	1.60	10.46	0.12	0.97	0.09	0.57	1.15
LYO20180730_B_29	Soil	54.99	2.87	3.06	0.04	8.96	0.11	1.75	0.06	0.69	0.43
LYO20180731_B_60	Sodastraw	37.94	4.52	6.62	1.07	6.97	0.13	1.25	0.12	0.47	1.66
LYO20180730_B_61	Sodastraw	37.21	6.52	5.34	1.40	10.80	0.13	1.15	0.10	0.55	1.35
LYO20180730_C_47	Crust Basalt	33.11	6.39	5.44	0.64	9.23	0.08	0.94	0.08	0.69	1.12
LYO20180731_E_10	Soil	47.96	1.63	2.88	0.00	8.42	0.07	3.25	0.05	0.82	0.32
LYO20180731_F_08	Polyps	71.63	0.94	1.35	0.00	1.24	0.10	0.10	0.05	0.69	0.28
LYO20180731_F_09	Crust Basalt	39.67	6.11	5.03	1.40	10.14	0.10	0.85	0.09	0.57	1.02
LYO20180731_G_10	Cauliflower	63.48	4.95	0.00	0.49	0.00	0.59	0.00	0.04	0.67	0.00
LYO20180731_H_01	Coralloid	79.01	0.19	0.00	0.00	0.00	0.12	0.00	0.04	0.69	0.00
LYO20180731_H_06	Coralloid	75.20	0.09	0.00	0.00	0.00	0.09	0.00	0.05	0.73	0.00
LYO20180731_H_15	Coralloid	78.61	0.21	0.00	0.00	0.04	0.11	0.00	0.04	0.70	0.02
LYO20180731_H_17_A	Coralloid	74.99	2.09	0.00	0.00	0.00	0.29	0.00	0.04	0.72	0.00
LYO20180731_H_17_B	Crust	77.80	0.40	0.00	0.00	0.26	0.11	0.00	0.04	0.71	0.04
LYO20180731_H_19	Crust	74.35	2.10	0.00	0.00	0.00	0.29	0.00	0.04	0.70	0.00
LYO20180731_I_11	Cauliflower	77.60	0.47	0.00	0.00	0.00	0.10	0.00	0.04	0.72	0.00
LYO20180731_J_12	Crust Basalt	41.56	8.73	5.75	1.75	9.91	0.16	0.77	0.08	0.50	1.03
LYO20180731_J_14	Coralloid	37.40	20.62	0.25	2.17	0.00	0.73	0.00	0.02	0.59	0.02
LYO20180731_J_18	Cauliflower	75.18	0.47	0.00	0.00	0.43	0.09	0.00	0.04	0.75	0.00
POS20180801_B_13	Crust Basalt	36.99	8.40	7.23	2.54	11.61	0.08	0.11	0.11	0.46	1.03
POS20180801_D_05	Crust Basalt	37.76	8.22	7.19	2.64	11.78	0.26	0.03	0.10	0.54	0.75
POS20180801_D_07	Crust Basalt	39.64	7.93	6.90	3.89	11.35	0.16	0.01	0.09	0.56	0.64
POS20180801_D_09	Polyps	43.45	14.33	1.91	2.88	1.18	0.27	0.00	0.03	0.65	0.25
POS20180801_E_15	Crust Basalt	39.47	6.86	6.71	1.59	12.64	0.06	1.24	0.09	0.56	0.71
POS20180801_E_16	Cauliflower	27.66	19.02	0.23	4.80	0.00	0.39	0.00	0.02	0.77	0.01
POS20180801_G_08	Crust Basalt	33.25	7.81	8.12	2.41	13.59	0.05	0.06	0.10	0.54	0.72

Appendix D2: Trace Elements

Sample ID	Sample Type	Y	Zr	Nb	Ba	Ni	Cu	Zn	Cr	Co	Rb
		ppm	ppm	ppm	ppm	ppm	ppm	ppm	ppm	ppm	ppm
CRI20180731_B_13	Crust basalt	11	52	19	0	175	175	112	203	3	0
CRI20180731_Backroom	Cauliflower	0	21	7	0	114	221	0	134	2	17
CRI20180731_C_10	Crust Basalt: popcorn	28	83	5	374	65	34	59	61	23	21
CRI20180731_C_11	Crust basalt	27	81	6	358	74	36	51	69	22	21
CRI20180731_D_12	Polyps	2	0	9	0	74	14	58	89	2	4
GOL20180729_B_13	Polyps	2	28	11	0	163	260	0	178	1	13
GOL20180729_C_02	Crust basalt	23	88	7	208	144	255	201	129	15	41
GOL20180729_E_14	Tan ooze basalt chips	30	110	7	2	104	163	12	69	22	53
GOL20180729_G_02	Polyps	10	26	9	0	126	226	33	143	3	17
GOL20180729_G_03	Coralloid	22	47	11	0	165	473	0	178	5	15
LYO20180730_A_16	Sodastraw	0	0	0	0	54	67	52	0	23	0
LYO20180730_B_12	Yellow mat basalt	0	0	0	0	65	51	55	18	22	0
LYO20180730_B_29	Soil	0	0	0	0	105	103	74	102	10	0
LYO20180731_B_60	Sodastraw	0	0	0	0	41	146	7	0	35	0
LYO20180730_B_61	Sodastraw	0	0	0	0	58	31	67	0	24	0
LYO20180730_C_47	crust basalt	40	179	8	789	48	42	73	7	21	45
LYO20180731_E_10	Soil	29	201	13	436	90	46	108	107	9	140
LYO20180731_F_08	Polyps	20	75	14	11	189	195	0	151	6	25
LYO20180731_F_09	Crust basalt	37	159	8	637	96	141	135	58	20	42
LYO20180731_G_10	Cauliflower	16	55	11	0	226	2372	0	189	1	12
LYO20180731_H_01	Coralloid	25	50	12	0	193	1012	0	201	1	15
LYO20180731_H_06	Coralloid	28	47	13	0	231	1003	0	218	1	12
LYO20180731_H_15	Coralloid	40	65	15	0	197	1244	0	200	1	8
LYO20180731_H_17_A	Coralloid	0	35	8	0	178	43	13	184	1	15
LYO20180731_H_17_B	crust	33	74	16	0	209	1164	0	195	2	10
LYO20180731_H_19	Crust	0	35	8	0	145	112	15	181	1	15
LYO20180731_I_11	Cauliflower	0	0	0	0	176	277	0	199	1	0
LYO20180731_J_12	Crust Basalt	32	144	7	710	56	51	50	29	21	38
LYO20180731_J_14	Coralloid	0	21	7	0	57	22	43	88	1	12
LYO20180731_J_18	Cauliflower	25	57	16	0	174	146	22	198	1	9
POS20180801_B_13	crust basalt	36	94	5	368	50	48	53	55	25	10
POS20180801_D_05	Crust basalt	24	73	5	0	62	39	57	69	22	12
POS20180801_D_07	Crust basalt	22	67	6	0	73	24	60	80	21	11
POS20180801_D_09	Polyps	10	53	6	0	77	84	23	96	6	14
POS20180801_E_15	Crust basalt	28	112	7	557	68	31	69	59	21	50
POS20180801_E_16	Cauliflower	2	35	10	0	57	17	62	77	1	21
POS20180801_G_08	Crust basalt	23	76	5	0	72	40	57	115	24	20

Appendix E - Electron Microprobe Elemental Maps

Quantitative Electron Microprobe analyses were performed at the Texas A&M University Materials Characterization Facility using a Cameca SXFive electron microprobe equipped with a LaB_6 source, a thermos EDS system, and a CL (Cathodoluminescence) detector. The scan area consisted of a rectangular 2568 by 996 μm section within a polyp speleothem (CRI20180731_D_12) thin section. Maps are oriented such the rightmost side is the upward direction of the speleothem.

Appendix E1: Grayscale Backscatter Image of CRI20180731_D_12 Transect Area

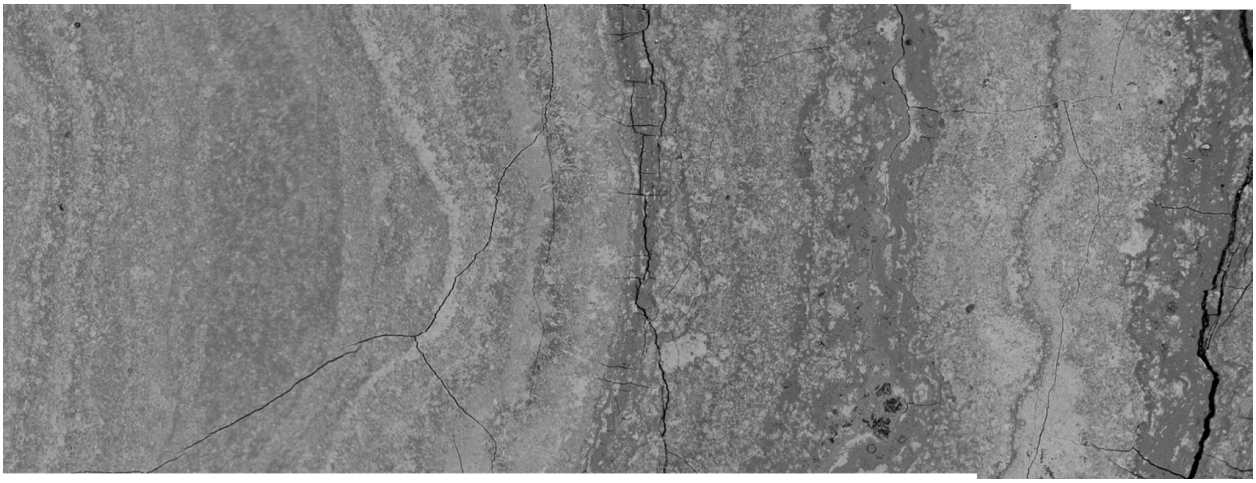

Backscattered electron image of the CRI20180731_D_12 polyp transect area. Leftmost side of the image represents the basalt portion of the transect, and the rightmost side towards the top of the transect (closest to the tip of the polyp speleothem).

Appendix E2: Elemental Maps: SiO_2, CaO, MgO, P_2O_5, SrO, SO_3

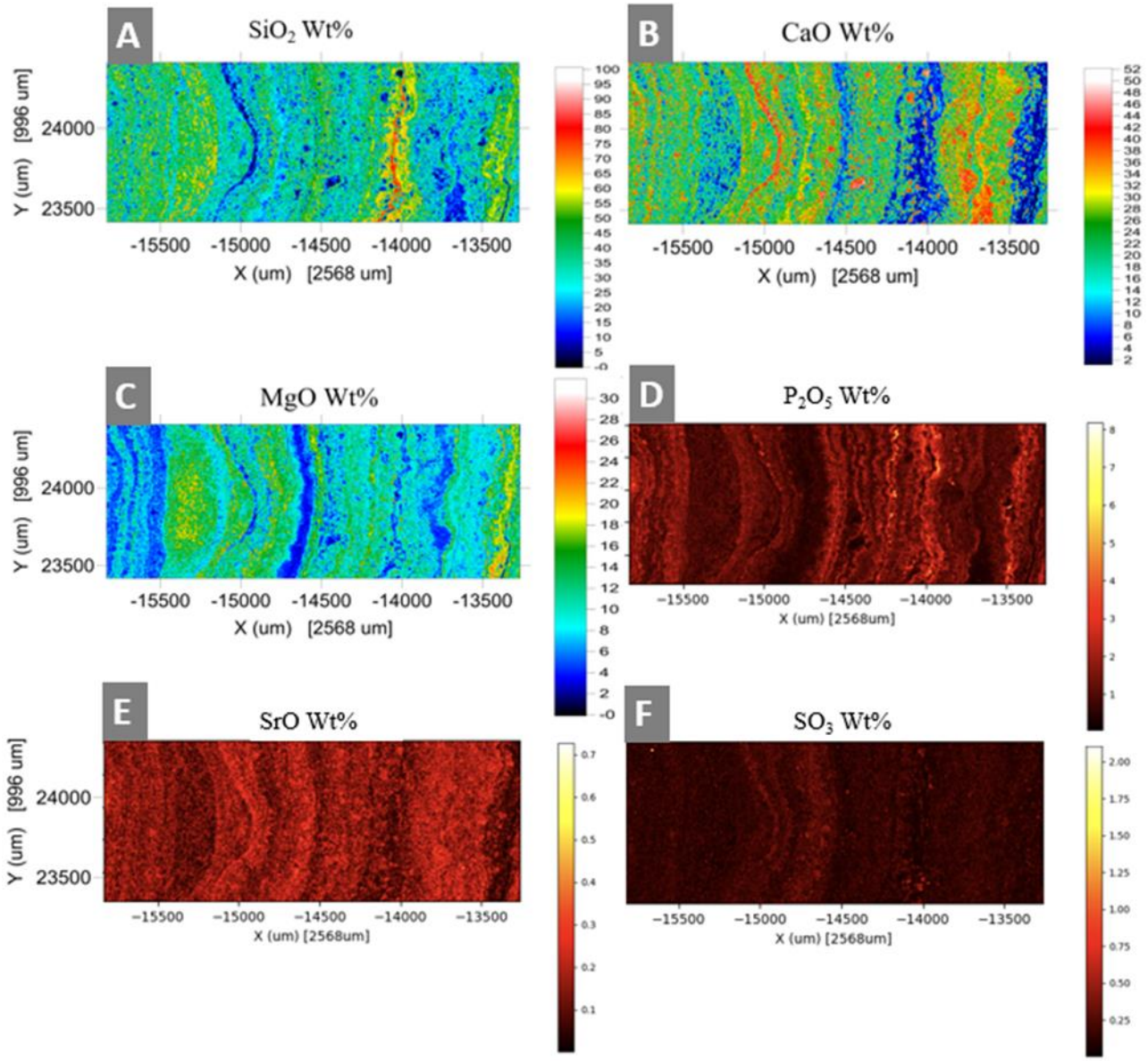

Elemental distribution maps of CRI20180731-D-12 polyp speleothem transect. A) SiO_2 map; B) CaO map; C) MgO map; D) P_2O_5 map; E) SrO map; F) SO_3 map. Maps A-C wt.% are represented by the following color scale: Black denotes below detection limits, while blue grading into cyan, green, yellow, orange, red, and white denotes increasing concentrations. Maps D-F are represented by the following color scale: Black denotes below detection limits, while maroon grading into red, orange, yellow, and white denote increasing concentrations.

Appendix E3: Elemental Maps: Al_2O_3, FeO, K_2O

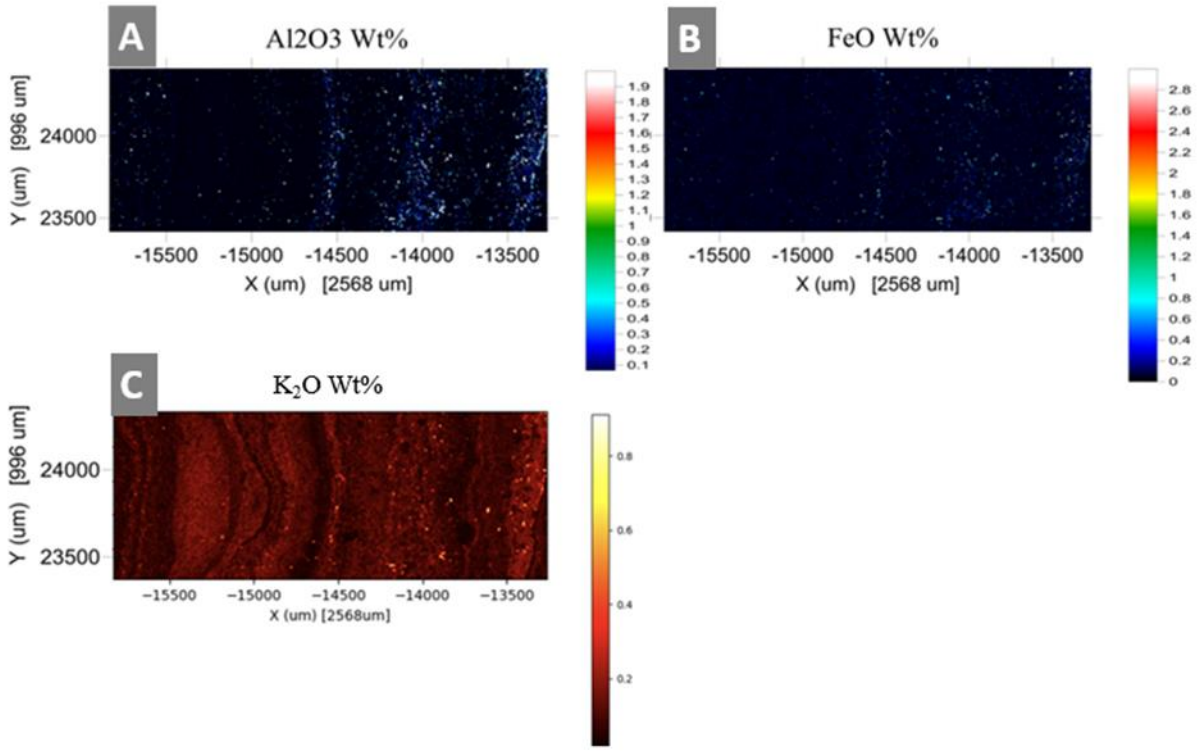

Elemental distribution maps of CRI20180731-D-12 polyp speleothem transect. A) Al_2O_3 map; B) FeO map; C) K_2O map. Maps A-B wt.% are represented by the following color scale: Black denotes below detection limits, while blue grading into cyan, green, yellow, orange, red, and white denotes increasing concentrations. Map C is represented by the following color scale: Black denotes below detection limits, while maroon grading into red, orange, yellow, and white denote increasing concentrations.

Appendix E4: Cu2O Elemental Map

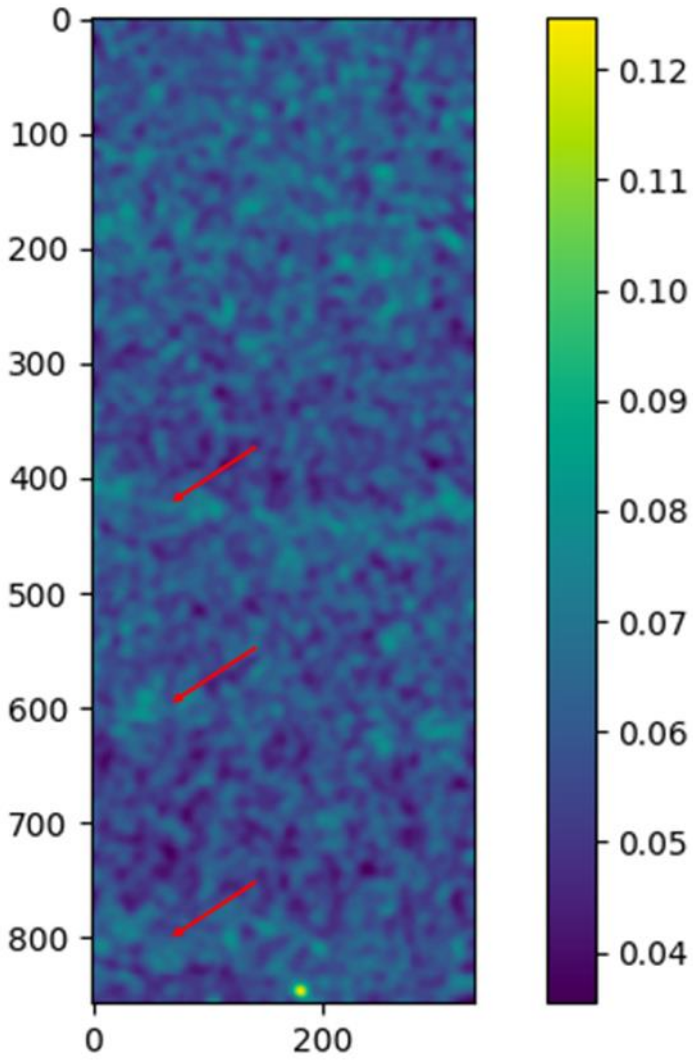

Elemental map of Cu_2O in polyp speleothem CRI20180731_D_12. Arrows point to location of Cu_2O rich lamina, which may correspond to SiO_2 rich lamina. Note that this map shifted 60 degrees clockwise from the other maps, leading to an "upside-down" orientation (the bottom of the image represents nearest to the tip of the speleothem).

Appendix F - X-ray Diffraction Spectra

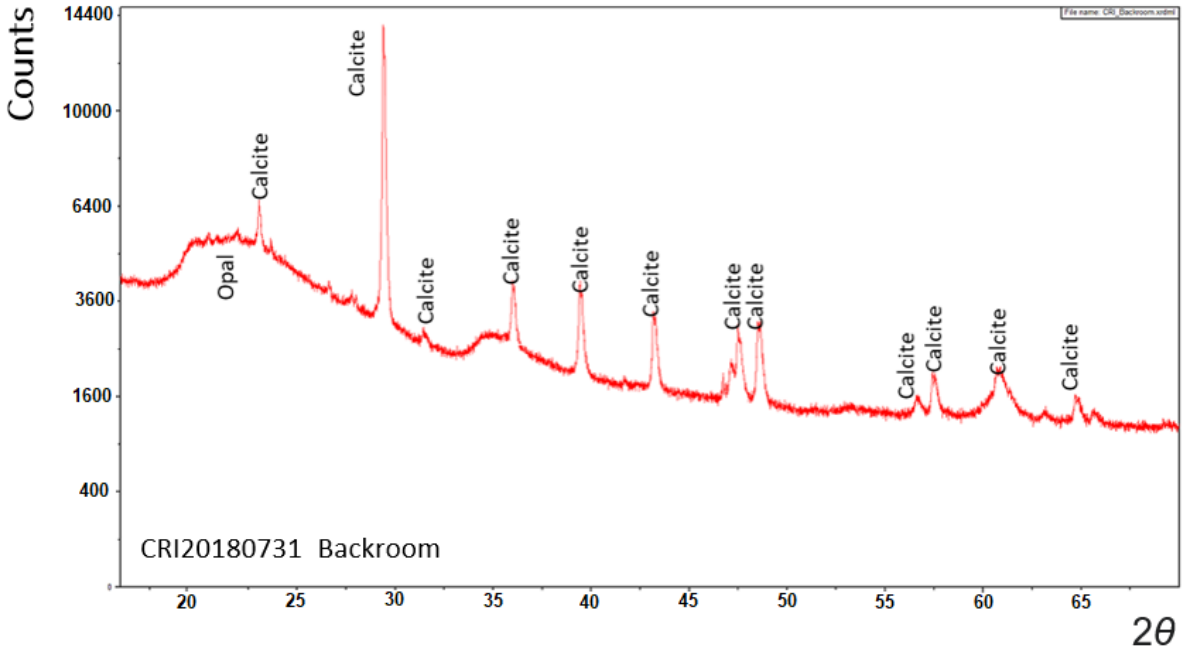

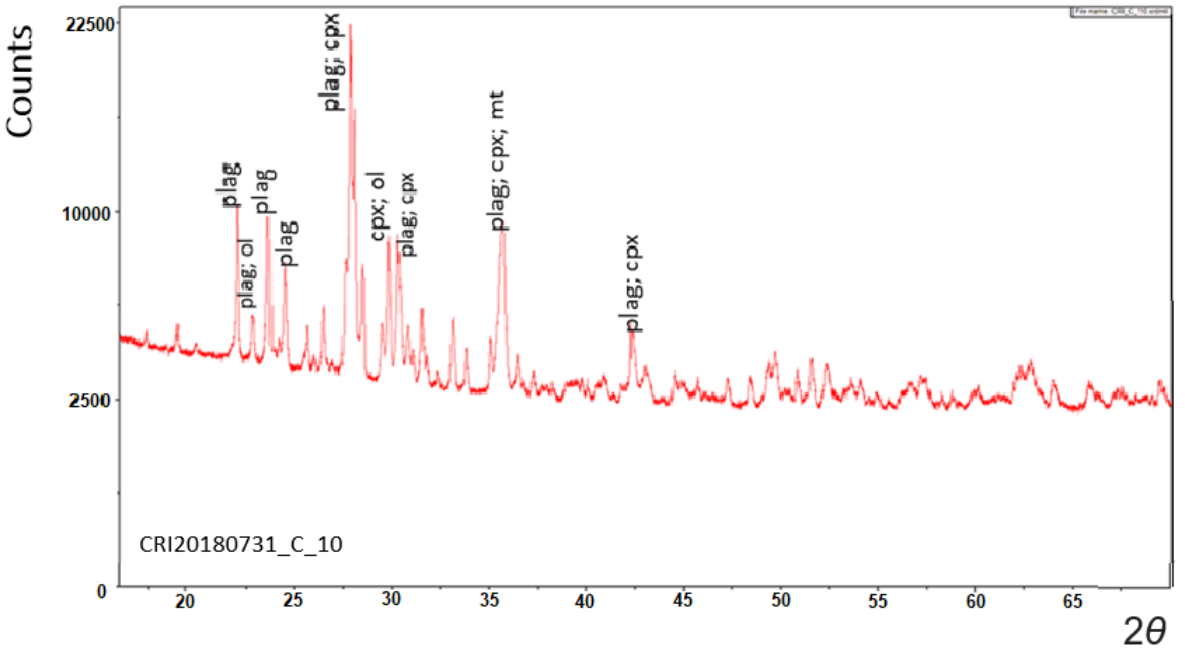

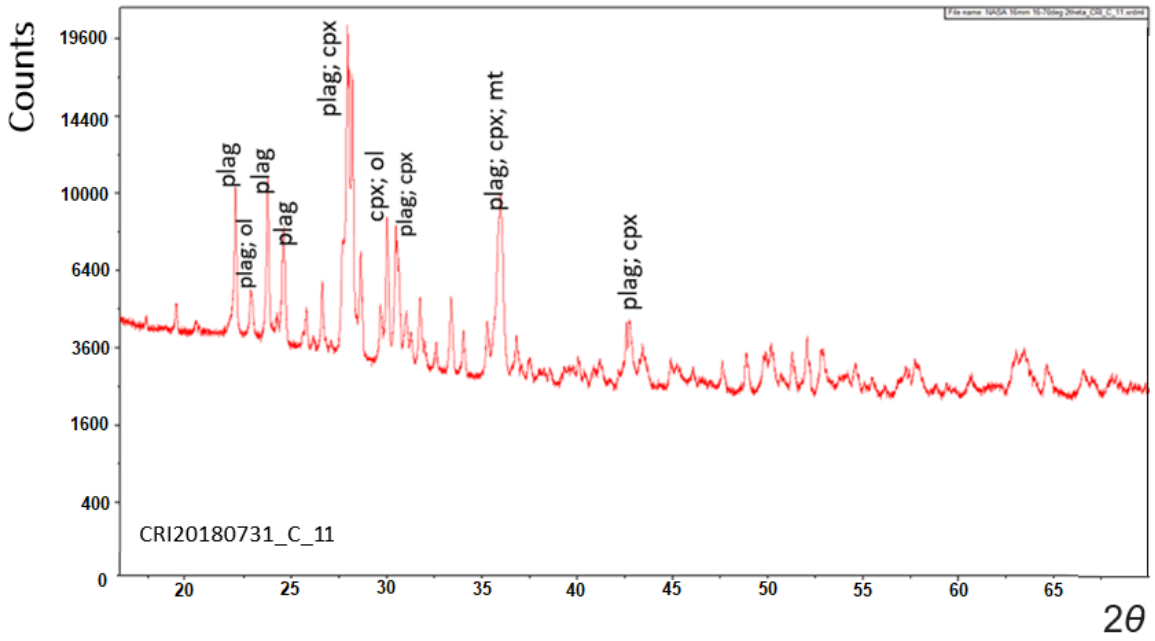
Counts
19600
14400
10000
6400
3600
1600
400
0
plag
plag; ol
plag
plag
plag; cpx
cpx; ol
plag; cpx
plag; cpx; mt
plag; cpx
CRI20180731_C_11
20
25
30
35
40
45
50
55
60
65
2θ

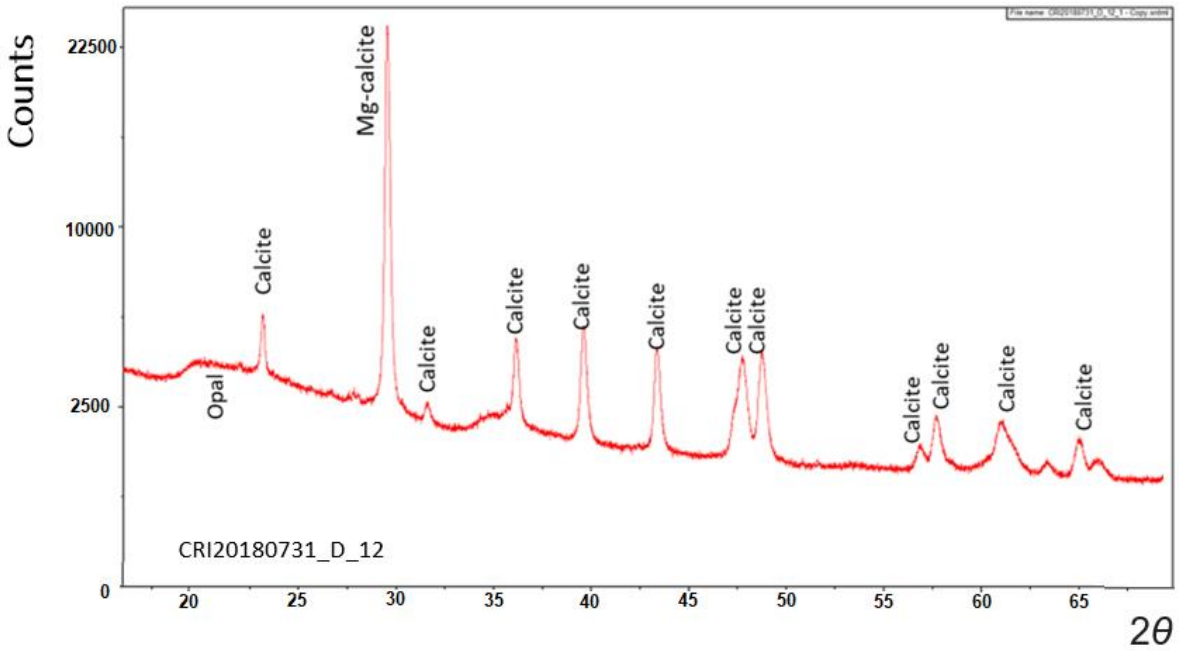
Counts
22500
10000
2500
0
Opal
Calcite
Mg-calcite
Calcite
Calcite
Calcite
Calcite
Calcite
Calcite
Calcite
Calcite
Calcite
Calcite
CRI20180731_D_12
20
25
30
35
40
45
50
55
60
65
2θ

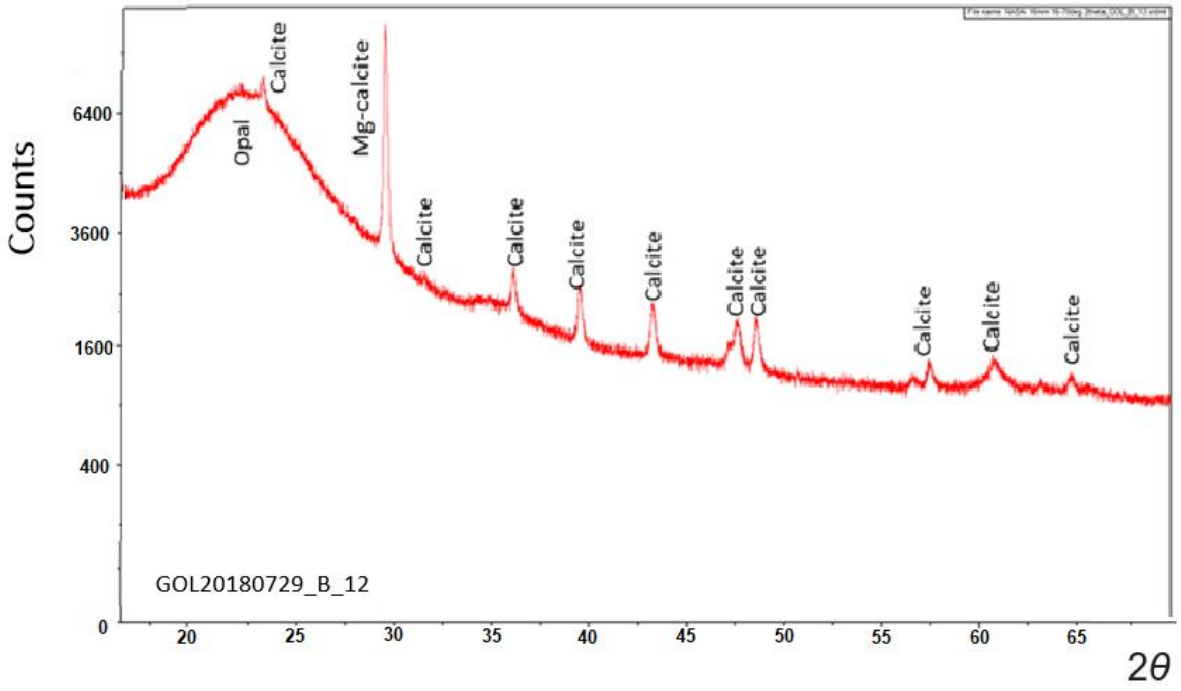
Counts
6400
3600
1600
400
0
Opal
Calcite
Mg-calcite
Calcite
Calcite
Calcite
Calcite
Calcite
Calcite
Calcite
Calcite
Calcite
GOL20180729_B_12
20
25
30
35
40
45
50
55
60
65
2θ

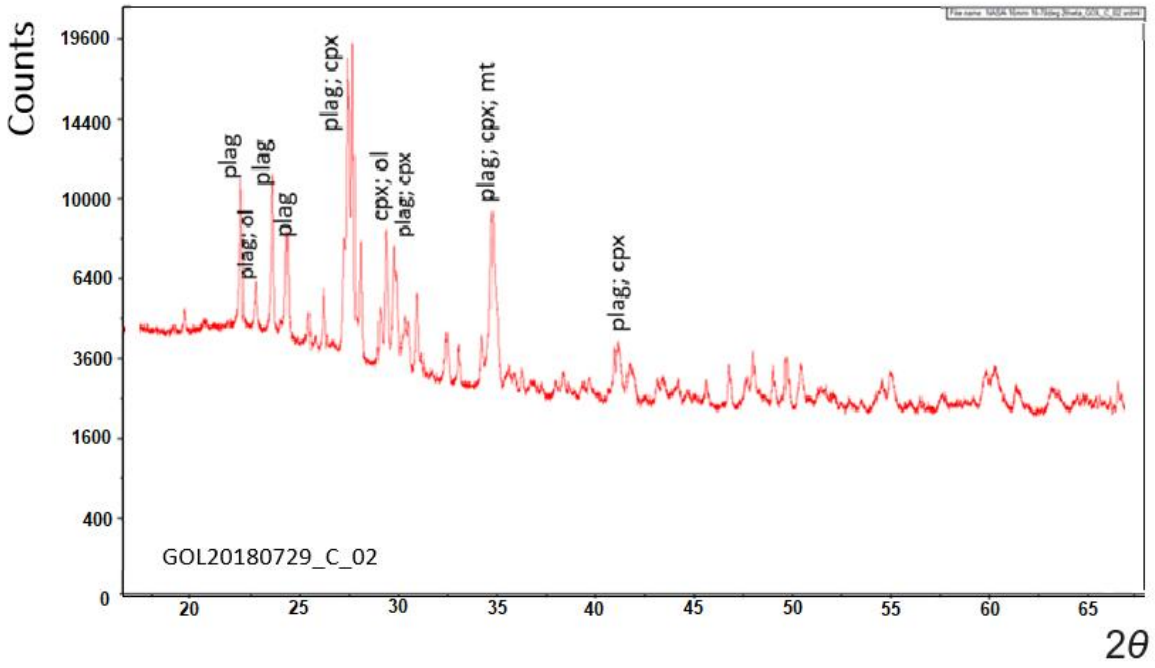
Counts
19600
14400
10000
6400
3600
1600
400
0
plag
plag; ol
plag
plag
plag; cpx
cpx; ol
plag; cpx
plag; cpx; mt
plag; cpx
GOL20180729_C_02
20
25
30
35
40
45
50
55
60
65
2θ

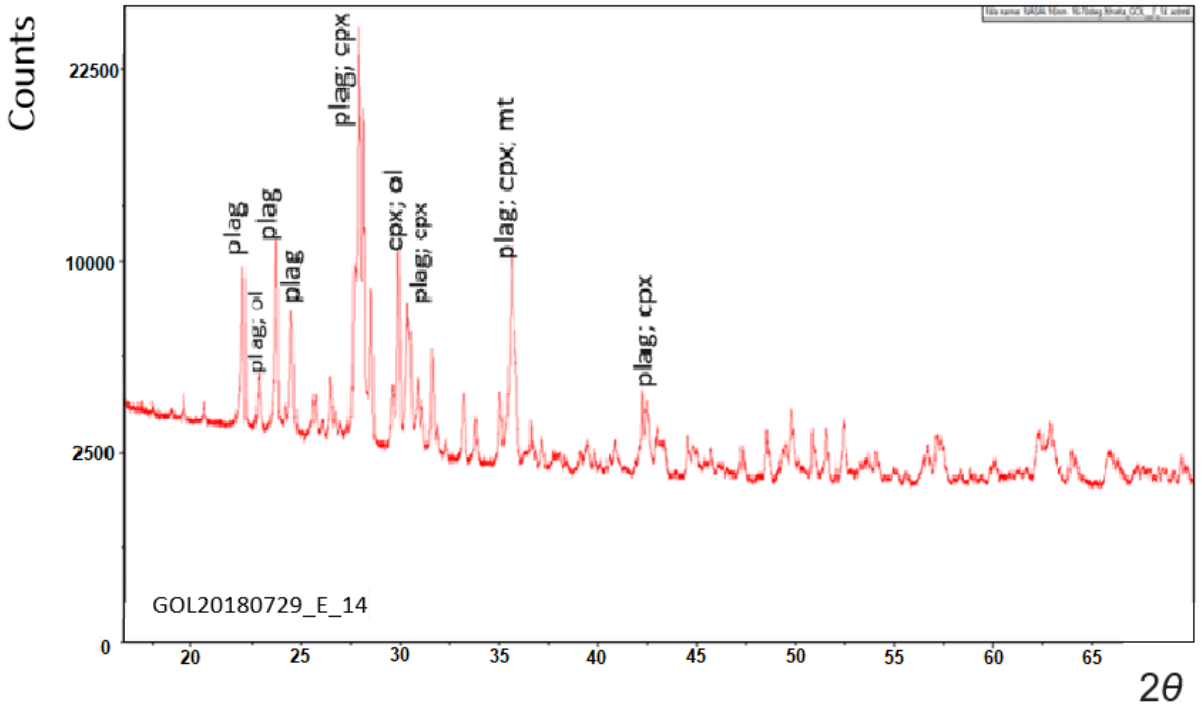
Counts
22500
10000
2500
0
plag
plag; ol
plag
plag
plag; cpx
cpx; ol
plag; cpx
plag; cpx; mt
plag; cpx
GOL20180729_E_14
20
25
30
35
40
45
50
55
60
65
2θ

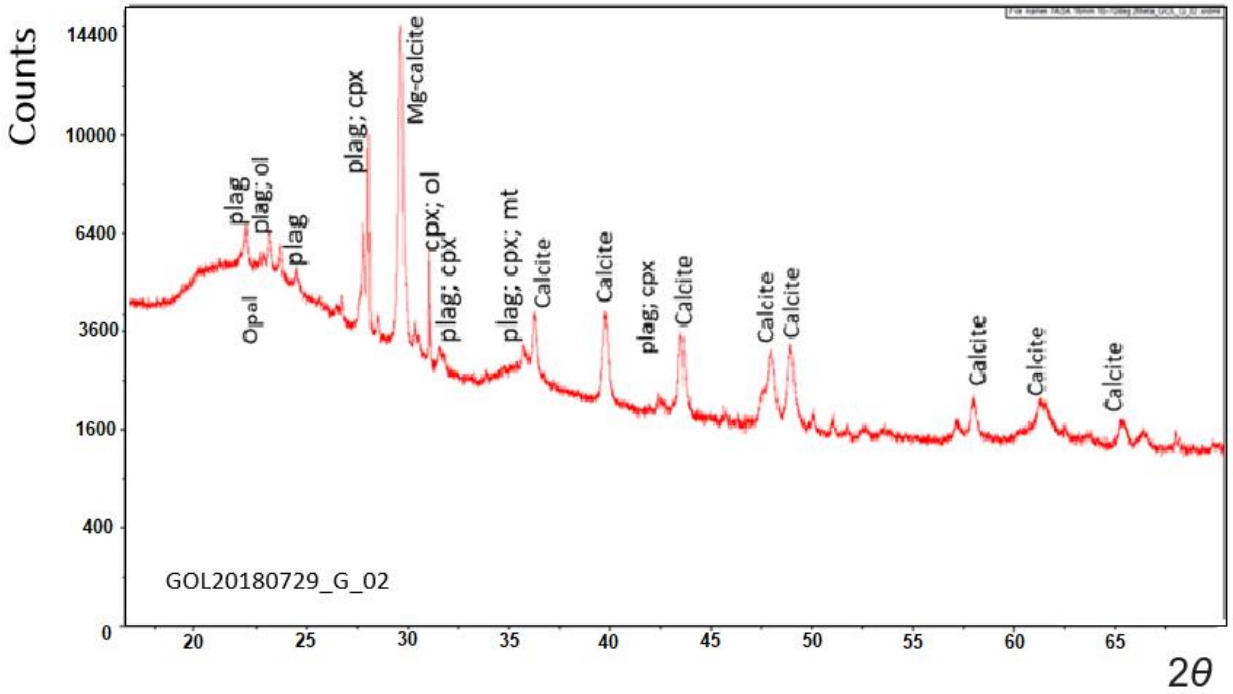
Counts
14400
10000
6400
3600
1600
400
0
plag
plag; ol
Opal
plag
plag; cpx
Mg-calcite
cpx; ol
plag; cpx
plag; cpx; mt
Calcite
Calcite
plag; cpx
Calcite
Calcite
Calcite
Calcite
Calcite
GOL20180729_G_02
20
25
30
35
40
45
50
55
60
65
2θ

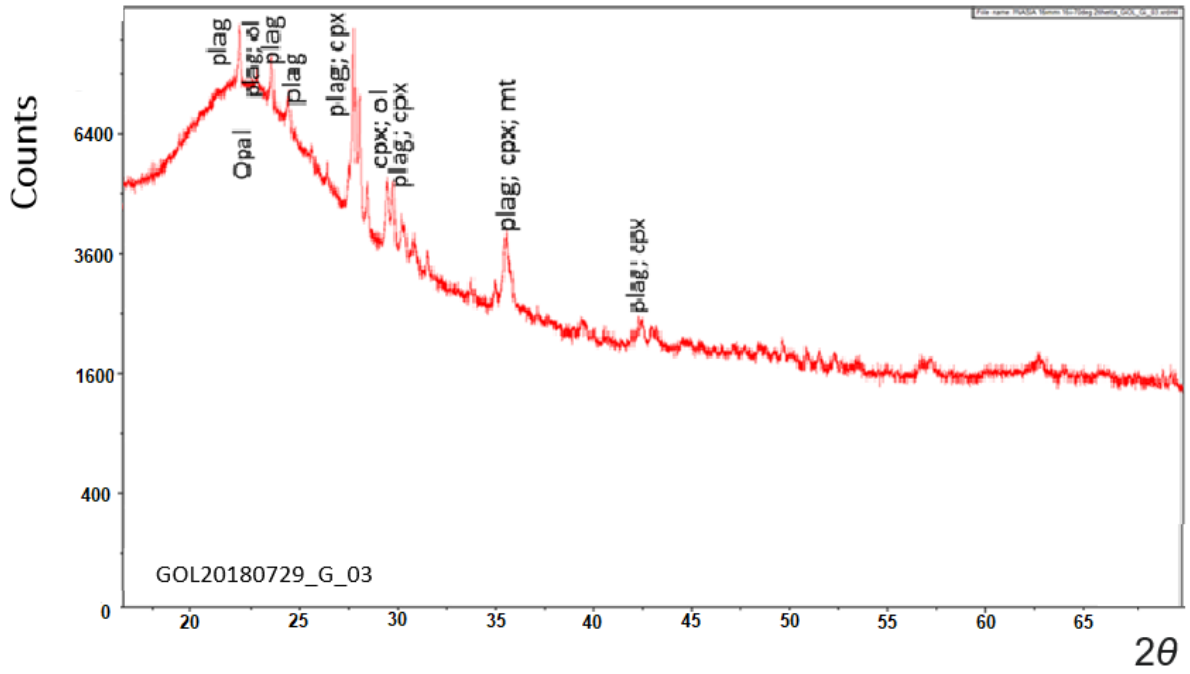
Counts
6400
3600
1600
400
0
plag
plag; ol
plag
plag
plag; cpx
Opal
cpx; ol
plag; cpx
plag; cpx; mt
plag; cpx
GOL20180729_G_03
20
25
30
35
40
45
50
55
60
65
2θ

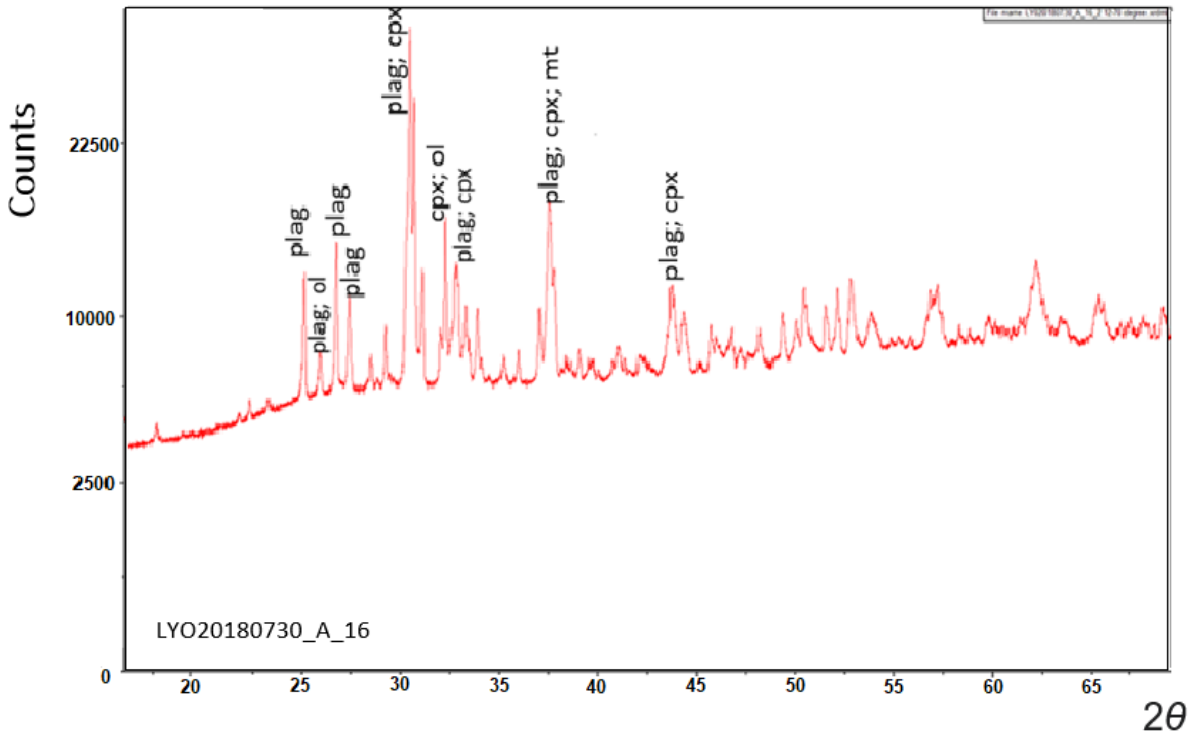
Counts
22500
10000
2500
0
plag
plag; ol
plag
plag
plag; cpx
cpx; ol
plag; cpx
plag; cpx; mt
plag; cpx
LYO20180730_A_16
20
25
30
35
40
45
50
55
60
65
2θ

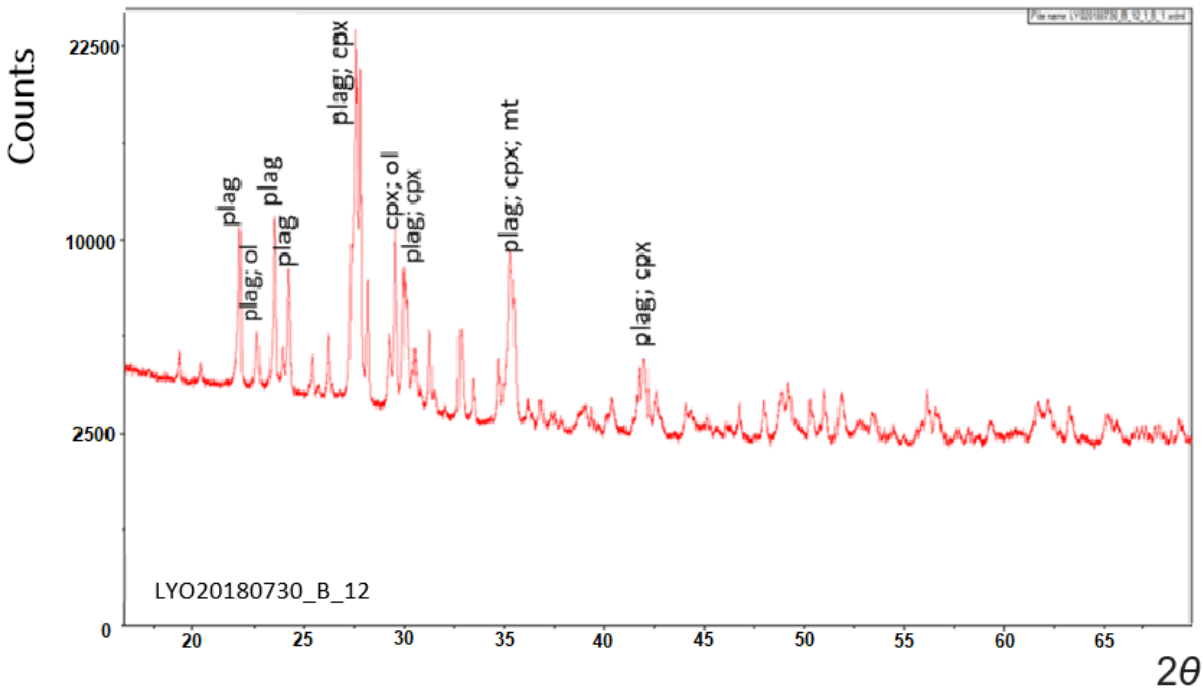
Counts
22500
10000
2500
0
plag
plag; ol
plag
plag
plag; cpx
cpx; ol
plag; cpx
plag; cpx; mt
plag; cpx
LYO20180730_B_12
20
25
30
35
40
45
50
55
60
65
2θ

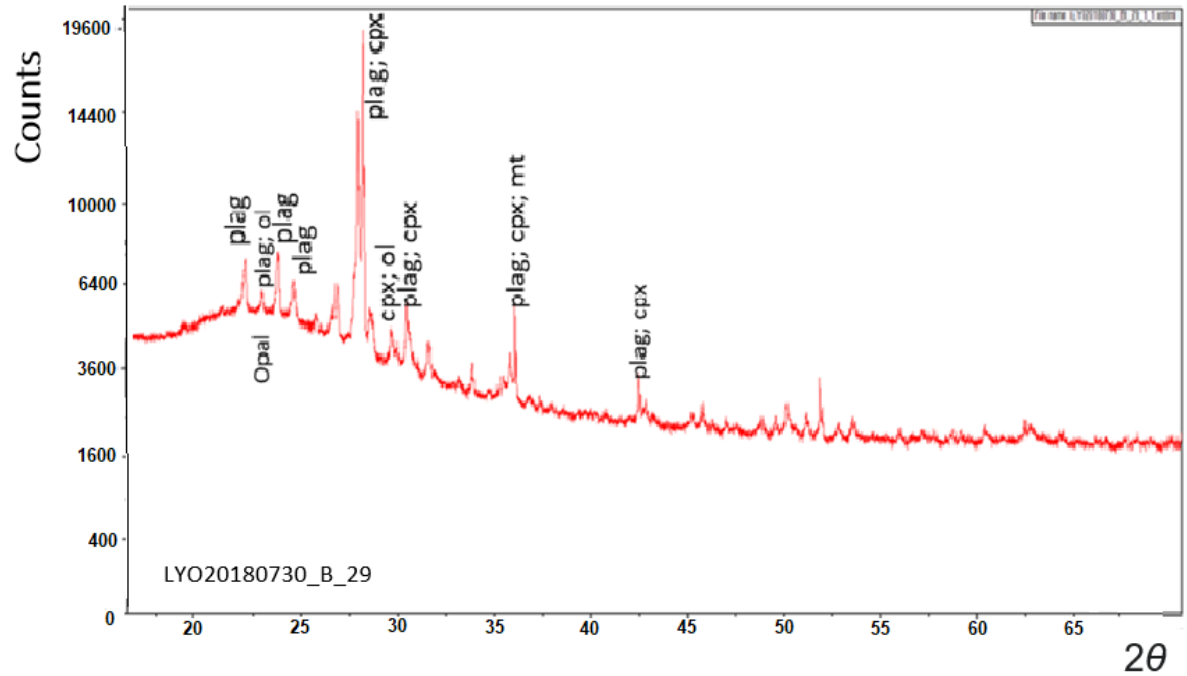
Counts
19600
14400
10000
6400
3600
1600
400
0
plag
plag; ol
plag
plag
Opal
plag; cpx
cpx; ol
plag; cpx
plag; cpx; mt
plag; cpx
LYO20180730_B_29
20
25
30
35
40
45
50
55
60
65
2θ

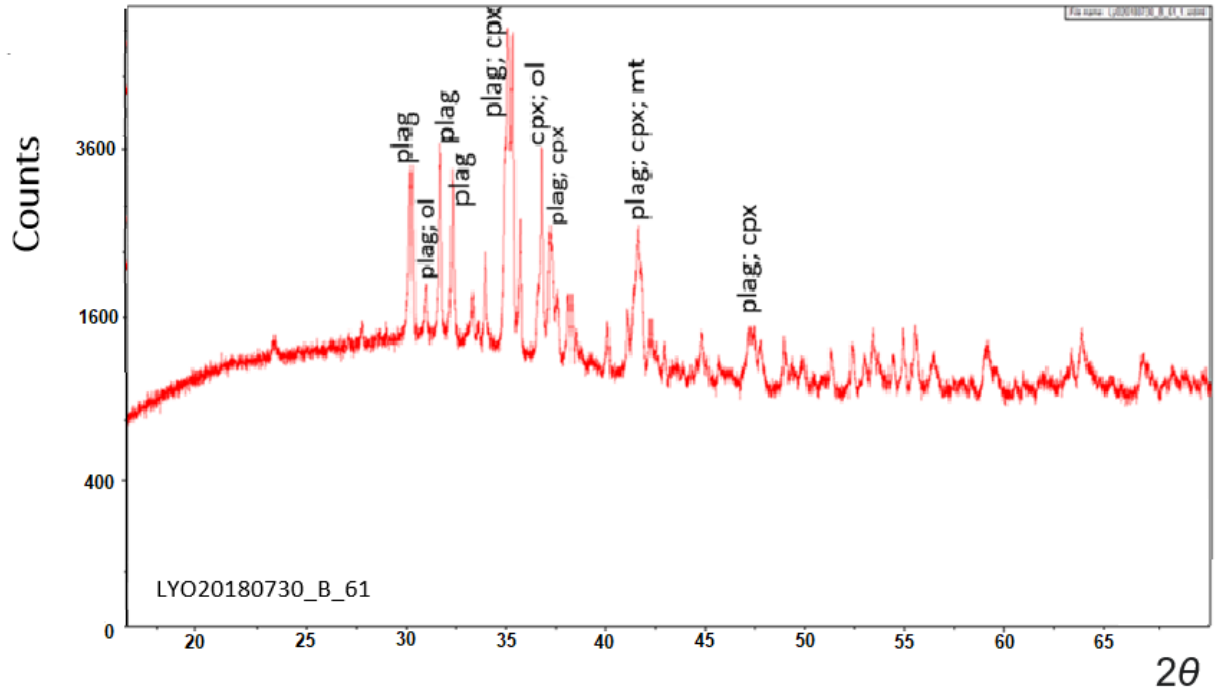
Counts
3600
1600
400
0
plag
plag; ol
plag
plag
plag; cpx
cpx; ol
plag; cpx
plag; cpx; mt
plag; cpx
LYO20180730_B_61
20
25
30
35
40
45
50
55
60
65
2θ

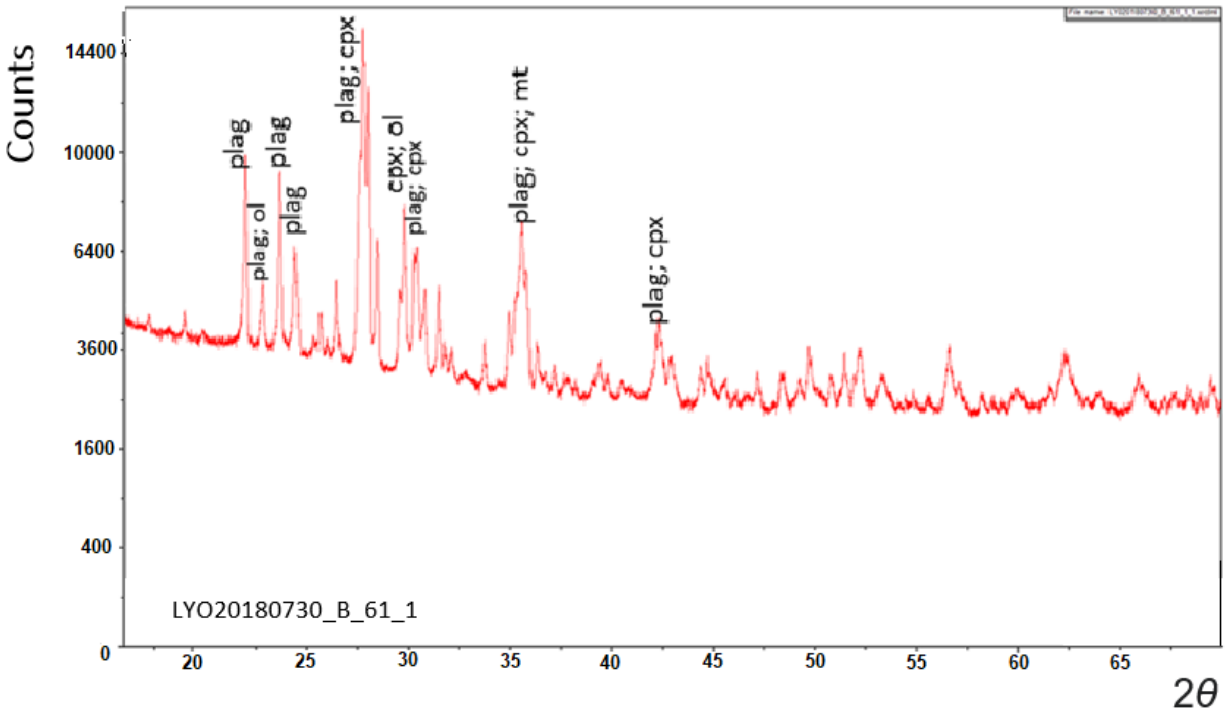
Counts
14400
10000
6400
3600
1600
400
0
plag
plag; ol
plag
plag
plag; cpx
cpx; ol
plag; cpx
plag; cpx; mt
plag; cpx
LYO20180730_B_61_1
20
25
30
35
40
45
50
55
60
65
2θ

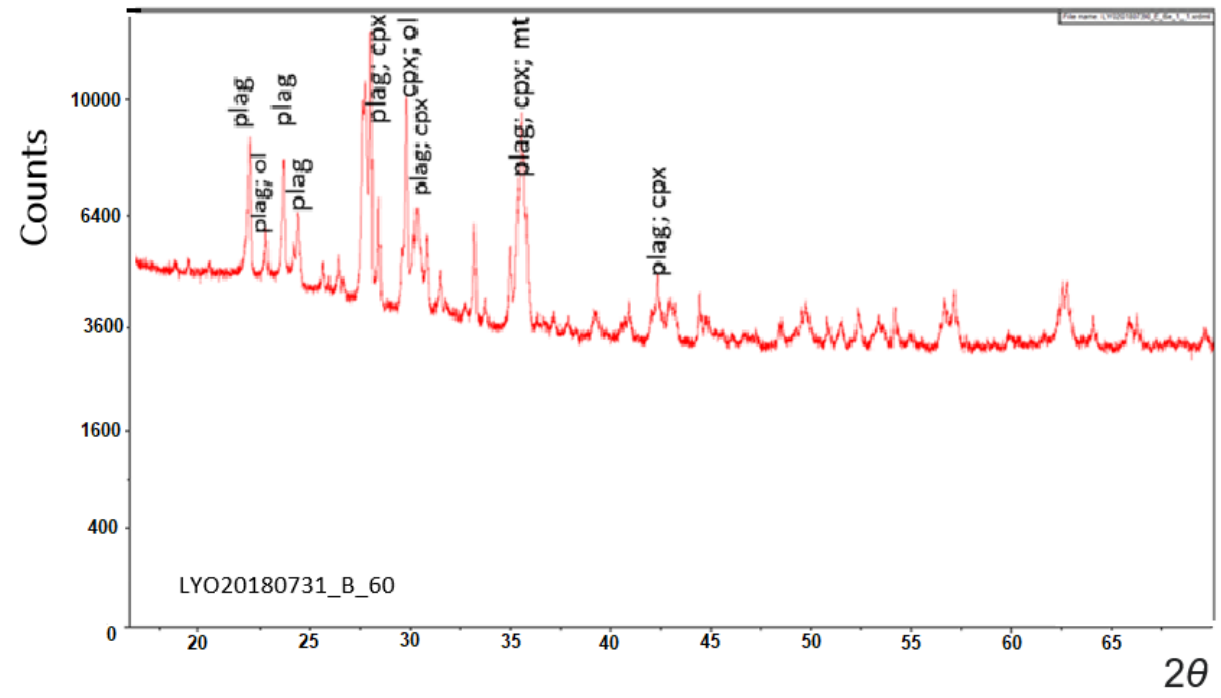
Counts
10000
6400
3600
1600
400
0
plag
plag; ol
plag
plag
plag; cpx
cpx; ol
plag; cpx
plag; cpx; mt
plag; cpx
LYO20180731_B_60
20
25
30
35
40
45
50
55
60
65
2θ

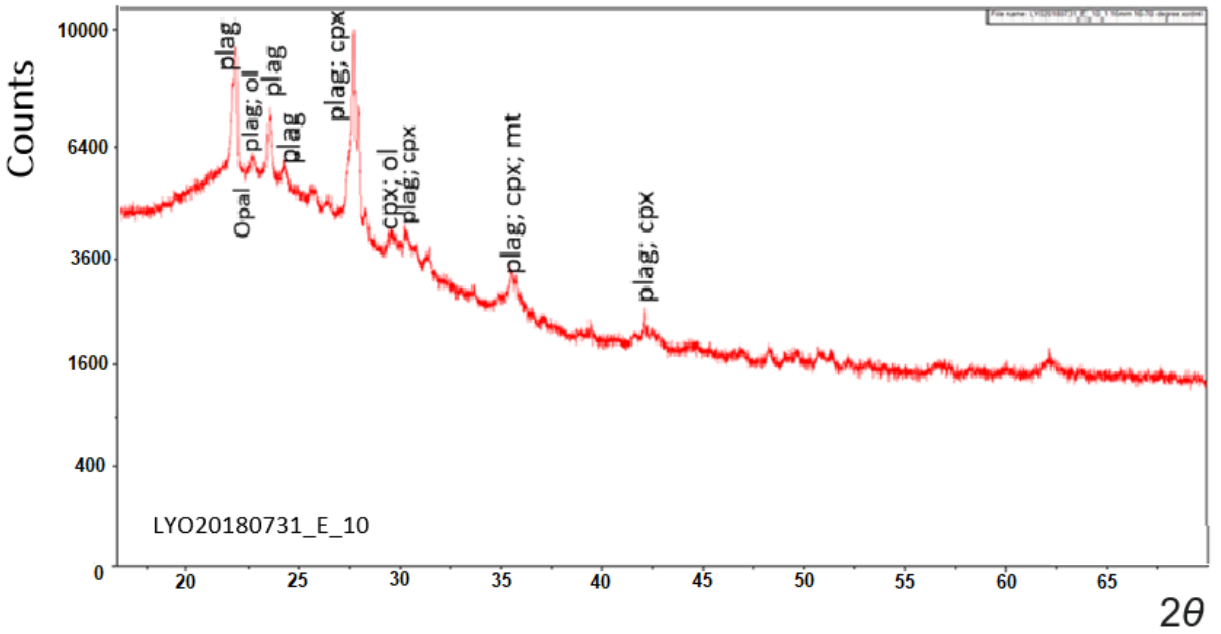
Counts
10000
6400
3600
1600
400
0
plag
plag; ol
plag
plag
plag; cpx
Opal
cpx; ol
plag; cpx
plag; cpx; mt
plag; cpx
LYO20180731_E_10
20
25
30
35
40
45
50
55
60
65
2θ

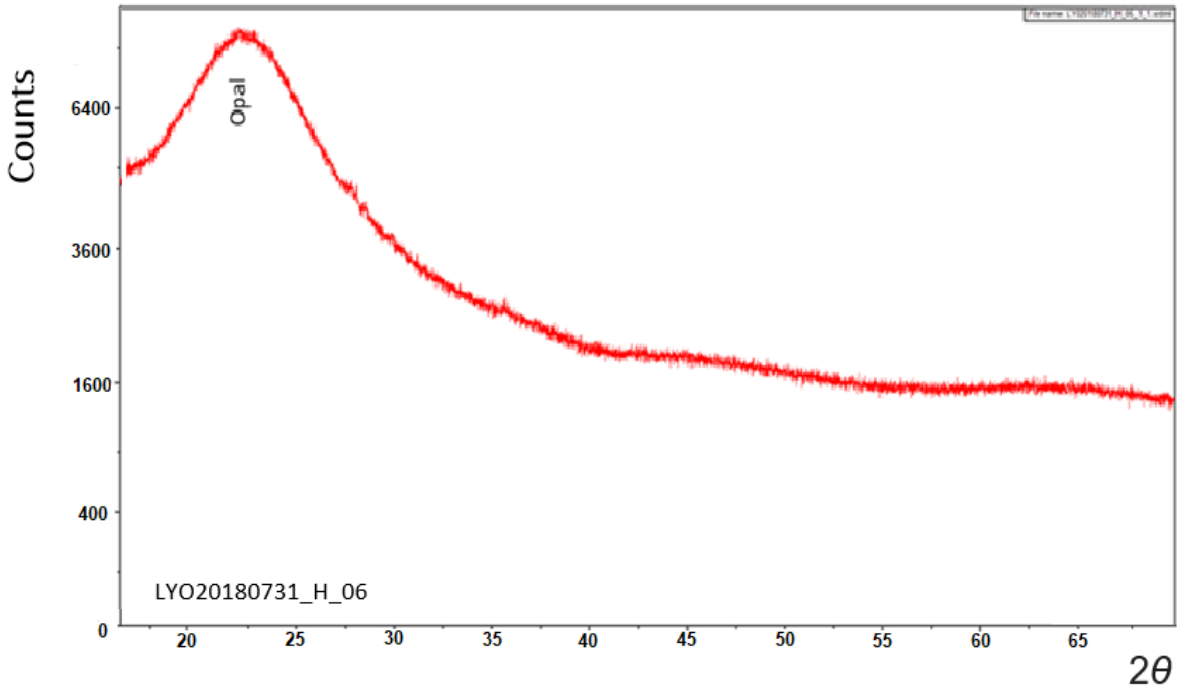
Counts
6400
3600
1600
400
0
Opal
LYO20180731_H_06
20
25
30
35
40
45
50
55
60
65
2θ

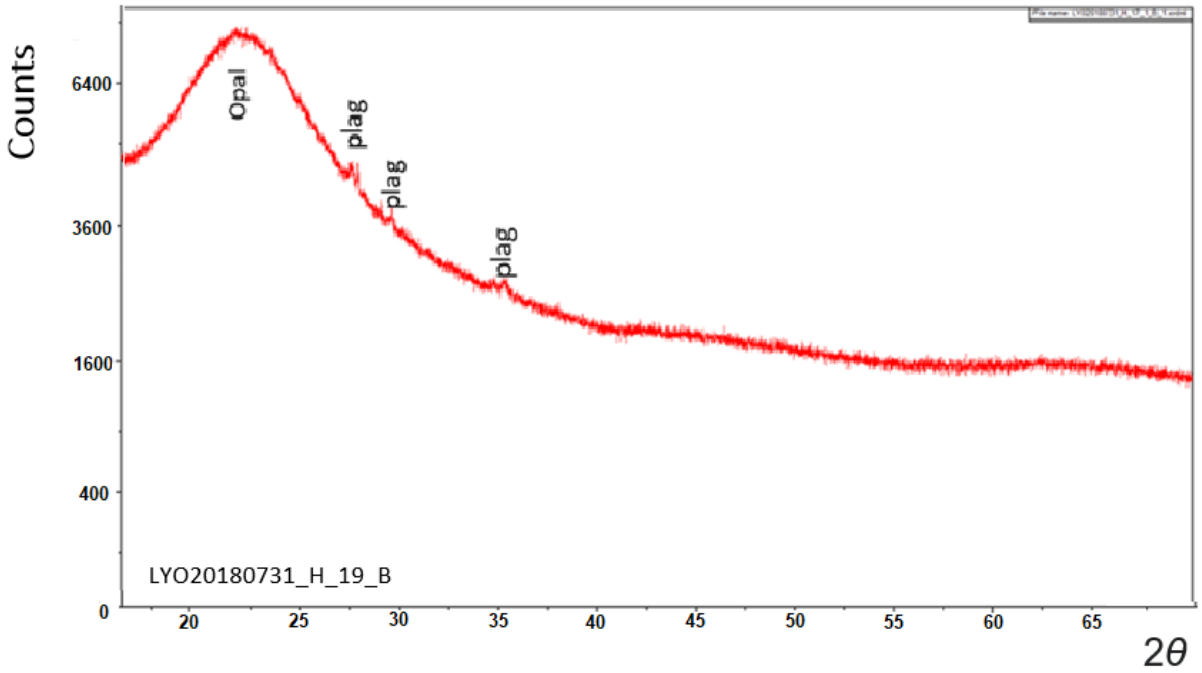
Counts
6400
3600
1600
400
0
Opal
plag
plag
plag
LYO20180731_H_19_B
20
25
30
35
40
45
50
55
60
65
2θ

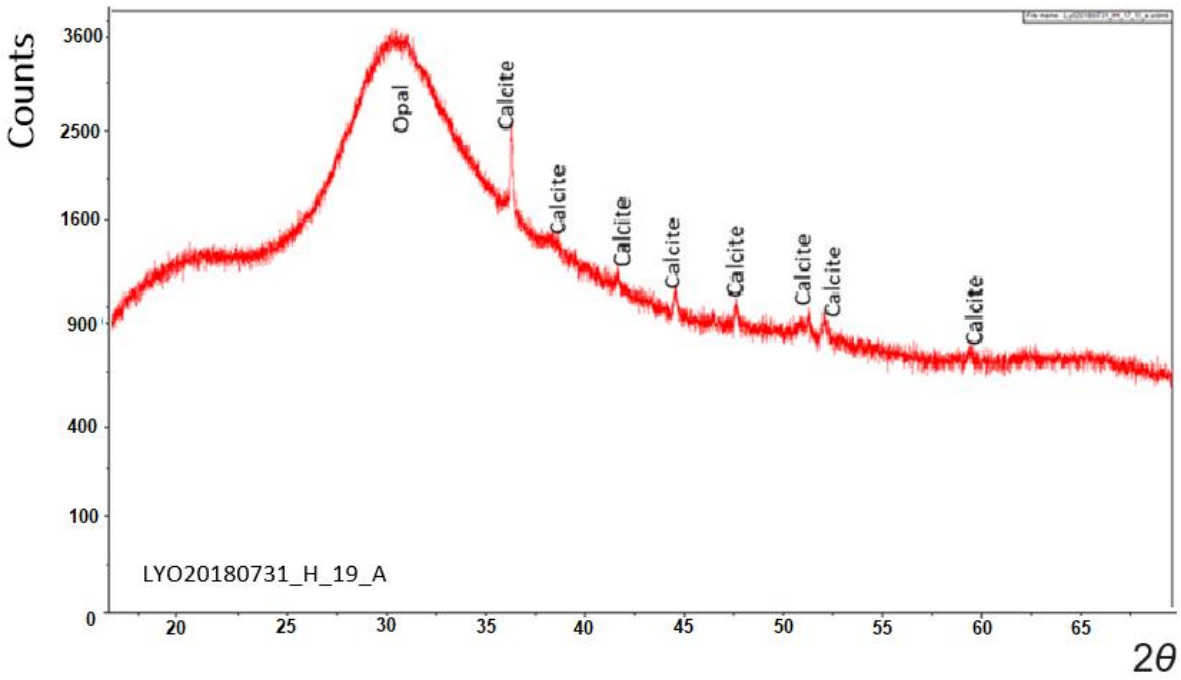
Counts
3600
2500
1600
900
400
100
0
Opal
Calcite
Calcite
Calcite
Calcite
Calcite
Calcite
Calcite
Calcite
LYO20180731_H_19_A
20
25
30
35
40
45
50
55
60
65
2θ

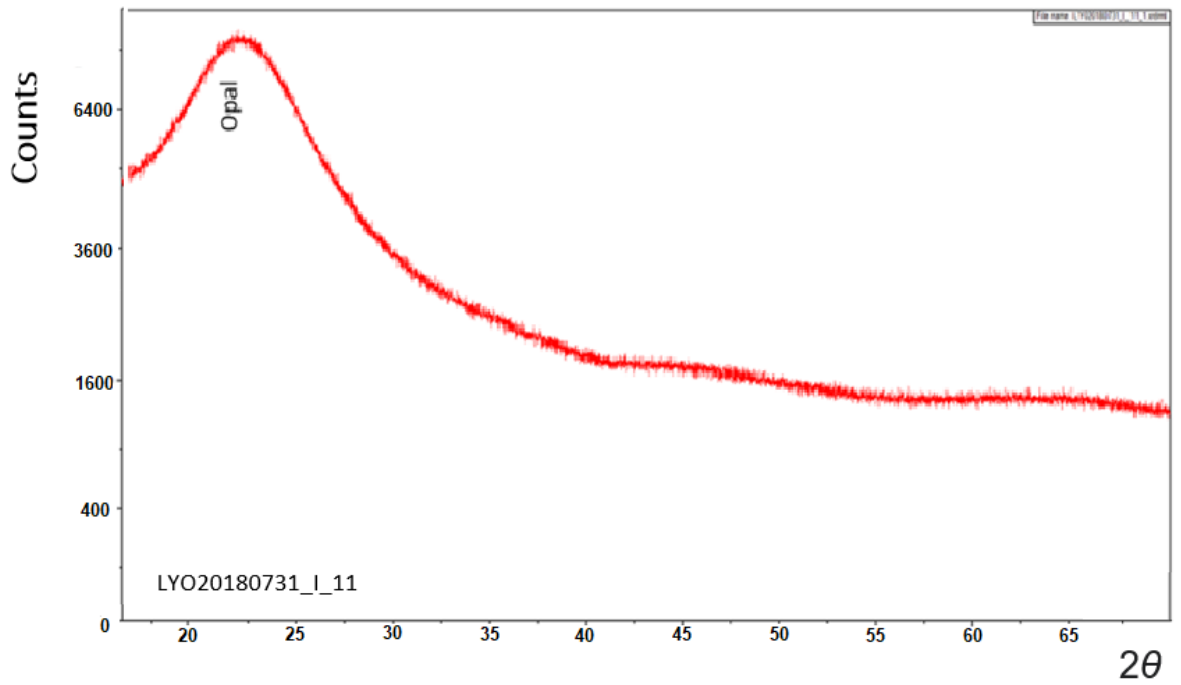
Counts
6400
3600
1600
400
0
Opal
LYO20180731_I_11
20
25
30
35
40
45
50
55
60
65
2θ

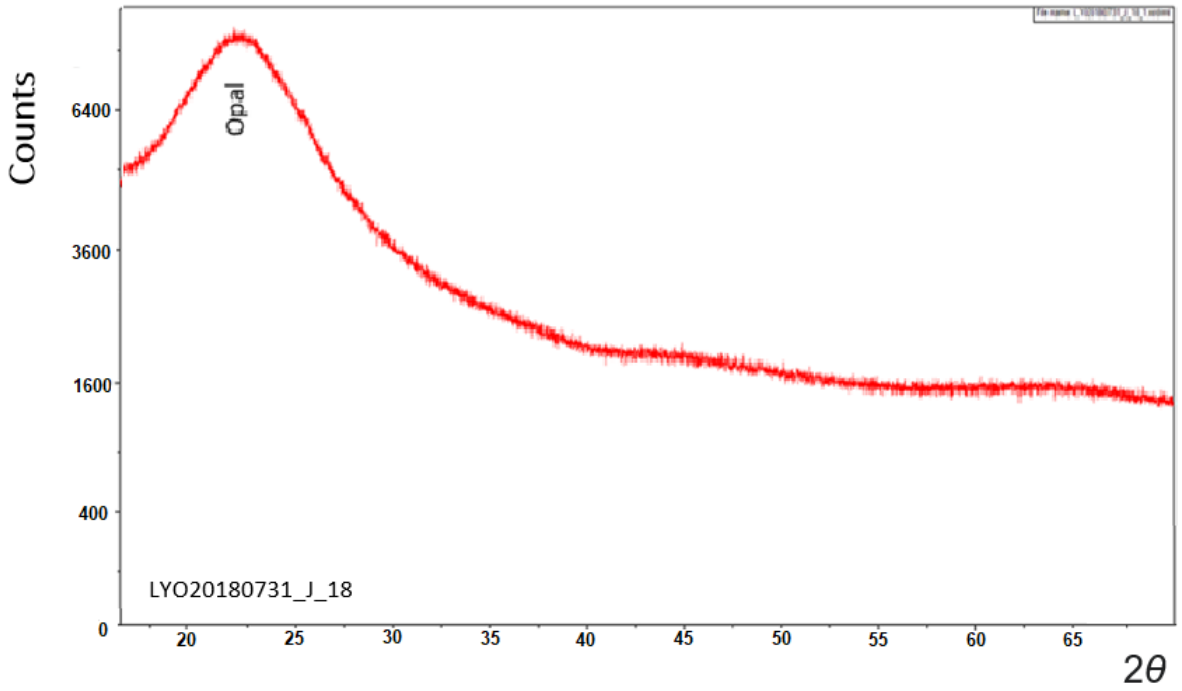
Counts
6400
3600
1600
400
0
Opal
LYO20180731_J_18
20
25
30
35
40
45
50
55
60
65
2θ

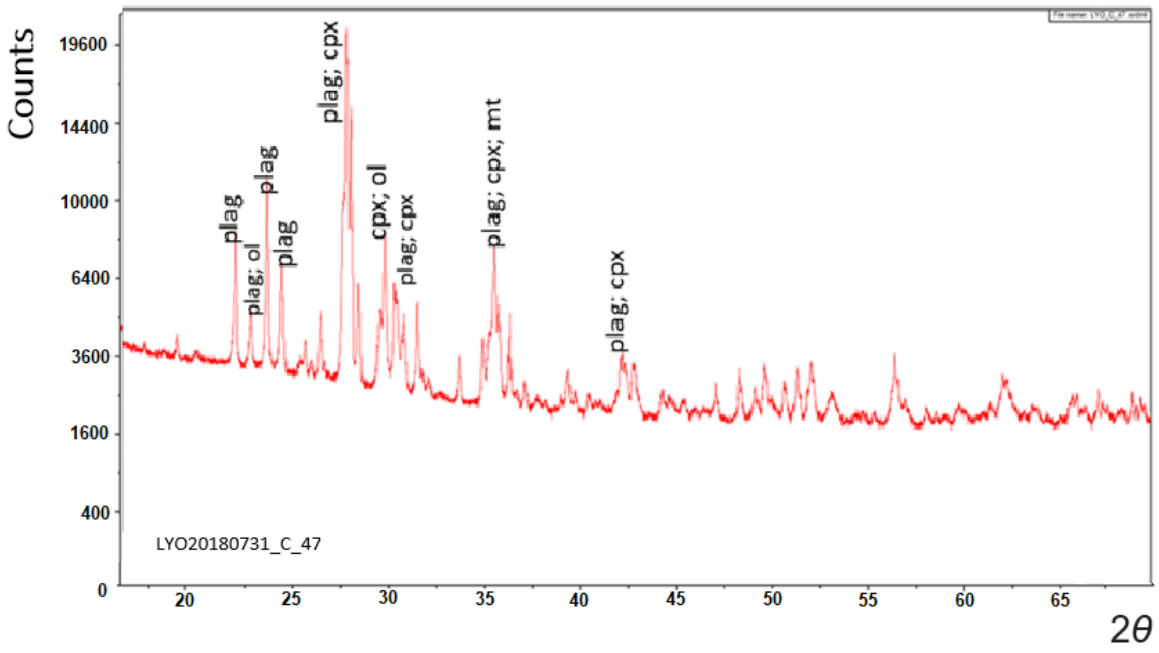
Counts
19600
14400
10000
6400
3600
1600
400
0
plag
plag; ol
plag
plag
plag; cpx
cpx; ol
plag; cpx
plag; cpx; mt
plag; cpx
LYO20180731_C_47
20
25
30
35
40
45
50
55
60
65
2θ

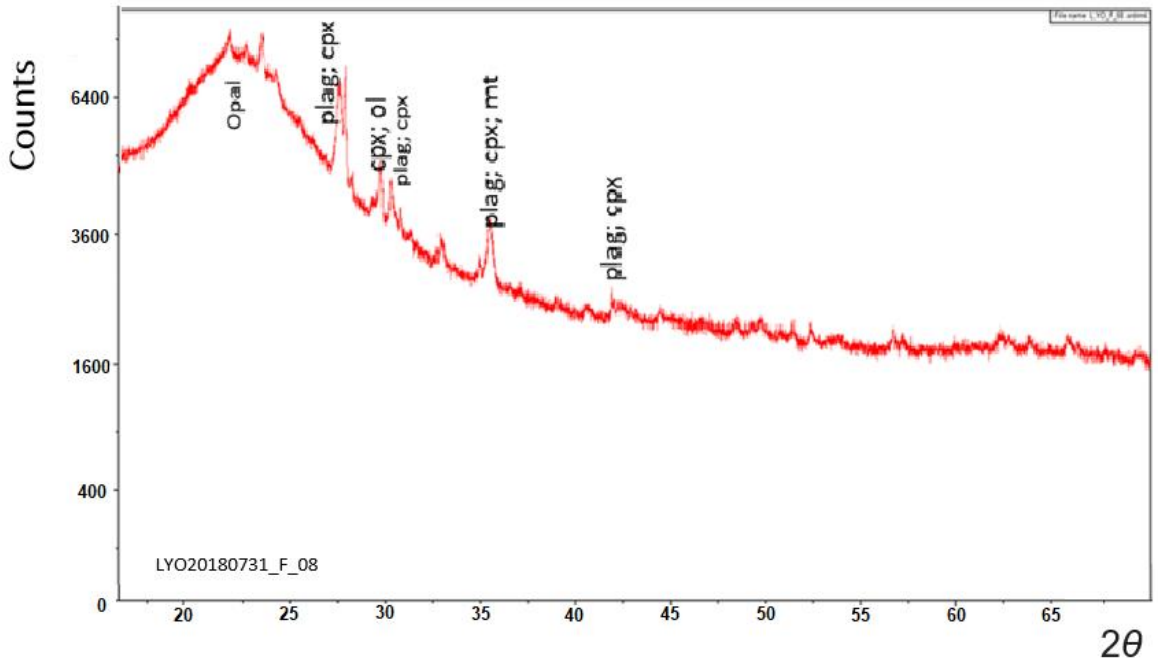
Counts
6400
3600
1600
400
0
Opal
plag; cpx
cpx; ol
plag; cpx
plag; cpx; mt
plag; cpx
LYO20180731_F_08
20
25
30
35
40
45
50
55
60
65
2θ

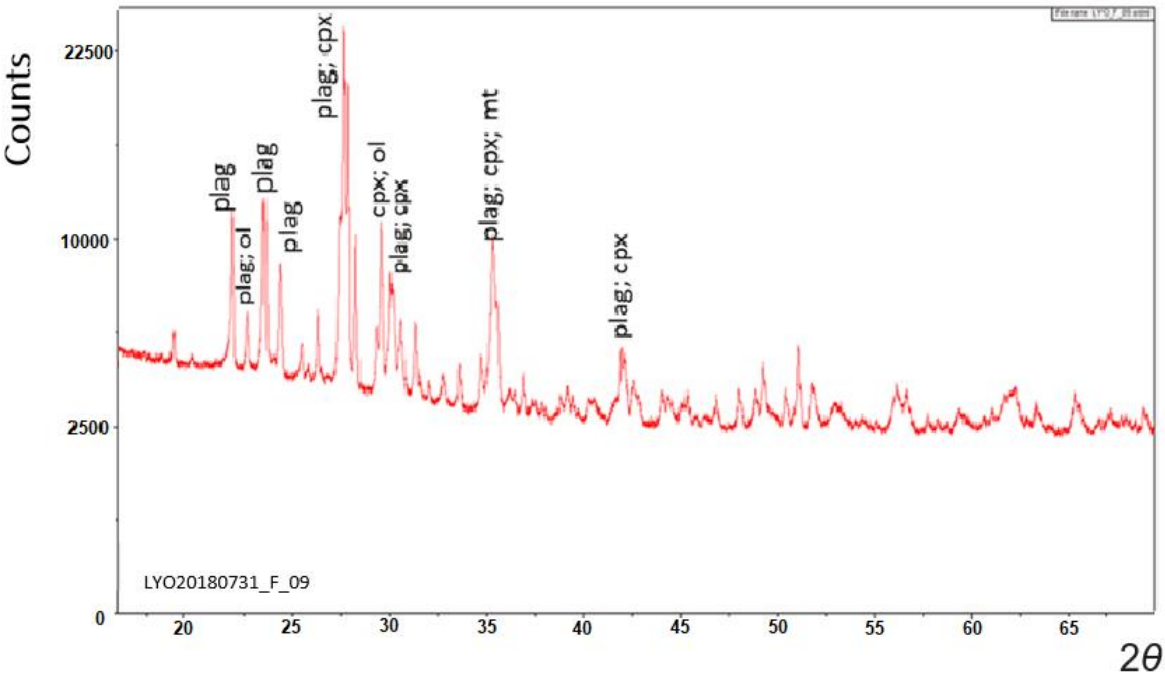
Counts
22500
10000
2500
0
plag
plag; ol
plag
plag
plag; cpx
cpx; ol
plag; cpx
plag; cpx; mt
plag; cpx
LYO20180731_F_09
20
25
30
35
40
45
50
55
60
65
2θ

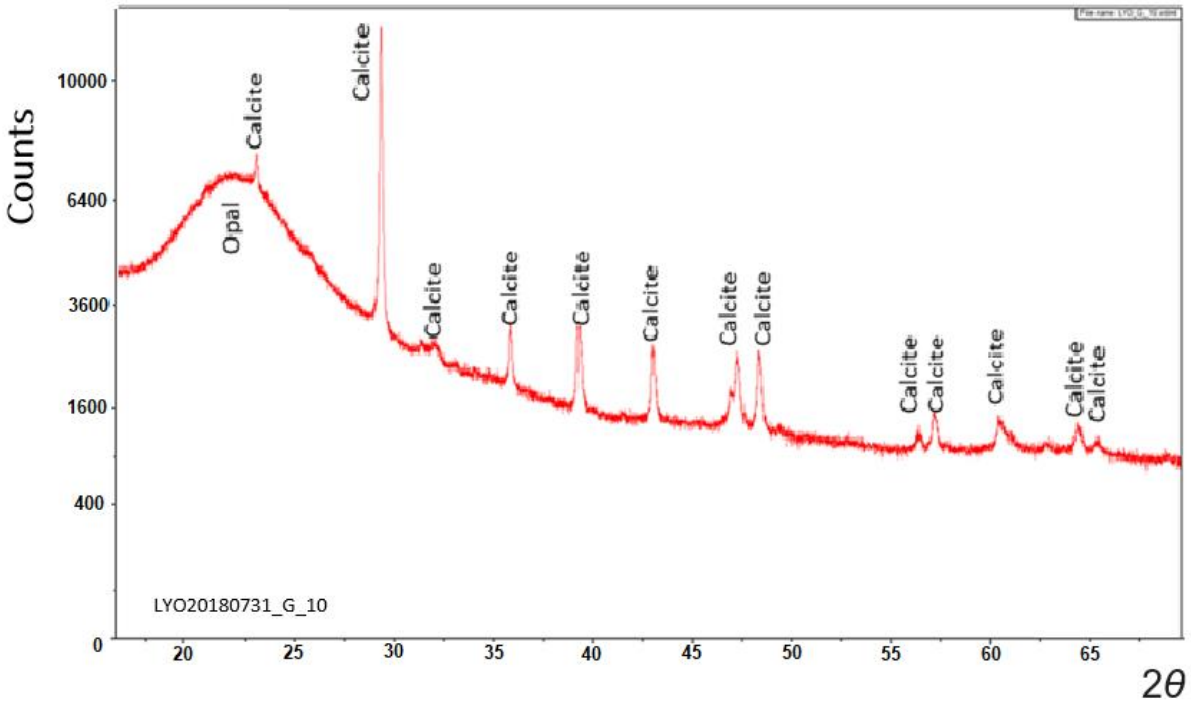
Counts
10000
6400
3600
1600
400
0
Opal
Calcite
Calcite
Calcite
Calcite
Calcite
Calcite
Calcite
Calcite
Calcite
Calcite
Calcite
Calcite
LYO20180731_G_10
20
25
30
35
40
45
50
55
60
65
2θ

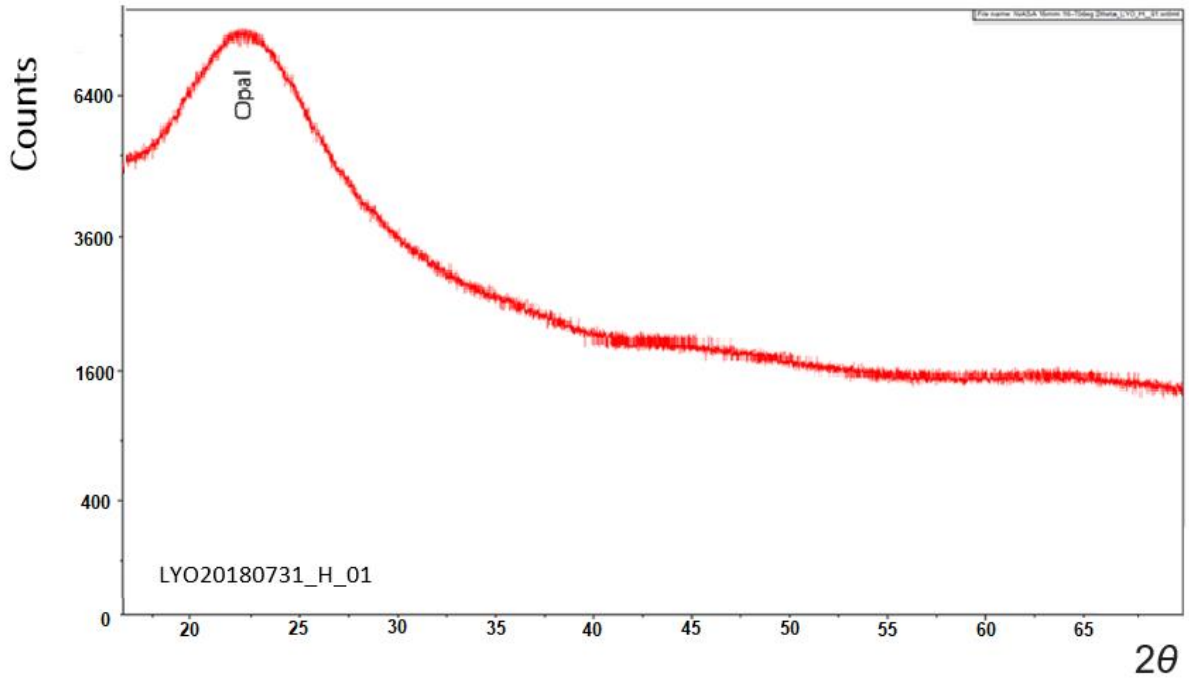
Counts
6400
3600
1600
400
0
Opal
LYO20180731_H_01
20
25
30
35
40
45
50
55
60
65
2θ

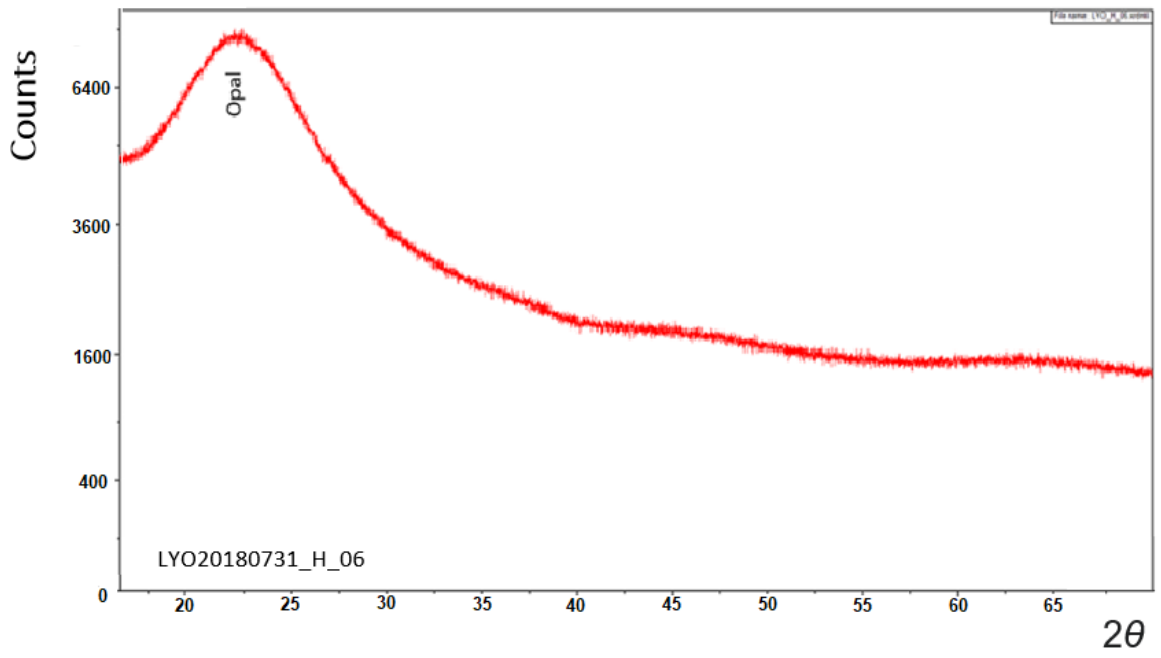
Counts
6400
3600
1600
400
0
Opal
LYO20180731_H_06
20
25
30
35
40
45
50
55
60
65
2θ

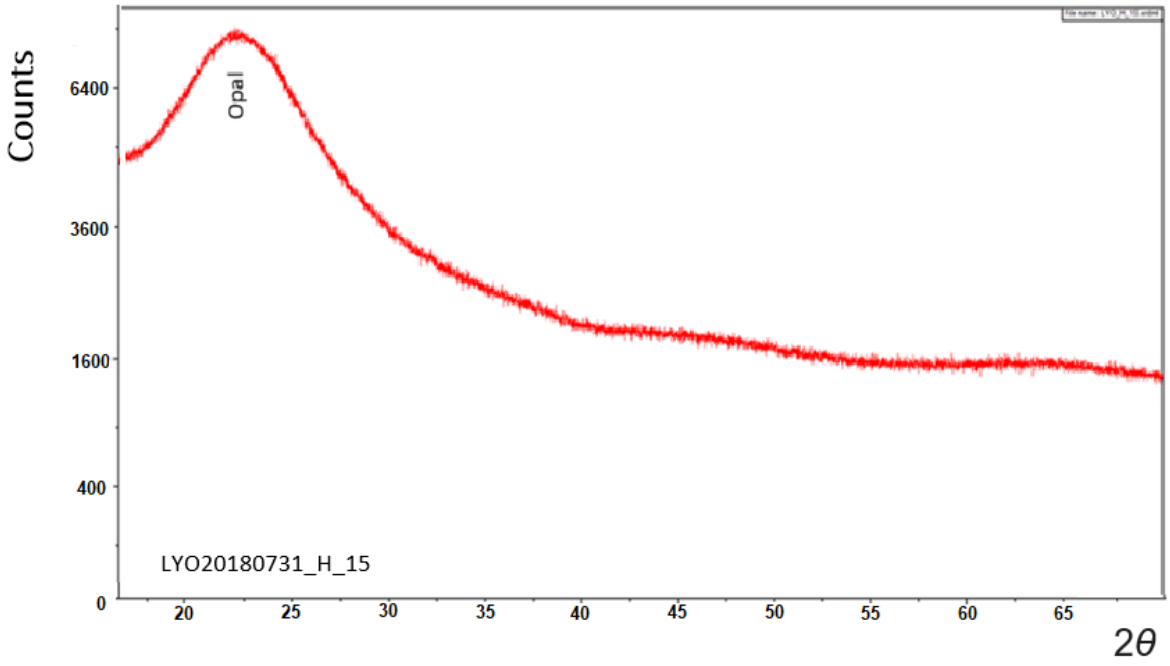
Counts
6400
3600
1600
400
0
Opal
LYO20180731_H_15
20
25
30
35
40
45
50
55
60
65
2θ

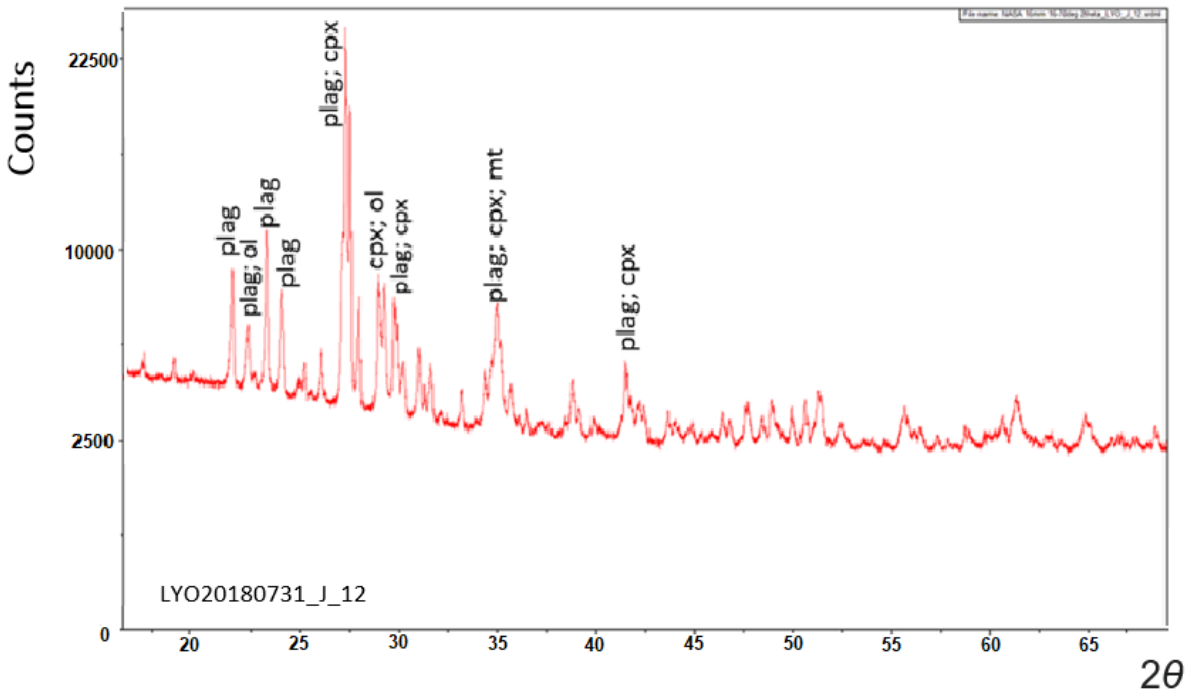
Counts
22500
10000
2500
0
plag
plag; ol
plag
plag
plag; cpx
cpx; ol
plag; cpx
plag; cpx; mt
plag; cpx
LYO20180731_J_12
20
25
30
35
40
45
50
55
60
65
2θ

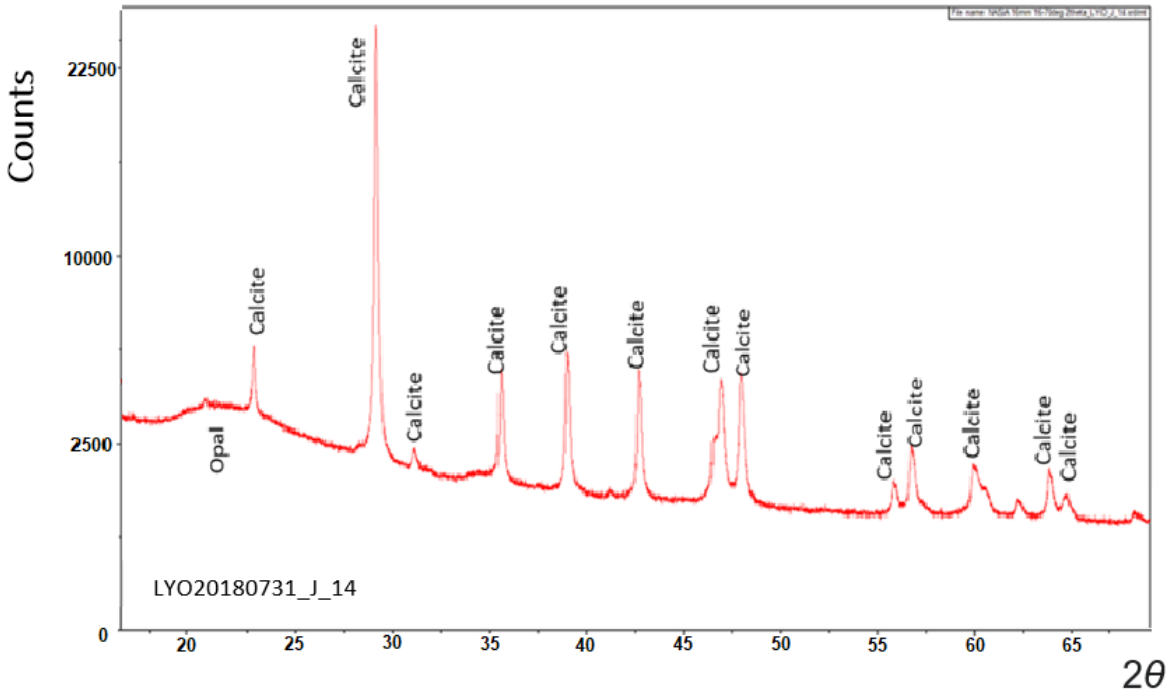
Counts
22500
10000
2500
0
Calcite
Calcite
Opal
Calcite
Calcite
Calcite
Calcite
Calcite
Calcite
Calcite
Calcite
Calcite
Calcite
LYO20180731_J_14
20
25
30
35
40
45
50
55
60
65
2θ

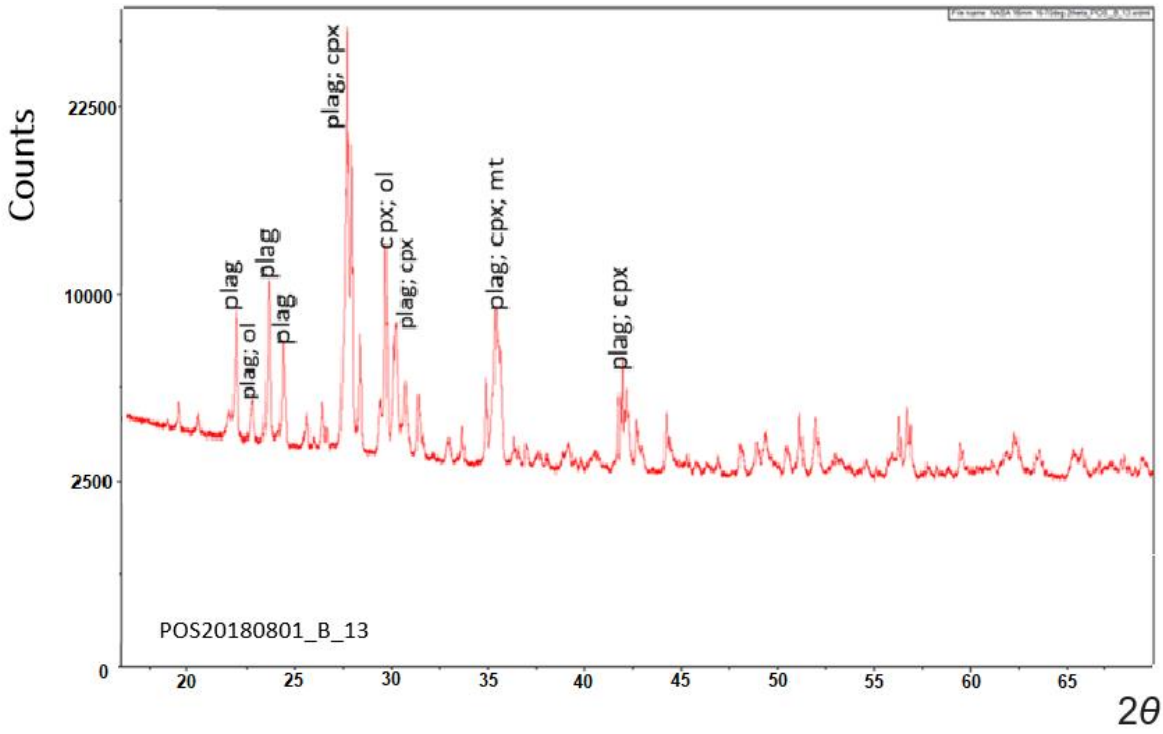
Counts
22500
10000
2500
0
plag
plag; ol
plag
plag
plag; cpx
cpx; ol
plag; cpx
plag; cpx; mt
plag; cpx
POS20180801_B_13
20
25
30
35
40
45
50
55
60
65
2θ

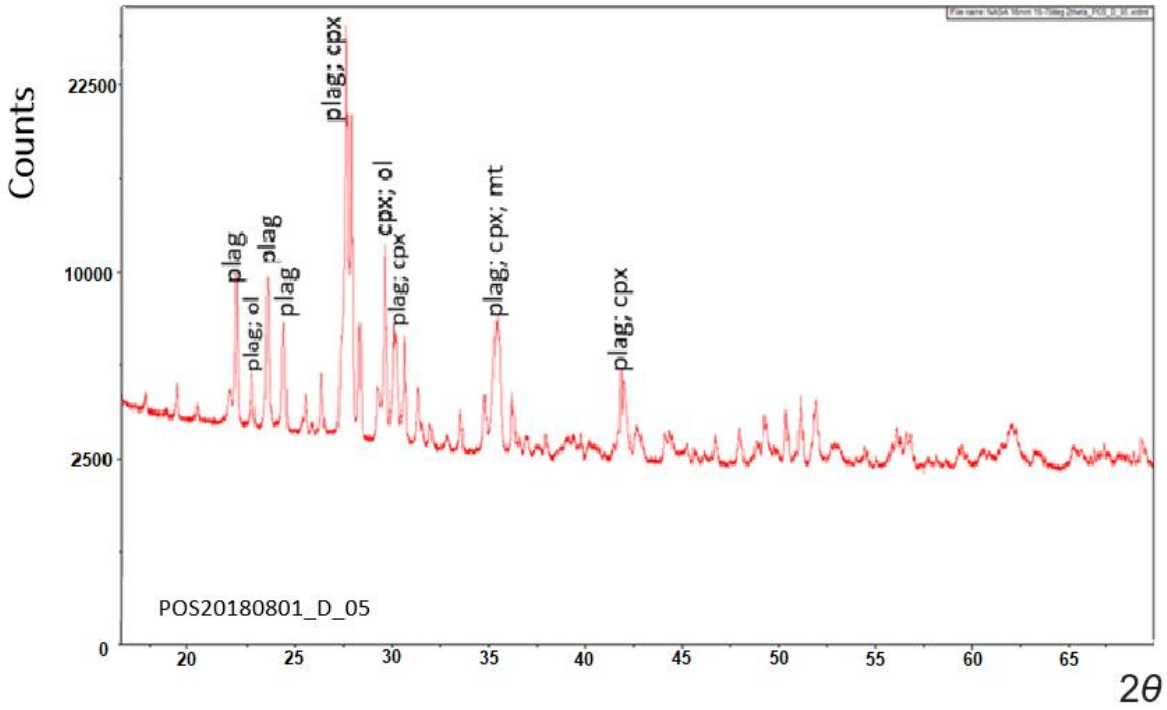
Counts
22500
10000
2500
0
plag
plag; ol
plag
plag
plag; cpx
cpx; ol
plag; cpx
plag; cpx; mt
plag; cpx
POS20180801_D_05
20
25
30
35
40
45
50
55
60
65
2θ

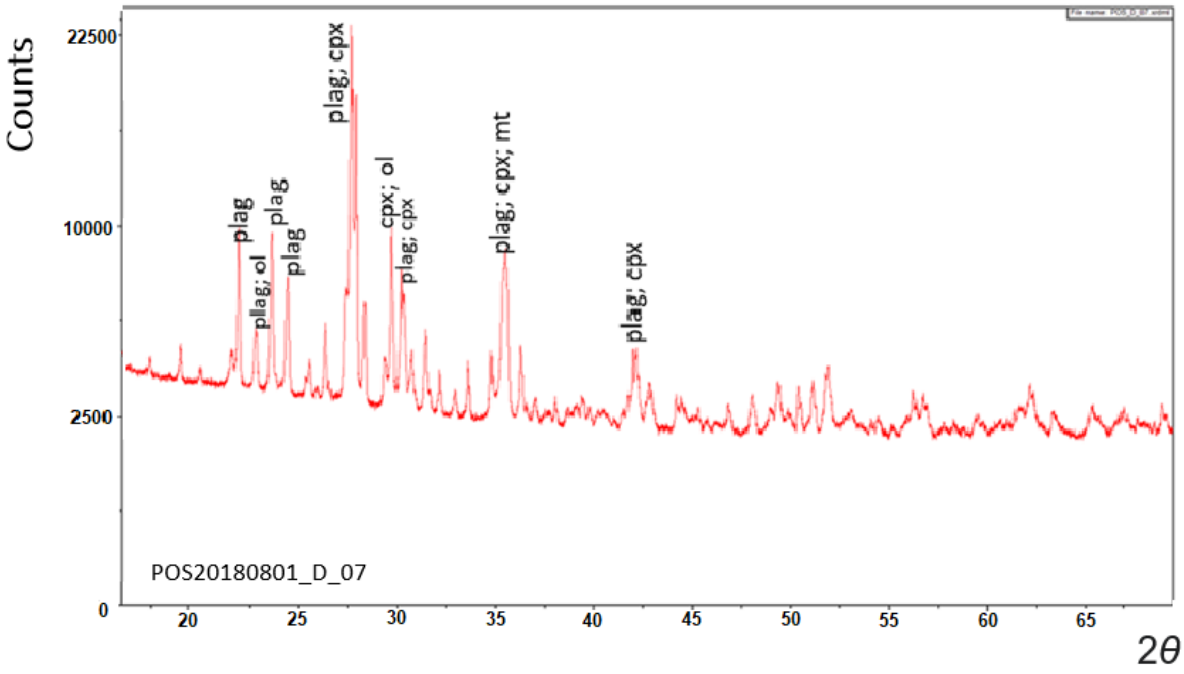
Counts
22500
10000
2500
0
plag
plag; ol
plag
plag
plag; cpx
cpx; ol
plag; cpx
plag; cpx; mt
plag; cpx
POS20180801_D_07
20
25
30
35
40
45
50
55
60
65
2θ

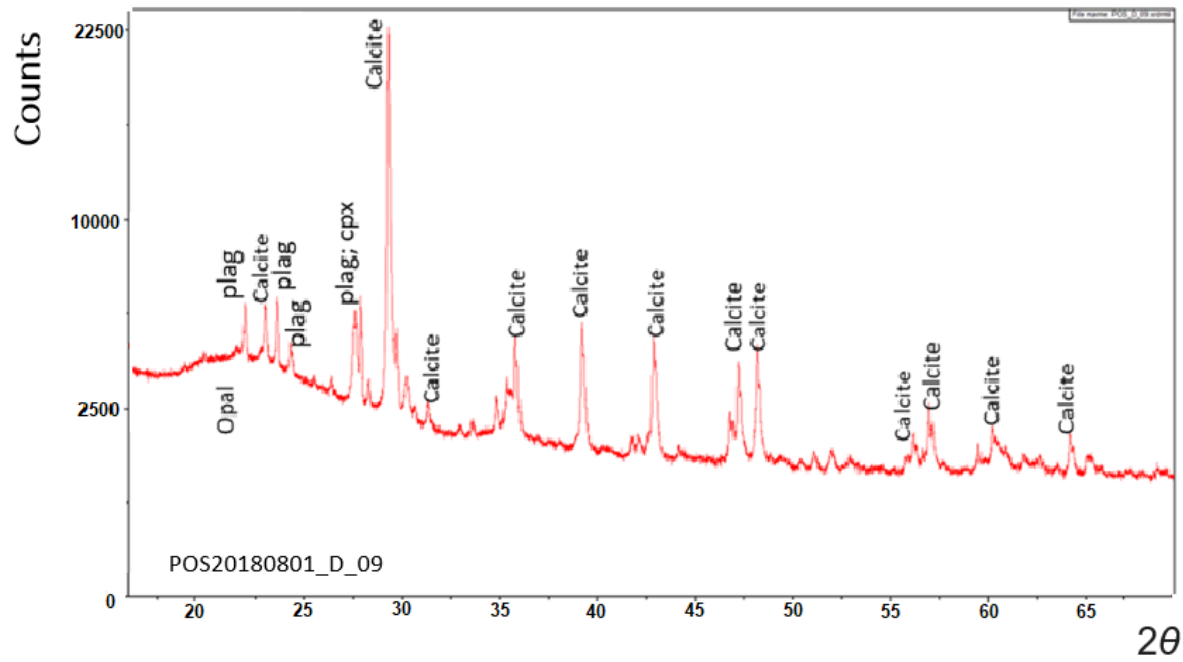
Counts
22500
10000
2500
0
Opal
plag
Calcite
plag
plag
plag; cpx
Calcite
Calcite
Calcite
Calcite
Calcite
Calcite
Calcite
Calcite
Calcite
Calcite
POS20180801_D_09
20
25
30
35
40
45
50
55
60
65
2θ

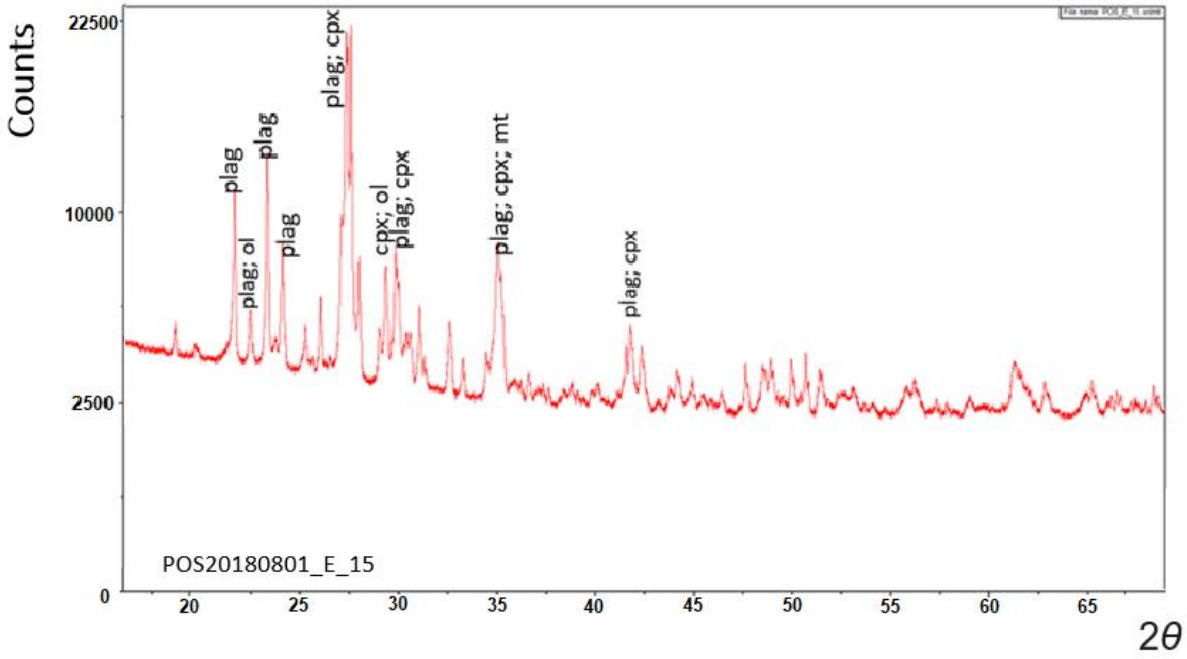
Counts
22500
10000
2500
0
plag
plag; ol
plag
plag
plag; cpx
cpx; ol
plag; cpx
plag; cpx; mt
plag; cpx
POS20180801_E_15
20
25
30
35
40
45
50
55
60
65
2θ

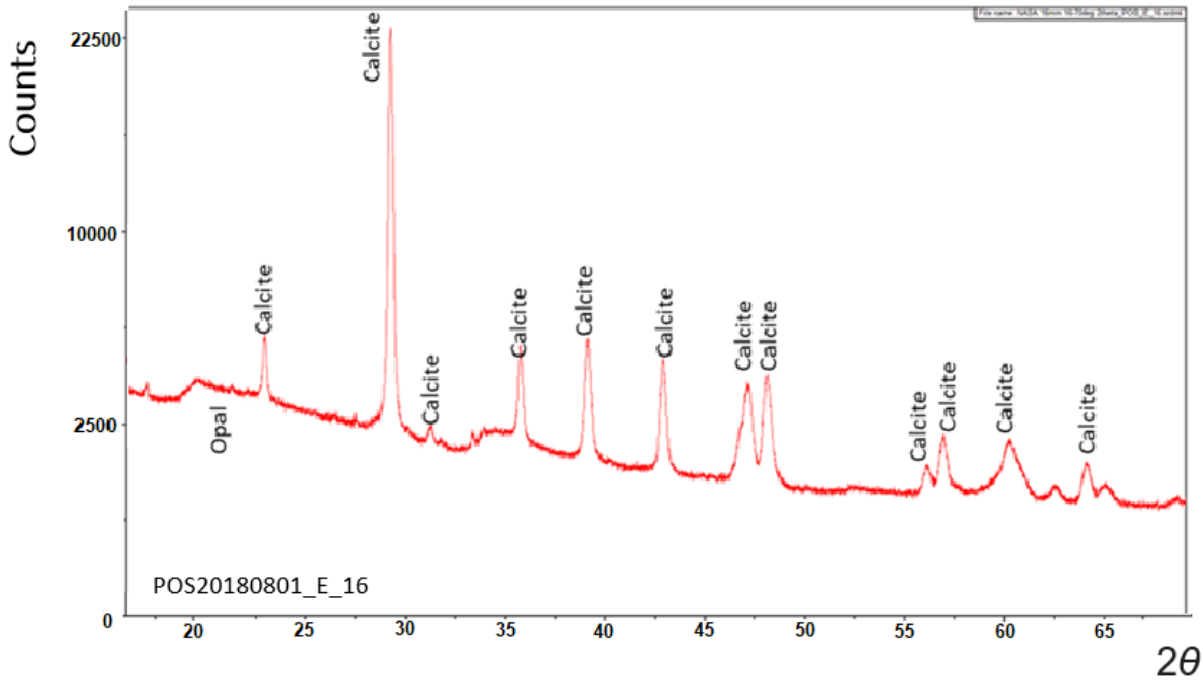
Counts
22500
10000
2500
0
Opal
Calcite
Calcite
Calcite
Calcite
Calcite
Calcite
Calcite
Calcite
Calcite
Calcite
Calcite
POS20180801_E_16
20
25
30
35
40
45
50
55
60
65
2θ

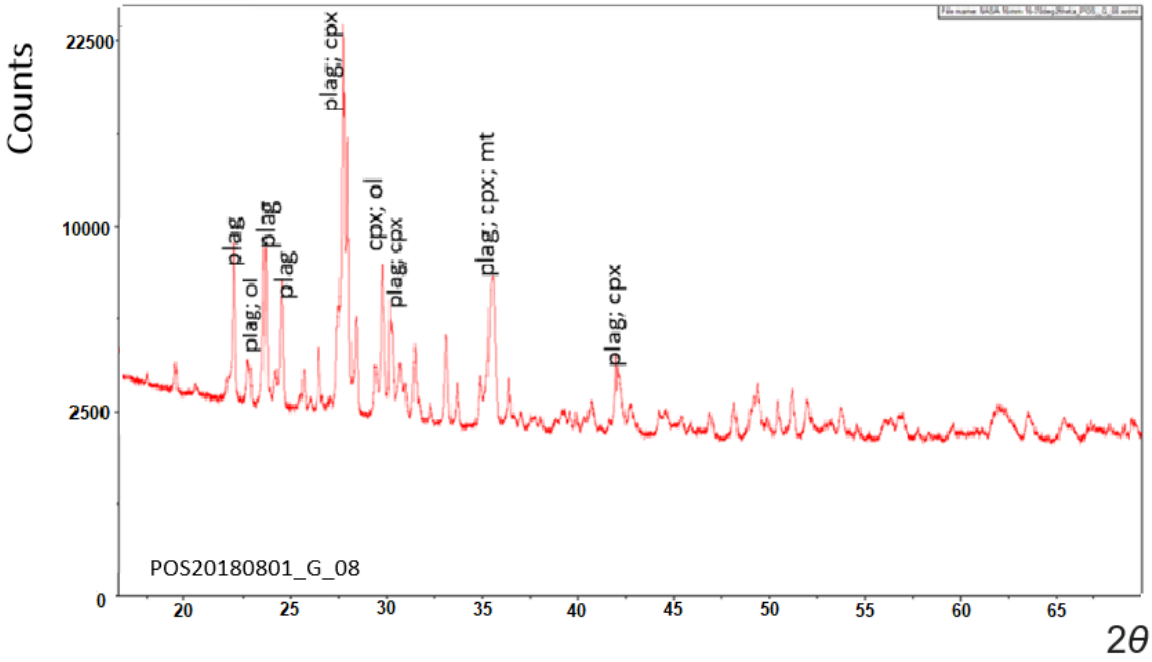
Counts
22500
10000
2500
0
plag
plag; ol
plag
plag
plag; cpx
cpx; ol
plag; cpx
plag; cpx; mt
plag; cpx
POS20180801_G_08
20
25
30
35
40
45
50
55
60
65
2θ

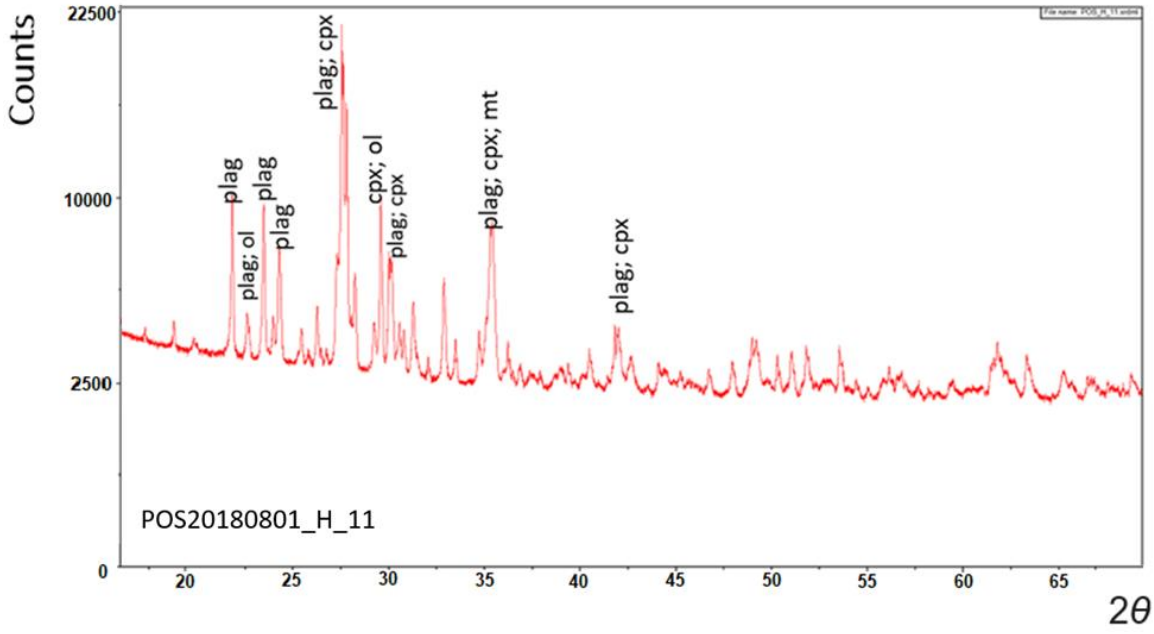
Counts
22500
10000
2500
0
plag
plag; ol
plag
plag
plag; cpx
cpx; ol
plag; cpx
plag; cpx; mt
plag; cpx
POS20180801_H_11
20
25
30
35
40
45
50
55
60
65
2θ

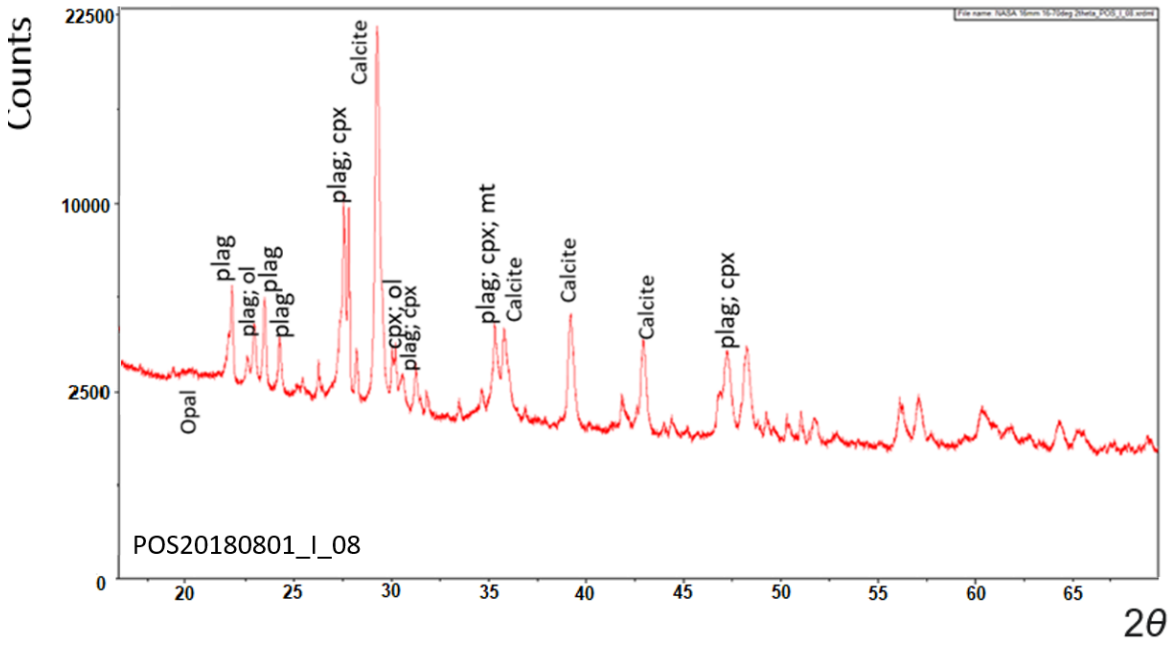
Counts
22500
10000
2500
0
Opal
plag
plag; ol
plag
plag
plag; cpx
Calcite
cpx; ol
plag; cpx
plag; cpx; mt
Calcite
Calcite
Calcite
plag; cpx
POS20180801_I_08
20
25
30
35
40
45
50
55
60
65
2θ

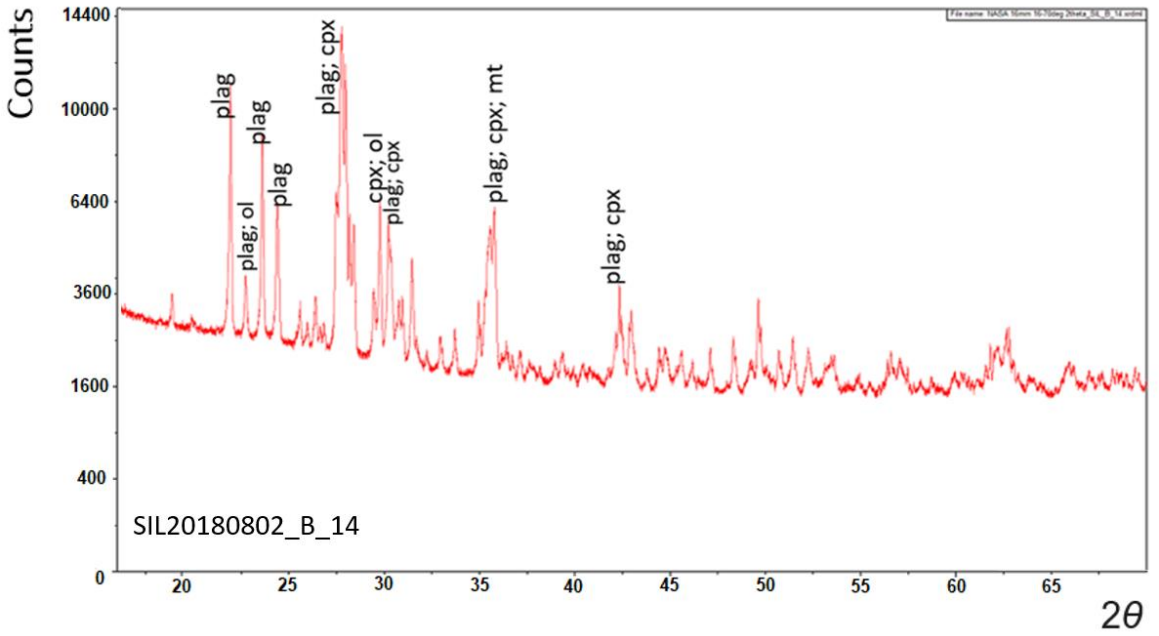
Counts
14400
10000
6400
3600
1600
400
0
plag
plag; ol
plag
plag
plag; cpx
cpx; ol
plag; cpx
plag; cpx; mt
plag; cpx
SIL20180802_B_14
20
25
30
35
40
45
50
55
60
65
2θ

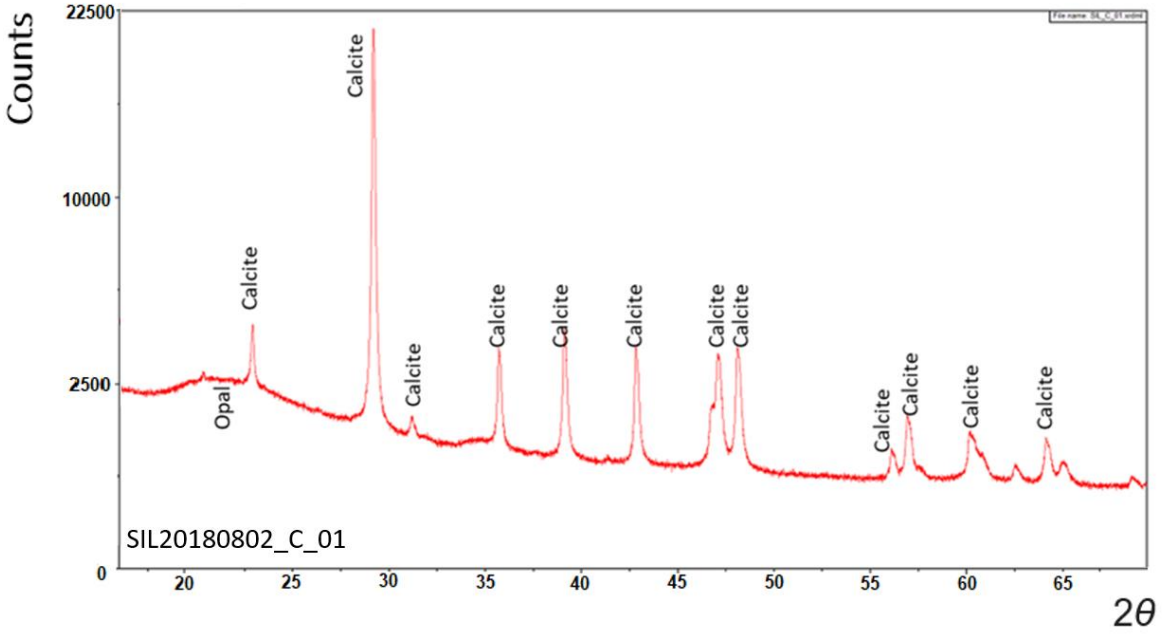
Counts
22500
10000
2500
0
Calcite
Calcite
Opal
Calcite
Calcite
Calcite
Calcite
Calcite
Calcite
Calcite
Calcite
Calcite
SIL20180802_C_01
20
25
30
35
40
45
50
55
60
65
2θ

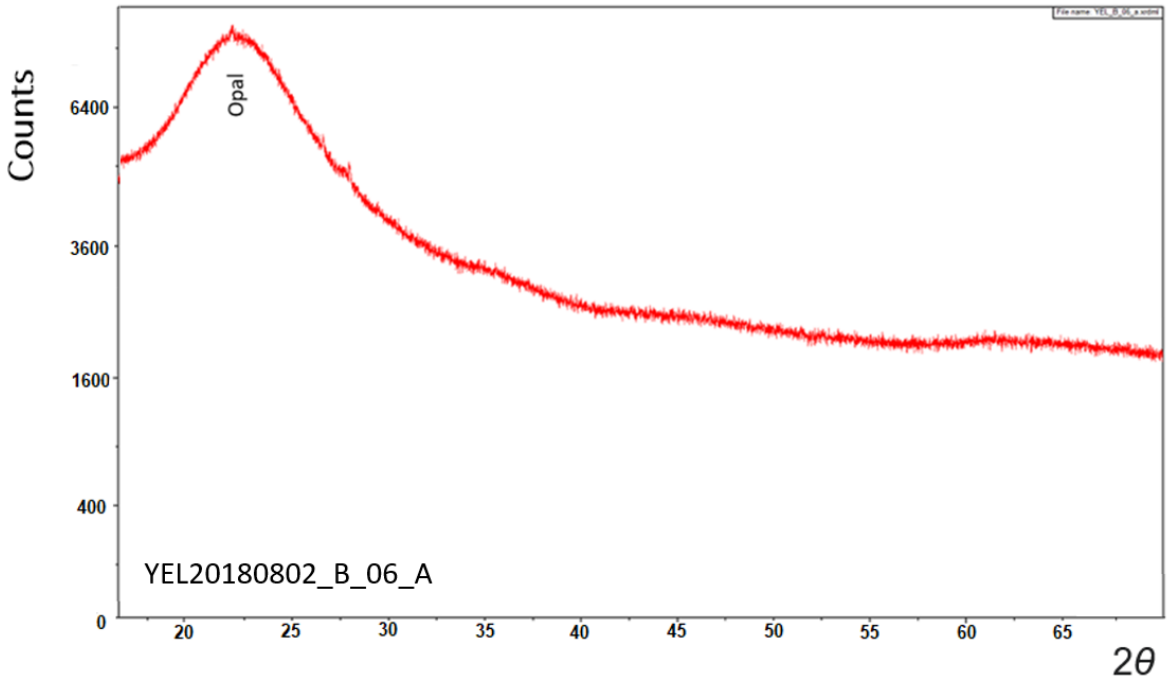
Counts
6400
3600
1600
400
0
Opal
YEL20180802_B_06_A
20
25
30
35
40
45
50
55
60
65
2θ

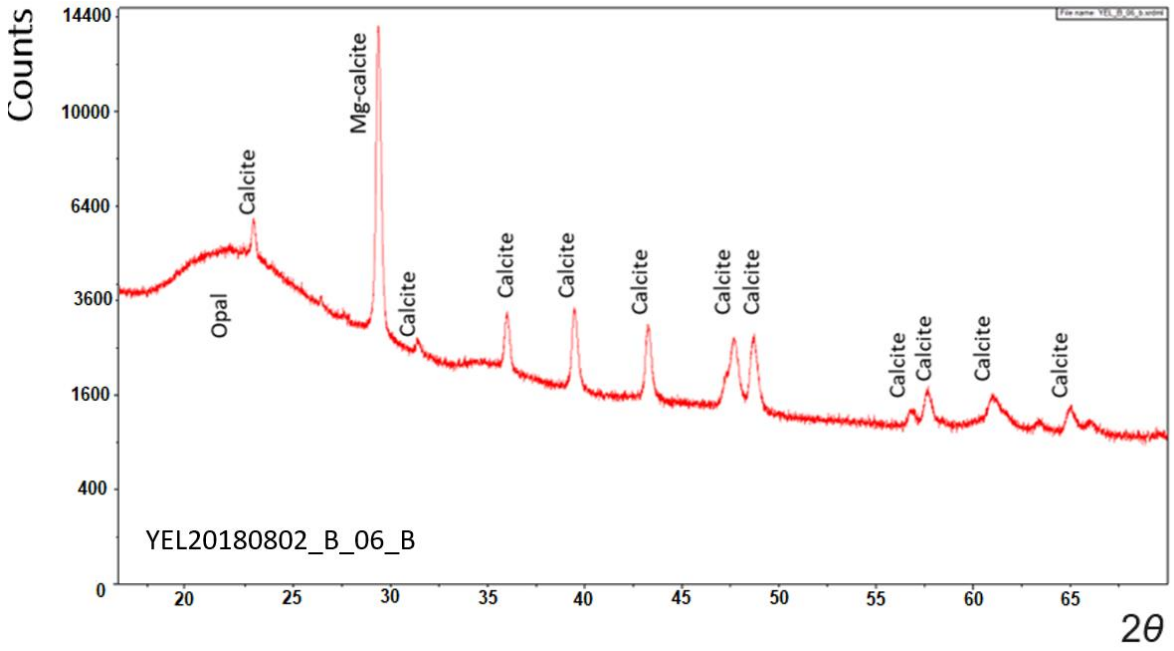
Counts
14400
10000
6400
3600
1600
400
0
Opal
Calcite
Mg-calcite
Calcite
Calcite
Calcite
Calcite
Calcite
Calcite
Calcite
Calcite
Calcite
YEL20180802_B_06_B
20
25
30
35
40
45
50
55
60
65
2θ

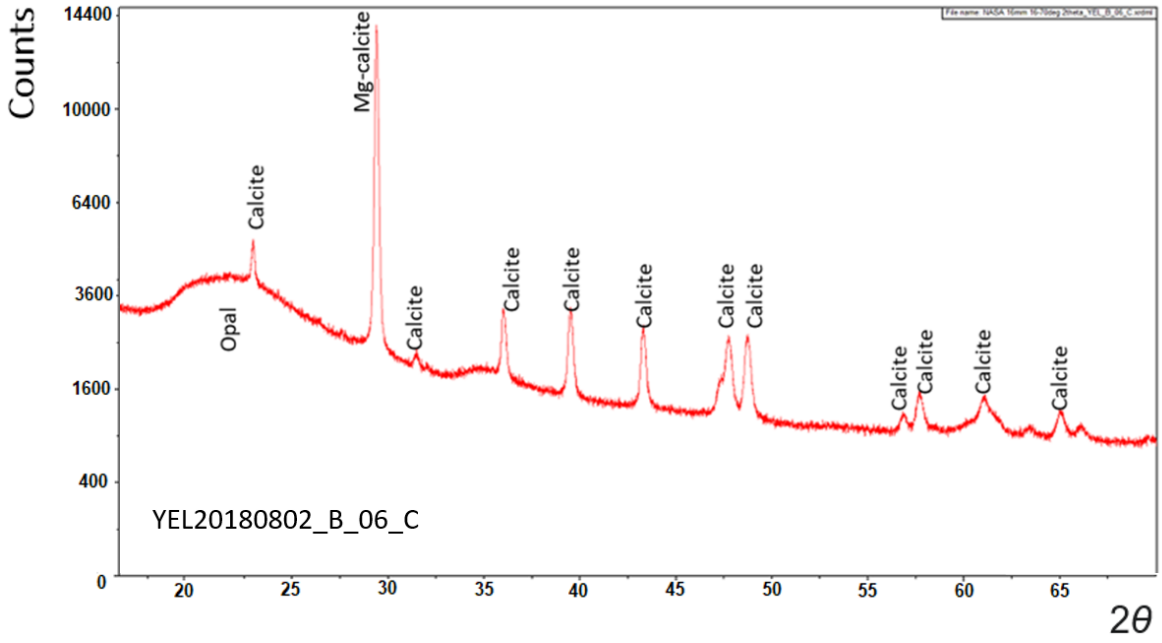
Counts
14400
10000
6400
3600
1600
400
0
Opal
Calcite
Mg-calcite
Calcite
Calcite
Calcite
Calcite
Calcite
Calcite
Calcite
Calcite
Calcite
YEL20180802_B_06_C
20
25
30
35
40
45
50
55
60
65
2θ